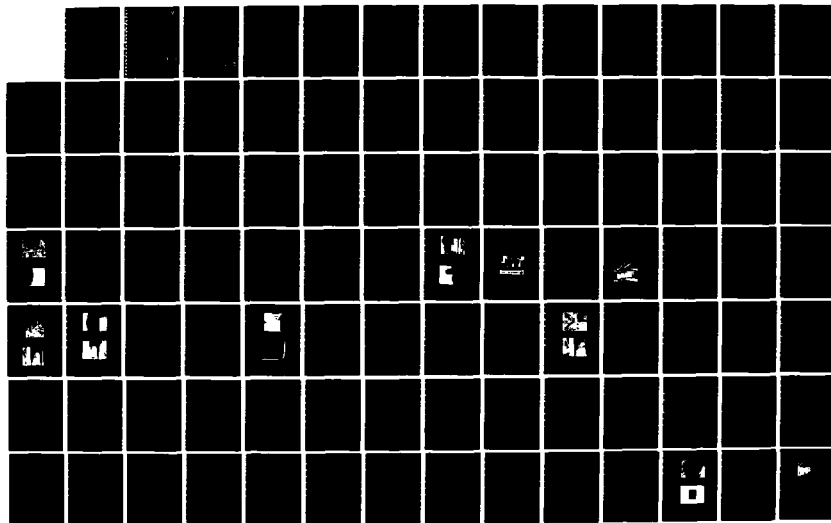
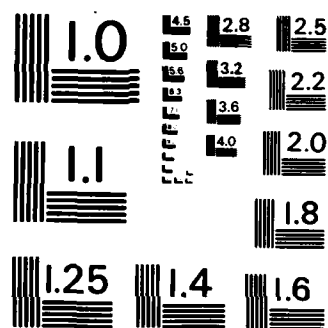


AD-A139 836

EXPERIMENTAL INVESTIGATION OF THE TURBULENT LARGE SCALE 1/3  
TEMPORAL FLOW IN T. (U) CATHOLIC UNIV OF AMERICA  
WASHINGTON DC SCHOOL OF ENGINEERING A. E P ROOD  
MAR 84 DTNSRDC-HA84-1 F/G 20/4 NL

UNCLASSIFIED





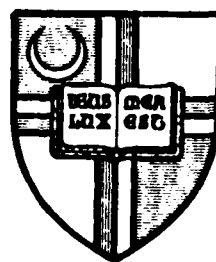
MICROCOPY RESOLUTION TEST CHART  
NATIONAL BUREAU OF STANDARDS-1963-A

AD A139836

DTIC FILE COPY

EXPERIMENTAL INVESTIGATION OF THE  
TURBULENT LARGE SCALE TEMPORAL FLOW IN  
THE WING-BODY JUNCTION

SCHOOL OF ENGINEERING  
& ARCHITECTURE



The Catholic University of America  
Washington, DC 20064

DTIC  
ELECTE  
APR 5 1984  
S D L

DISTRIBUTION STATEMENT A

Approved for public release;  
Distribution Unlimited

84 04 04 018

Accession For	
NTIS GRA&I	<input checked="checked" type="checkbox"/>
DTIC TAB	<input type="checkbox"/>
Unannounced	<input type="checkbox"/>
Justification	
By _____	
Distribution/	
Availability Codes	
Dis	Avail and/or Special
Al	



4

THE CATHOLIC UNIVERSITY OF AMERICA

EXPERIMENTAL INVESTIGATION OF THE  
TURBULENT LARGE SCALE TEMPORAL FLOW IN  
THE WING-BODY JUNCTION

A DISSERTATION

Submitted to the Faculty of The  
School of Engineering and Architecture  
Of The Catholic University of America  
In Partial Fulfillment of the Requirements  
For the Degree  
Doctor of Philosophy

by

Edwin P. Rood, Jr.

Washington, D. C.

1984

DTIC  
ELECTE  
APR 5 1984  
S D D

DISTRIBUTION STATEMENT A

Approved for public release;  
Distribution Unlimited




EXPERIMENTAL INVESTIGATION OF THE TURBULENT LARGE SCALE  
TEMPORAL FLOW IN THE WING-BODY JUNCTION

by

Edwin P. Rood, Jr.

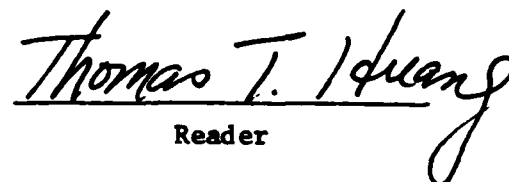
— An experimental investigation of the fluid dynamic flow in the wing-body junction was made to reveal the existence of large scale, time-dependent structures. These temporal features are discussed relative to the three major parts of the mean flow: the onset boundary layer, the wing-body junction flow characterized by the horseshoe root vortex, and the wing-body junction wake flow. Distinct flow structures, distinguished by bandwidths, were observed in all parts of the flow. One type of structure was due to the distortion of the existing structure of the onset boundary layer by the wing. A second and a third structure were newly created in the flow by the presence of the wing. These unique structures along the body were boundary layer phenomena, clearly distinguishable from ordinary Strouhal-type shedding at the wing trailing edge.

The measurements distinguishing the structures were made using applications of two-point spectral correlation analyses of the flow velocities. The application of this established procedure was made possible by modern high speed data techniques. An orderly framework of definitions and discussion is presented around which additional research can be performed to discover the details of the flow structure. 

This dissertation was approved by Mario J. Casarella, Ph.D.  
as Director, and by Timothy W. Kao, Ph.D. and  
Thomas T. Huang, Ph.D. as Readers.

  
Director

  
Reader

  
Reader

## TABLE OF CONTENTS

	Page
ACKNOWLEDGEMENTS.....	vi
LIST OF TABLES.....	viii
LIST OF ILLUSTRATIONS.....	viii
LIST OF SYMBOLS.....	xv
CHAPTER 1 - INTRODUCTION.....	1
1.1 Objective of the Research	
1.2 Experimental Method	
CHAPTER 2 - PHYSICAL FEATURES OF THE MEAN FLOW.....	5
2.1 Introduction to the Global Features	
2.2 Detailed Description of the Flow	
2.2.1 Classification of the Flow	
2.2.2 Discussion of Flow Regions	
2.3 Review of the Literature	
2.4 Rational for the Temporal Measurement	
CHAPTER 3 - DESCRIPTION OF THE EXPERIMENT.....	20
3.1 The Low Turbulence Wind Tunnel	
3.2 The Wing	
3.3 The Wall	
3.4 The Coordinate System	
3.5 Probe Positioning Devices	
3.6 Instrumentation	
3.7 Error Analysis	
CHAPTER 4 - MEAN FLOW MEASUREMENT RESULTS.....	52
4.1 The Onset Boundary Layer	
4.1.1 Velocity Profiles	
4.1.2 Turbulence Intensity	
4.2 Flow in the Wing-Body Junction	
4.2.1 Wall Pressures	

- 4.2.2 Three-Component Velocities
- 4.2.3 Flow Visualization of Separations
  - 4.2.3.1 Wing-Body Junction Flow Separations
  - 4.2.3.2 Wing-Body Junction Wake Flow Separations
  - 4.2.3.3 Wing Tip Flow Separations

CHAPTER 5 - TECHNIQUE FOR MEASUREMENT OF LARGE SCALE TEMPORAL  
FLOW.....83

- 5.1 Development of the Technique
- 5.2 Statistical Description of the Temporal Flow
  - 5.2.1 Historical Approach: Correlation Function
  - 5.2.2 Modern Approach: Spectral Density
- 5.3 Statistical Measurements
- 5.4 The Coherence
- 5.5 Further Applications of the Statistical Description
- 5.6 Low Frequency Limitations
  - 5.6.1 Discussion of the Problem
  - 5.6.2 Application to Results
- 5.7 Exploratory Results (6:1 Elliptic Nose)
  - 5.7.1 Leading Edge Correlations
  - 5.7.2 Upstream Correlations
  - 5.7.3 Mid-Wing Correlations
  - 5.7.4 Trailing Edge Correlations
  - 5.7.5 Downstream Correlations
  - 5.7.6 Significant Conclusions
- 5.8 Tests to Verify Fluid Dynamic Origin of Temporal Flow
  - 5.8.1 Sequential Measurements With and Without Wing
  - 5.8.2 Acoustic Pressure and Free-Stream Fluctuations
  - 5.8.3 Mechanical Vibration Tests
  - 5.8.4 Single-Point Two-Probe Correlations
  - 5.8.5 Effect of Varying Velocity
  - 5.8.6 Tunnel Leakage
- 5.9 Identification and Isolation of Trailing Edge Shedding Frequencies

CHAPTER 6 - LARGE SCALE TEMPORAL FLOW MEASUREMENT RESULTS (1.5:1.0 ELLIPTIC NOSE).....	159
6.1 Method for Presentation	
6.1.1 Correlation Contours	
6.1.2 Scaling Quantities	
6.1.3 The Investigated Flow Regions	
6.2 Spatial Structure of Onset Boundary Layer (Region I)	
6.3 Spatial Structure of Wing-Body Junction Flow	
6.3.1 Infinite Chord Length Wing	
6.3.1.1 Region II (Pressure Driven Boundary Layer)	
6.3.1.2 Region III (Leading Edge Separation Region)	
6.3.1.3 Region IV (Developed Secondary Flow)	
6.3.1.4 Summary Comments	
6.3.2 Finite Chord Length Wing	
6.3.2.1 Region III (Leading Edge Separation Region)	
6.4 Spatial Structure of Wing-Body Junction Wake Flow (Region VI)	
CHAPTER 7 - THE MEASUREMENT RESULTS: INTERPRETATION, CONJECTURE, CONCLUSIONS.....	213
7.1 Interpretation of the Two-Point Correlation Contours	
7.1.1 Contours in the Onset Boundary Layer	
7.1.2 Contours in the Wing-Body Junction	
7.1.3 Integrated Flow Structure	
7.2 Conjecture About the Large Scale Time Dependent Flow Structure	
7.2.1 The Onset Boundary Layer (Region I)	
7.2.2 The Effect of the Wing	

- 7.2.2.1 Region II (Pressure Driven Boundary Layer)
- 7.2.2.2 Region III (Leading Edge Separation Region)
- 7.2.2.3 Region IV (Developed Secondary Flow)

### 7.2.3 The Special Effects of the Trailing Edge

- 7.2.3.1 Region V (Trailing Edge Separation Region)
- 7.2.3.2 Region VI (Wake-Boundary Layer Region)

## 7.3 Conclusions

LIST OF LITERATURE CITED.....	238
BIBLIOGRAPHY.....	241

## ACKNOWLEDGEMENTS

There were many contributors to the success of this research. A few were prominent, and I would like to acknowledge their influence.

I thank Dr. Choung M. Lee, and the Office of Naval Research, for the financial support provided through the David Taylor Naval Ship R&D Center (DTNSRDC) that made the performance of this work possible, and especially for the encouragement to pursue research in unexplored areas.

I would like to express special gratitude to Mr. Gabriel L. Santore of DTNSRDC. As my supervisor, Mr. Santore gave me the self-confidence to imagine, propose and test the various hypotheses that formed the beginnings of this research. Without Mr. Santore's support this research would not have had a beginning.

By far the most important contributor to my completion of this work was Professor Mario Casarella, my dissertation director. I believe that he went beyond the expected duties of his position by spending countless hours listening to my ideas and plans, appropriately correcting and guiding my course as the evolving research seemed to open more doors than it was closing. Professor Casarella's perception, consideration, and patience were instrumental in my completion of this research.

I am also grateful to the readers of this dissertation: Professor Timothy Kao, who first introduced me to the phenomena of fluid mechanics as observed through vorticity; and Dr. Thomas T. Huang, who influenced me through his experimental finesse and insistence on the highest research standards.

I am very appreciative of the enlightening discussions I had with Dr. David J. Peake of NASA and Professor Roger Simpson of Virginia Polytechnic Institute and State University. My thanks are also directed to Mr. Daniel J. Sheridan and Mr. Vincent J. Monacella, of DTNSRDC, who opened the channels for the ONR support I received.

I am appreciative to Ms. Esdale McInnis of the DTNSRDC library for responsive, and often innovative, professional searches for references I requested. In many instances, the reference was obscure, the source misidentified, or the documentation only available from another library (even from another nation), or from the author. In every instance she produced the reference.

The manuscript was typed by Mrs. Kay Adams. She is a remarkable person; her bright uncomplaining personality was refreshing amid the seemingly endless revisions of text.

There are numerous others who contributed to this research; most of them are colleagues at DTNSRDC. It is significant and a credit to the DTNSRDC organization that it actively promotes academic pursuits by its associates. I hope that I can be the asset in which it believes that it has invested.

And, finally, I thank my wife, Linda, and children, Jaime and Samantha, for supporting and enduring my academic pursuits. I believe that I have become a better person for them as a result of the discipline required in the preparation of this dissertation.



## LIST OF TABLES

Figure		Page
4-1	Boundary Layer Parameters.....	55

## LIST OF ILLUSTRATIONS

1-1	Schematic of the Simplified Flow in the Wing- Body Junction.....	4
2-1	The Flow Partition.....	8
2-2	Hypothetical Flow Structure for the Wing-Body Junction Flow for a Turbulent Onset Boundary Layer.....	11
3-1	General Arrangement of Wind Tunnel.....	21
3-2	Traverse Assembly Mounted on Tunnel Roof.....	22
3-3	Tunnel Inlet Trip.....	22
3-4	Pressure Spectrum in Tunnel Free Stream.....	24
3-5	Investigated Wing Profiles.....	25
3-6	Photograph of Compression Clamp Holding Tail Piece for Finite Chord Length Wing.....	29
3-7	Photograph of Compression Clamps Holding Extended Parallel Mid-Section Piece for Infinite Chord Length Wing.....	29
3-8	Boundary Layer Trip Wires Installed on Noses of Wings.....	30
3-9	Photograph of the Wing and Wall Configuration.....	32
3-10	The Coordinate System.....	34
3-11	Traverse Positioning Device.....	36
3-12	Circular Section Rod Protruding Into Test Section....	36
3-13	Probe Holder Assembly.....	37
3-14	Fixed Probe Assembly.....	37

	Page
3-15	Schematic of the Velocity Measurement System..... 39
3-16	Photograph of Pitot-Static Tube in Position..... 40
3-17	Close-Up Photograph of Pitot-Static Tube..... 40
3-18	Calibration Set-Up to Determine Angles Between Hot Film Elements..... 45
3-19	Temperature Probes Installed Downstream from Wing in Tunnel..... 45
3-20	Schematic of the Pressure Measurement System..... 48
4-1	Locations for Velocity Profiles..... 53
4-2	Velocity Profile Matches for P(-2.5, $y/\delta$ , 1.5) for $U_0 = 36$ m/s..... 56
4-3	Velocity Profile Matches for P(-2.5, $y/\delta$ , 1.5) for $U_0 = 18$ m/s..... 57
4-4	Velocity Profile Matches for P(-2.5, $y/\delta$ , -1.5) for $U_0 = 36$ m/s..... 58
4-5	Velocity Profile Matches for P(-2.5, $y/\delta$ , -1.5) for $U_0 = 18$ m/s..... 59
4-6	Velocity Profile Matches for P(-6.5, $y/\delta$ , 1.5) for $U_0 = 38$ m/s..... 60
4-7	Velocity Profile Matches for P(-6.5, $y/\delta$ , 1.5) for $U_0 = 19$ m/s..... 61
4-8	Velocity Profile Matches for P(-6.5, $y/\delta$ , -1.5) for $U_0 = 38$ m/s..... 62
4-9	Velocity Profile Matches for P(-6.5, $y/\delta$ , -1.5) for $U_0 = 19$ m/s..... 63
4-10	Turbulence Intensity Profile for Onset Boundary Layer..... 66
4-11	Wall Pressures Upstream From the Wing..... 68
4-12	Wall Pressures Along Upstream Pressure Ridge..... 69
4-13	Wall Pressures Along Side of Wing..... 70
4-14	Cross-Stream Velocities at P (2.00, $y/\delta$ , $z/t > 0.0$ ).. 72

Figure		Page
4-15	Contours of Constant Longitudinal Velocity in the Plane ( $2.00, y/\delta, z/t > 0.0$ ).....	73
4-16	Surface Flow Visualization Results in Wing-Body Junction.....	75
4-17	Additional Surface Flow Visualization Results.....	77
4-18	Flow Visualization Results for Separated Trailing Edge Flow.....	79
4-19	Schematic of Trailing Edge Separation.....	80
4-20	Wing Tip Flow Visualization Results.....	82
5-1	Schematic Comparison of Measured Correlation Functions for Previous and Present Measurements.....	96
5-2	Example Lowest Frequency Spectral Content of Two-Point Lateral Velocity Correlations.....	98
5-3	Example Measured Correlation Function for Lowest Frequency Two-Point Lateral Velocity Correlations....	99
5-4	Streamwise Locations of Measurement Planes for Global Experimental Description of Temporal Flow.....	103
5-5	Leading Edge Correlations.....	105
5-6	Cross-Boundary Layer Velocity Correlations at Leading Edge Region.....	108
5-7	The Dependency of Relative Phase on Upstream Position of Second Probe.....	110
5-8	The Effect of Flow Antisymmetry on the Upstream Correlations.....	113
5-9	Correlation Measurements for Mid-Wing and Leading Edge Velocities.....	115
5-10	Mid-Wing Plane-of-Symmetry Correlations for $ z/t  = 0.5$ .....	117
5-11	Mid Wing Plane-of-Symmetry Correlations for $ z/t  < 0.5$ .....	118
5-12	Plane-of-Symmetry Correlations With Reference Probe Well Inside Boundary Layer and Near the Wing.....	122

Figure		Page
5-13	Plane-of-Symmetry Correlations Showing Cross-Stream Spatial Extent Well Outside Nominal Boundary Layer...	125
5-14	Plane-of-Symmetry Velocity Correlations Showing Non-Zero Coherence Outside Nominal Boundary Layer and Relatively Far From Wing.....	128
5-15	Plane-of-Symmetry Correlations Showing Strong Outer-Inner Boundary Layer Coherence.....	129
5-16	Mean Velocity Profiles for $x/t = 3.0$ Showing Asymmetry Produced by Wing at Small Incidence Angle..	132
5-17	Correlations Between Mid-Wing and Trailing Edge Regions.....	133
5-18	Two-Point Velocity Correlations in One Leg of Root Vortex at Trailing Edge ( $x/t = 5.12$ ).....	134
5-19	Low Frequency Out-of-Phase Correlations for One Side of Plane-of-Symmetry.....	136
5-20	Trailing Edge Correlations Showing Phase Shift for Increased Values of $z/t$ .....	138
5-21	Asymmetric Wake Profiles Produced by Spatially Unequal Vortex Legs for Wing at Incidence.....	140
5-22	Two-Point Velocity Correlations Downstream from Wing.....	141
5-23	Representative Downstream Correlations.....	143
5-24	Correlations Across Vortex Boundary for Higher Frequency 50 Hz Temporal Flow.....	144
5-25	Correlations Across Vortex Boundary for Lower Frequency 4 Hz Temporal Flow.....	145
5-26	Comparison of Velocity Correlations With and Without the Wing Present.....	148
5-27	Example Acoustic Pressure-Boundary Layer Velocity Correlations.....	150
5-28	Example Mechanical Vibration Test Results for Correlations of Structural Acceleration With Flow Velocity in Wing-Body Junction.....	151
5-29	Example Test Results Showing Nearly Identical Output When Probes Placed in Close Proximity.....	153

Figure		Page
5-30	Measurements of the Peak Coherence Frequency as a Function of Velocity.....	154
5-31	Data Showing Shedding Frequency at Trailing Edge of $a/b = 6.0$ Elliptic Nose Wing.....	156
5-32	Data Showing Shedding Frequency at Trailing Edge of $a/b = 1.5$ Elliptic Nose Wing.....	158
6-1	Example Calculation of $S_y$ from Measurement Data.....	161
6-2	Schematic Showing Locations of Measurement Planes for the Infinite and Finite Chord Length Wings.....	164
6-3	Contours of Constant $S_y$ for the Onset Boundary Layer for the First Wall Location.....	166
6-4	Contours of Constant $S_y$ for the Onset Boundary Layer for the Second Wall Location.....	167
6-5	Example Spectral Distribution of Correlation Measurement Data for the Onset Boundary Layer.....	168
6-6	Example Spectral Distribution of Correlation Measurement Data as Functions of Free Stream Speed.....	169
6-7	Contours of Constant $S_y$ for the Fixed Probe at $y_0/\delta = 0.40$ .....	172
6-8	Contours of Constant $S_y$ for the Fixed Probe at $y_0/\delta = 0.60$ .....	173
6-9	Contours of Constant $S_y$ in Region II.....	174
6-10	Example Spectral Distributions of Correlation Measurement Data for Region II.....	175
6-11	Contours of Constant $S_y$ in Region III Upstream from the Wing Leading Edge.....	176
6-12	Contours of Constant $S_y$ in Region III Downstream from Wing Leading Edge ( $P_A$ Close to Wing).....	178
6-13	Contours of Constant $S_y$ in Region III Downstream from Wing Leading Edge ( $P_A$ Far from Wing).....	179
6-14	Example Spectral Distributions of Correlation Measurement Data for Region III.....	181

Figure		Page
6-15	Across-Wing Contours of Constant $S_y$ for Region III ( $y_0/\delta, z_0/t$ ) = (0.15, -0.15).....	183
6-16	Across-Wing Contours of Constant $S_y$ for Region III ( $y_0/\delta, z_0/t$ ) = (0.25, -0.25).....	184
6-17	Across-Wing Contours of Constant $S_y$ for Region III ( $y_0/\delta, z_0/t$ ) = (0.38, -0.38).....	185
6-18	Across-Wing Contours of Constant $S_y$ for Region III ( $y_0/\delta, z_0/t$ ) = (0.60, -0.60).....	186
6-19	Across-Wing Contours of Constant $S_y$ for Region III ( $y_0/\delta, z_0/t$ ) = (0.15, -0.38).....	187
6-20	Across-Wing Contours of Constant $S_y$ for Region III ( $y_0/\delta, z_0/t$ ) = (0.25, -0.75).....	188
6-21	Across-Wing Contours of Constant $S_y$ for Region III ( $y_0/\delta, z_0/t$ ) = (0.25, -0.50).....	189
6-22	Across-Wing Contours of Constant $S_y$ for Region III ( $y_0/\delta, z_0/t$ ) = (0.38, -0.15).....	190
6-23	Example Across-Wing Spectral Distributions of Correlation Measurement Data for Symmetric Probe Positions in Region III.....	192
6-24	Example Across-Wing Spectral Distributions of Correlation Measurement Data for Non-Symmetric Probe Positions in Region III.....	193
6-25	Across-Wing Contours of Constant $S_y$ for Region IV ( $y_0/\delta, z_0/t$ ) = (0.15, -0.15).....	195
6-26	Across-Wing Contours of Constant $S_y$ for Region IV ( $y_0/\delta, z_0/t$ ) = (0.40, -0.40).....	196
6-27	Across-Wing Contours of Constant $S_y$ for Region IV ( $y_0/\delta, z_0/t$ ) = (0.15, -0.40).....	197
6-28	Across-Wing Contours of Constant $S_y$ for Region III for Finite Chord Length Wing ( $y_0/\delta, z_0/t$ ) = (0.15, -0.15).....	199
6-29	Across-Wing Contours of Constant $S_y$ for Region III for Finite Chord Length Wing ( $y_0/\delta, z_0/t$ ) = (0.25, -0.25).....	200

Figure		Page
6-30	Contours of Constant $S_y$ for Region VI ( $P_A$ in Wing Shadow).....	203
6-31	Example Spectral Distributions of Correlation Measurement Data for Region VI ( $P_A$ in Wing Shadow).....	204
6-32	Contours of Constant $S_y$ for Region VI for Bandwidth III ( $P_A$ Outside Wing Shadow).....	208
6-33	Contours of Constant $S_y$ for Region VI for Bandwidth II ( $P_A$ Outside Wing Shadow).....	209
6-34	Example Spectral Distributions for Correlation Measurement Data for Region VI Showing Bandwidth Separation.....	211
7-1	Joint Probability Density Function Contours for Two-Point Velocity Correlations.....	217
7-2	Ranges of $u_B'/\sigma_B$ for 0.7 Probability of Occurrence for Several Values of $u_A'/\sigma_A$ .....	218
7-3	Example Auto-Correlation Functions for Onset Boundary Layer.....	221
7-4	Spatial Location of Integrated Flow Structure Immediately Downstream from the Wing Trailing Edge.....	225
7-5	Jetting Model of Flow Structure.....	227
7-6	Eddy Model of Flow Structure.....	227
7-7	Schematic of Flow Structure and Separations at Wing Trailing Edge.....	233
7-8	Schematic of Flow Parts in Vicinity of Rolled Up Vortex.....	234
7-9	Schematic Identifying Physical Sources for Anti-Symmetric Pockets of Correlated Flow Fluctuations....	235

# LIST OF SYMBOLS

$A(t)$	time history of signal A
$B(t)$	time history of signal B
$c$	chord length of wing
$C_p$	pressure coefficient, $(p-p_s)/(1/2 \rho U_o^2)$
$f$	frequency (Hz)
$\tilde{f}$	non-dimensional frequency, $f\delta/U_o$
$G$	shape parameter
$G_{AB}$	cross-power spectral density at positions A and B $\overline{v_A' v_B'} / \Delta f$
$H$	shape parameter
$K$	correlation coefficient for spectral component (a function of $f$ )
$n_d$	number of independent ensembles in the averaging process
$N$	total number of ensembles
$p$	pressure
$p_s$	static pressure
$p_t$	total pressure
$P_{-x}$	position of probe at location "x"
$S_\gamma$	correlation contour variable, $\cos(\phi_B - \phi_A) \sqrt{\gamma_{AB}}^2$
$R_\delta$	boundary layer thickness Reynolds number, $U_o \delta / \nu$
$R_o$	momentum thickness Reynolds number $U_o \theta / \nu$
$t$	thickness of wing; time
$u$	local velocity; velocity parallel to x-axis; longitudinal velocity
$U_o$	free stream velocity
$v$	velocity parallel to y-axis; transverse velocity; voltage of measurement signal
$(x, y, z)$	coordinate scales, see section 3.4
$(x_o, y_o, z_o)$	coordinates of fixed probe
$\alpha$	angle of incidence of wing
$\gamma_{AB}^2$	$ \phi_{AB} ^2 / (\phi_A \phi_B)$ , the coherence
$\delta$	boundary layer thickness, value of $y$ where $u/u_o = 0.99$ ; incremental change in the quantity prefixed by $\delta$



$\delta^*$	displacement thickness
$\epsilon$	error
$\theta$	momentum thickness
$\mu$	viscosity
$\nu$	kinematic viscosity
$\rho$	mass density
$\tau$	time delay
$\phi$	phase angle
$\phi_{AB}$	cross-power spectral density at positions A and B, $\overline{u_A' u_B'} / \Delta f$
$\tilde{\phi}$	non-dimensional power spectral density, $\phi / \delta U_0$

**Subscripts:**

A	value at position A; position of probe producing signal A(t)
---	--

**Superscripts:**

(')	instantaneous fluctuations about mean
(-)	overbar: ensemble average; e.g. the numerical average obtained by summing the individual time history spectra and dividing by the total number of spectra

## CHAPTER 1

### INTRODUCTION

#### 1.1 Objective of the Research

The objective of this research was to measure the large scale temporal structure of the turbulent boundary layer flow about a wing-body junction which gives rise to a horseshoe root vortex. This flow is a complex interaction between the onset boundary layer, the vortex legs, and the wing wake. Measurements were made to confirm the existence of quasi-periodic structure and to determine some of the governing physics of the temporal features of the vortex. These temporal features are not evident from time-averaged measurements of the flow and have not been previously studied. Consequently, the knowledge gained from this study is fundamental, and should prove useful for guiding further research applicable to specific problems in machinery or propulsor design such as unsteady (intermittent) separation, and rotor vibration problems.

In the context of this investigation, the following definitions are given to the terms large scale, low frequency, quasi-periodic and coherent. The meaning of large scale is that the organized motion of the structure encompasses a spatial extent

large relative to the wing thickness or the boundary layer thickness. Low frequency implies a temporal periodicity at least an order of magnitude larger than the ratio of the wing thickness to the flow velocity. The temporal structure of the flow is quasi-periodic, meaning that the motion is cyclic for short time durations, but is uncorrelated over long time durations. There is an element of randomness present in the velocity field. The flow is coherent within the meaning that organized motion, or structure, superposed on the mean flow is spatially and temporally confined. "Spatially confined" means that at every instant in time the definite phase relationship between the particle velocities in the structure is over a subregion of the entire fluid domain. "Temporally confined" means there is a definite time scale characterizing the autocorrelation of the structure.

There is no information in the open literature directly addressing the large scale, low frequency flow about a wing-body junction. This study is an attempt to characterize the problem, which is best approached through a thorough understanding of the complex mean flow patterns in the wing-body junction. The mean flow may suggest physical mechanisms (and the locations where those mechanisms might be expected to be observed) that govern the temporal structure. It was concluded from previous studies of the mean flow that unsteady motion could be expected in the vicinity of the primary three-dimensional separation at the wing leading edge, and in the separated flow at the wing trailing edge.

Preliminary measurements using this hypothesis as a guide, and a subsequent reevaluation, have led to the premise that primary attachment, and possibly secondary separation, at the leading edge region may be responsible for the initiation of conditionally stable temporal structure. Furthermore, it is shown as a result of this investigation that the trailing edge pressure condition on the wing is an important factor in determining the organization, growth and spatial dominance of these and additional instabilities generated near the wing trailing edge. Evidence is also presented that the large scale time dependent structure emitted from the wing-body junc-

tion is in part related to the large-scale structure in the onset boundary layer.

## 1.2 Experimental Method

The wing-body junction flow was established by mounting a streamlined wing-like protuberance onto a flat wind tunnel wall (the body). The set-up is shown in Figure 1-1. The wing was a constant two-dimensional section with a semi-elliptic nose profile, a section of parallel middle-body, and a circular arc tail profile. The onset wall boundary layer was generated along the entire inlet length of the wind tunnel, was thick relative to the wing, and was fully turbulent with a momentum thickness Reynolds number of at least 5500. The detailed description of the experiment can be found in Chapter 3.

A pitot tube was used to measure the mean velocity in the onset boundary layer and an x-array hot film probe was used to measure the velocity components at selected positions around the wing. The surface static pressure was measured on the body (the wall) in the vicinity of the nose of the wing. The large scale temporal flow was measured using two-point velocity correlations obtained with single element hot film probes. Specifically, the auto-spectral densities, the coherence, and the relative phase were experimentally obtained and used to determine the space-time extent of the temporal flow. Oil dot and oil film techniques were employed to assess mean features of the flow to provide clues to explain the physical sources for the temporal flow.

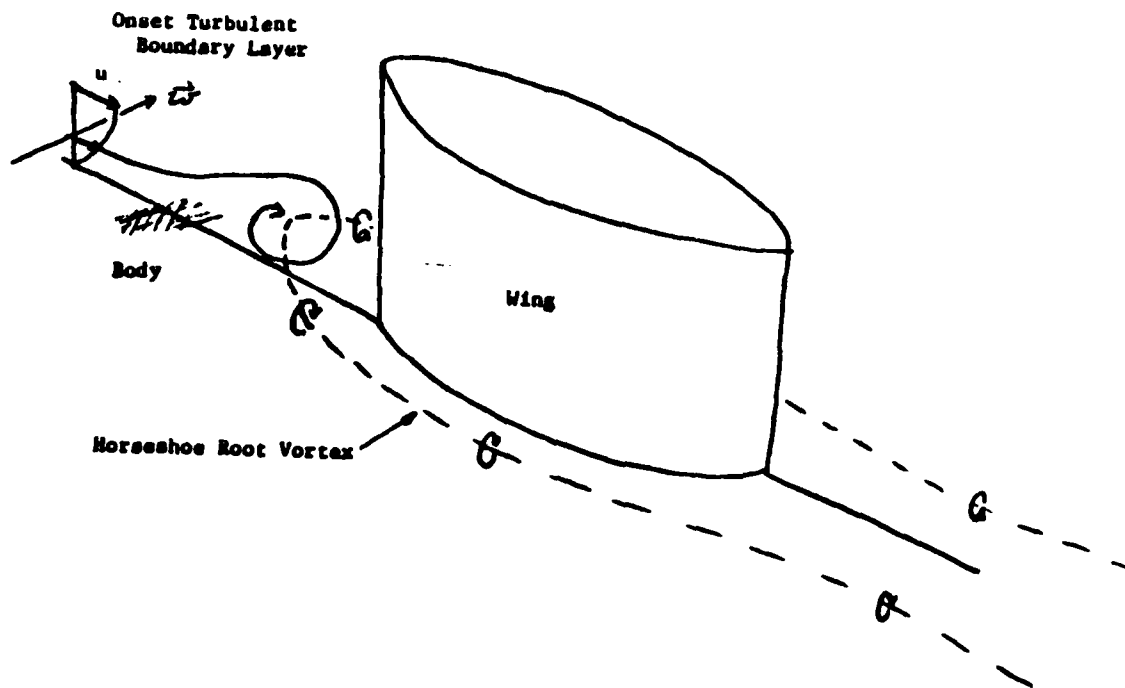


Figure 1-1: Schematic of the Simplified Flow in the Wing-Body Junction

## CHAPTER 2

### PHYSICAL FEATURES OF THE MEAN FLOW

#### 2.1 Introduction to the Global Features

The flow around a wing-body junction is complex. It consists of a turbulent boundary layer-pressure gradient-viscous wake interaction that is pressure driven in some restricted regions, Reynolds stress driven in other regions, and viscous dominated in most other regions. The essential feature of the interaction, the horseshoe root vortex, was shown in the schematic of Figure 1-1.

The figure depicts a streamlined protuberance, the wing, mounted normal to a surface, the body. The body is sufficiently large that a turbulent boundary layer exists upstream from the wing. The wing extends out from the body a distance far enough that there is two-dimensional potential flow around a considerable portion of the wing between the boundary layer and the wing tip. This specification differentiates the wing from a simple roughness element submerged within the boundary layer. The wing is streamlined so that there are no flow separations attributed to break-away at a body corner. More precisely, there is no "two-dimension-

al" separation, with separation line parallel to the wing mid-chord line, other than that which may occur very near the trailing edge as the wake is formed.

In the simplest conception the vorticity present in the onset boundary layer is wrapped around the leading edge of the wing to form the horseshoe root vortex. The fluid approaching the wing encounters an adverse pressure gradient coincident with the presence of the wing, and is slowed. Meanwhile, fluid off to the side of the wing passes by the wing without experiencing much effect. Consequently, fluid elements in one part of a vortical line element are decelerated relative to fluid in other parts. The subsequent wrapping of the vorticity line element around the leading edge results in the appearance of a region of concentrated vorticity known as the root, or horseshoe, vortex.

The effect of this skewing of the transverse vorticity is the generation of streamwise vorticity and a three-dimensional flow velocity. Whereas the flow upstream from the wing has one component of velocity, which is directed in the streamwise direction, the flow in the root vortex has components in a plane normal to the streamwise direction due to the existence of the streamwise vorticity. These components comprise the so-called secondary flow.

The flow does not recover to its original state downstream from the wing. The root vortices persist. Furthermore, there are complex interactions between the vortices, the separated flow near the wing trailing edge, and the viscous wake of the wing. Throughout all of this disruption of the flow, the root vortices remain inside the boundary layer from which they were generated; that is, they do not lift up and away from the body. Nevertheless, the customary boundary layer approximations useful in flow calculations are invalid; the flow is described by elliptic differential equations.

The complete detailed description of the flow is quite complicated. The flow will now be explained in more depth.

## 2.2 Detailed Description of the Flow

In order to discuss the many features of the flow about the

wing-body, it is convenient to divide the flow into various regions according to the governing dynamics of the physical features. The various regions are shown in Figure 2-1. In addition to the single spiral corresponding to the primary root vortex, there are additional spirals corresponding to two secondary vortices. These spiraling flows are associated with three-dimensional flow separation, which further adds to the complexity of the flow. The highlights of the flow regions are presented below.

To a considerable degree, the description is conjecture, consistent with observations and measurements. The reason for this is that the detailed flow, especially in the separated region, has not been sufficiently measured. There is further discussion of this observation in Section 2.3.

The discussion below is strictly applicable only to turbulent onset boundary layers. The flow for laminar boundary layers is less ambiguous because it can be studied with low speed flow visualization such as the smoke wire.

#### 2.2.1 Classification of the Flow

The turbulent boundary layer - wake interaction flow around a wing attached to a body consists of three major parts, which are further divided into seven regions. Part One of the flow is concerned with the onset turbulent boundary layer and the three-dimensional separation at the leading edge. It is in this part that the primary root vortex, and possibly secondary vortices, are established. The flow leaves the leading edge region, and the associated strong pressure gradients, and enters Part Two. The exact division between Part One and Part Two is arbitrary, but it is clear that there is no strong pressure gradient in Part Two, although there may be a small gradient as the trailing edge is approached. The horseshoe root vortex experiences viscous diffusion and the effects of counterrotation effected by anisotropy of the Reynolds stresses. The flow is slowly varying in the streamwise direction; the flow is in some sense in equilibrium. The flow experiences a rising pressure gradient as it nears the trailing edge of the wing and enters Part Three. The exact division between



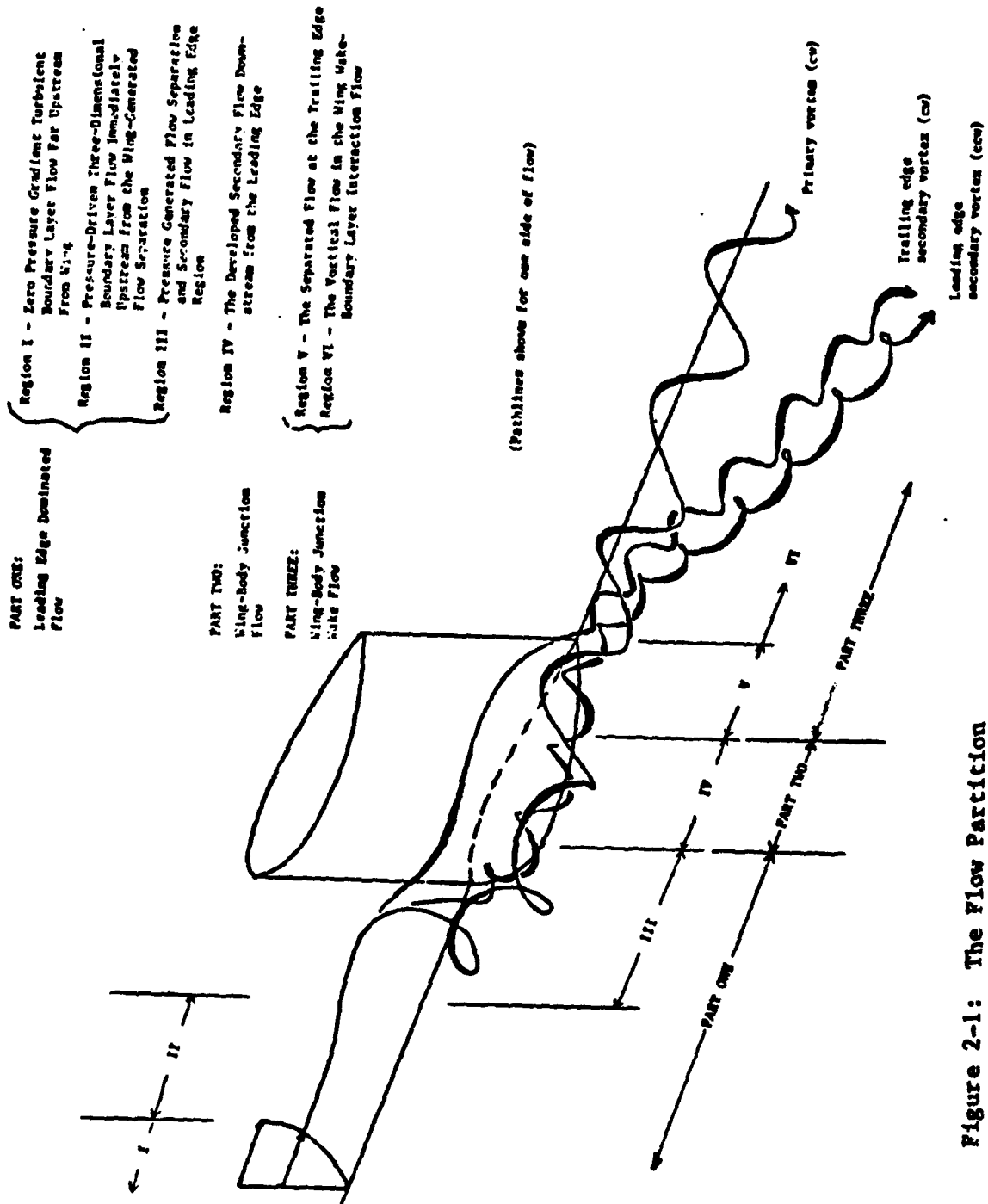


Figure 2-1: The Flow Partition

Part Two and Part Three of the flow is also arbitrary; however, the secondary flow in Part Three is rapidly changing in the streamwise direction. Characteristics of the flow are a downward movement along the wing towards the body and/or a movement away from the wing characteristic of imminent flow separation. A new vortex springs from the wing-body junction to form a v-shaped wedge behind the wing. Inside of this wedge the flow is viscous wake.

As shown in Figure 2-1, the three parts of the flow are denoted the Leading Edge Dominated Flow, the Wing-Body Junction Flow, and the Wing-Body Junction Wake Flow. These designations are a mix of terms gleaned from the literature; there is no set terminology that has evolved yet. In fact, the problem at hand is known variously as the wing-body junction, boundary layer - wake interaction, blade-end wall, and numerous other names.

#### 2.2.2 Discussion of the Flow Regions

REGION I: Zero pressure gradient turbulent boundary layer flow far upstream from the wing

The onset boundary layer in the ideal situation is two-dimensional and fully developed in that the mean velocity profile follows the nominal  $1/7$  - power law, and the momentum thickness Reynolds number is of the order 5000 or larger. A spectral analysis of the flow shows no peaks or "bumps" on the otherwise smooth distribution. The velocities are uncorrelated in the horizontal plane for nominal distances beyond one boundary layer thickness for the frequencies characterizing the temporal flow. There may be measurable correlation for very low frequencies, but these are clearly separable by spectral analysis techniques from the temporal features of the flow to be investigated.

REGION II: Pressure-driven three-dimensional boundary layer flow immediately upstream from the wing-generated flow separation

The onset turbulent boundary layer encounters the adverse pressure gradient established by the presence of the wing. The three-dimensional pressure profile exhibits a ridge extending upstream with diminishing height, and sloping off on either

side of the ridge. The pressure ridge extends upstream a distance of order 10 wing thicknesses for a 6:1 semi-elliptic (major axis) nose. As the nose is made more slender (the ratio  $n:1$  made larger), or the boundary layer made thinner ( $\delta/t$  decreased in value) the pressure ridge length upstream diminishes.

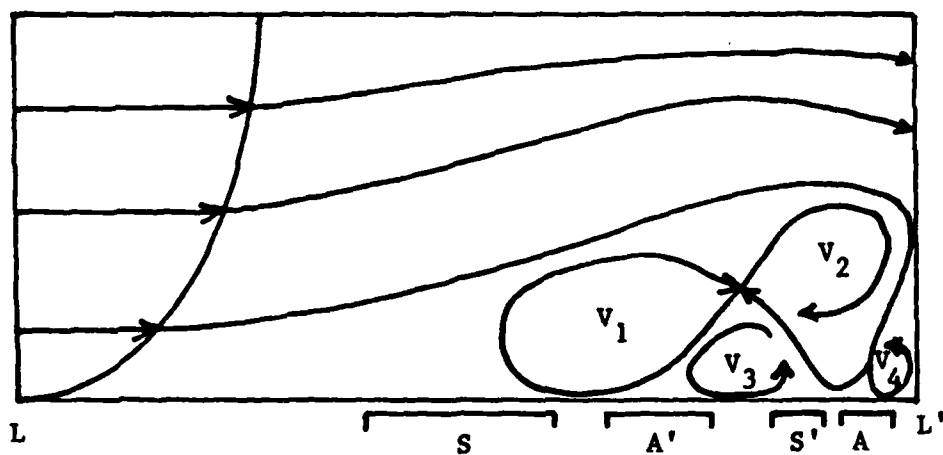
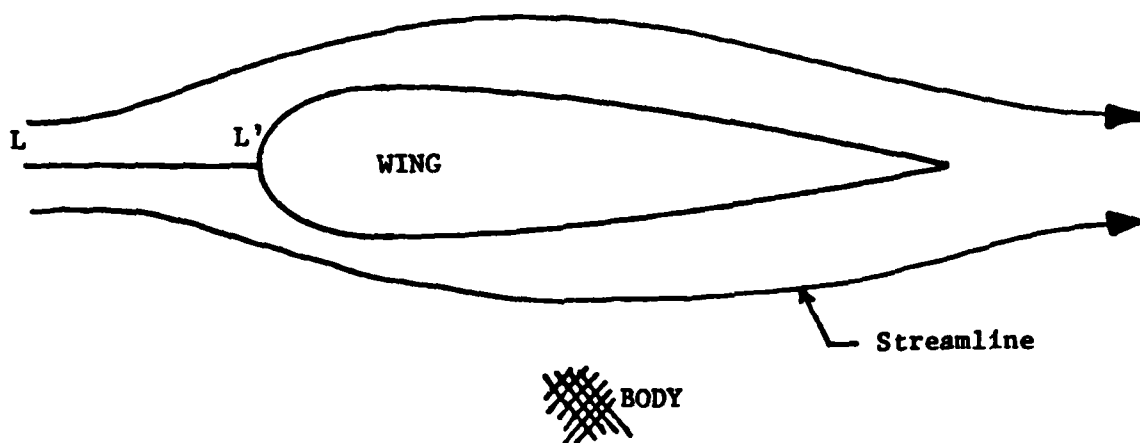
The pressure gradient has two effects on the velocity field. First, the pressure gradient produces a change in the velocity distribution that decreases the streamwise velocity component and increases the vertical velocity component. The effect on the vorticity is the appearance of "true" vortical motion as  $\delta v/\delta x$  obtains non-zero values at the expense of  $\delta u/\delta y$  with the constraint that the vorticity ( $\delta v/\delta x - \delta u/\delta y$ ) remains constant. Second, the vorticity vector is skewed by the transverse velocity gradient to generate streamwise vorticity from transverse vorticity.

REGION III: Pressure generated flow separation and secondary flow in leading edge region

This region includes the actual three-dimensional separation of the flow and the concurrent establishment of concentrated vorticity in the so-called horseshoe root vortex which wraps around the leading edge with its legs trailing downstream. Several descriptions of the separated flow appear in the literature. A reasonable depiction is shown in Figure 2-2.

The existence of the secondary attachment  $A'$ , shown in the figure, is a matter for debate. It may be important for explaining the physical origin of temporal flow associated with the separated region. This is because the concentration of attachment fluid in a small area is one clue suggesting the existence of large scale time dependent flow structures. In this small area there are large velocities and velocity gradients. Therefore small movement of the attachment zone would produce relatively large changes in the velocity at a given point in the field.

In any case, there is no doubt that a primary vortex is established in the leading edge region. The vortex diameter is of the order of the boundary layer thickness and is located within the region on the order of the boundary layer thickness ahead of the wing



S and S' are primary and secondary separations  
 A and A' are primary and secondary attachments  
 $v_1$ ,  $v_2$ ,  $v_3$ , and  $v_4$  are vortices

Figure 2-2: Hypothetical Flow Structure for the Wing-Body  
 Junction Flow for a Turbulent Onset Boundary Layer

leading edge for wing thicknesses greater than the boundary layer thickness.

REGION IV: The developed secondary flow downstream from the leading edge (Reynolds stress driven)

In this region the pressure gradients in the streamwise direction are relaxed. The vortex diffuses, and at the same time relatively small secondary flow opposing the root vortex is generated by the anisotropy of the Reynolds stress tensor. (This flow is secondary flow of the second kind, or stress-induced secondary flow; it is differentiated by Prandtl (1926) from secondary flow of the first kind, or skew-induced secondary flow, and by Young (1977) from secondary flow of the third kind, or vortex-shedding secondary flow.)

REGION V: The separated flow at the trailing edge

Adverse pressure gradients reappear as the flow encounters the trailing edge region. There is a curving flow along the wing towards the body and the secondary vortex in the junction breaks away from the wing, although it remains close to the body. A viscous wake is generated at the trailing edge of the wing. Immediately outside, or at the edge of the wake, another secondary vortex is established as a result of the downward flow along the wing. This secondary vortex is counterrotating relative to the secondary vortex originated at the wing leading edge.

At the trailing edge, and downstream, the primary vortex legs (one on each side of the wing) are free to mutually interact. Because they are large and transport significant amounts of streamwise momentum across the flow it is expected that they contribute significantly to separation features in the wing trailing edge region.

REGION VI: The vortical flow in the wing wake-boundary layer interaction flow

The four counterrotating secondary vortices (two on each side of the wing center plane) diverge as the wake in the boundary layer expands downstream. The primary vortex legs continue downstream, crossing over (on top of) the secondary vortices. The mutually

interacting vortices and the separated flow from along the wing span provide the basic features of the flow. The temporal flow initiated in the wing-body junction is convected into this complicated flow.

### 2.3 Review of the Literature

A literature review revealed that there is a considerable amount of experimental data applicable only to the mean boundary layer. Generally, the studies can be classified according to one of the three flow regimes discussed previously. Studies of the flow in Part One, the leading edge dominated flow, pertain mostly to flow visualization studies using oil film techniques with sparse supplementing pressure and velocity measurements. Studies of the flow in Part Two involve extensive velocity measurements to examine the diffusion of the root vortices and the generation of secondary flow of the second kind (Reynolds stress driven). Studies of the flow in Part Three concentrate on oil film flow visualizations to assess the effects of the vortices on trailing edge separation and the wake growth, and on velocity measurements to evaluate root vortex growth.

There is no documentation or suggestion of any studies of the large scale flow structure in the wing-body interaction flow for a turbulent boundary layer. The studies of turbulence are notwithstanding because they are restricted to measurements with zero time and space separation although by definition "turbulence" means time dependent. On the other hand, the review of the literature for the mean flow for the wing-body junction reveals gross features which provide clues revealing the possibility and origin of coherent flow structures. It is expected that flow regions encompassing large changes in the mean flow quantities would be associated with the onset of large scale temporal flow. These regions are associated with flow separations.

The applicable literature is directed toward two areas of related interest: the aerodynamic wing-body junction and the turbomachinery blade-end wall interaction. The aerodynamic relevance is for the local drag resulting from the secondary flow and for the

downstream influence of the trailing vortices on local separation. The turbomachinery relevance adds the effects of the vortices on heat transfer and the impact of the vortices on the performance of downstream blades. There is no single reference that thoroughly addresses all three Parts of the flow. However, there are two references that stand out from the others because of their comprehensiveness although they are lacking detail in many respects. These primary references are the doctoral dissertation by Shabaka (1979) and a report by Sepri (1973).

Shabaka investigated the flow for Parts One and Two, with special emphasis on the relative importance of turbulence terms. His work was intended for input to the development of computer prediction methods, although he provides no computations. Consequently, he measured the spatial extent of the interaction flow and ascertained the general invalidity of law of the wall and simple turbulence models for the wing-body junction. His measurements, for a 6:1 semi-elliptic nose on a wing of very large chord length, include wall static pressures, mean three-component velocities, and single-point double and triple velocity correlations relevant to Reynolds stress and kinetic energy evaluations.

The significance of Shabaka's results to the present work is the information about the physical size of the root vortices. This information was required to choose appropriate instrumentation relative to the physical size of the flow. The work of Shabaka is noticeably lacking in definition of the precise flow in the vicinity of the leading edge separation. However, such experimentally obtained data is also absent from all other references, a fact which reflects the difficulty inherent in making the required measurements.

Sepri provides the most complete flow visualization analysis published, although it consists solely of oil film studies. His elaborate investigation of an NACA 0012 wing mounted on a flat plate includes all three parts of the flow, and in particular demonstrates the effects of wing incidence. The notable feature revealed by his studies is the flow line of attachment in the

leading edge Region III between the primary separation and the wing. The distinguishing feature in this respect for the wing at incidence is the unmistakable divergence of the oil film streaks on both sides of that attachment line. In the limit as the incidence angle approaches zero degrees the attachment line moves toward, and appears to lie very close to, the line marking the physical intersection of the wing and the body.

The oil film studies are enhanced by three-component mean velocity measurements in the trailing edge region and downstream of the wing. Notable again is the effect of wing incidence on the relative sizes of the root vortices; it is observed that the vortex on the high pressure side of the wing spatially grows, and the vortex on the low pressure side spatially contracts, with the result that the vortex legs remain unequal in size downstream from the wing.

Sepri made no flow velocity measurements in the vicinity of the three dimensional separation at the leading edge. Sepri provides a hypothetical description of the flow in the separated region, including four counterrotating vortices, two separation and two attachment lines, and an interior saddle point (where flow streamlines both converge and diverge). Although the description is reasonable, and obeys topological rules, it is not substantiated because flow field measurements were not obtained.

The above two references are recommended primary sources for information about the mean flow for the wing-body junction flow because they are the most comprehensive. Among the important references supplementing the above are three doctoral dissertations. Oguz (1981) examines the effect of boundary layer thickness on a wing similar to that of Shahaka. Baker (1978) examines the root vortex about a circular cylinder. The applicability of the results to the present study is restricted by the bluff trailing edge. Pal (1981) examines wake development downstream from the wing-plate junction. All of these dissertations are deficient in detail sufficient to precisely describe the three-dimensional separations both upstream from the leading edge and in the trailing edge region of the wing.



An important source of experimental data for downstream velocity profiles is a report by Love (1963). It is the earliest known effort to systematically examine the features of the horseshoe vortex for relatively blunt wing profiles. Love measured transverse velocity profiles across the flow and parallel to the wall at downstream stations behind circular cylinders, circular arc profiles, and elliptic profiles. Among the conclusions are two important observations:

1) the shape of the wing has a marked effect on the general nature of the flow downstream, while the size or the flow velocity have little effect.

2) the downstream flow is strongly dependent on the point of separation of the boundary layer on the wing.

These conclusions mean that vortex development at the leading edge of the wing is conditioned by trailing edge factors.

Love is also to be credited with making the distinction between (a) downward flow at the leading edge attributable to the total pressure gradient, and (b) downward flow attributable to the horseshoe vortex. Although Love's explanation is somewhat difficult to follow, the distinction between the two is apparently the concentration of vorticity in the upstream region near the body in contrast to the distribution of vorticity far from the body but inside the boundary layer that impinges on the leading edge region. Both effects produce downward flow components.

There are additional references that provide supplemental information. Chu and Young (1974) continued the work of Sepri, especially with respect to the effect of wing incidence on the downstream velocity profiles. Barber (1978) provides insight into the individual effects of wing thickness and boundary layer thickness. He specifically discusses the possible interaction between the root vortex, trailing edge separation, and the downstream velocity profiles. The data are sparse, and serve to support the

conjecture rather than to experimentally define the phenomena. Dechow and Felsch (1977) and Pierce and McAllister (1980) have made measurements of the flow upstream from the leading edge in Region II. The measurements were not made in the actual vortical flow inasmuch as the intent of the measurements was to verify the applicability of stress models for predictive techniques. In this sense the wing-body configuration was a device to produce a pressure-driven three-dimensional boundary layer. Another reference providing supplementary information with respect to three dimensional flow separation is the AGARDograph by Peake and Tobak (1980). The presumption that separated flow obeys topological rules is further investigated in papers by Tobak and Peake (1979), (1981).

The only documented attempt to directly associate flow field measurements with oil film flow visualizations at the leading edge Region II was made by East and Hoxey (1969). The data are incomplete although an apparent relationship is revealed between features of the oil film and the location of the minimum static pressure in the flow field.

The flow in the wing-body junction has escaped numerical study. An accurate computation would involve a solution of the complete Navier-Stokes equation. This procedure is precluded by computer memory and time limitations. The assessment by Sung (1983) provides a critical evaluation of the problem.

As stated earlier, there are no reported measurements in the open literature of time dependent flow structure in the wing-body junction for the turbulent boundary layer. On the other hand, cyclic flow structure has been observed by Peake, et al (1965) and by Schwind (1962) for the laminar boundary layer. Those authors specifically warn, however, that the observed differences in the oil film patterns and the known differences in dynamics between laminar and turbulent boundary layers might lead to the expectation that the turbulent flow is not cyclic.

One physical source for time dependent large scale flow structure is the periodic oscillation of the three dimensional separation. A series of journal articles written by Simpson, et al

(1981), and (1983) describes comprehensive experimental results for unsteady two-dimensional separation. It is notable that ordinary separation produced by an adverse pressure gradient is a dynamic time-dependent phenomena although such techniques as oil film flow visualization imply that the separation is fixed in location. These references are listed here because of the potential applicability to the three-dimensional flow about the wing-body junction.

Additional references not discussed above are listed in the bibliography to complete the list of references on the wing-body turbulent boundary layer interaction.

#### 2.4 Rational for the Temporal Measurement

Examination of the mean velocity features prompted conjecture that the flow in the wing-body junction contains large scale temporal motion. The fact that the flow is separated was sufficient reason to perform an investigative study. In the absence of geometry fixing separation, such as a sharp edge, the flow is generally unsteady for several simple flows. Consider as examples the separating flows on a cylinder and on a flat plate subjected to an adverse pressure gradient.

The vortex shedding phenomenon associated with a cylinder is well known. The point of separation for the flow on the cylinder surface is a periodic function of time as the wake rolls up to form and shed the vortices Schlichting (1979, p.28). Peake and Tobak (1980) summarize data showing that the surface location for separation for inclined axisymmetric bodies is a function of time. It is concluded that separation is associated with the formation of temporal flow structure, at least for the case of wake formation. This situation is certainly applicable to the trailing edge flow (Region V). However, the presence of body curvature in the above examples is not necessary to produce the temporal flow.

Simpson, et al (1981) culminated a decade of research with the important observation that a flat plate two-dimensional separating flow is characterized by a frequency associated with the presence of coherent flow structures. The significant difference between the

flat plate temporal flow and the cylinder turbulent flow is apparently that the velocity fluctuations of the fluid in the temporal structure are small for the flat plate and large for the cylinder. Although the separating flow for the wing-body junction is three-dimensional, the flow reversal at the origin of the root vortex is similar to the two-dimensional case at least in the plane of symmetry. Furthermore, it would be expected that the flow in the trailing edge region of the wing, and inside the boundary layer, would experience unsteady separation phenomena that would be clearly distinguishable from the usual trailing edge vortex shedding that occurs outside the boundary layer.

The conclusion from the above arguments was that a search for turbulent large scale temporal flow associated with the wing-body junction would be fruitful.

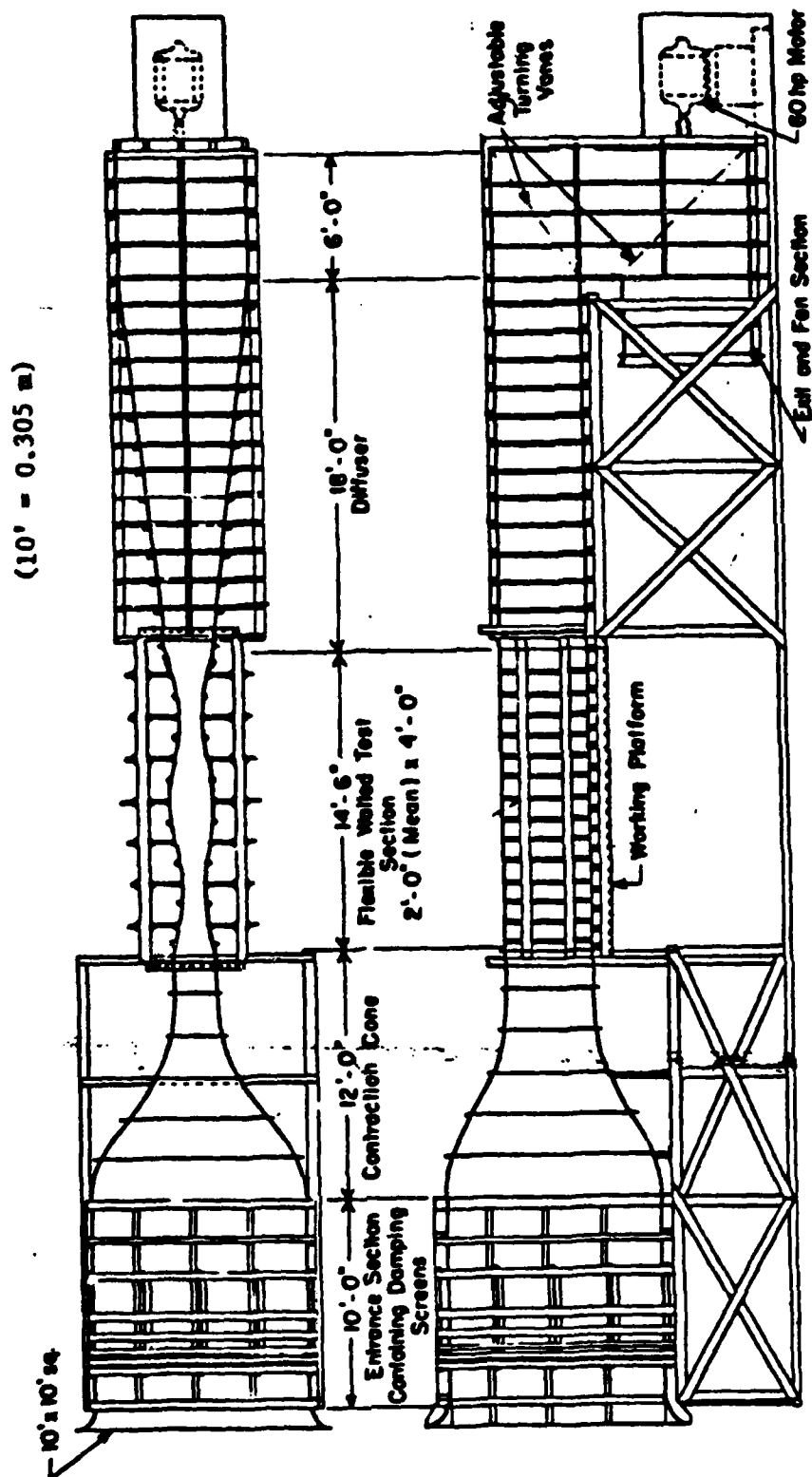
## CHAPTER 3

### DESCRIPTION OF THE EXPERIMENT

#### 3.1 The Low Turbulence Wind Tunnel

The experiment was conducted in the Low Turbulence Wind Tunnel at the David Taylor Naval Ship R&D Center. The general arrangement of the tunnel is shown in Figure 3-1 from Scottron and Shaffer (1965). For this investigation the test section walls were positioned straight and in parallel although they are deformable as shown in the figure. The center of the test section is characterized by a turbulence level of less than 0.2 percent, both as reported by Scottron and Shaffer and as verified in the present study. The test section of the tunnel is 4.4 m long, 1.2 m high, and 0.6 m wide. The removable test section top contains transparent panels which were replaced with slotted rectangular pieces through which the measurement probe traverse assembly protruded; see the photograph in Figure 3-2.

The maximum tunnel speed is about 40 m/s; however, the ambient noise level outside the tunnel at that speed presents a hardship to test personnel. Although the preliminary exploratory



Ref: Scottron and Shaffer (1965)

Figure 3-1: General Arrangement of Wind Tunnel

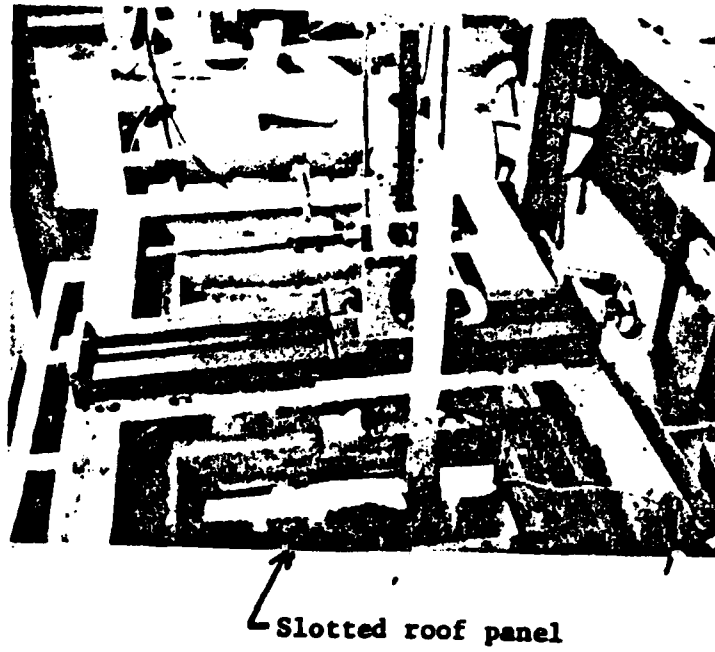


Figure 3-2: Traverse Assembly Mounted on Tunnel Roof



Figure 3-3: Tunnel Inlet Trip

investigation was for a speed of 38.1 m/s, the speed was therefore reduced to 30.5 m/s for the detailed measurements without an observed change in the flow features but with a substantial reduction in noise level outside the tunnel.

Preliminary investigation of the wind tunnel boundary layer indicated a flow structure of large spatial extent with a 6 Hz characteristic frequency at a tunnel speed of 38.1 m/s. That flow structure was removed by placing a 6.4 mm x 2.4 m long cylindrical rod on the wall of the large entrance section on the downstream side of the screens as shown in Figure 3-3. The rod presumably stabilized otherwise transient conditions produced by the low Reynolds number inlet flow.

The dynamic pressure determined from measurements with a pitot-static tube placed in the tunnel 30.5 m/s freestream was low frequency spectrally analyzed, and was determined to have a maximum period of 30 s. The spectral output is in Figure 3-4. The integrated pressure spectrum is equivalent to a velocity amplitude fluctuation of 2 percent at a tunnel free stream speed of 38 m/s. The relatively long tunnel speed fluctuation period established the minimum data acquisition time for mean flow measurements.

### 3.2 The Wing

The investigated wing profiles had semi-elliptic noses, parallel-sided mid-sections, and circular arc tails. In all there were two nose shapes, three lengths of parallel-sided mid-section (including none at all), and one tail shape. Not all combinations of geometry were investigated; those that were are in Figure 3-5.

The nose shape is designated by the ratio  $a/b$  of the ellipse semi-axes, where "a" is the length of the axis in the chordwise direction of the wing. The ratios  $a/b = 1.5$  and  $6.0$  were examined in this study, although not in a systematic manner. The  $a/b = 6.0$  nose was used for the preliminary studies to assess the feasibility of studying large scale time dependent flow structure in the wing-body junction and to test the proposed measurement techniques. The detailed investigation that ensued used the  $a/b = 1.5$  nose. That blunter nose produced a larger root vortex



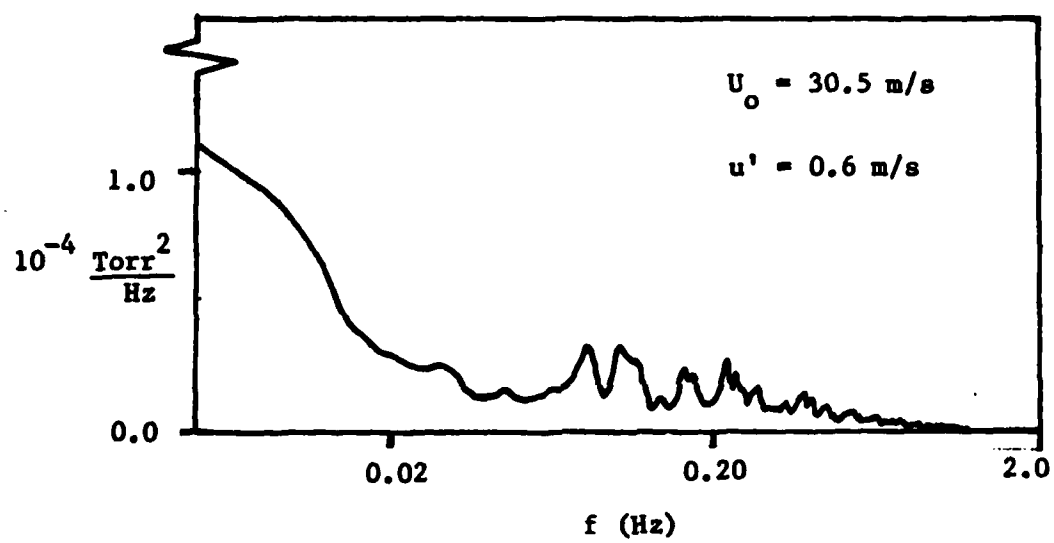
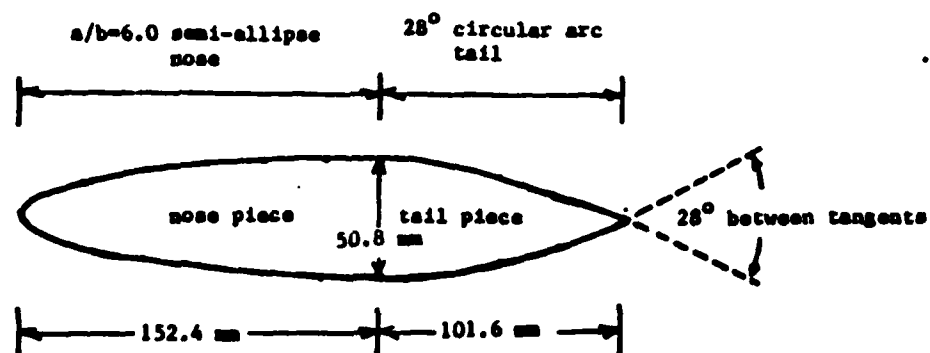


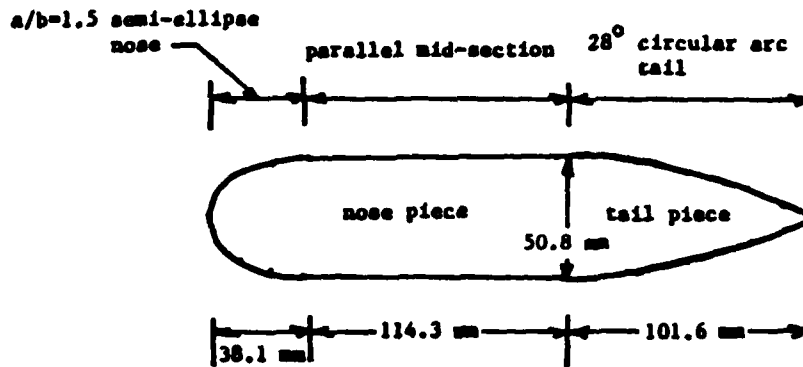
Figure 3-4: Pressure Spectrum in Tunnel Free Stream



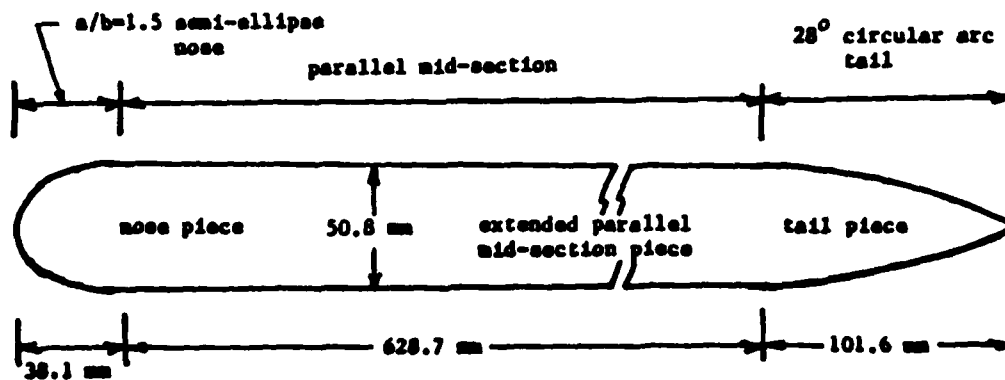
3-5(a): Profile for Preliminary Investigation

Figure 3-5: Investigated Wing Profiles

## Finite Chord Length Wing



## Infinite Chord Length Wing



3-5(b): Profiles for Detailed Investigation

which lead to spatially more extensive, hence more easily measured, flow structure. As an added bonus, it turned out that the observed frequency bands associated with various flow structures were more easily distinguished for the  $a/b = 1.5$  nose than for the  $a/b = 6.0$  nose.

The  $a/b = 6.0$  semi-elliptic nose profile for the preliminary investigation was directly joined to the 28-degree circular arc tail; see Figure 3-5(a). On the other hand, the  $a/b = 1.5$  semi-elliptic nose profile had a length of parallel-sided mid-section between the nose and the 28 degree circular arc tail; see Figures 3-5(b) and 3-5(c). The total length of parallel-sided mid-section was short (2.25 wing thicknesses) for the finite chord length wing and long (10.0 wing thicknesses) for the "infinite" chord length wing. In all there were three profiles examined, which are designated the  $a/b = 6.0$  finite chord length wing, the  $a/b = 1.5$  finite chord length wing, and the  $a/b = 1.5$  infinite chord length wing.

Other variations in the wing profile design geometries were held to a minimum to isolate the effects of nose radius and wing chord length. All three profiles were the same thickness (50.8 mm). The profiles for the  $a/b = 6.0$  and the  $a/b = 1.5$  finite chord length wings were equal in chord length (254 mm), with a chord length to wing thickness ratio of 5. The profile for the infinite chord length  $a/b = 1.5$  wing had a chord length to wing thickness ratio of 17.

The wings were of constant profile in the spanwise direction and extended from the wall a distance of 229 mm, or 4.5 times the nominal boundary layer thickness. The wing tips were cut square; i.e., there was no rounding or contouring of the tip. The loci of wing leading and trailing edge points were along straight lines normal to the wall. That is, the wing was a right cylinder normal to the wall.

The wing nose and tail pieces were manufactured from wood and were finished with a hard sealant. The extended parallel mid-section was made of two plastic sheets sandwiching a block of wood.

The various pieces were configured to dovetail together at assembly in the wind tunnel.

The wings were attached to the wall using a threaded rod protruding normal to the wall and through spanwise holes in the wings. A nut on the rod was used to tightly press the wing against the wall. The spanwise hole was located through the nose pieces for the two finite chord length wings. A clamp, shown in Figure 3-6, was in turn attached to the threaded rod with a second nut to press the tail piece against the wall. The short parallel mid-section for the  $a/b = 1.5$  profile was a part of the nose piece and therefore did not require clamping. For the larger infinite chord length wing both the nose and the tail were secured by threaded rod, while the extended parallel mid-section piece was clamped at each end to the tips of the nose and tail pieces. The clamping arrangement is shown in Figure 3-7.

Boundary layer trips were installed on each side of the noses of the wings a short distance back from the leading edge. The trips were 0.5 mm diameter wire taped to the wing at spanwise intervals to hold the wires down, as shown in Figure 3-8. The purpose of the trips was two-fold: first, to stimulate turbulent flow over the wing, and, second, to spatially fix transition to reduce or eliminate "contamination" of the flow by unsteady effects. Without the trips, the location of the transition would have been expected to fluctuate and produce time dependent flow structures that perhaps could not be readily distinguished from the other unsteady effects of interest.

### 3.3 The Wall

The wall on which the wing was mounted was a large flat plate of clear plexiglas. This plate was installed parallel to the wind tunnel side walls, rather than to either the top or the bottom wall, to minimize "end wall effects" on the flow around the wing. As described above, the tunnel side walls were 122 cm in height whereas the tunnel top and bottom walls were only 61 cm in width.

The plexiglas plate, which effectively replaced the wind tunnel side wall, extended from the tunnel top to the tunnel bot-



Viewing  
Upstream

**Figure 3-6:** Photograph of Compression Clamp Holding Tail Piece  
for Finite Chord Length Wing



Viewing  
Downstream

**Figure 3-7:** Photograph of Compression Clamps Holding Extended  
Parallel Mid-Section Piece for Infinite Chord Length  
Wing

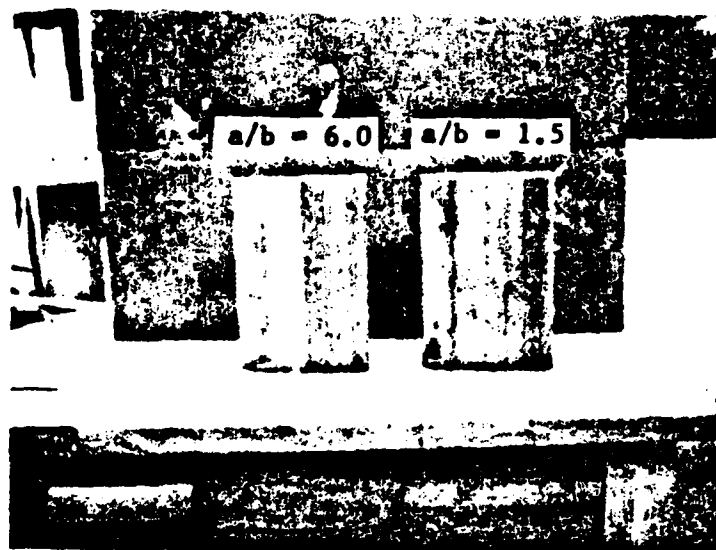


**Figure 3-8: Boundary Layer Trip Wires Installed on Noses of Wings**

tom. The wing was mounted normal to the plexiglas wall and protruded horizontally into the tunnel flow, with equal distances between the wing and the tunnel top, and the wing and the tunnel bottom. The wing and wall configuration is shown in Figure 3-9.

The plexiglas wall was installed with a clearance between it and the tunnel wall to permit installation of pressure tap tubing. As shown in Figure 3-9, an upstream ramp was used to literally lift the tunnel boundary layer from the tunnel wall and onto the plexiglas wall. This procedure established a relatively thick onset boundary layer for the wing, and eliminated problems of flow alignment at the plate leading edge. A turning block of radius 61 cm was used to turn the flow from the ramp and onto the plexiglas wall. Oil dot and tuft flow visualization studies showed no evidence of flow separation on the wall downstream from the block. Furthermore, laterally displaced two-point velocity correlations did not show non-zero values indicative of flow separation.

The plexiglas wall terminated downstream at a support block which presented a backward facing step transition for the flow. The step transition was immediately upstream from the divergent flow outlet for the test section. Certainly there was unsteady flow downstream from the block and into the divergent outlet, but its presence was not evident in the upstream flow from measurements in this investigation.

Plexiglass was chosen for the wall material to allow observation of the numerous pressure tap tubes to verify their proper connections when the tunnel wall was installed in place. The plexiglas material also made the wall easier to handle than a heavier metal wall.

The wing selected for study was initially aligned geometrically to the assumed wind tunnel flow direction by locating it along a scribe line on the plexiglas wall. The scribe line was located from the locus of points equidistant from the tunnel floor. Changes in the wing incidence of  $\pm 2$  deg. from the assumed zero degree alignment produced relatively small measurable effects for the time dependent flow near the wing. It was concluded that pre-



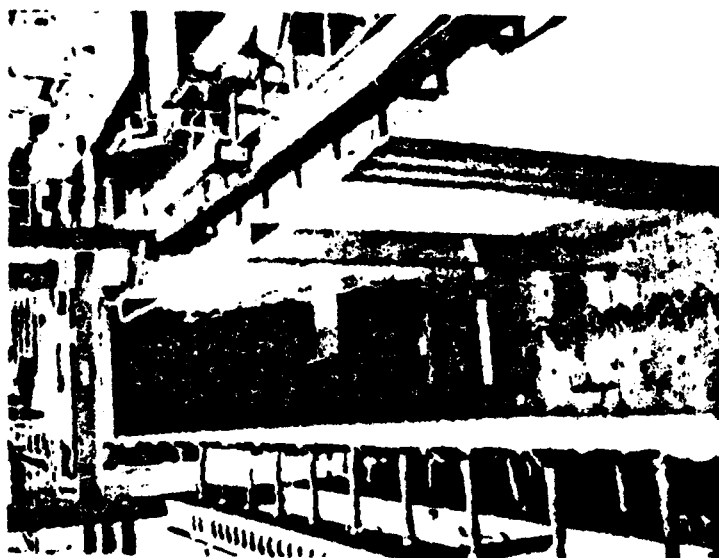
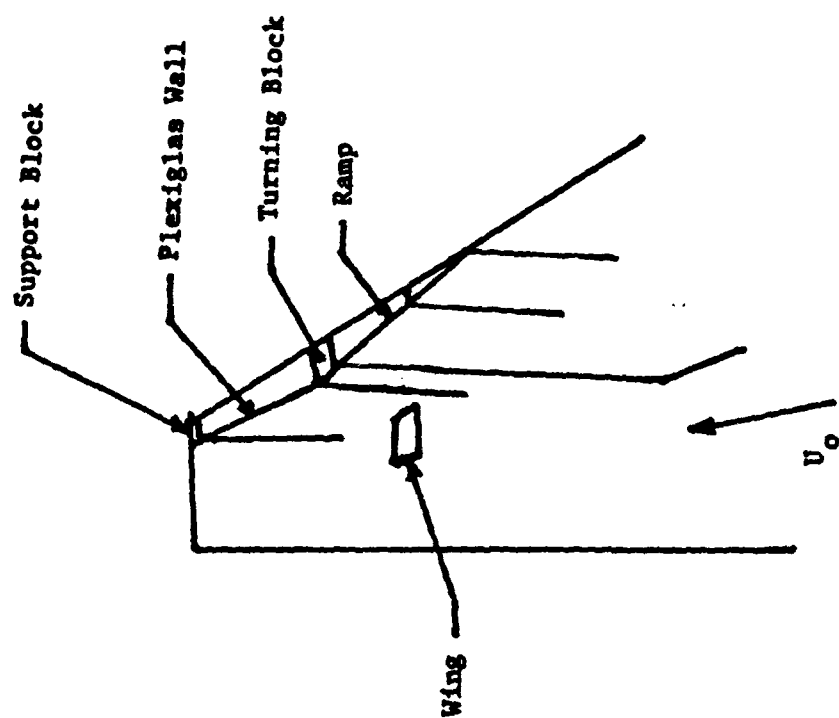


Figure 3-9: Photograph of the Wing and Wall Configuration

cise alignment of the wing was not necessary to quantify the flow near the wing for the purpose of this investigation. However, the preliminary time dependent flow measurements several wing chord lengths downstream from the wing were observed to be sensitive to small changes in incidence angle. For those measurements the zero incidence alignment of the wing was verified by obtaining symmetric measured mean wake profiles. These observations of incidence sensitivity mean that a more precise method of determining wing angle of incidence may have to be developed for precision wake measurements.

### 3.4 The Coordinate System

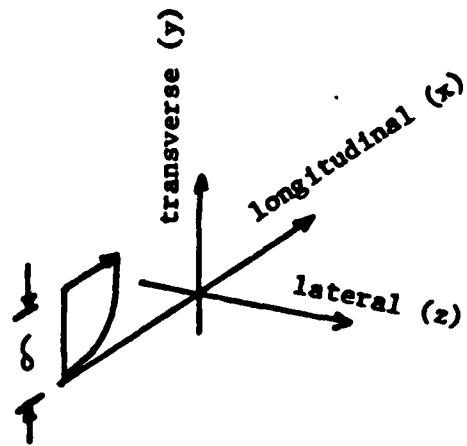
The coordinate system for the experiment is shown in Figure 3-10. The coordinate directions are defined similarly to the conventions used by Shabaka (1979) and by Oguz (1981) in previous studies of the mean wing-body junction flow. The coordinate system origin is located on the wall at the intersection with the wing leading edge. The coordinate system is identified with customary boundary layer directions in Figure 10(a). The positive direction of  $x$  is in the longitudinal, or streamwise, direction, and the positive direction of the coordinate  $y$  is across the boundary layer and normal to the wall; i.e., in the transverse direction. The coordinate  $z$  is defined in the direction across the boundary layer, perpendicular to the mean flow direction and parallel to the wall; i.e., in the lateral direction.

As in the previous studies, the coordinate  $z$  in the notation  $P_A(x,y,z)$  specifying the location of the point  $P_A$  is defined relative to the wing surface. Hence otherwise possible positions  $P_A$  inside the wing are excluded from the coordinate range of  $P_A(x,y,z)$  where  $x,y,z$  can assume all values from  $-\infty$  to  $+\infty$ .

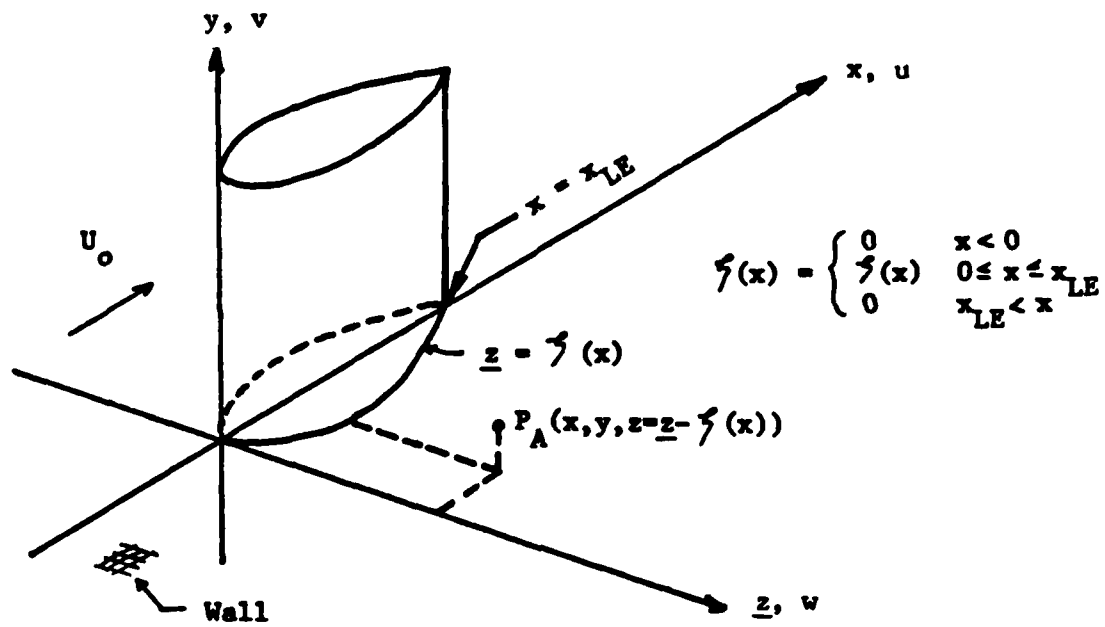
### 3.5 Probe Positioning Devices

The temporal flow was measured by correlating flow velocity fluctuations at two probes, one of which was fixed in position while the second was traveled to sequential positions.

The traverse for the traveling probe consisted of two devices to provide independent probe positioning in the  $y$  and  $z$  direc-



3-10(a): Boundary Layer Directions



3-10(b): Coordinate Directions

Figure 3-10: The Coordinate System

tions from outside the tunnel. The first device was a massive mill table mounted outside the tunnel and supported by the twin I-beams forming the tunnel top framework; see Figure 3-11. The mill table provided continuous positioning in the y-direction with a scale resolution of 0.0001 in (0.00254 mm). The second device, also shown in Figure 3-11, was a reciprocating ball guided plate with scale resolution of 1/64 in (0.40 mm). The guided plate provided positioning in the z-direction, and was rigidly bolted to the mill table.

Positioning of the traveling probe in the longitudinal direction was accomplished by adjustment of the probe holder assembly, described below, or by moving the entire mill table along the tunnel I-beams.

A piece of angle arm, guided by a notched plate attached to the guided plate support, extended from the traverse toward the tunnel roof. Circular section rod was mounted into a block attached to the end of the angle arm, and extended through a slot in one of the plexiglas viewing windows of the tunnel and into the test section; see Figure 3-12.

The slot in the viewing window was covered nearly entirely by tape except where the traverse arm passed through. This procedure minimized tunnel cross flows produced by the pressure differential between the tunnel and the atmosphere.

A probe holder, shown in Figure 3-13, was attached to the rod and held the hot film probe. The probe holder assembly allowed considerable adjustment flexibility in probe positioning through the use of set screws and clamps to hold parts in position.

The fixed probe for the two-point velocity correlation measurements was held in position by a similar assembly rigidly attached to the tunnel floor; see Figure 3-14. The position of the fixed block holding the circular section rod was changed by bolting it at rearranged positions on a flat plate secured to the tunnel floor.

The shedding frequencies of the probe support apparatus were much larger than the measured frequencies of interest and were observed to be predicted by the customary formula  $fd/U=0.2$ .

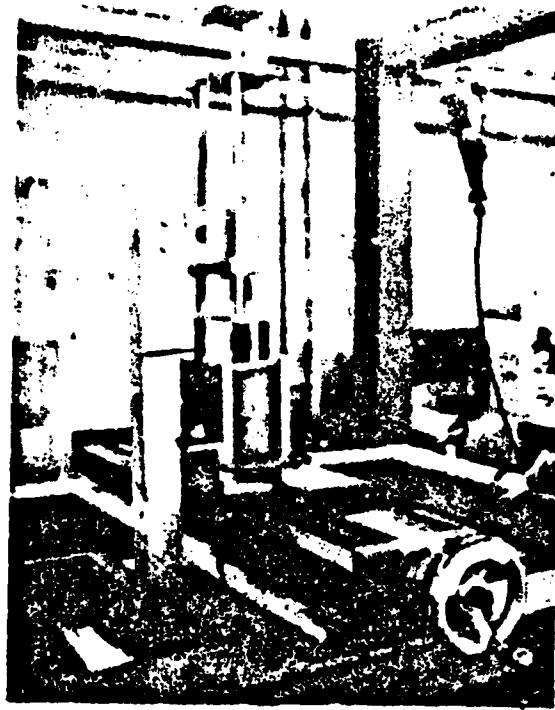


Figure 3-11: Traverse Positioning Device



Figure 3-12: Circular Section Rod Protruding Into Test Section



Figure 3-13: Probe Holder Assembly

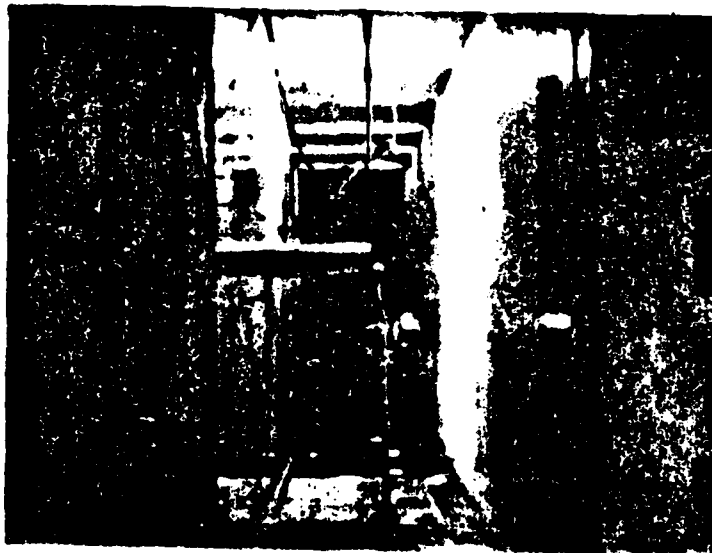


Figure 3-14: Fixed Probe Assembly

The accuracy of the traveling probe position is estimated to have been  $\pm 1.3$  mm in both the x and y directions attributed to flexibility in the cantilevered arms between the traverse mechanisms and the probe. This error bound was determined by comparison of visual observations of the probe with the tunnel at zero speed and at test speed. The stiffness in the z-direction was larger; the error is estimated to have been  $\pm 0.8$  mm. The accuracy of the fixed probe, attached to the tunnel floor, is estimated to have been  $\pm 0.8$  mm in all directions.

### 3.6 Instrumentation

#### 3.6.1 Velocity Measurement System

The time dependent velocities and the mean values of the three components of velocity in the wing-body junction flow were measured with hot film anemometry. An arbitrarily chosen pitot-static tube was used for the primary velocity measurement, and was also used to measure the tunnel free stream speed.

A schematic of the velocity measurement system is shown in Figure 3-15. The two hot films used for velocity measurements were maintained approximately  $200^{\circ}\text{C}$  above the ambient temperature using temperature compensation probes for control resistances. The anemometer bridge voltages were low pass filtered and d.c. suppressed before being input to a Nicolet 660B Dual Channel FFT Analyzer for spectral correlation analysis. The power spectral density, coherence, and relative phase between the signals was output from the Nicolet 660B to a Tektronix plotter to produce hard copies of the processed data.

##### 3.6.1.1 Pitot-Static Tube Measurement of Free Stream Velocity

The anemometer bridge voltages were calibrated against the wind tunnel free stream speed as determined by a reference pitot-static tube positioned in the free stream. The reference pitot-static tube was located at  $P_A$  (-20, 36, 36 cm) for all the measurements. A photograph of the tube is shown in Figure 3-16. The pressures at the pitot-static tube were measured with the pressure measurement system described in Section 3.6.2. The tube was commercially manufactured and is shown in Figure 3-17. The



**Figure 3-15: Schematic of the Velocity Measurement System**



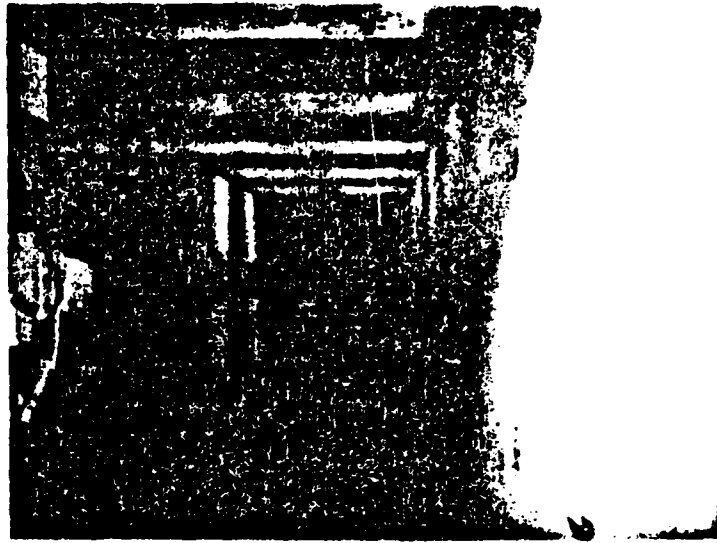


Figure 3-16: Photograph of Pitot-Static Tube in Position

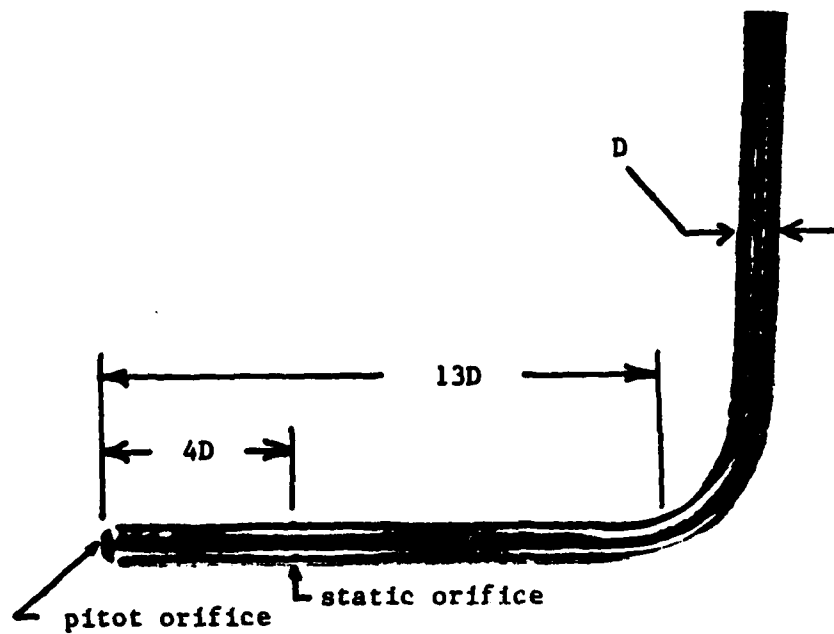


Figure 3-17: Close-Up Photograph of Pitot-Static Tube

nose was rounded, and the stem was 3 mm circular tubing. The pitot pressure orifice was 13 stem diameters forward from the vertical support, and the static pressure orifices were 4 diameters aft of the nose and 9 stem diameters forward from the vertical support.

A determination of the tunnel air speed was made by subtracting the reference static pressure from the pitot pressure, via the differential transducer, to obtain the tunnel dynamic pressure at the tube. The customary conversion from pressure to velocity was made after a determination of air density from a chart using measurements of the tunnel air temperature, pressure, and relative humidity. Those quantities were measured with the standard tunnel instrumentation, and are believed to have been of sufficient accuracy to determine the density to within 0.5 per cent. Although there were no readily available standards against which the instrumentation could be compared, they were checked against a second set of instrumentation and found to be in agreement within the reading resolution ( $\pm 0.25^\circ\text{F}$ ,  $\pm 0.5\%$  R.H.,  $\pm 0.005$  in. Hg). Although a common bias error may have been present for both instrumentation sets, the environmental conditions did not change substantially throughout the test so that relative differences in tunnel speeds resulting from determination of the density are negligible.

#### 3.6.1.2 Numerical Processing of Hot Film Output

The anemometer bridge voltages were low pass filtered at 10K Hz to remove unwanted signals such as the megahertz range noise from the anemometer feedback circuit. The filtered signals were input to the Nicolet 660B, which was used to obtain discrete numerical values of the time dependent analog bridge voltage output.

To maximize the A/D resolution of the Nicolet 660B, the input signal was d.c. suppressed to limit the voltage input to values between -1 volt and +1 volt for the range of velocities under measurement. With this procedure the span for the anemometer bridge voltages was resolved into 4096 parts producing an A/D resolution of 0.25 mv. Examination of the instantaneous digitized time history of the voltages produced by the time dependent flow in the

wing-body junction showed that the resolution interval was at least an order of magnitude smaller than the observed fluctuations in the wing-body junction flow.

The Nicolet 660B was operated in the SIG ENH mode to obtain numerical averages of the input voltages. The voltages were digitized at a rate of two samples/second for at least 30 seconds, the tunnel fluctuation period. These numerical averages were related to the flow speed by calibration.

The hot films were calibrated by placing them in the assumed free stream flow about the model at a position in the same y-z plane as the measurements were to be made. The tunnel speed was varied and determined from the reference pitot-static probe located at  $P_A$  (-20, 36, 36 cm). It is estimated that the "free stream" at the probe calibration position may have been 2 percent larger than at the reference pitot-static tube position because of blockage effects.

For low frequency resolution the filtered and d.c. suppressed anemometer analog outputs were d.c. coupled to the Nicolet 660B. The Nicolet 660B was operated in the DUEL 1K mode for the correlation and spectral analysis of the two-point measurements. To accurately perform the analysis over the frequency range of interest (usually 0.5 to 200 Hz), an analog filter internal to the Nicolet 660B was used to provide at least 70dB attenuation of frequencies that would cause aliasing. The filtered analog signals were digitized to provide numerical time histories of the data. The digitized time histories were numerically processed using Fast Fourier Transform techniques to produce spectral correlation analyses of the data. The graphical output from the analyses was displayed nearly real time on a CRT screen, and was hard copied using a Tektronix plotter.

Both the frequency resolution and the number of ensemble time histories of data were programmable input to the Nicolet 660B. The resolution was chosen to be either 0.25 Hz or 0.50 Hz, and the number of time history ensembles was usually chosen to be 400. The choice for the number of ensembles was governed by statistical

uncertainty considerations, which are discussed later in Section 3.7. The number of ensembles was occasionally less than 400 in circumstances where the coherence of the signals was observed to be negligible for less than 400 ensembles. In either case, the data were analyzed with 50 percent redundancy to correct for power leakage at the spectral window. This procedure produced a statistically independent number of ensembles equal to  $1/2$  the number of analytical time history ensembles.

The selection of the frequency resolution automatically determined the sample rate, and hence the maximum resolvable frequency, in the operation of the Nicolet 660B. The maximum frequency resolved was either 100 or 200 Hz depending on the flow conditions.

It is noteworthy for additional experimental work that 400 ensembles of data analyzable to 100 Hz in bandwidth increments of 0.25 Hz required thirteen minutes for acquisition. A typical correlation contour with the fixed probe on one side of the wing and the traverse probe on the other side required 40 measurements for a total test time of 10 hours. It is apparent that even a small matrix of test conditions and measurement plane locations can require an impractical total test time in some circumstances.

The unfiltered hot film analog signals were also input to a.c. coupled oscilloscopes to provide convenient visual display of the signal. This practice provided assurance that the output from the anemometers remained stable; the turbulence signal had a particular "look" to it that disappeared whenever certain instrumentation problems occurred.

#### 3.6.1.3 Three-Component Mean Velocity

A TSI Model 1247 Cross Flow "X" Probe hot film array was used to measure the three components of the mean velocity in the wing-body junction flow. The hot film sensor diameter and length were 0.025 mm and 0.51mm, respectively. The distance between the sensors was also 0.51mm, and therefore the measurement volume was approximately  $(0.5 \text{ mm})^3$ . The x-array film was calibrated by moving the film to the tunnel free stream and measuring the analog output

for each film as a function of tunnel air speed. This procedure automatically accounted for the inclinations of the films to the flow and the resultant longitudinal cooling effect. Because the measured flow direction relative to the probe did not deviate substantially from the calibration flow direction, the calibrations were sufficiently accurate. The error in the longitudinal velocity was negligible, and the error in the cross-velocity was approximately 10 percent low in magnitude.

The x-array hot film probe was rotated to two successive positions to make measurements of the three velocity components. The error in this procedure was only a few percent because the longitudinal velocity was much larger than either the lateral or the transverse velocity. In all, four velocities were measured at each position in the flow: a nearly transverse component, a nearly lateral component, and a redundant pair of longitudinal component measurements. Measurement of the actual probe orientation and the angle between the film elements permitted trigonometric resolution of the velocities into the appropriate coordinate system components.

The angles between the films was determined using the method reported by Shabaka (1979), which essentially assumed a linearized form for the hot film output for velocity directions within about 10 degrees of the mean direction. A TSI Model 1125 Calibrator, modified with fixtures to produce the required probe orientation, was used to provide empirical input to the calculation. The measurement set-up is shown in Figure 3-18.

The probe orientation to the flow was determined by placing it in the tunnel free stream and visually aligning it parallel to the (assumed) mean flow direction nearly as possible. The lateral and transverse velocities were defined to be zero at this calibration position. The x-array hot film was then calibrated for voltage output as a function of tunnel air speed.

The probe was then placed in the appropriate measurement position. The measured velocity directions were therefore relative to the assumed velocity vector at the location where the calibra-

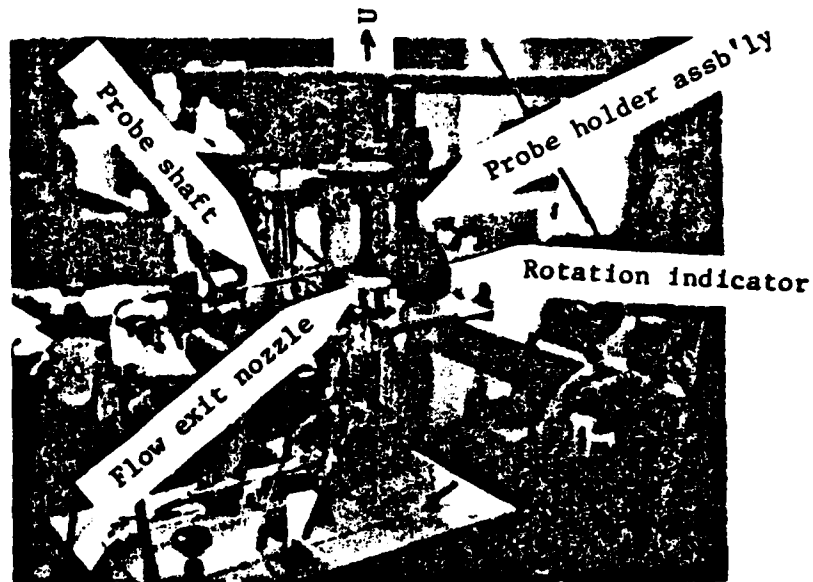


Figure 3-18: Calibration Set-Up to Determine Angles Between Hot Film Elements



Figure 3-19: Temperature Probes Installed Downstream from Wing in Tunnel

tion was performed. The calibration and measurement positions were always in the same plane ( $x = \text{constant}$ ) normal to the free stream flow.

#### 3.6.1.4 Two-Point Velocity Correlations

TSI Model 1262 Miniature Probes with Sensor Upstream hot films were used to measure the two-point velocity correlations. The cylindrical sensor element was 0.025mm in diameter and 0.51mm long. The single element films were aligned parallel to the wall to be mostly sensitive to fluctuations in the x-y plane. Because the flow was mostly in the longitudinal direction, the sensitivity of the films was much larger for the longitudinal fluctuations (x-direction) than for the tranverse (y-direction) fluctuations.

#### 3.6.1.5 Temperature Compensation for the Hot Films

The hot films were temperature compensated with TSI Model 1310 Temperature Compensating Probes with TSI Model 1325 Trimming Network resistors. To select values for the two adjustable compensation resistors, both the film and the compensation probe were placed in a refrigerator and cooled to near 0°C. From measurements of the film and temperature compensation probe resistances at a temperature of approximately 25°C (room temperature) and at the temperature near 0°C, values of the parallel and series resistances in the temperature compensation probe were set to suppress the hot film response to ambient temperature variations. A laboratory-type mercury thermometer was used to measure the temperature at which the film and temperature compensation probe resistances were measured. Operation of the hot film included measurements of the tunnel temperature. This measurement was made by placing a third TSI Model 1310 Temperature Compensating Probe in the flow, and using it with the constant current bridge of a TSI Model 1054A anemometer to produce an output voltage proportional to temperature. The output voltage from this probe was measured with a Fluke 8050A Digital Multimeter and recorded along with the hot film velocity outputs to provide information for temperature corrections in the event that large temperature changes were encountered; none were.

The temperature measurement probe and the two temperature com-

pensating probes used to control the hot film temperatures were placed downstream from the wing and to one side of the wake. The photograph in Figures 3-19 shows the probes installed in the tunnel.

### 3.6.2 Pressure Measurement System

The pressure measurement system was used to acquire the mean wall pressures and the reference pitot-static tube pressures from which the free stream velocity was determined. A schematic of the pressure measurement system is shown in Figure 3-20. Two scan-valves were used to route the desired pressure to be measured to a Barocel Model 572D 10 Torr pressure transducer, which was electronically conditioned by an electronic manometer. The output from the electronic manometer was in both digital and analog form. The manufacturers claimed accuracy for the Barocel system is an indicated pressure within 0.7% of the applied pressure, or 0.001 Torr, whichever is larger. The accuracy of the signal conditioning was periodically verified by placing the internal calibration load on the system electronics. There was no pressure calibration of the system other than to compare its output against the response of an inclined-tube manometer to ascertain that there was no gross inaccuracy (relative to the manufacturer's specifications).

#### 3.6.2.1 Reference Pressure

The reference pressure for the differential pressure transducer for all pressure measurements was the tunnel static pressure measured by the reference pitot-static tube.

#### 3.6.2.2 Wall Pressure Measurements

Mean static wall pressure measurements were made using carefully constructed pressure taps in the wall. Special care was taken to produce clean, square, and flush taps. The pressure taps consisted of 3/64 in. I.D (5/64 in. O.D.) steel tubing mounted through holes drilled in the plexiglas wall. The holes were drilled on a numerically controlled drilling machine to assure uniform holes normal to the plate and without burrs. However, in manufacture the plate rippled where the holes were closely spaced. The surface distortion was not measured, and was not visually noticeable. However, the unevenness of the surface could be felt by



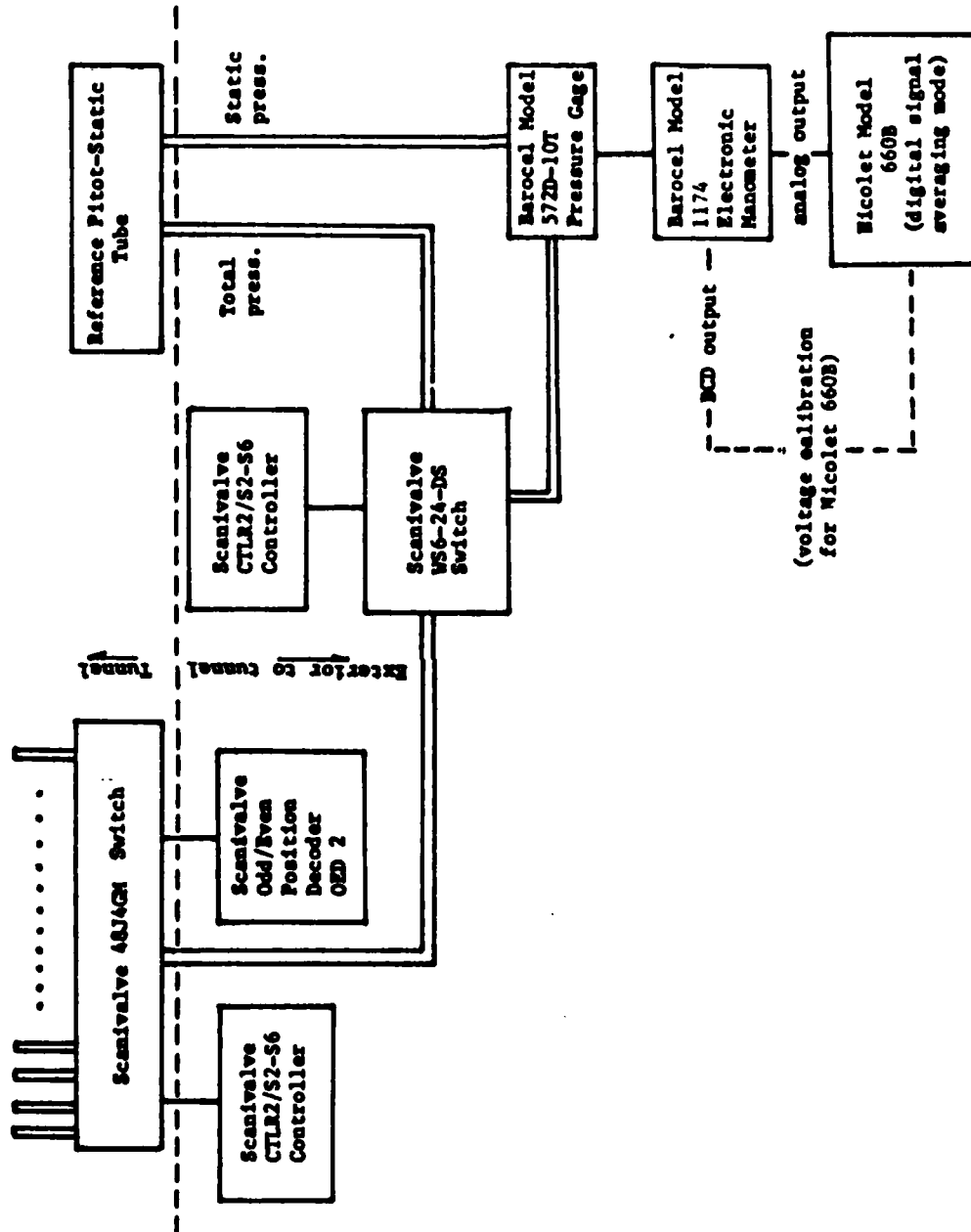


Figure 3-20: Schematic of the Pressure Measurement System

running a hand over it. The surface distortion is not believed to have affected the measurements in the experiment.

The pressure tubes were manufactured by hand. Each tube was cut to the desired length after first running a solid wire through it to minimize crimping at the cut. The end to be inserted into the drilled wall holes was carefully ground to make the finished end flat, free of burns, and square to the tube. The finished tubes were cemented into the wall holes. Tygon 1/16-in. ID tubing was used to route the pressures to the Scanivalve Model 48J4GM pressure switch and manifold. This scanivalve switch was used to sequentially select the pressures to be measured; see Figure 3-20.

A second scanivalve switch was used to alternately route the pre-selected wall pressure and the reference pitot pressure to the Barocel pressure transducer. The pressure measurement output from the electronic manometer consisted of both a digitized display and an analog signal. The digital display output was updated so rapidly that it was difficult to read fluctuating voltages by eye. Therefore, the analog output was input to the Nicolet 660B and digitally averaged to produce the actual measurement data. The Nicolet 660B output was calibrated against the electronic manometer digital output display under conditions when the pressures were steady.

The resolution of the Nicolet 660B was set at 0.024 mv., or 0.0024 percent of the range of the pressure transducer. This resolution was two orders of magnitude smaller than the voltage corresponding to the smallest measured pressures.

The analog signal was digitized at one sample/two seconds for 32 seconds. This record length corresponded to the nominal period of the small amplitude tunnel oscillations; see Section 3.1.

### 3.6.2.3 Free Stream Velocity for the Hot Film Measurements

A different arrangement was provided for the measurement of the output voltage from the electronic manometer for measurement of the free stream velocity for the hot film measurements; see Figure 3-15. For those measurements the pressures on the pitot-static

tube were measured and converted to free stream velocities. Because the Nicolet 660B was dedicated to processing hot film data, an averaging DVM was used to obtain the analog output from the electronic manometer. The averaging period was 10 seconds.

### 3.7 Error Analysis

The dominant errors in this investigation are attributable to two sources: 1) probe positioning error and 2) statistical uncertainty in the spectral correlation analysis. Explanations of the terms for which error bounds are discussed below are found in Chapters 5 and 6. However, the error analysis is presented in this section as part of the description of the experiment.

The probe positioning error given in Section 3.5 was  $(\Delta x, \Delta y, \Delta z) = (\pm 1.3, \pm 1.3, \pm 0.8 \text{ mm})$  for the traverse probe and  $(\pm 0.8, \pm 0.8, \pm 0.8 \text{ mm})$  for the fixed probe. As the consequence, the error in the positions of the correlation contours are  $(\pm 2.1, \pm 2.1, \pm 1.6 \text{ mm})$ , or  $(\Delta x/t, \Delta y/\delta, \Delta z/t) = (\pm 0.04, \pm 0.04, \pm 0.03)$ . Because the errors were determined from estimates of traverse rigidity, the errors are bias-type in that whole sections of the correlation contours may be in error in the same direction.

A review of the measurement results shows that shifts in the contours within that range do not produce dramatic changes in the data; do not change any of the conclusions; and do not require caveats to qualify the data.

The statistical uncertainty in the data is attributed almost entirely to precision error limited by the number of ensembles  $N$  of time history data. The reference for the formulas used for the error analysis is Bendat and Piersol (1980).

The relative uncertainty in the power spectral densities is

$$\epsilon = \frac{1}{\sqrt{n_d}} = 7\%$$

where  $n_d = 200$  in the present investigation, in which  $N = 400$  ensembles of data were processed with 50 percent redundancy.

The relative uncertainty for the quantity  $|S_y| = (\gamma^2)^{1/2}$

(see Section 6.1) is derived from the relative uncertainty in the coherence:

$$\epsilon(\gamma^2) = \frac{\sqrt{2}}{\sqrt{n_d}} \frac{|1 - \gamma^2|}{|\gamma^2|^{1/2}}$$

and is presented in the following table:

Measured Value for $ S_Y $	Interval in Which True Value $ S_Y $ Lies	
	2/3 Probability	9/10 Probability
0.2	0.14 - 0.24	0.04 - 0.28
0.3	0.26 - 0.36	0.20 - 0.40
0.4	0.36 - 0.44	0.30 - 0.48

The interpretation of the table is that there is a 2/3 (or 9/10) probability that the true value of  $|S_Y|$  falls within the interval of values shown in the appropriate column opposite the particular value for the measured  $|S_Y|$ .

The uncertainty in the relative phase is given in the following table using the formula:

$$\epsilon(\phi_B - \phi_A) = \frac{(1 - \gamma^2)^{1/2}}{|\gamma| \sqrt{2n_d}}$$

Measured Value for $ S_Y $	Uncertainty in $\phi_B - \phi_A$	
	2/3 Probability	9/10 Probability
0.2	14°	28°
0.3	9°	18°
0.4	6°	12°

The table shows that the true phase is indicated by the measured phase if it is known in advance that the phase must be either "in-phase" or "out-of-phase," even for small values of  $|S_Y|$ . Hence observations of the measured phase were a more sensitive indication of spatial extent of the flow structure than was the actual value for  $|S_Y|$ .

## CHAPTER 4

### MEAN FLOW MEASUREMENT RESULTS

#### 4.1 The Onset Boundary Layer

Mean values of the velocity and of the turbulence intensity were measured in the onset boundary layer. The measurements were compared with classical flat plate data to demonstrate that the onset boundary layer was similar and can be considered a classical flat plate turbulent boundary layer. The mean velocities were also measured to provide boundary value input to numerical computations to be made in the future.

##### 4.1.1 Velocity Profiles

Total head pressure profile measurements were obtained at the four locations shown in Figure 4-1 to determine velocity profiles for the onset boundary layer. In the figure, the position  $P(0,0,0)$  is where the wing leading edge intersected the wall when the wing was installed; it was not installed for these measurements. The profiles were evaluated to determine the similarity of the onset flow to textbook published data for developed flat plate turbulent boundary layers. The measured profiles were used in

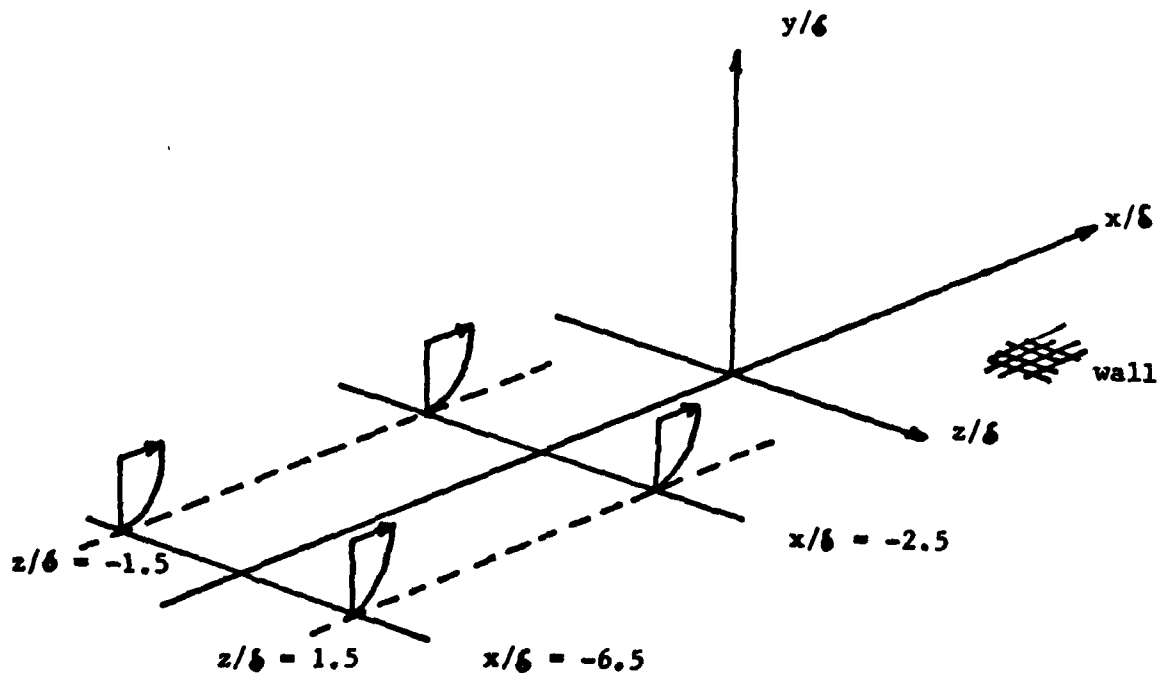


Figure 4-1: Locations for Velocity Profiles

integrations to obtain values for the momentum thickness  $\theta$  and the displacement thickness  $\delta^*$ , and which are tabulated in Table 4-1.

The values for  $\theta$  were used to calculate the momentum thickness Reynolds number,  $R_\theta = U_0 \theta / \nu$ , which was compared to the minimum value,  $R_\theta = 5000$ , considered necessary by Rao (1971) for a developed turbulent boundary layer. As shown in the table, the higher speed  $U_0 \sim 37 \text{ m/s}$  produced a very large value for the Reynolds number indicative of a fully developed turbulent boundary layer. The data for  $U_0 \sim 18 \text{ m/s}$  produces a Reynolds number below 5000, yet the flow parameters indicate a nearly turbulent flow. It is concluded that the higher speed turbulent flow was well beyond the onset of full development. The shape parameters  $H$  were computed and found comparable to values expected for smooth wall turbulent boundary layers ( $H < 1.5$ ). Those computed values for  $H$  are also tabulated in the table.

The total head profiles were converted to velocity profiles by assuming constant static pressure across the boundary layer. The velocity profiles were matched to an accepted logarithmic law of the wall velocity distribution to determine the shear stress at the wall. The matching is shown in Figures 4-2(a) through 4-9(a). The obtained shear stress was then input to logarithmic velocity defect law calculations for comparison with published data. Those results are shown in Figures 4-2(b) through 4-9(b).

The purpose of the comparison was to establish consistency with previously published data; the defect law calculations depend on the logarithmic fit in the above calculations but the two methods are empirically related in the classical literature. It is observed from the figures that the compared data are generally consistent in that they are near the empirical line representing the classical relationship. The error bias is above the line for  $U_0 = 37 \text{ m/s}$  and below the line for  $U_0 = 18 \text{ m/s}$ . Some improvement in the consistency between law of the wall and the velocity defect matches could be expected by an adjustment in the coefficients for the "universal" profiles. However, the purpose of the present measurement was to demonstrate a reasonable "equilibrium" turbulent boundary layer, and to provide credence that there was nothing peculiar

$x/\delta$ (nominal)	$z/\delta$ (nominal)	$U_o$ m/s	$\delta$ mm	$\delta^*$ mm	$\Theta^{(1)}$ mm
-2.5	+1.5	36.6	48	5.3	3.8
		18.3	46	5.0	3.6
	-1.5	36.6	51	5.2	3.7
		18.3	46	5.3	3.9
-6.5	+1.5	37.8	52	4.4	3.3
		18.3	51	4.3	3.2
	-1.5	37.8	46	4.7	3.4
		18.6	46	4.9	3.6

$x/\delta$ (nominal)	$z/\delta$ (nominal)	$H$	$R_\theta$	$\frac{u^*}{U}$ (law of the wall)	$\frac{u^*}{U}$ (H fit) (2)	$G$ (law of the wall) (3)	$G$ (H fit) (3)	$C_f$ (law of the wall) (4)
-2.5	+1.5	1.39	9400	0.033	0.041	8.41	6.79	0.0022
		1.40	4400	0.037	0.042	7.75	6.77	0.0027
	-1.5	1.41	9100	0.035	0.043	8.53	6.94	0.0023
		1.37	4700	0.036	0.039	7.26	6.70	0.0028
-6.5	+1.5	1.35	9000	0.034	0.038	7.67	6.82	0.0023
		1.35	4100	0.037	0.038	6.93	6.82	0.0028
	-1.5	1.40	8400	0.033	0.042	8.53	6.76	0.0022
		1.35	4500	0.035	0.038	7.41	6.83	0.0024

Notes:

(1) Cubic fit of data near wall

(2) Calculated from Eq. (7-73) in Hinze (1975):

$$\frac{u^*}{U_o} = \frac{1.0 - \left( \frac{1.0}{H - 0.04} \right)}{6.3}$$

(3) Calculated from Eq. (6-69) in White (1974):

$$G = \frac{U_o}{u^*} \left( 1.0 - \frac{1.0}{H} \right)$$

$$(4) C_f = 2.0 \left( \frac{u^*}{U_o} \right)^2$$

Table 4-1: Boundary Layer Parameters



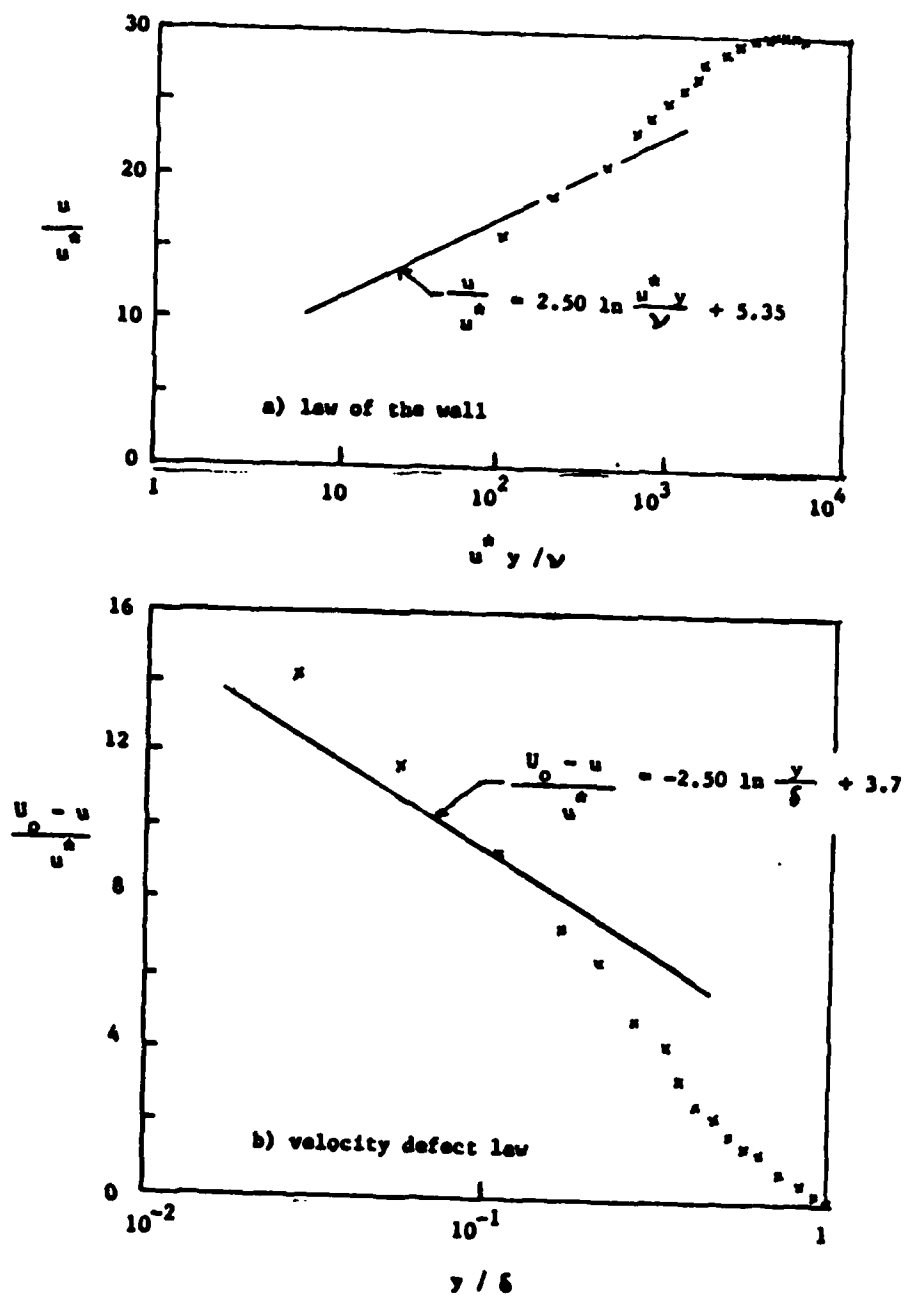


Figure 4-2: Velocity Profile Matches for  $P(-2.5, y/\delta, 1.5)$  for  $U_0 = 36 \text{ m/s}$

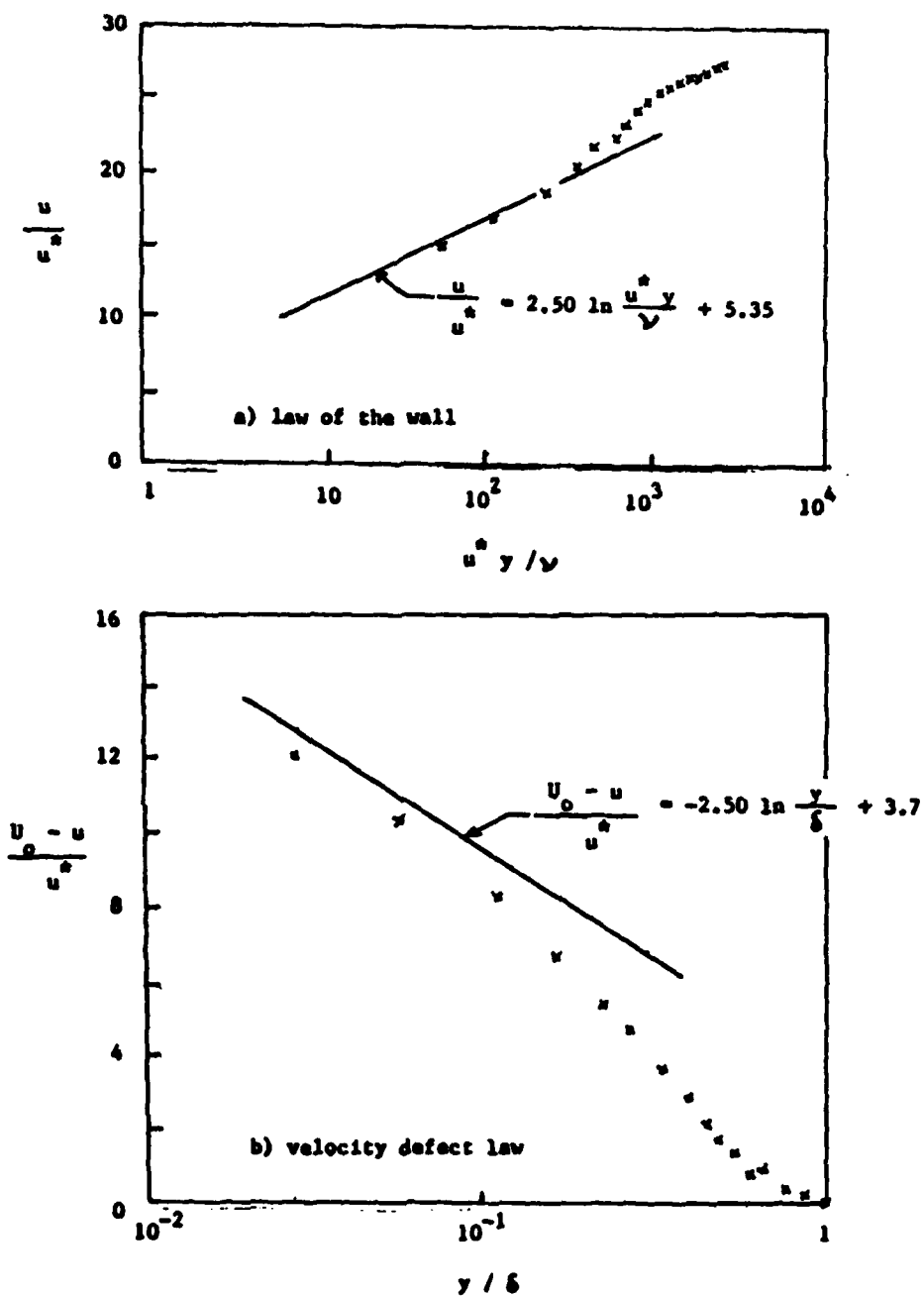


Figure 4-3: Velocity Profile Matches for  $P(-2.5, y/\delta, 1.5)$   
for  $U_0 = 18 \text{ m/s}$

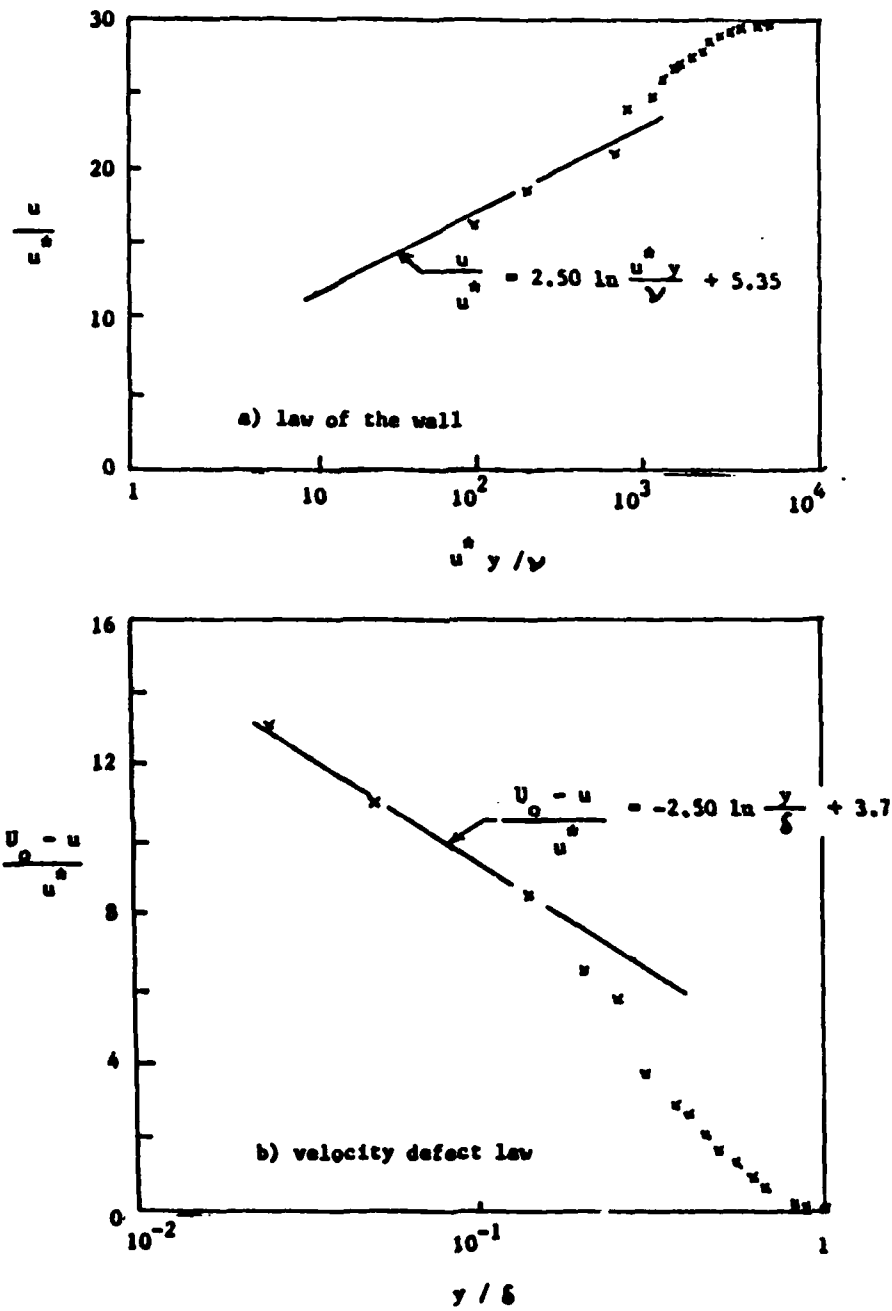


Figure 4-4: Velocity Profile Matches for  $P(-2.5, y/\delta, -1.5)$   
for  $U_0 = 36 \text{ m/s}$

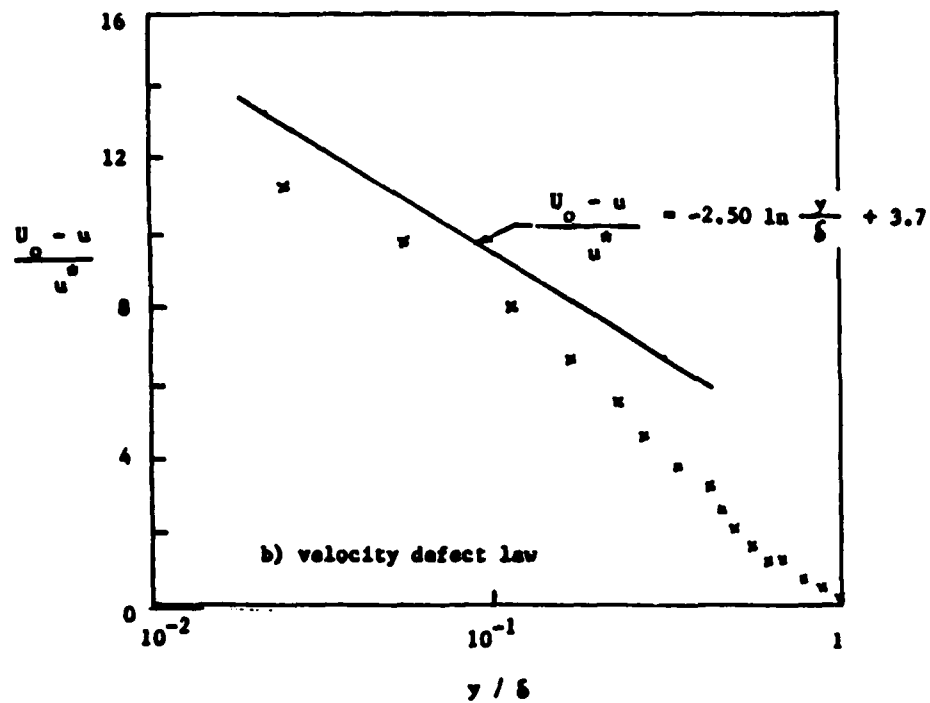
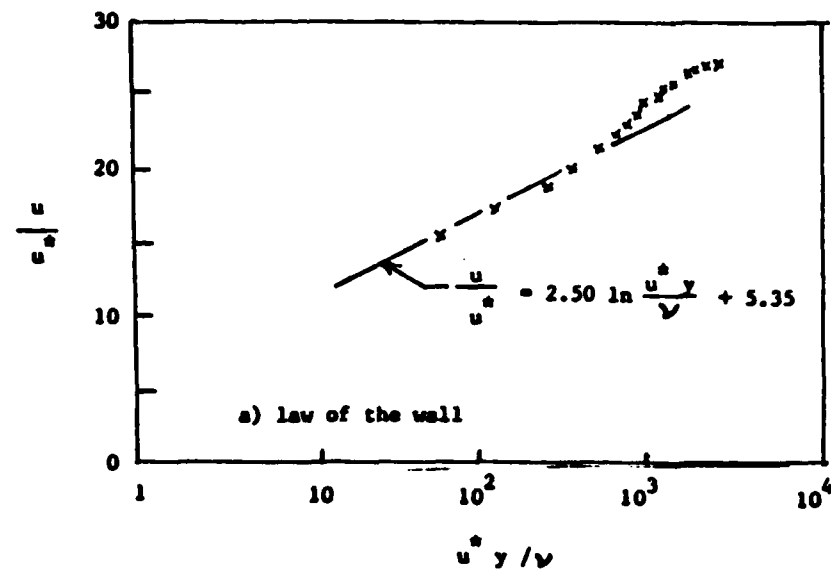


Figure 4-5: Velocity Profile Matches for  $P(-2.5, y/\delta, -1.5)$  for  $U_0 = 18 \text{ m/s}$

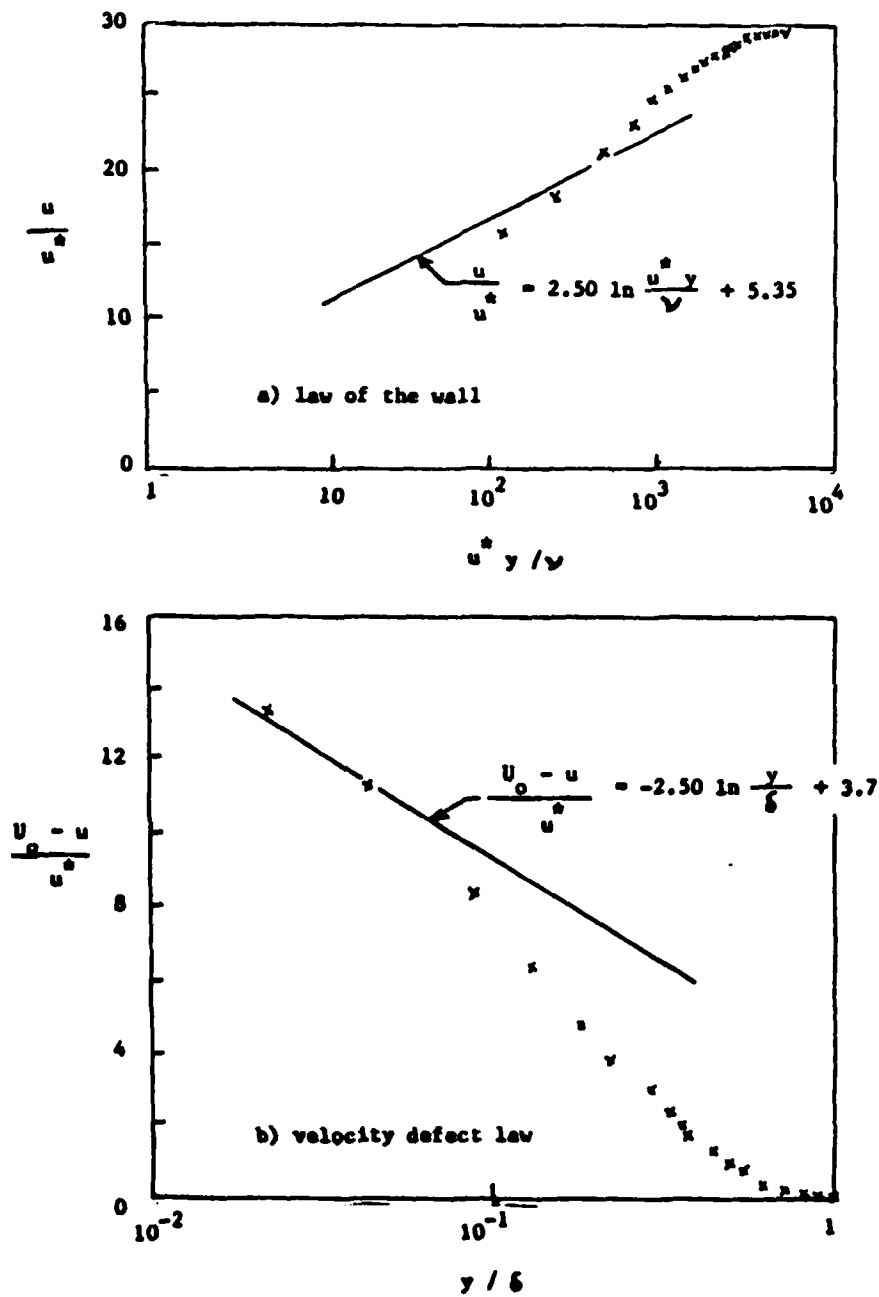


Figure 4-6: Velocity Profile Matches for  $P(-6.5, y/\delta, 1.5)$   
for  $U_0 = 38 \text{ m/s}$

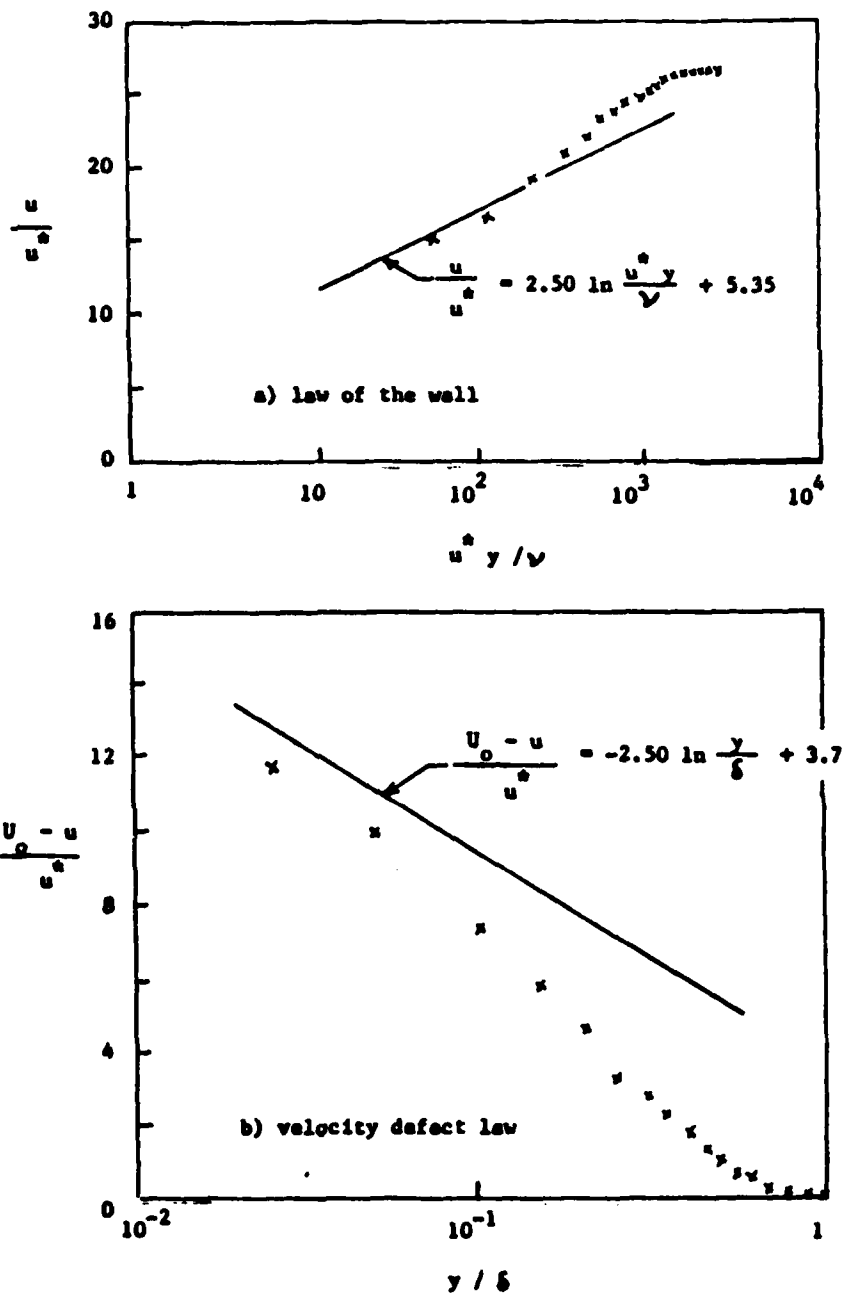


Figure 4-7: Velocity Profile Matches for  $P(-6.5, y/\delta, 1.5)$  for  $U_o = 19 \text{ m/s}$

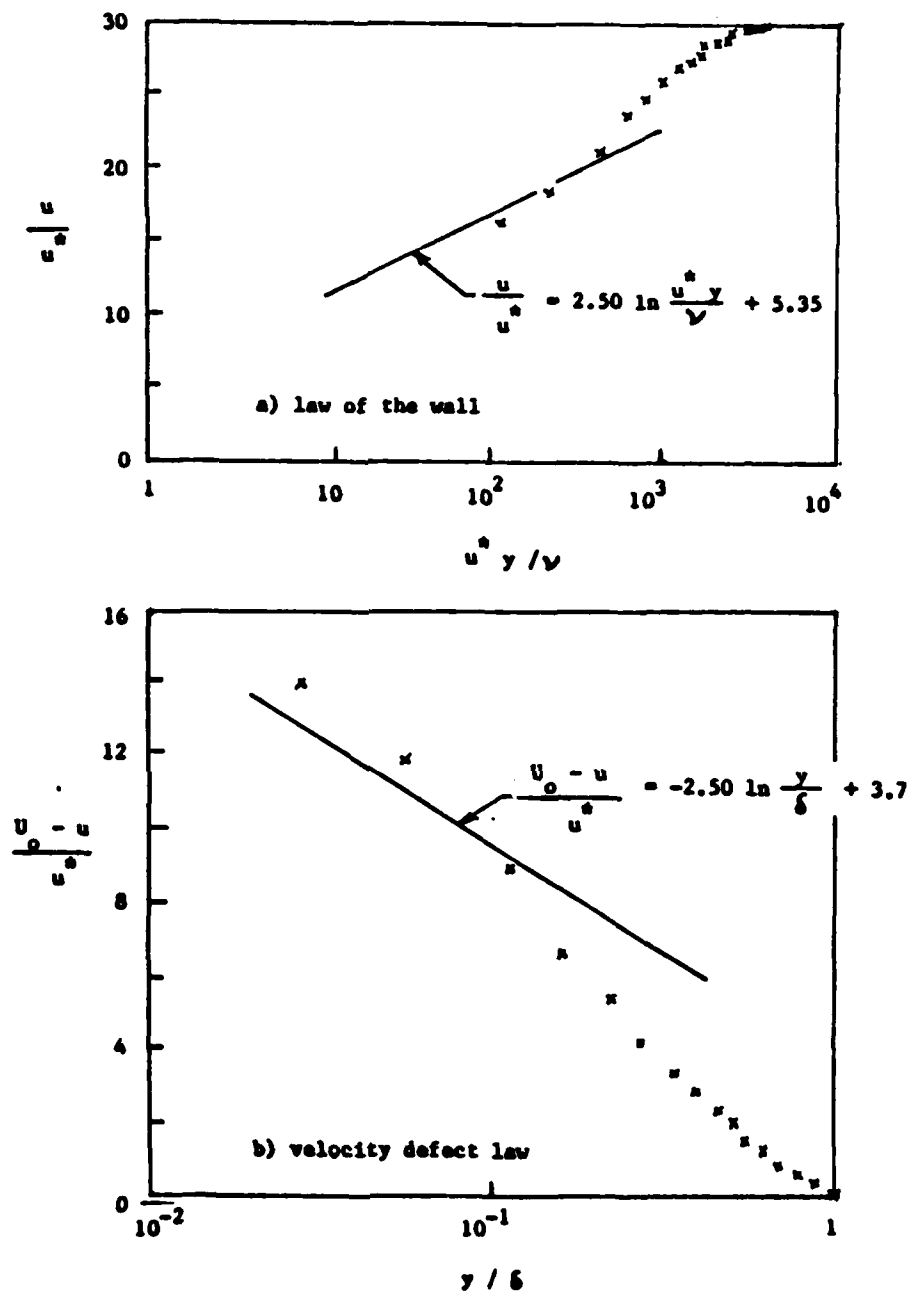


Figure 4-8: Velocity Profile Matches for  $P(-6.5, y/\delta, -1.5)$  for  $U_0 = 38 \text{ m/s}$

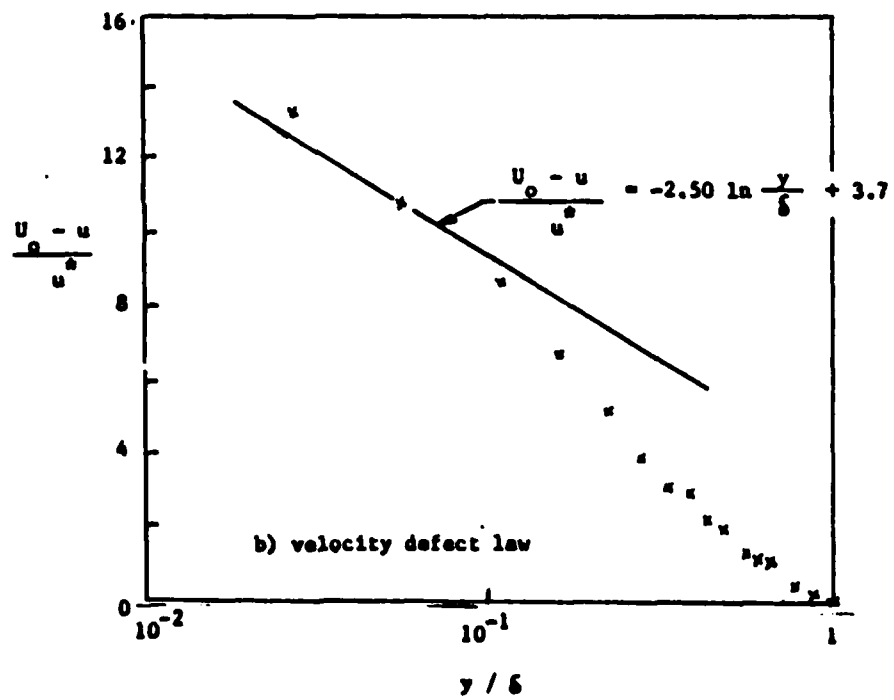
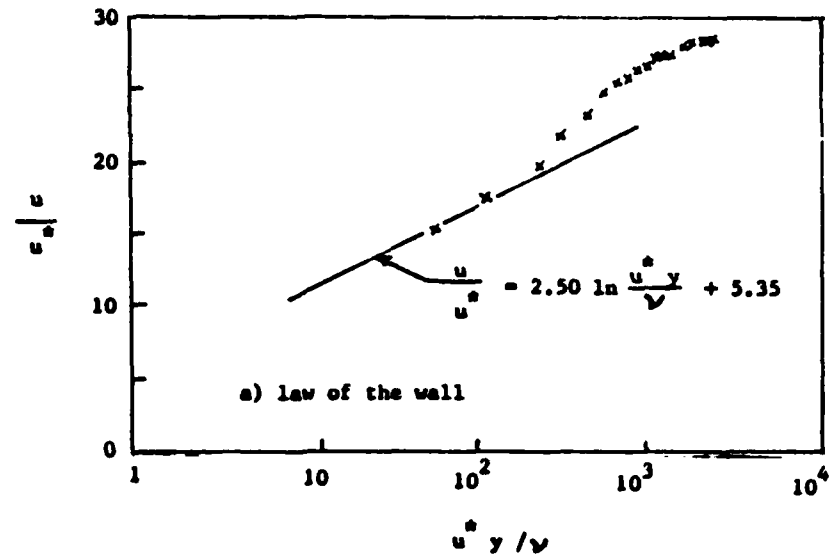


Figure 4-9: Velocity Profile Matches for  $P(-6.5, y/\delta, -1.5)$  for  $U_0 = 19 \text{ m/s}$



in the onset flow to produce the measured temporal flow in the wing-body junction.

In a second check of consistency in the measured data, shear stresses obtained from the computed  $H$  by direct comparison with previously published data were compared with the values that were obtained for law of the wall matching. Both values are shown in the table. The values obtained from the law of the wall profile matching were up to 25 percent less than those obtained directly using the calculated value for  $H$ .

A second shape parameter,  $G$ , was therefore calculated using White (1974) to evaluate the accuracies of the two values for the shear stress. The calculated values for  $G$  for the present measurements are given in Table 4-1. For both methods of obtaining the shear stress, the value for  $G$  ( $>6.5$ ) indicates an adverse pressure gradient in the tunnel. The smaller value for the shear stress leads to a large calculated value for  $G$ , indicating a substantial adverse pressure gradient in the tunnel, which is not reasonable. Although the larger value for the shear stress also indicates an adverse pressure gradient, it is small with an equivalent change in velocity equal to 1 percent/foot.

The inconsistency in the two methods for obtaining the shear stresses is observed relative to previously obtained flat plate data, and does not necessarily indicate that there is something strange about the onset boundary layer. An explanation may be found in an error in the measurement distance  $y$  from the wall, or in the geometric conditions producing the boundary layer. It may be that the converging tunnel inlet and the ramp leading to the plate on which the wing was mounted had effects on the turbulent boundary layer not present for a true flat plate condition.

The data may be made wholly consistent if either the shear stress, calculated from the law of the wall profile, is increased or the value for  $H$ , calculated from the velocity profile, is decreased. However, it is not likely that the calculated value for  $H$  is in substantial error.

A third, separate calculation of the shear stress was made

from the gradient of the momentum (loss) thickness,  $C_f = 2 d\theta/dx$ , which also indicated that the shear stress obtained from the law of the wall profile is too small. If this is the case then an explanation may be that the measured value for  $y$  is larger than the effective value for  $y$ . Because the law of the wall matching was made for  $y \leq 0.2$  in., a small change in the value for  $y$  could lead to substantial relative changes in the value for  $u^*$ .

The conclusion from the above computations and comparisons is that the turbulent boundary layer for  $U_0 \sim 37$  m/s is fully developed since it nearly fulfills the expected characteristics for flat plates. Specifically, the momentum thickness Reynolds number is large ( $>5000$ ) and the data can be described by both the law of the wall and the velocity defect law. The shape factor  $H$  has values expected for a developed flat plate turbulent boundary layer.

#### 4.1.2 Turbulence Intensity

The turbulence intensity was obtained from the low pass filtered data from the x-array hot film; the analog signal was filtered at 200 Hz. The turbulence intensity profile is shown in Figure 4-10. Also shown in the figure is a classical flat plate result from Hinze (1975). The lower intensity of the present measurements is attributed to the filtering of the analog signal. It is believed that the measurements are otherwise comparable.

#### 4.2 Flow in the Wing-Body Junction

The mean wall pressure and flow velocity were measured at selected positions in the wing-body junction flow of the  $a/b = 1.5$  infinite chord length wing. The measurements were made to assess the overall characteristics of the mean flow. Specifically, the wall pressures were measured to determine the length and breadth of the upstream pressure ridge produced by the stagnation on the wing leading edge, and to verify the presence of low pressures to the side of the wing produced by flow accelerations. In addition, all three components of the mean velocity were obtained in the plane  $(x_0/t, y/t, z/t) = (2.00, y/t, z/t)$ , where the secondary flow

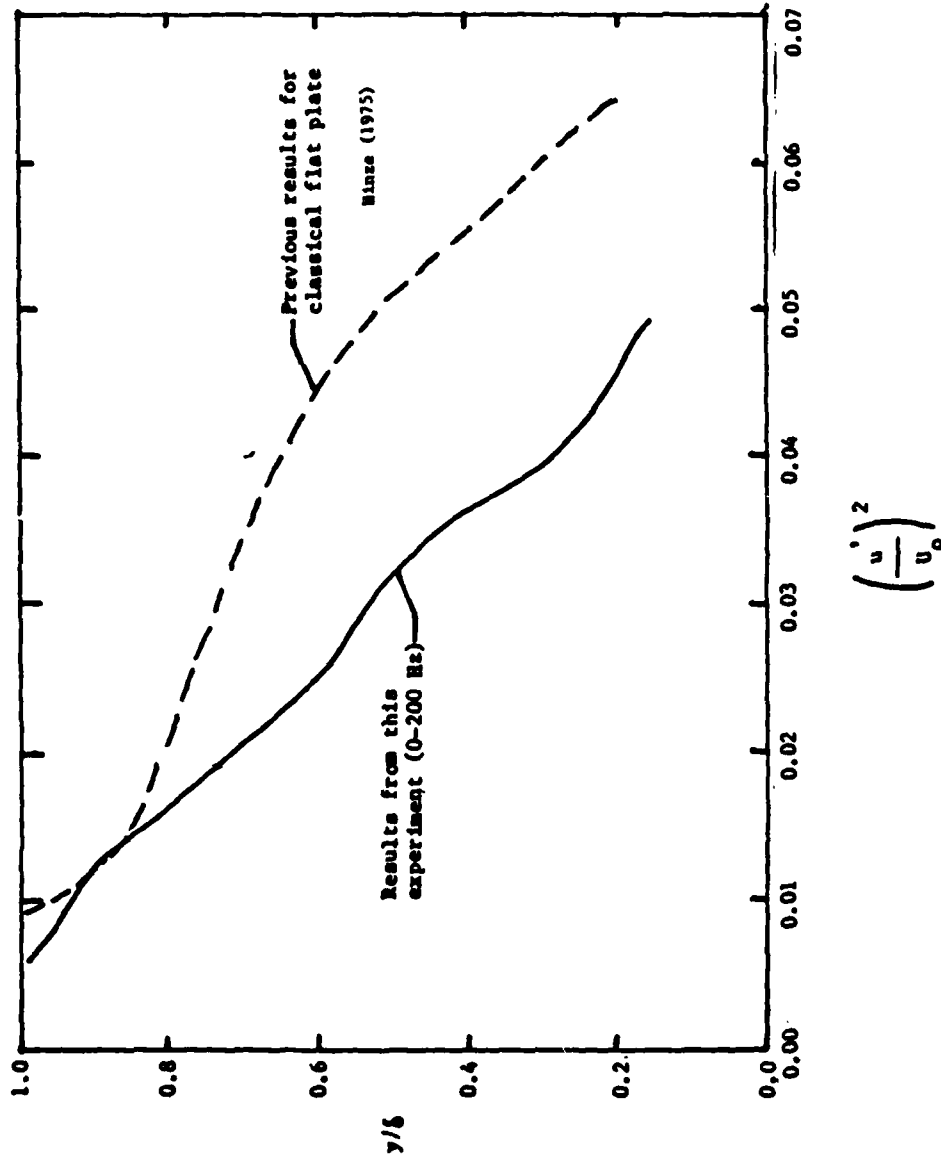


Figure 4-10: Turbulence Intensity Profile for Onset Boundary Layer

"horseshoe vortex" was well developed, to demonstrate the strong flow distortion that resulted from the vortical transport.

Flow visualization studies using oil dot and oil film techniques were also conducted to assess the type and degree of three-dimensional separations present both in the wing-body junction flow and at the tip of the wing.

The results from the pressure, velocity, and flow visualization measurements were compared and found to be mutually supporting.

#### 4.2.1 Wall Pressures

The measured mean wall pressures are presented as pressure coefficients

$$C_p = \frac{p - p_s}{p_t - p_s} = \frac{\Delta p}{\frac{1}{2} \rho U_\infty^2}$$

where  $p$  is the static pressure at the position  $(x/t, 0.0, z/t)$  and  $p_t$  and  $p_s$  are the total head and static pressures measured with the reference pitot static tube.

The error in  $C_p$  attributable to variation in the freestream static pressure with position,  $x$ , was calculated to be less than  $\pm 0.01$  when the boundary layer growth on the wind tunnel walls and tunnel blockage produced by the wing were considered. The maximum error in  $C_p$  produced by the Baracel measurement system was an additional  $\pm 0.0007$ .

The wall pressures for positions  $x/t < 0$  upstream from the wing are shown in Figure 4-11. The wall pressure is observed to be peaked at  $z/t = 0.0$  along the  $z/t$  axis, with a cusp in the direction along the  $x$ -axis. The  $C_p$  surface can be visualized as a pressure ridge extending upstream in the negative direction of the  $x$ -axis. The  $C_p$  contour along the  $x$ -axis, which corresponds to the pressure ridge, is shown in Figure 4-12. It is seen that the ridge extends at least 5 wing thicknesses upstream.

The pressure coefficients  $C_p$  for positions along the side of the wing ( $x/t > 0$ ) are shown in Figure 4-13. The accelerated flow around the wing leading edge produced the large negative coef-

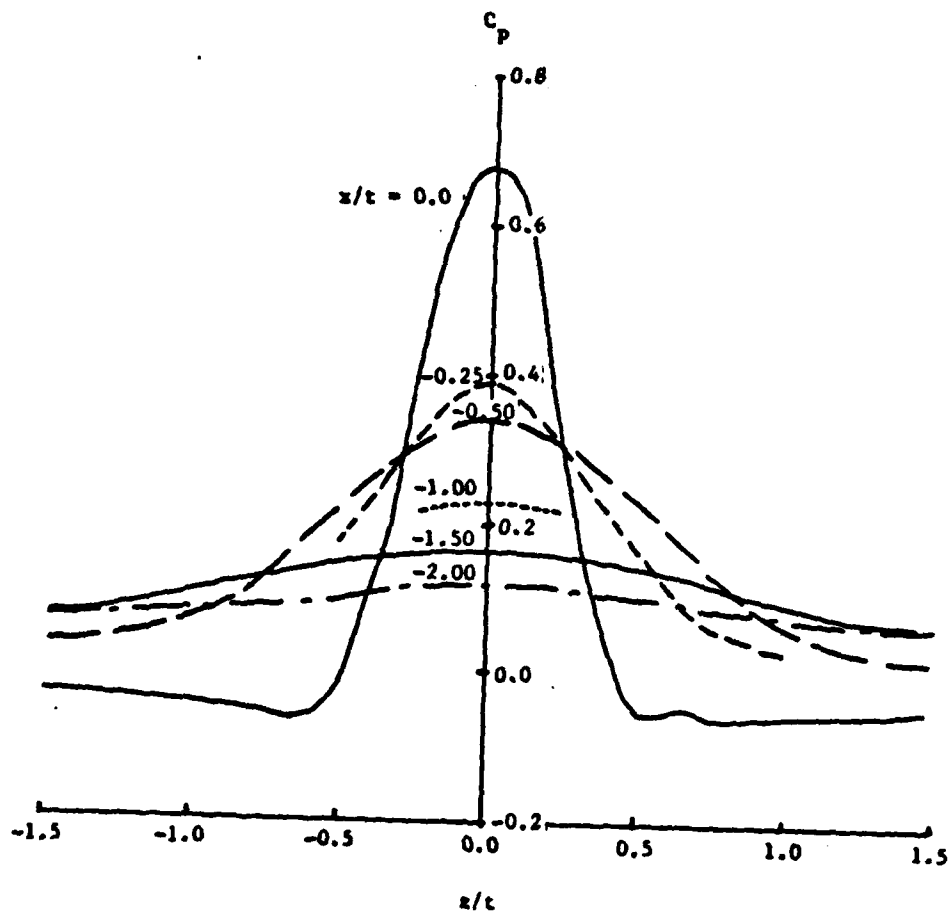


Figure 4-11: Wall Pressures Upstream From the Wing

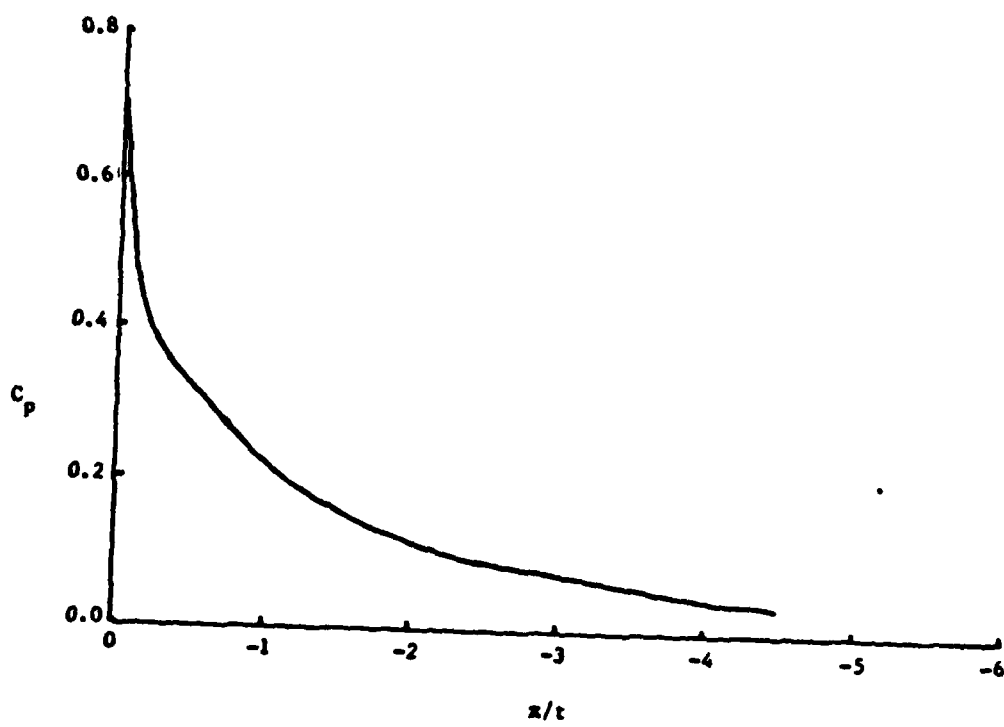


Figure 4-12: Wall Pressures Along Upstream Pressure Ridge

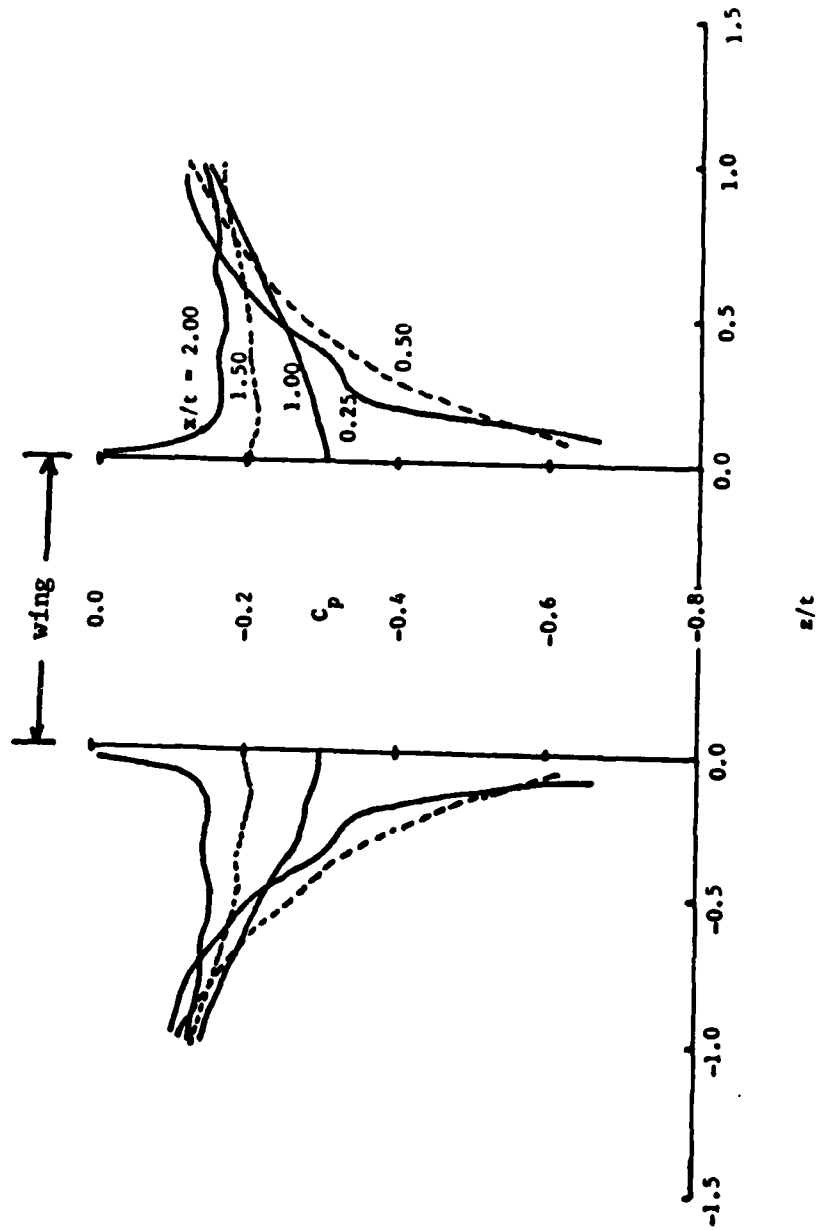


Figure 4-13: Wall Pressures Along Side of Wing

ficients, associated with low pressures, shown in the figure. the pressures rapidly relaxed toward  $C_p = 0.0$  as the fluid traveled downstream in the direction of increasing  $x/t$ , but even at  $x/t = 2.0$  the pressures were still negative.

#### 4.2.2 Three Component Velocities

Measurements were made of the three velocity components ( $u/U_0$ ,  $v/U_0$ ,  $w/U_0$ ) in the plane ( $x/t = 2.00$ ,  $y/\delta$ ,  $z/t > 0$ ). The measurement probe was an x-film array, and successive measurements were made with the "x" in two planes to obtain the three velocity components (the longitudinal component was measured in both cases). The cross-stream velocity  $\vec{v} + \vec{w}$  is shown in Figure 4-14, and iso-velocity contours for the magnitude of the longitudinal velocity  $\vec{u}$  are shown in Figure 4-15. The significant feature for both figures is the evidence that the transport of axial momentum by the cross-stream velocities associated with the horseshoe vortex literally inverted the boundary layer. High longitudinal momentum fluid was transported into the boundary layer at the same time that low longitudinal momentum was transported out. The effect was similar to a jetting of the fluid down into the wing-body intersection, then out along the body (away from the wing) and up into the wall boundary layer.

It should be noted that this view differs in perspective from the notion that "the vortex" turns the boundary layer over. The difference in perspective accounts for the downstream deterioration of the well-defined vortex line at the wing leading edge. As the vortex is swept around the leading edge, strong shear and diffusivity forces rapidly disperse the vortex "core" so that the notion of a vortex, in contrast to distributed vorticity, is no longer appropriate. Hence Figures 4-14 and 4-15 are not reflective of a vortex with a core.

The results in Figures 4-14 and 4-15 are in substantial agreement with the features observed by Shabaka (1979) and by Oguz (1981).

#### 4.2.3 Flow Visualization of Separations

Oil dot and oil film flow visualization studies were per-



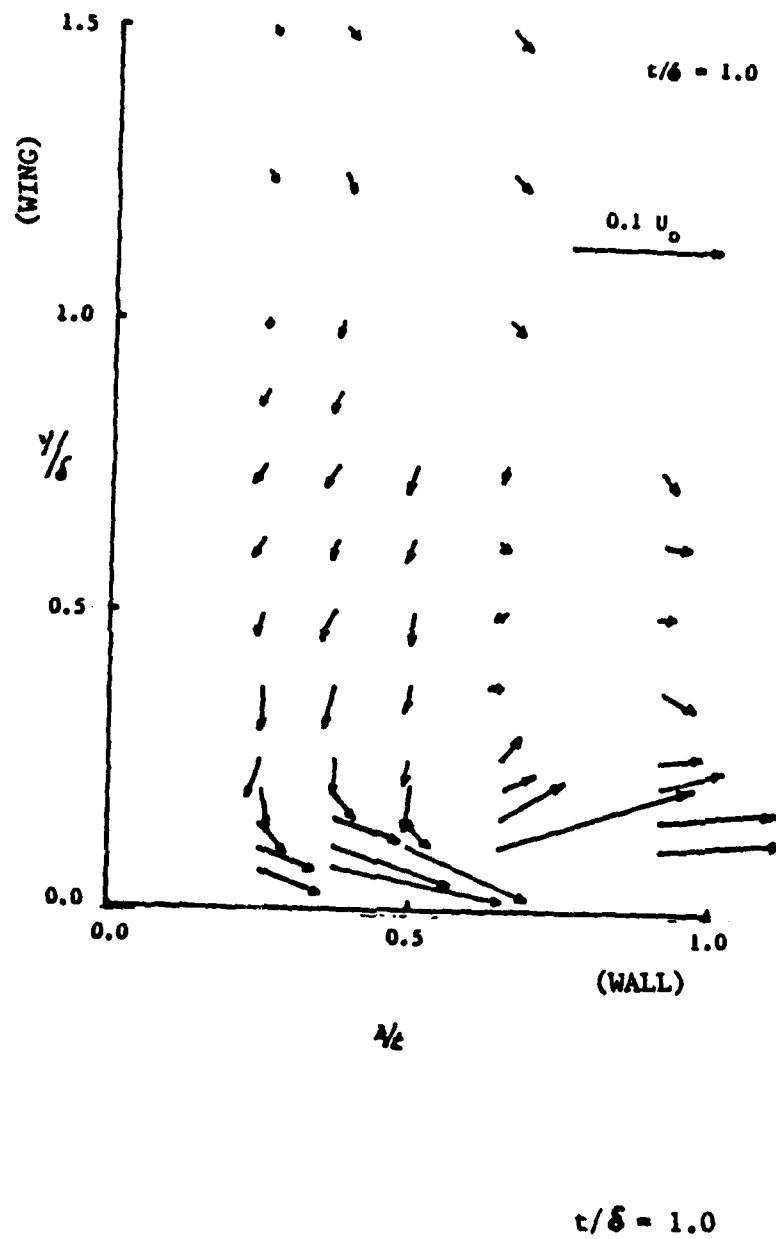


Figure 4-14: Cross-Stream Velocities at  $P(2.00, y/\delta, z/t > 0.0)$

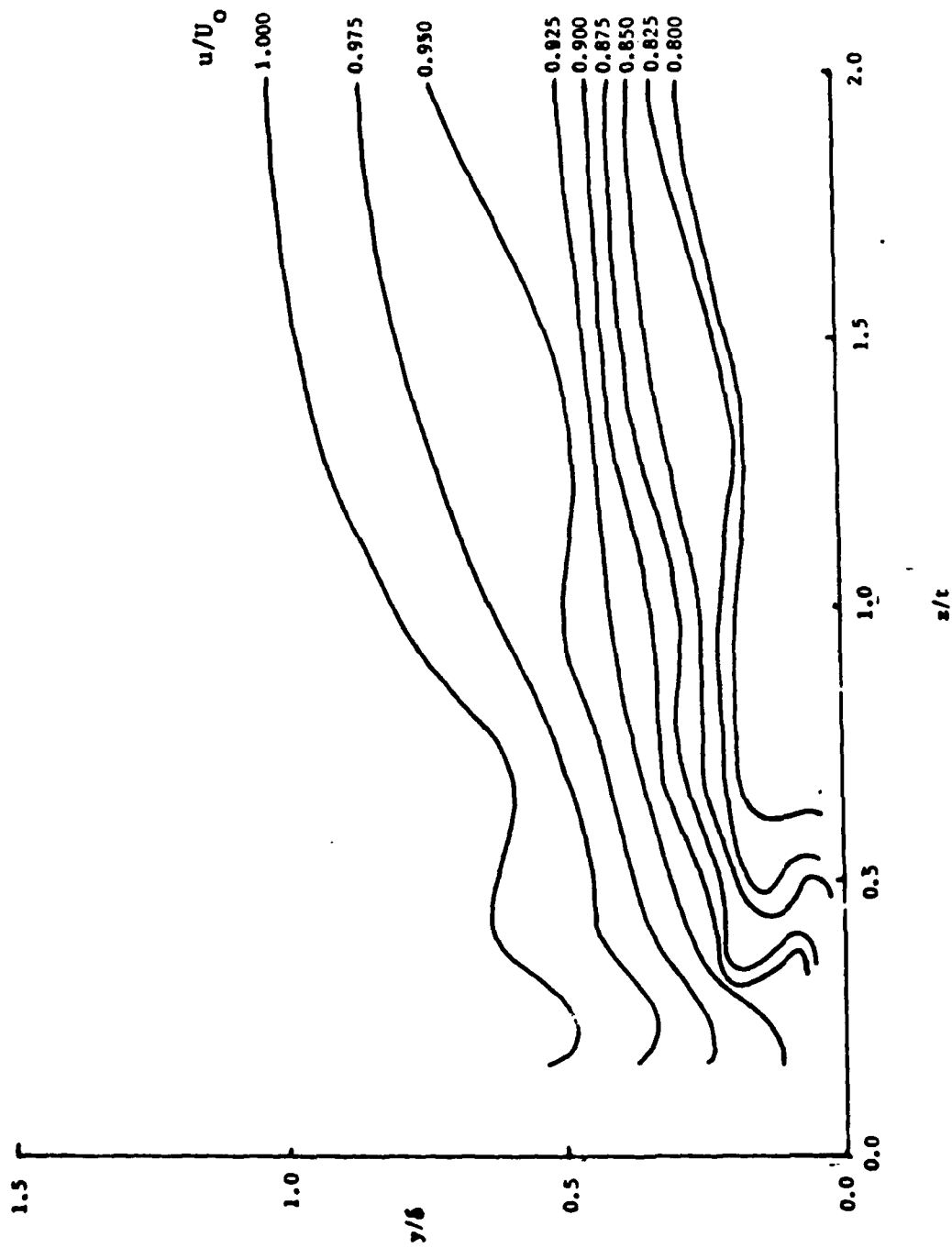


Figure 4-15: Contours of Constant Longitudinal Velocity in the Plane  $(2.00, y/\delta, z/t \geq 0.0)$

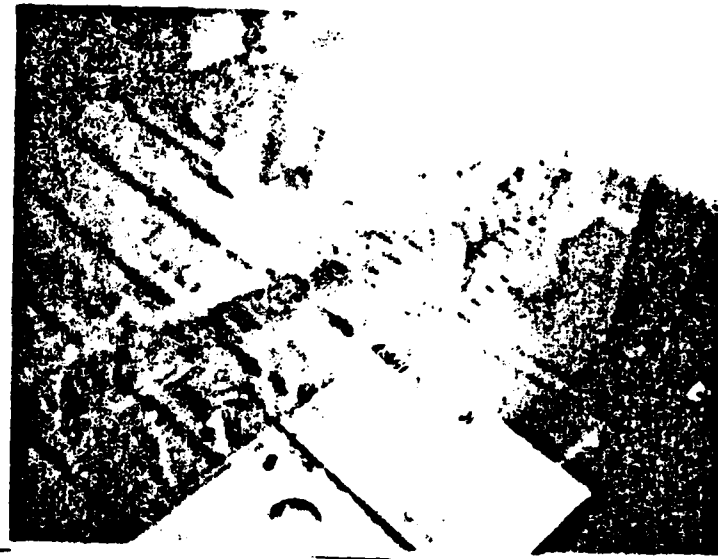
formed to evaluate the type and degree of three-dimensional flow separation associated with the wing-body junction and junction wake flows, and to make comparisons with previously published results. In addition, visualization studies were made to evaluate the size of the separation bubble produced by the trip wire and to demonstrate that the flow at the tip of the wing did not produce spanwise distortion of the flow in the wing-body junction.

#### 4.2.3.1 Wing-Body Junction Flow Separations

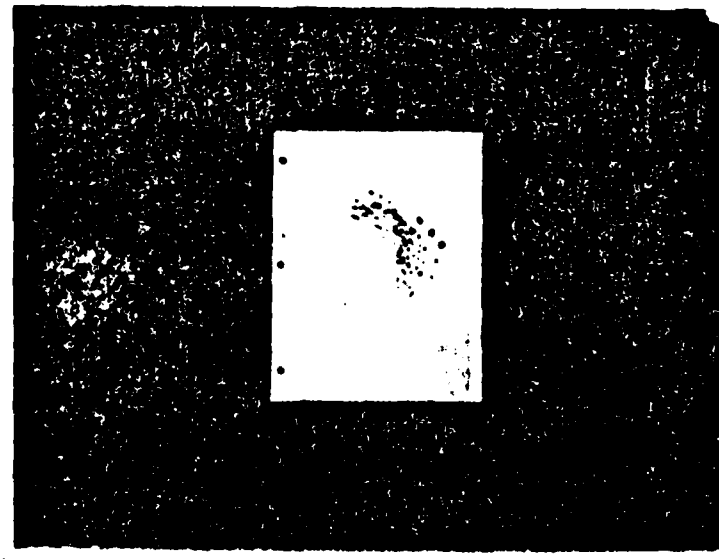
The photographs in Figure 4-16 show results from oil dot applications to the wing-body junction using a viscous mixture of motor oil and lampblack. The oil dots were applied to the wing and the wall in the leading edge region of the  $a/b = 1.5$  elliptic nose infinite chord length wing. Because the wall was vertical along the direction of gravitation forces, the oil dot mixture was more viscous than required for a horizontal surface to minimize the flow of the dots in response to gravitational forces. Of course, the sensitivity of the oil dot flow to fluid stress was diminished. The variability of the dot sizes in Figure 4-16 is accounted for by the addition of ever larger dots during the study. The tunnel was stopped to allow addition of oil. This technique was an attempt to force the oil to flow in regions of low stress, and was not very successful.

Figure 4-16 (a) shows two important features: the desired small separation produced by the trip wire on the wing, and the equally desired absence of separation at the wing "shoulder" where the elliptic nose faired into the parallel middlebody. The trip wire produced a small separation bubble about 5 mm long behind the wire. It is concluded that the trip did not stimulate large separation on the wing which itself could be the source for unsteady fluid motion.

Figure 4-16(b) shows the oil dot pattern on the wall in the region of the wing leading edge. The figure is actually a photograph of the piece of plastic tape shown in Figure 4-16(a) after having been removed from the tunnel and mounted on a sheet of paper for closer study. An outline of the relative position of the nose is also shown on the paper. The oil dot pattern exhibits the



4-16(a)



4-16(b)

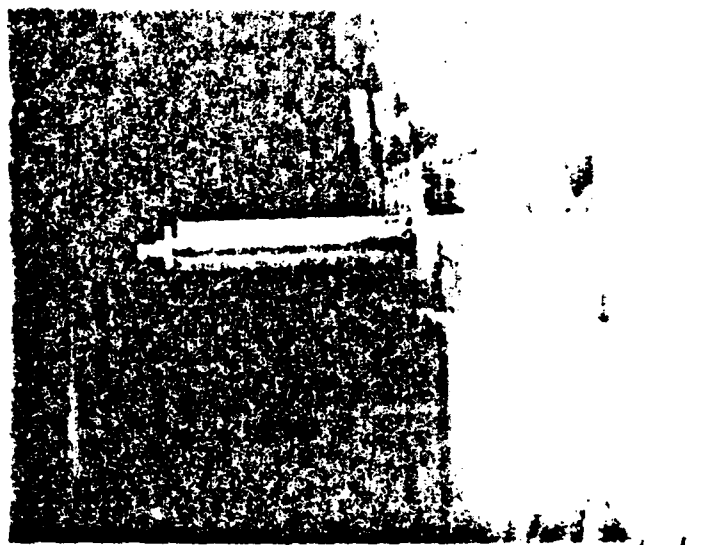
Figure 4-16: Surface Flow Visualization Results in Wing-Body Junction

expected features associated with the horseshoe root vortex. The flow on the wall at the wing leading edge was initially out and away from the wing surface before being swept around the wing shoulder. The oil dot streaks converge in the region of flow separation about 20 mm from the wing shoulder. This result is expected. However, there appears to be a second convergence about 4 mm from the wing and on the wall. The two convergence regions are separated by a region where the dots did not move; hence a region of relatively low wall stress. It is not obvious from Figure 4-16(b) alone whether the relatively low stresses were in a region of flow attachment or whether the second set of convergence lines were perhaps produced by flow accelerations around the wing trip wire.

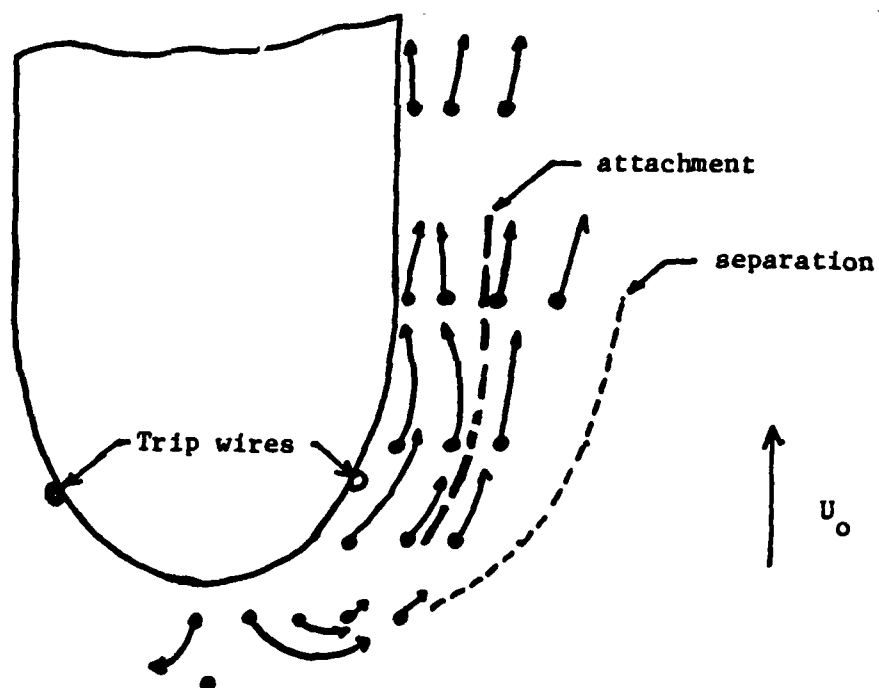
A second flow visualization test was made to learn more about the vortex flow at the leading edge of the wing and to better define the wall region where the low stresses were observed. The results are shown in Figure 4-17.

Figure 4-17(a) shows photographed results for the oil dots on and around the leading edge of the wing. It is observed that oil dots on the wing near the extreme leading edge traveled toward the wall rather than in a downstream direction. On the other hand, the direction of travel is observed to have been mostly in a downstream direction for oil dots to the immediate side of the extreme leading edge. The downward force of the fluid in the root vortex at the leading edge was relatively strong, as evidenced by the oil dot displacement, for at least a distance of one-half the boundary layer thickness.

The photograph in Figure 4-17(a) does not clearly show the oil dot displacements on the wall at the side of the wing nose. In this case white tape was not used, and reflections from the plexiglas wall were superimposed on the oil dot images in the photograph. The sketch in Figure 4-17(b) shows the oil dot displacements, with the arrow origin located at the initial position of the oil dot, the shaft the path of the displacement, and the head the final position. The oil dots curved toward the wing at  $x/t = 0.50$ ,



4-17(a)



4-17(b)

Figure 4-17: Additional Surface Flow Visualization Results

AD-A139 836

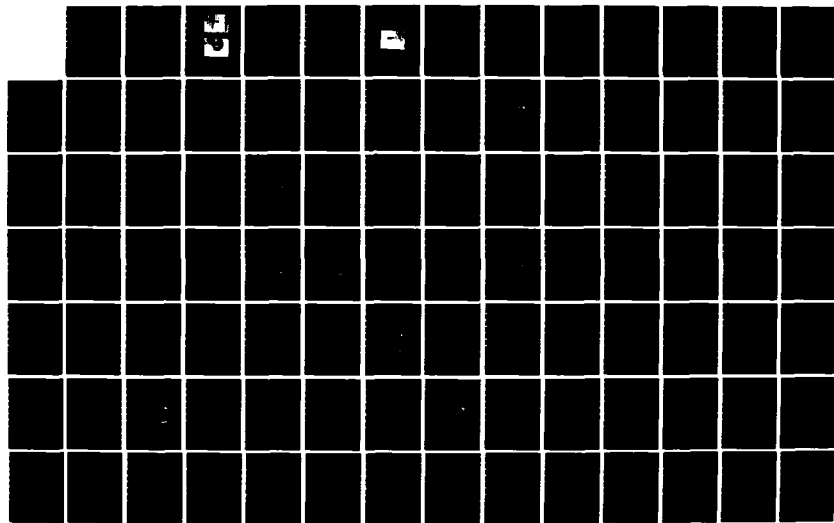
EXPERIMENTAL INVESTIGATION OF THE TURBULENT LARGE SCALE  
TEMPORAL FLOW IN T. (U) CATHOLIC UNIV OF AMERICA 2/3  
WASHINGTON DC SCHOOL OF ENGINEERING A. E P ROOD

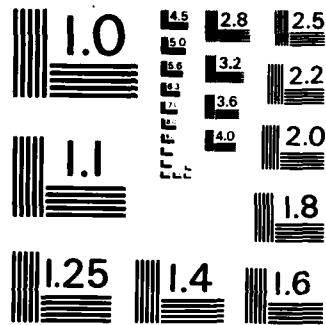
UNCLASSIFIED

MAR 84 DTNSRDC-HA84-1

F/G 20/4

NL





MICROCOPY RESOLUTION TEST CHART  
NATIONAL BUREAU OF STANDARDS-1963-A



as if indicating an attachment line between the wing and the primary separation line. This result is consistent with the pattern shown in Figure 4-16(b), and discussed above.

Although the region of low stress, or flow attachment, suggests the existence of a secondary vortex counterrotating relative to the primary vortex, there was no suggestion of a secondary vortex in the cross-stream velocities shown in Figure 4-14. Those velocities were obtained in the plane  $(2.0, y/\delta, z/t)$ , which was downstream from the oil dot pattern shown in Figure 4-17(b). It is possible that the secondary vortex was dispersed sufficiently while traveling that distance to not be immediately evident in the velocity measurements.

On the other hand, the curvature of the oil dots toward the wing (at  $x/t = 0.5$ ) may in part be produced by the trip wire on the wing. The high velocities in the junction as a result of vortex transport probably fill in behind the small separation bubble produced by the wire. On contact with the wing, if this is the case, the high velocity flow may have produced the small spanwise (toward the tip) displacement of oil dots on the wing, and near the wall, at  $x/t = 0.75$ .

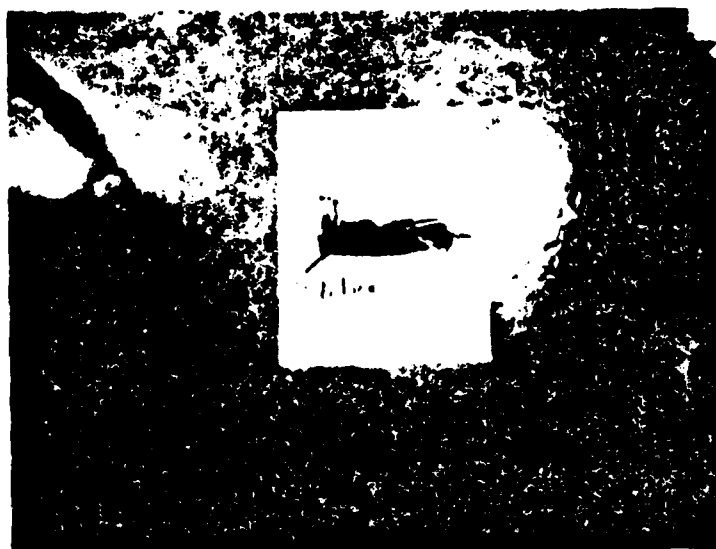
It is concluded from Figures 4-16 and 4-17 that the  $a/b = 1.5$  elliptic nose wing produced a primary separation vortex of the type observed by previous investigators, and that there may be secondary features of the separated flow that are not fully evident from the present study.

#### 4.2.3.2 Wing-Body Junction Wake Flow Separations

Figure 4-18 shows oil film flow visualizations of the separated flow at the trailing edge of the  $a/b = 1.5$  elliptic nose finite chord length wing. Figure 4-18(a) shows the oil film separation line on the wing. Figure 4-18(b) is a photograph of the oil film, which was actually applied to a piece of tape which was removed from the wing for the photograph. Figure 4-19 is a drawing that shows the location of the separation line on the wing. The significant feature of the separation line is the curvature toward the trailing edge inside the boundary layer. Whereas the separa-



4-18(a)



4-18(b)

Figure 4-18: Flow Visualization Results for Separated Trailing Edge Flow

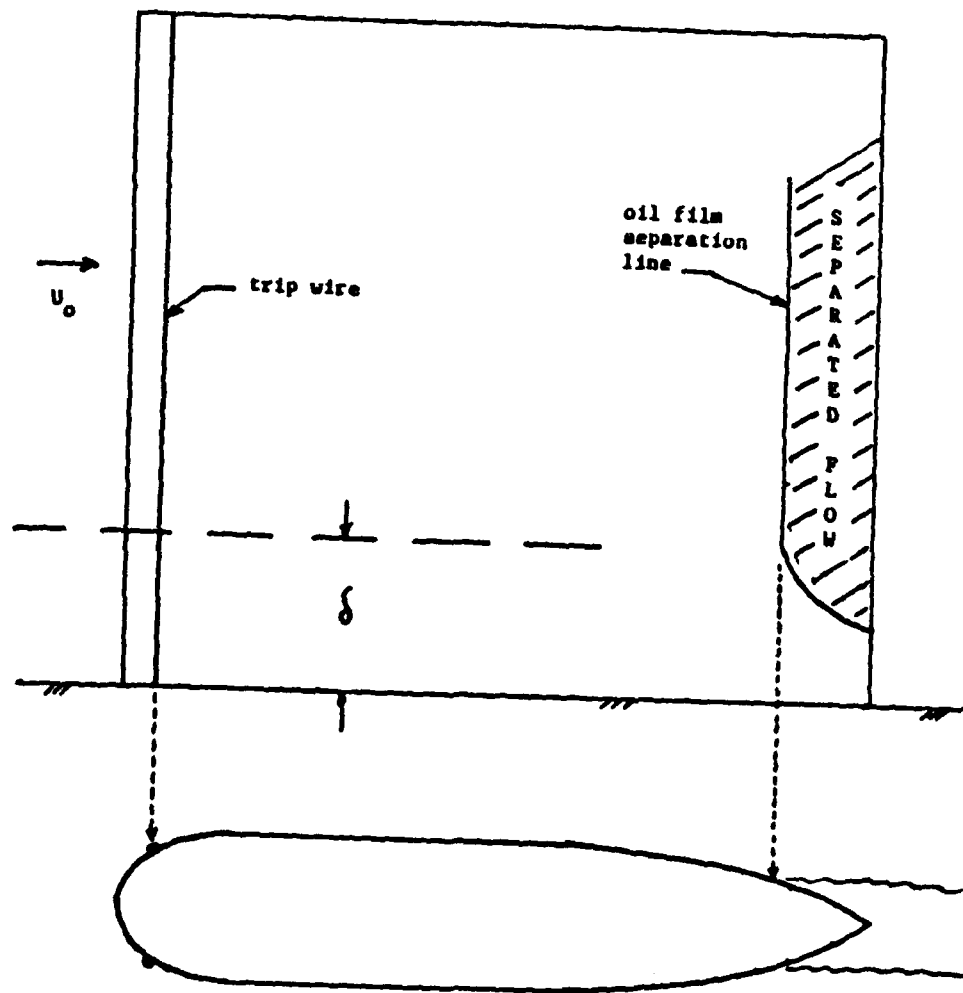


Figure 4-19: Schematic of Trailing Edge Separation

tion line defining the separated flow region was parallel to the trailing edge outside the boundary layer, the mean flow was unseparated within the inner half of the boundary layer. Apparently the horseshoe vortex transports fluid with sufficiently high energy into the junction to overcome the high pressures at the trailing edge and to prevent separation in this case.

#### 4.2.3.3 Wing Tip Flow Separation

Figure 4-20 shows oil dot flow visualizations made at the wing tip to show that it was not associated with large spanwise effects distorting the wing-body junction flow. The measurements were made with the  $a/b = 1.5$  elliptic nose infinite chord length wing. As shown in the figure, the oil dots represent flow up and over the tip that produced little spanwise displacement of the oil dots except those very near the tip; those were displaced toward the tip. It is concluded that the tip, at least in the leading edge region, did not produce flow distortion in the wing-body junction.



Figure 4-20: Wing Tip Flow Visualization Results

## CHAPTER 5

### TECHNIQUE FOR MEASUREMENT OF LARGE SCALE TEMPORAL FLOW

#### 5.1 Development of the Technique

It was anticipated that the large scale temporal flow would be a subtle feature superimposed on the mean flow, and that sophisticated techniques would be required to measure its presence and extent. A tentative hypothesis was made that the temporal flow would be associated with an inherent instability or natural frequency of the flow, and therefore would be characterized by a single frequency. However, the excitation or forcing function for the oscillation was hypothesized to be associated with the random flow fluctuations in the onset boundary layer. It was anticipated that the temporal flow amplitude might vary with time, and that the randomly changing flow would then exhibit a range of corresponding frequencies. Therefore, it was anticipated that the temporal flow would be a narrow bandwidth disturbance superimposed on the general turbulence spectrum.

The measurement objective was first to detect the presence of the temporal flow structure, and second to determine the spatial

and temporal extent of the structure. The detection was first attempted using a method developed by Strickland and Simpson (1975). It was concluded that the method was not applicable to the present problem, at least in its current state of development. A new detection method was developed using two-point velocity correlations. This new application of a standard statistical quantity solved many measurement problems simultaneously. Before describing the correlation technique, the application of the Strickland-Simpson method will be reviewed both because it is instructive about the flow, and because it merits further development for use with the wing-body junction flow.

Strickland and Simpson (1975) experimentally related the boundary layer characteristic bursting frequency to the peak frequency in the log normal distribution of the first moment of the wall shearing stress power spectral density. The reasoning behind this association follows from the observation of Rao, et al. (1971) that mean burst periods are distributed according to the log normal law. Strickland and Simpson reasoned that a long time averaged spectrum of the shear stress would be almost identical in frequency distribution to a histogram compiled from burst frequencies for the same data. However, an adjustment had to be made to the spectrum, namely multiplying it by the frequency, to obtain the log normal distribution. The calculations are as follows:

$$\int \frac{\text{PSD } df}{(\int \text{PSD } df)} = \int \frac{f \text{ PSD}}{(\int \text{PSD } df)} d(\ln f)$$

where PSD is the shearing stress power spectral density as a function of the frequency  $f$ . The first moment of the power spectral density,  $f \text{ PSD}$ , when plotted as a function of  $\ln f$  was almost identical to a normal distribution curve. The curve was nearly identical to the histogram for the burst periods, causing Strickland and Simpson to conclude that measured long time spectral averages were equivalent to measured periods for individual bursts. This was a significant advancement in frequency measurement technology because it greatly simplified the process.

Simpson et al (1981) later applied the technique to separating flows where the characteristic velocity fluctuation as a function of distance from the wall was related to the outer flow variables  $U$  and  $\delta$ , the boundary layer outer velocity and thickness. Again the justification for this technique is reasoned by Rao, et al (1971) who observed an inner and outer boundary layer coupling such that burst frequency phenomena extend across the entire boundary layer. Upstream from the separating flow Simpson's results produced values for  $U/f\delta$  nearly identical to those compiled by Rao using histograms. In the separating flow the values for  $U/f\delta$  were up to five times larger, presumably because the flow speed was smaller than  $U$  although the flow structure was unchanged in length scale.

The Strickland-Simpson method was applied to the present flow to detect the presence of large-scale structure. However, the peak frequency was at least an order of magnitude larger than the frequency that was eventually measured for the large scale low frequency organized motion in the wing-body junction.

This initial analysis also demonstrated that the amplitude of the power spectral density associated with the large scale motion would usually be so small that it merely produced a bulge in the general background spectrum rather than a peak. Resolution of the bulge was very difficult because the general spectrum in the wing-body junction flow was grossly distorted as the root vortices literally churned the boundary layer. There was, therefore, no common spectral distribution for the junction flow, and the presence of a bulge in the spectrum could not always be detected or associated with large-scale motion. Conversely, the motion did not always produce a bulge. Sometimes it was a filling in of an inflected region. These observations were not obvious at first, but were realized as the preliminary measurement efforts were tediously and laborously carried out.

It was eventually concluded that the large-scale motion was not the turbulent burst phenomenon as evidenced by the peak in the log normal distribution of the velocity and that its frequency could not be surely detected, or measured, with peaks in either the spectrum or the first moment of the spectrum.



An informal reexamination of the measurement objectives relative to the nature of the wing-body junction flow was then made. It was considered that the alternate approach of discerning the spatial extent of the organized motion first might prove more fruitful than the above attempt to discern frequency first. The definition of large scale structure includes the notion of a phase related distribution of fluid velocities in an organized motion confined in space. In theory the fluctuating velocities in the structure are correlated. Therefore, in practice the spatial extent of the structure may be determined by mapping contours of correlation values. Because the organized motion is quasi-deterministic, and therefore has characteristics of random motion, the evaluation of the correlation between positions in the flow must be made using practical application of statistical theory.

A second stage of preliminary measurements produced fruitful results. Correlations were obtained between velocities at positions far enough apart that turbulence integral length scales were greatly exceeded. This implied that the correlations were associated with large scale structure not inherent to the otherwise flat plate boundary layer. Most rewarding was the observation that the cross-spectral power spectral density produced a narrow bandwidth spectrum. This provided additional support that the large-scale structure was coherent.

The remarkable result from this two-point measurement technique was that the large-scale structure could be discriminated from the background turbulence even when there was no bulge in either of the power spectral density distributions at the two measurement positions.

An added benefit from this measurement technique was that the fluctuations in the individual horseshoe root vortex legs were separable. This occurred because the large-scale structure originated in the wing-body junction flow produced antisymmetric fluctuations in the vortex legs so that the relative phase was nearly 180 degrees. The meaning of this observation will now be discussed in detail.

Consider fluctuations on one side of the nominal plane of symmetry of the flow, as defined by the plane of symmetry of the wing, relative to fluctuations on the other side. It would be expected, for example, that temporal oscillations of the separating flow at the horseshoe vortex origin would be either fore and aft or side to side. The former would produce fluctuations in-phase for downstream positions symmetric to the plane of symmetry. The meaning of symmetric here is in the sense of a mirror image. In-phase fluctuations imply invariance of the flow to reflection through the plane of symmetry. Side-to-side oscillations of the flow at the origin would also produce symmetric flow, but the phase relationship between the velocities would be 180 degrees.

If the frequency of the motion is sufficiently low, then moderate displacements of the nominally symmetric measurement positions, or moderate asymmetry of the flow, would not be important to the relative phase, changing it by a small value from its basically in-phase or out-of-phase value.

In this study the fluctuations were found to be out of phase. The added benefit from this is that one is able to distinguish fluctuations traveling down one side of the wing from fluctuations traveling down the other side, even after the flows merge downstream from the wing, if one fluctuating structure dominates the other. This happens, for example, for the wing at incidence when the higher pressure vortex temporally dominates the lower pressure vortex, as discussed later.

The step-by-step measurement process that was developed is as follows:

1. Analog output from measurement at position  $P_A$  and measurement at position  $P_B$  is simultaneously sampled at a predetermined rate for a predetermined length of time.
2. Harmonic analysis producing magnitude and phase using a Fast Fourier Transform is performed on the time record of data.

$$S_A = |S_A| \cos \phi_A + j |S_A| \sin \phi_A, \text{ where } S_A = S_A(f)$$

$$S_B = |S_B| \cos \phi_B + j |S_B| \sin \phi_B, \text{ where } S_B = S_B(f)$$

3. The power spectral density and the cross-power spectral density are computed:

$$[G_{AA}] = S_A S_A^* = |S_A|^2$$

$$[G_{BB}] = S_B S_B^* = |S_B|^2$$

$$[G_{AB}] = S_B S_A^* = |S_B| |S_A| \cos(\phi_B - \phi_A) + j |S_A| |S_B| \sin(\phi_B - \phi_A)$$

4. Steps 1-3 are repeated until predetermined precision criteria have been met. The results are ensemble averaged to produce the following quantities:

$$\text{Power spectral density } G_{AA} = \overline{|S_A|^2}$$

$$G_{BB} = \overline{|S_B|^2}$$

$$\text{Cross power spectral density, } G_{AB} = \overline{|S_B| |S_A| \cos(\phi_B - \phi_A) + j |S_A| |S_B| \sin(\phi_B - \phi_A)} \text{ amplitude}$$

$$\overline{(\phi_B - \phi_A)} \text{ phase}$$

Coherence

$$\gamma_{AB}^2 = \frac{G_{AB} G_{AB}^*}{G_{AA} G_{BB}}$$

## 5.2 Statistical Description of the Temporal Flow

This section presents the reasoning underlying the development of the measurement process described above.

### 5.2.1 Historical Approach: Correlation Function

The historical approach to measuring the correlation between stochastic processes relied on the cross-correlation function  $R_{AB}(\tau)$  defined as follows

$$R_{AB}(\tau) = \frac{1}{\rho} \int_0^{\rho} A(t) B(t+\tau) dt \quad \rho \rightarrow \infty$$

This measurement was appropriate for the analog data analysis instrumentation available before the invention of electronic data processors and the discovery of the Fast Fourier Transform. Nevertheless, it is instructive to proceed with this historical approach in developing a statistical description of the temporal flow, and the transition to the modern spectral approach can be easily made.

The signals  $A(t)$  and  $B(t)$  are the velocities at two positions in the flow. Of course, the velocities can be for the same position in which case the integrand is  $A(t) A(t+\tau)$  which gives rise to the auto-correlation function  $R_{AA}(\tau)$ . The velocities are stochastic processes, and are considered stationary for this study. Although the large scale temporal flow is best described by measuring the instantaneous velocity at all positions in the flow simultaneously, practicality does not allow this, and in this study the flow was measured at only two positions at one instant. Those positions were variable throughout the flow.

The velocities are classed as a bivariate time series pair. Because they are interactive they are said to arise on a similar footing contrasted to a casually related pair for which one variable is a function of the other in a true cause and effect relationship. The objective for this study was to study the interaction between the velocities and to describe it in terms useful for further analysis.

Many assumptions were made about the bivariate process which were necessary to make headway with a statistical description. The assumptions made are described in detail by Jenkins and Watts (1968). Principally it was assumed that the stochastic stationary process represented by the bivariate time series  $A(t)$  and  $B(t)$  may be adequately described by the lower moments of their probability distributions. Specifically, the mean, variance, and covariance were assumed sufficient to describe the process. In practice the description involves measured variations of these fundamental probability distribution quantities. For instance,

time lags are introduced to measure the nonrandom features of the processes, and Fourier transforms are employed to allow spectral analysis techniques.

The present study of large scale temporal flow relies on the theoretical validity of the cross-correlation function,  $\rho_{AB}(\tau)$  to describe the predictive association between the series  $A(t)$  and  $B(t)$ . The definition of the cross-correlation function is

$$\rho_{AB}(\tau) = \frac{R_{AB}(\tau)}{(R_{AA}(0) R_{BB}(0))^{1/2}}$$

where  $R_{AA}(0)$  and  $R_{BB}(0)$  are employed to normalize the correlation for the different scales at A and B and where the means for A and B are set to zero. To prevent confusion here it is noted that other definitions of this function are in use. For example, Bendat and Piersol (1980) refer to this function as the correlation coefficient function.

If  $\rho_{AB}(\tau)$  is identically zero for all values of  $\tau$ , the bivariate process is uncorrelated. Furthermore, if  $A(t)$  and  $B(t)$  are normal processes, they are mutually independent. If they are not normal processes, they may or may not be independent. Fluid mechanics phenomena are often only approximated by a normal process. Therefore it is possible that  $A(\tau)$  and  $B(\tau)$  would be mutually dependent but exhibit zero correlation according to the definition of "correlation."

If  $\rho_{AB}(\tau)$  is not identically zero for all values of  $\tau$ , the bivariate process is correlated. There is at least a linear dependence of one variable on the other. The meaning of "dependence" is that there is an interaction between the variables, not necessarily that there is a causal relationship.

Historically analog techniques were used to measure the cross correlation function. These techniques were notoriously inaccurate for low frequency phenomena because of the long measurement times required.

### 5.2.2 Modern Approach: Spectral Density

The introduction in modern times of the electronic processor and the Fast Fourier Transform led to the spectral analysis approach to correlation assessments, which was used in this investigation. The analysis is digital and nearly real time. The accuracy of low frequency processes, such as those encountered in this study, is vastly improved because the spectral resolution is not dependent on technically difficult analog bandpass filtering.

Mathematically the cross-correlation function  $R_{AB}(\tau)$  and cross-spectral density  $G_{AB}(f)$  are Fourier transform pairs. Therefore, the methods are in principle equivalent.

### 5.3 Statistical Measurements

A Nicolet Model 660B Dual Channel FFT Analyzer was used to perform the statistical measurements. The analyzer was a complete processor. It was used to digitally sample the analog velocity signals,  $A(t)$  and  $B(t)$ , and to compute the auto-spectral density functions, the cross-spectral density function, the coherence, and the transfer function. These quantities provided the necessary information to statistically describe the large-scale temporal flow and to permit use of the data in further applications.

The basic functions of the Nicolet signal processor were to digitize a predetermined time length of data, called the record, at a predetermined rate, and to perform a Fourier series analysis using the nearly real time Fast Fourier Transform (FFT). The results from successive records were averaged to produce statistically precise results. Data acquisition was continuous with the data being simultaneously processed because of the speed of the calculation process.

The Fast Fourier Transform converted the signals  $A(t)$  and  $B(t)$  to the spectral information  $S_A$ ,  $S_B$ ,  $\phi_A$ , and  $\phi_B$  where the  $S$ 's and  $\phi$ 's are the amplitudes and phases of the Fourier series terms:

$$S_A = |S_A| \cos \phi_A + j |S_A| \sin \phi_A \quad \text{where, eg: } A(t) = \sum_{k=-\infty}^{\infty} S_A(f_k) e^{j2\pi f_k t}$$

$$S_B = |S_B| \cos \phi_B + j |S_B| \sin \phi_B \quad f_1 = \Delta f = f_k - f_{k-1}$$

The auto-spectral density was computed as an ensemble average of the record time histories:

$$G_{AA} = \overline{S_A S_A^*}$$

$$G_{BB} = \overline{S_B S_B^*}$$

The cross-spectrum density was similarly calculated; there is, however, relative phase information in addition to amplitude information:

$$G_{AB} = \overline{S_B S_A^*}$$

$$= |S_A| |S_B| \cos(\phi_B - \phi_A) + j |S_A| |S_B| \sin(\phi_B - \phi_A)$$

The coherence, about which more will be said in the next section was calculated as follows:

$$\gamma_{AB}^2 = \frac{G_{AB} G_{AB}^*}{G_{AA} G_{BB}}$$

and is a function of frequency, both in the numerator and the denominator.

The transfer function, useful for further application of the measurements, was calculated as follows:

$$H_{AB} = \frac{G_{AB}}{G_{AA}}$$

#### 5.4 The Coherence

The coherence,  $\gamma_{AB}^2$  is a function of frequency. A discussion of the meaning and usefulness of the coherence is in order because it is the single most critical measurement result on which this study is based. It is used to assess the interaction between velocities, and subsequently the space-time extent of the large scale temporal flow.

If the signals  $A(\tau)$  and  $B(\tau)$  are correlated, then  $G_{AB}$  is not identically zero because, by definition,  $R_{AB}(\tau)$  is not identically zero. Therefore,  $\gamma_{AB}^2$  is nonzero for correlated signals. An interpretative statement about the coherency will be made after demonstration of its resemblance to the squared correlation coefficient.

The cross-correlation function was defined previously

$$\rho_{AB}(\tau) = \frac{R_{AB}(\tau)}{(R_{AA}(0) R_{BB}(0))^{1/2}}$$

For each value of the lag  $\tau$ ,  $\rho_{AB}(\tau)$  expresses the degree of linear dependence between A and B. A Fourier transform of the correlation function produces

$$K_{AB}(f) = \frac{G_{AB}(f)}{(R_{AA}(0) R_{BB}(0))^{1/2}}$$

which provides a measure of the correlation between the spectral components of A and B. Because  $G_{AB}$  contains phase information, the value for  $K_{AB}(f)$  is dependent on the relative phase between the signals. A measure of the correlation between the signal magnitudes alone can be made by forming the complex conjugate of  $K_{AB}(f)$ , and taking the product

$$K_{AB}^2(f) = K_{AB}(f) K_{AB}(f)^* = \frac{G_{AB} G_{AB}^*}{R_{AA}(0) R_{BB}(0)}$$

Now,  $R_{AA}(0)$  and  $R_{BB}(0)$  are simply the mean square amplitudes of the signals A and B. If the signal consisted of only the frequency  $f$ , then  $R_{AA}(0) = G_{AA}$  and  $R_{BB}(0) = G_{BB}$ . Therefore

$$K_{AB}^2(f) = \frac{G_{AB} G_{AB}^*}{G_{AA} G_{BB}} \equiv \gamma_{AB}^2$$

Hence,  $\gamma_{AB}^2$ , "the coherency (sic) plays the role of a correlation



coefficient defined at each frequency  $f$ " (Jenkins and Watts, 1968, p.353). Note that no statement regarding linearity is necessary here; the definition of correlation coefficient does not depend on linearity; only certain interpretations of the coefficient are based on linearity assumptions.

The coherence then is a normalized measure of the correlation between the spectral components of A and B where the biasing effects of phase have been removed by the product of  $G_{AB}$  and its conjugate.

It will be shown in the next section that the coherence can be used, with appropriate assumptions, to predict the spatial extent of the large scale temporal flow.

### 5.5 Further Applications of the Statistical Description

All of the measurements performed in this study are necessary, but not rigorously sufficient to completely describe the interaction between A and B. If A and B are not normally distributed then higher order moments are necessary to provide the full description. There are two possible sources of non-normal fluctuations in the present study: the nonlinear relation between the field point velocity of a vortex and the distance to the center of the vortex, and the anisotropy of the turbulent boundary layer. The effects of these non-normal fluctuations on the measurements reported in this study is unknown. But it is likely that the ultimate description of the interaction between the signals A and B can be expressed as an infinite sum of probability density function moments (Jenkins and Watts, 1968, p.75), of which the linear term is the dominant.

Therefore, it is proposed that the further application of the results of this study can safely assume linear dependence between A and B for a first order approximation. In this context the results fall neatly into the established theory and practice of bivariate linear theory, which is further discussed in Jenkins and Watts (1968).

### 5.6 Low Frequency Limitations

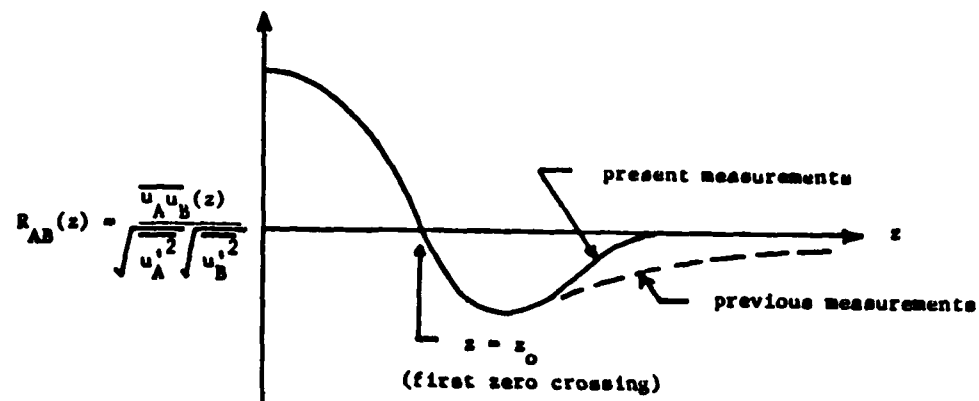
#### 5.6.1 Discussion of the Problem

Experimental investigation of large scale temporal flow in

a boundary layer generally implies the measurement of low frequency phenomena. An upper bound for the frequencies of interest can be obtained using the boundary layer thickness and the mean flow speed as scales for length and time. Although the upper bound was 600 Hz for the present investigation, the measured frequencies of interest were as low as 0.5 Hz. Until recently, practical techniques were not available to make accurate correlation measurements for signals at such low frequency (see Section 5.2).

Frequency measurements in the past were made by Fourier transform of analog generated correlation functions, and were known to be in error for low frequency signals. For at least this reason lateral correlations (two-point velocity correlations for separations in the  $z$ -direction) were measured only to the first zero crossing; see Favre, Gaviglio, and Dumas (1958), Champagne, Harris, and Corrsin (1970), and Comte-Bellot and Corrsin (1971). The negative correlations obtained for distances beyond the first zero crossing in these earlier studies were produced by instrumentation error as well as by fluid dynamic phenomena. Figure 5-1 schematically demonstrates this point. The dashed line represents results of questionable accuracy for  $f > f_0$ . Also shown in Figure 5-1 are the improved results obtained with the state-of-the-art signal processing used in the present investigation. This processing incorporated the inventions of the FFT and the semi-conductor computer chip, which were not available for the previous investigations. As a result, nearly real-time direct digital spectral decomposition of the velocity correlations were available for the present investigation. The low frequency cut-off for the instrumentation was substantially lowered as was the lower frequency bound for the measurements. It was possible to make accurate measurements in the region  $f > f_0$ .

For the present measurements to be credible it is necessary to show that the instrumentation low frequency cut-off was smaller than the low frequency end of the narrow band disturbance characterizing the large-scale temporal flow structure. Evidence that this objective was achieved is, firstly, that the lowest frequency



Note:  $R_{AB}(z > z_0) \neq 0.0$  implies low frequency

Figure 5-1: Schematic Comparison of Measured Correlation Functions for Previous and Present Measurements

of interest with significant non-zero value of the coherence is larger than the instrumentation low frequency cut-off, as shown in Figure 5-2, and, secondly, the second zero crossing for the lateral correlation function was measured, as shown in Figure 5-3.

The second zero crossing was a significant feature shown in the schematic Figure 5-1. It is also significant for another reason. It indicates that the measured flow disturbances were not physically bounded by the wind tunnel end walls, and hence represented wall boundary phenomena and not duct flow, as indicated by Comte-Bellot and Corrsin (1971).

### 5.7 Exploratory Results (6:1 Elliptic Nose)

Preliminary two-point velocity correlations were made to explore the large scale time dependent flow in the wing-body junction. The measurements were made to test the following hypotheses:

1. large scale time dependent flow exists in the wing-body junction flow
2. the frequency bandwidth is relatively narrow and consists of low frequencies (i.e.,  $f < 0.1 U/\delta$ )
3. the flow structure is convected downstream
4. two-point velocity correlation techniques using the spectrally distributed coherence can isolate the structure from the ambient turbulent background even in cases where the structure local velocities are on the order of the ambient velocities

All of these statements proved to be true in the preliminary measurements. Those measurements were made with the  $a/b = 6.0$  elliptic nose profile finite chord length wing (see section 3.2). However, the detailed correlation measurements that were made subsequent to the preliminary measurements were made with a blunter nose profile ( $a/b = 1.5$ ) both to separate the disturbance bandwidths and to provide a larger, and hence more easily measured, spatial extent for the secondary flow (the root vortex).

The separation of bandwidths was desirable for the following reasons. The downstream disturbance bandwidth produced

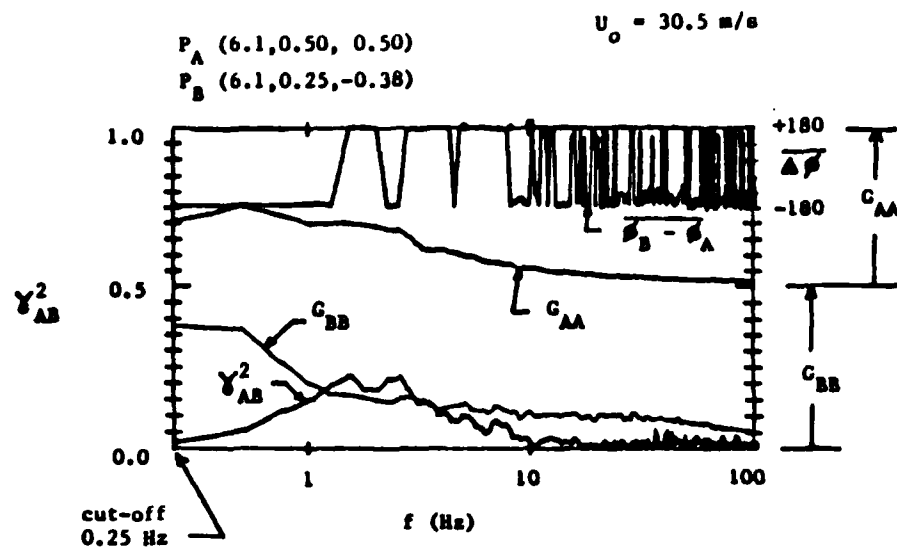


Figure 5-2: Example Lowest Frequency Spectral Content of Two-Point Lateral Velocity Correlations

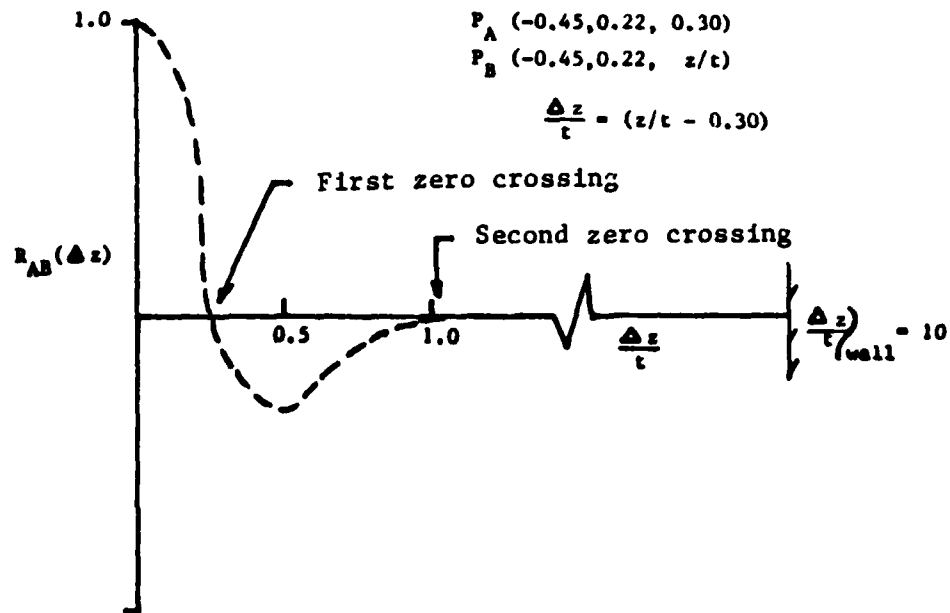


Figure 5-3: Example Measured Correlation Function for Lowest Frequency Two-Point Lateral Velocity Correlations

by the  $a/b = 6.0$  nose profile was numerically a subset frequency bandwidth within the larger bandwidth for the onset boundary layer structure. On the other hand, the  $a/b = 1.5$  nose profile produced a lower frequency bandwidth disturbance in a range of frequencies outside the bandwidth of the onset boundary layer structure. Although the structure in both cases must be considered the result of the wing-body junction flow, the structure in the latter case appears to be newly generated by the junction flow rather than the result of a re-distribution of energy in the onset boundary layer structure. The newly generated structure was a more appealing feature for study in this investigation where the existence of wing-body junction flow structure was to be proven.

The spatial extent of the horseshoe root vortex secondary flow was larger for the  $a/b = 1.5$  profile wing than for the  $a/b = 6.0$  profile. Therefore it was presumably easier to obtain accurate spatial definition of the correlation contours for the blunter profile. In view of the purpose of the investigation to assess the existence of flow structure, the decision to use the blunter profile was proper because it minimized risk.

The exploratory results from the preliminary measurements are reported both to show that the original hypotheses were true and to show, in comparison with the results for the detailed measurements, that the downstream bandwidth depends on the wing geometry. Two of the specific conclusions from the exploratory results, that the flow structure is convected downstream and that it grows in spatial extent far downstream from the wing, were intentionally not re-confirmed in the time-consuming detailed measurements because the data were limited to measurements in planes near the wing. It is believed that the general features individually observed for the preliminary and detailed measurements are applicable to both nose profiles.

The information presented in this section provides a global experimental description of the temporal flow upstream of the wing, along the wing-body junction, and downstream of the wing. The measurements were made in the nominal boundary layer and were not

the result of wing (Strouhal) vortex shedding observed outside the boundary layer. Furthermore, frequency bandwidth and spatial extent of the flow fluctuations were different than those of the undisturbed boundary layer; the time dependent flow structure downstream from the trailing edge was absent when the wing was removed and measurements made at the same positions as with the wing present.

Wind tunnel measurements of the lateral (z) two-point velocity correlations made without the wing present, i.e. in the onset boundary layer, indicate regions of negative correlation that are associated with large-scale structure inherent to the boundary layer. That data was obtained after the preliminary study and is presented in section 6.2.

The velocity correlations presented in this section as caused by the wing-body junction flow are clearly distinguishable from the onset boundary layer because 1) the frequency bandwidth is much smaller, although possibly a subset of the onset boundary layer bandwidth and 2) the spatial extent of the structure in the lateral direction is larger.

The data presented in this section were obtained for a wing incidence of 2.4 deg. The air speed in the tunnel was approximately 36.6 m/s.

Voltages nearly proportional to velocities were measured simultaneously at two positions in the flow with TSI hot wire anemometry. A single element was used at each position to measure the magnitude of velocity fluctuations. The analog anemometer output voltages were digitized, correlated, and analyzed by the Nicolet 660B Dual Channel FFT Analyzer.

The spectra were usually obtained for a bandwidth from 0 to 200 Hz. This bandwidth was chosen as a compromise between frequency resolution and sample time after examination of preliminary measurements which showed no pertinent information at higher frequencies.

The data in this section are presented as displayed by the Nicolet FFT Analyzer. That is, the presentation is in the units of



volts and Hz. The conversion from volts to velocity cannot be readily made because of the manner in which the span for the anemometer linearized output voltage was set; the probe was inside the boundary layer where the velocity was only roughly known. A ballpark approximation is a sensitivity of 46 m/volt-sec.

The voltages associated with the large-scale structure indicate velocity fluctuations on the order of one percent of the local mean velocity. Although this information provides conceptual notions as to the size of the structure, the actual existence of the structure is shown by relative spectra and by the nondimensional coherence rather than by absolute values of the velocity. For the present, the direct output voltages are sufficient to establish these relative values in the spectra. In either case the coherence is independent of linear calibration coefficients converting the voltages to velocities because they cancel in the computation. Therefore, the voltages alone without conversion to velocities are sufficient to determine the global features of the large scale organized temporal flow in the wing-wall junction region.

The measurements provide strong evidence for large scale organized motion in the junction flow. The evidence is developed by presentation of leading edge flow structure followed by upstream correlations indicating the convection of the structure along the pressure ridge. Then the structure will be followed as it traveled around the wing, interacted with the trailing edge conditions, and finally dominated the downstream flow. During this transit the bandwidth, and perhaps the physical make-up of the flow structure, changed substantially.

Initial description of the large scale temporal flow features was obtained by two-point velocity measurements in the leading edge region of the 6:1 elliptic nose. Figure 5-4 shows the measurement planes for this region as well as for other regions to be presented later. The reference position  $P_A (x/t, y/\delta, z/t) = P_A (-0.12, 0.25, -0.25)$  was to one side of the wing leading edge position and inside the upstream separation line indicated by the scour

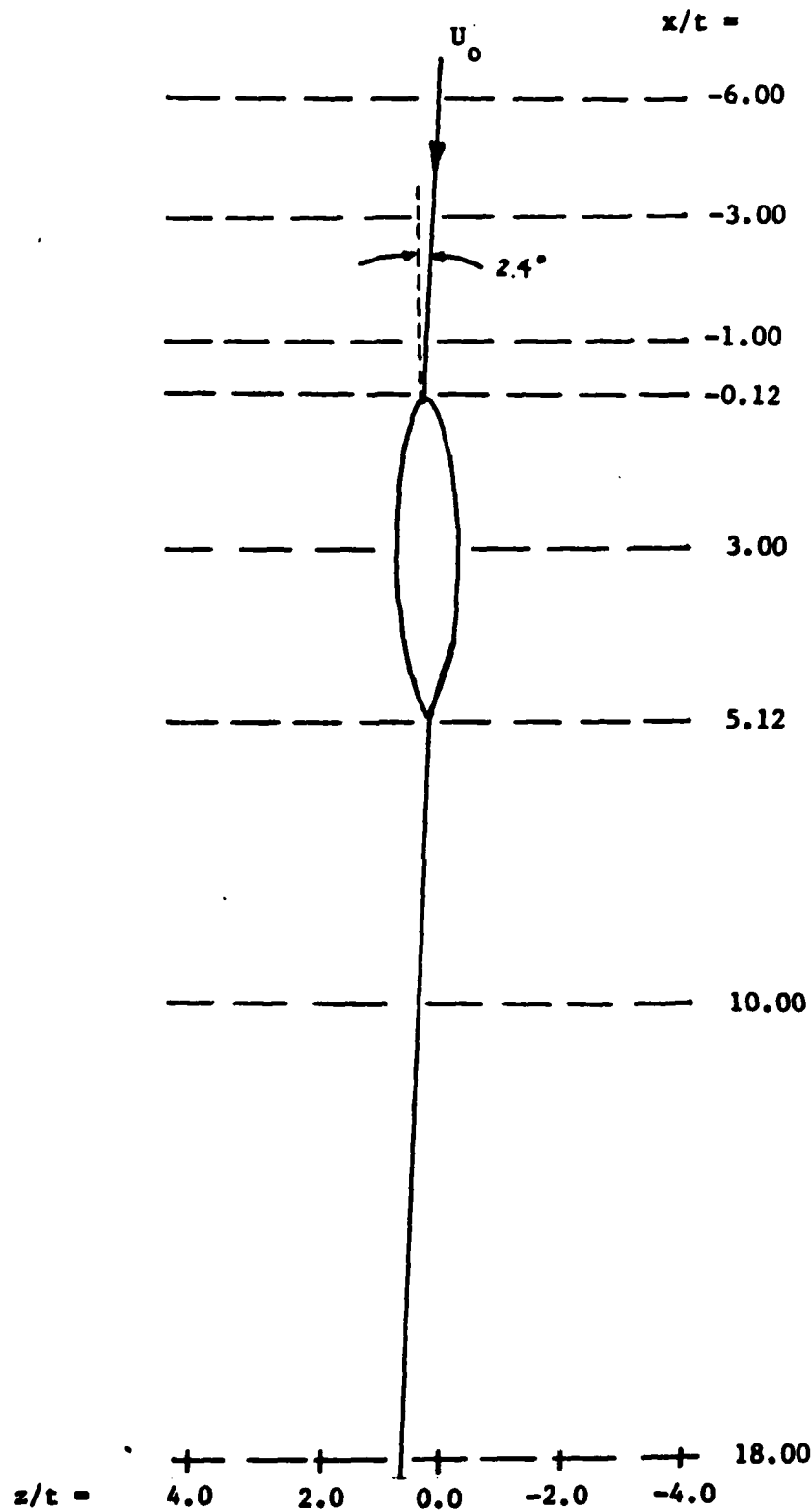


Figure 5-4: Streamwise Locations of Measurement Planes for Global Experimental Description of Temporal Flow

line found during oil film flow visualizations. On this basis, it is believed that the reference probe was inside the root vortex. A reference velocity measured at  $P_A$   $(-0.12, 0.25, -0.25)$  was correlated with velocity measurements from a second probe sequentially positioned on the other side of the plane of symmetry for the flow (at positive values of  $z/t$ ), then further from the wall (at larger values of  $y/\delta$ ), and finally upstream from the reference position (at more negative values of  $x/t$ ).

#### 5.7.1 Leading Edge Correlations

Figure 5-5 shows auto-spectral densities,  $G_{AA}$  and  $G_{B'B'}$ , coherence,  $\gamma_{AB'}^2$ , and relative phase  $\phi_{B'} - \phi_A$  for a correlation position  $P_{B'}$ , near the reference position,  $P_A$  (see Figure 5-5(a)); a correlation position  $P_{B'}$  in the symmetry plane for the wing-body configuration, (see Figure 5-5(b)); and a position  $P_B$  symmetrical (about the plane of symmetry) with the reference position  $P_A$  (see Figure 5-5(c)). This series of measurements was intended to show the effects of moving the probe away from the reference position  $P_A$  and across the plane of symmetry for the flow.

It is clearly seen in Figure 5-5(c) that the velocities at the symmetrical positions  $P_A$  and  $P_B$  were coherent from 2 to 200 Hz and were out-of-phase. That is, the temporal flow was antisymmetric although the wing-body configuration geometry was symmetric. The two other graphs in Figures 5-5(a) and 5-5(b) show that the velocities became in-phase as the probe was moved across the plane of symmetry and near to the reference position  $P_A$ . This was expected. Note that in no case were the power spectral densities peaked for the coherent bandwidth; the coherent velocities were apparently small in amplitude.

When the probes were very near each other the coherence had a peak at a frequency of approximately 50 Hz (Figure 5-5(a)). For correlations on opposite sides of the plane of symmetry the peak coherence occurred at a frequency of about 12 Hz (Figure 5-5(c)). It appears, then, that coherence at higher frequencies decreased faster with increasing probe separation distance than did the coherence for the lower frequencies. This was not unexpected

Note: scales distorted

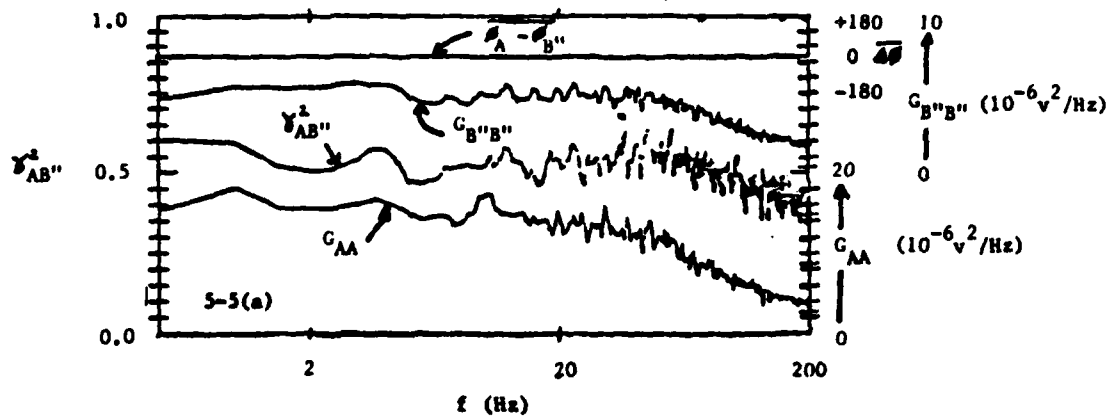
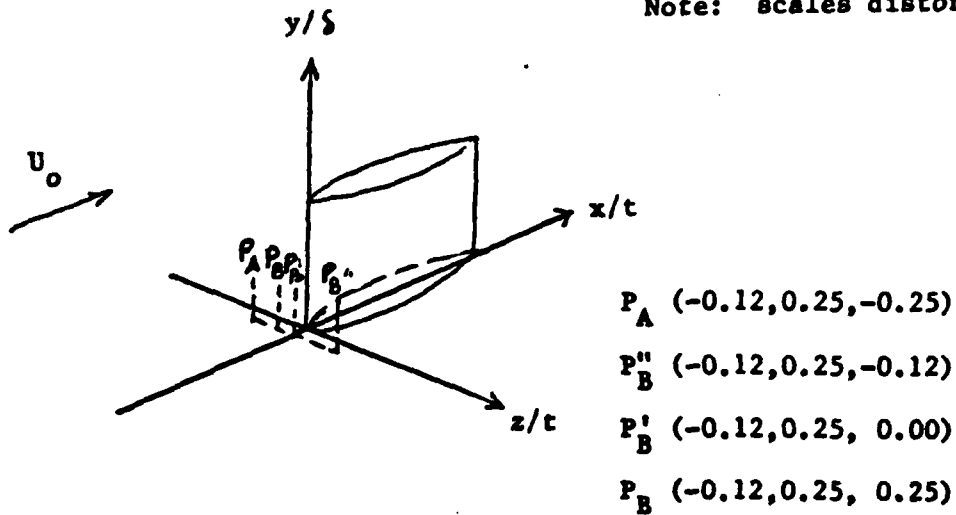
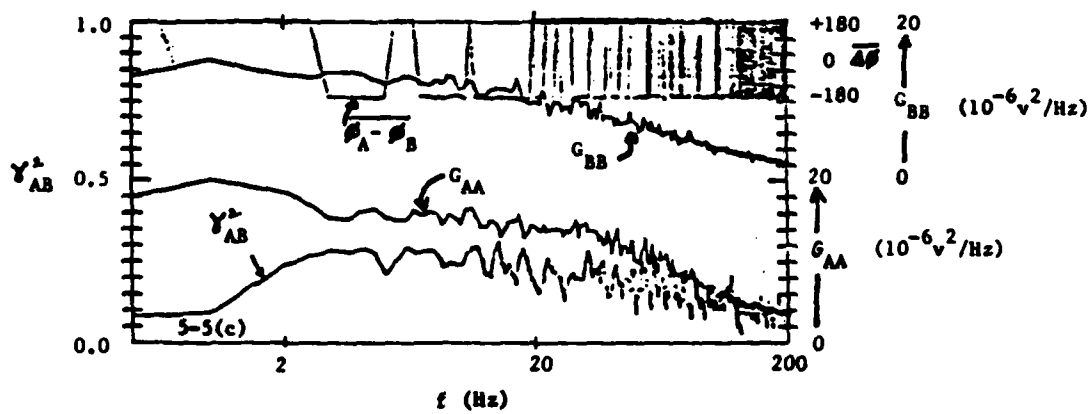
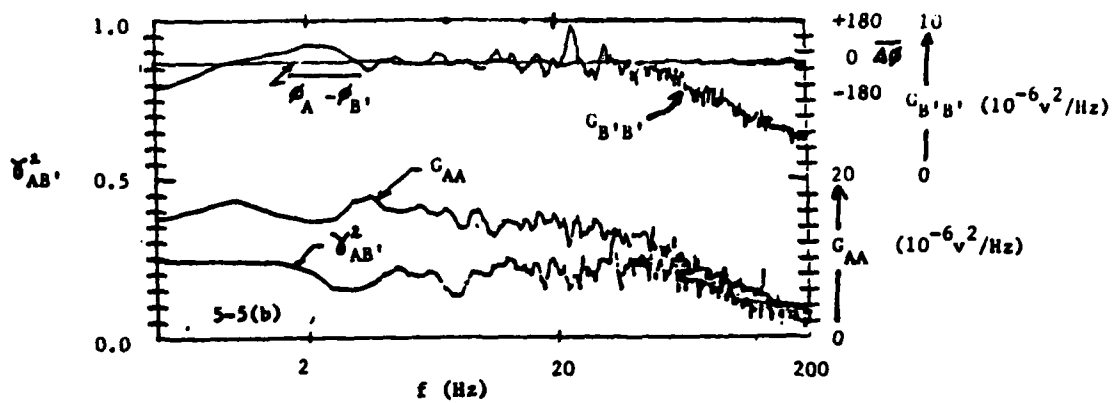


Figure 5-5: Leading Edge Correlations



because lower frequency implies larger spatial structure. It will be shown later that the lower frequency structure was characteristically of large spatial extent relative to the high frequency structure throughout the wing-body junction flow.

The extent of the large-scale structure across the boundary layer normal to the wall was evaluated by placing a probe at two positions  $P_C$  and  $P_C'$  in the y-direction and correlating the measurements with the velocity at  $P_A$ . The arrangement is shown in Figure 5-6. The reference probe was positioned at  $P_A$  (-0.12, 0.25, -0.25), and the second probe was placed consecutively at  $P_C$  (-0.12, 0.25, -0.20) and  $P_C'$  (-0.12, 0.50, -0.20). All three probes were inside the boundary layer.

Figure 5-6 (a) shows the results for  $P_C$  and  $P_A$ ; very strong coherence and in-phase signals are indicated. This is expected; the measurement positions were only slightly separated in the z-direction. The 2:1 ratio of the auto-spectral densities may be attributed partly to the proximity of the reference probe to the flow separation, whereas the second probe is near the quiescent vortex core, and partly to the fact that no attempt was made to electronically force the wire sensitivities to be identical.

Figure 5-6(b) shows that a relocation of the second probe to  $P_C'$  toward the outer boundary layer region greatly reduced, but did not remove, the coherence, and produced an increase in the phase relative to the reference probe output,  $\phi_{C'} - \phi_A$ . The phase shift is indicative of larger velocities at the second probe.

The conclusion is that at  $P_A$  (-0.12, 0.25, -0.25) the vertical extent of the structure was on the order of the boundary layer thickness. It was already shown that the transverse extent was at least one-half the boundary layer thickness. Therefore, the large-scale structure near the wing leading edge was apparently as wide as it was thick, and it permeated the entire boundary layer.

### 5.7.2 Upstream Correlations

Velocity measurements were made at positions upstream of the reference probe to obtain correlations with velocities measured with the reference probe maintained at  $P_A$  (-0.12, 0.25, -0.25).

Note: scales distorted

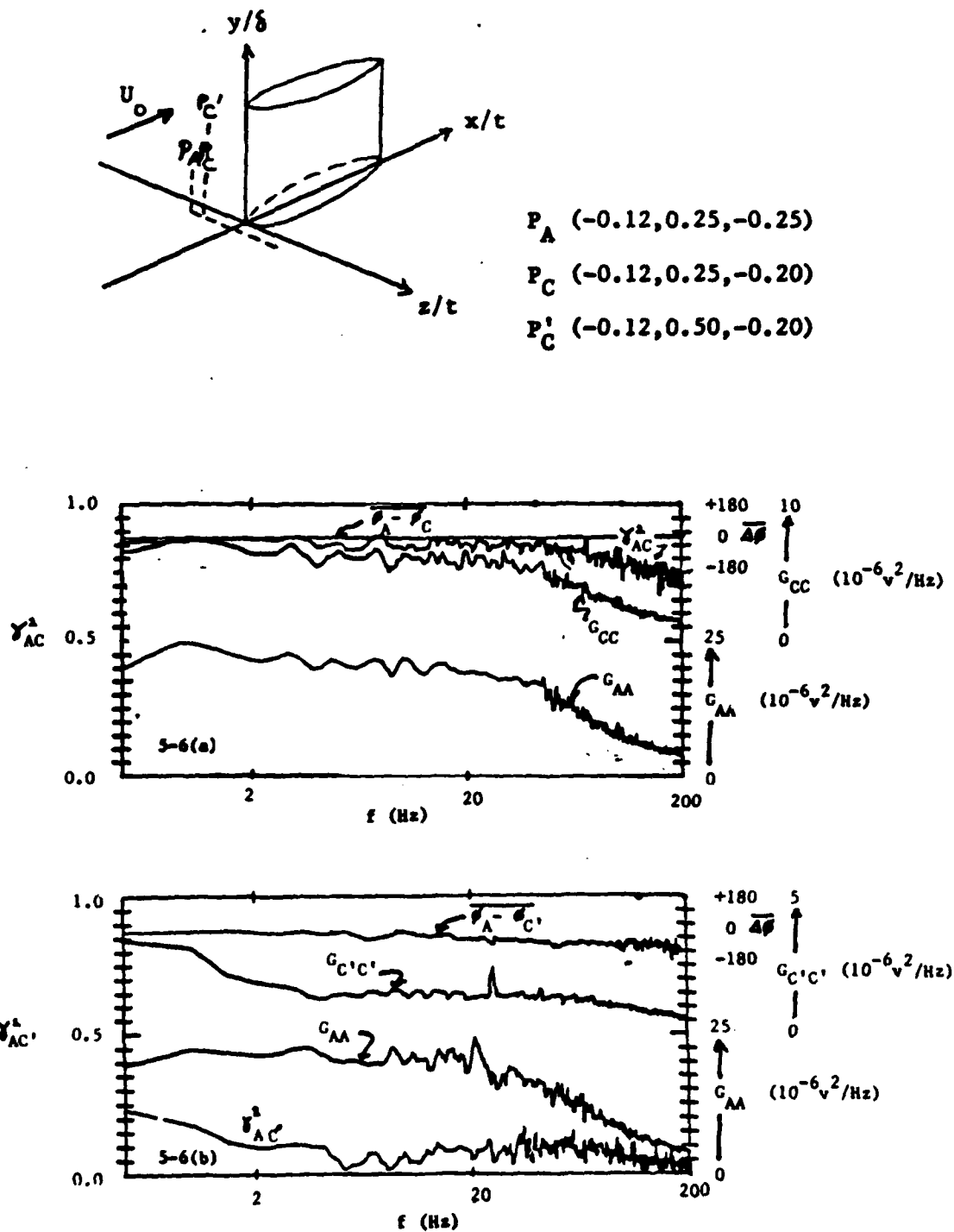


Figure 5-6: Cross-Boundary Layer Velocity Correlations at Leading Edge Region

The data were used to assess the streamwise extent of the temporal flow structure and to determine whether the fluctuations originated at the wing leading edge separation region, producing subsequent upstream flow reactions, or if they originated upstream and were convected downstream as organized motion.

The convection directions of flow events were determined by observing the measured change in the relative phase as the probe was moved upstream. A convected disturbance can be described at a fixed point "x" by the function  $\cos(2\pi f(t-t_0) - 2\pi fx/U_c)$  where  $U_c$  is the convection velocity in the direction of increasing x and  $\phi = (-2\pi fx/U_c)$  is the measured phase. The correlation between the moving probe and the reference probe, as measured in the actual experiment, produced a relative phase ( $\phi_{\text{ref}} - \phi_{\text{moving}}$ ) which should have decreased as the probe was moved upstream for convected disturbances:  $(\phi_{\text{ref}} - \phi_{\text{moving}}) = (\phi_A - \phi_B) = (-2\pi f\Delta x/U_c)$  where  $\Delta x = x_{\text{ref}} - x_{\text{moving}}$  and  $\Delta x$  increased as the probe was moved upstream.

In some cases small values of  $\Delta x$  made the relative phase too small to be accurately measured. However the effect of increasing f within the disturbance bandwidth in those cases revealed the sign of the phase  $(-2\pi f\Delta x/U_c)$ , and was useful for determining the convection direction of the event. The quantity  $(2\pi\Delta x/U_c)$  is the slope of  $(\phi_{\text{ref}} - \phi_{\text{moving}})$  as a function of f. In the case of  $\Delta x > 0$ , with the moving probe upstream from the fixed probe, a negative slope is interpreted to mean a downstream convection,

If the upstream fluctuations are actually reactions to the changing structure at the leading edge, then the upstream event should have lagged the change at the leading edge. In this case no convection of organized motion, in the Lagrangian sense, would be implied.

Figure 5-7 shows the effects of moving a second probe upstream relative to the reference probe fixed at  $P_A$  (-0.12, 0.25, -0.25). The figure shows a decrease in both the coherence and the relative phase as the second probe was moved from  $x = -1.0$  to  $x = -6.0$ . This result indicates that disturbances were convected



Note: scales distorted

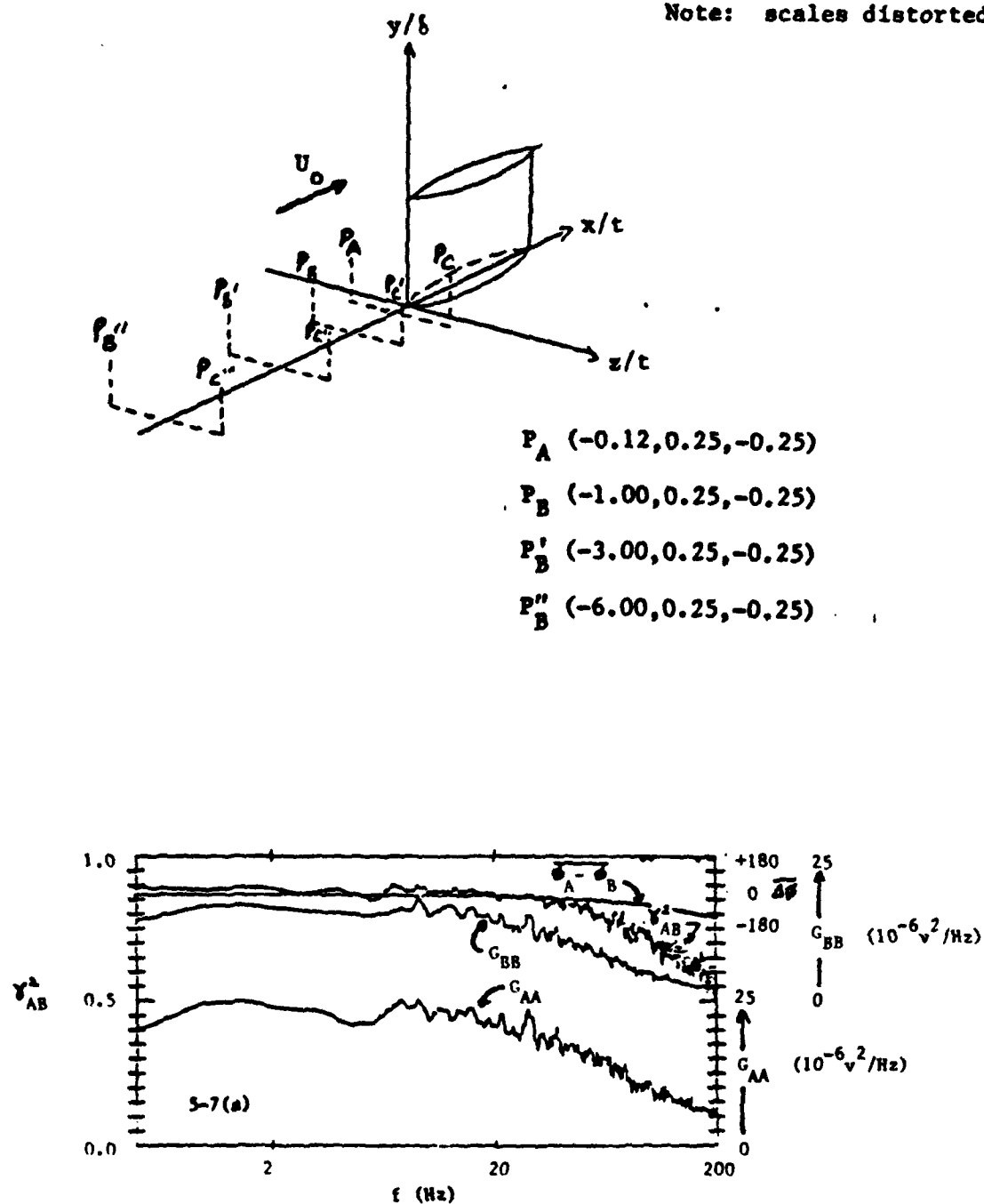
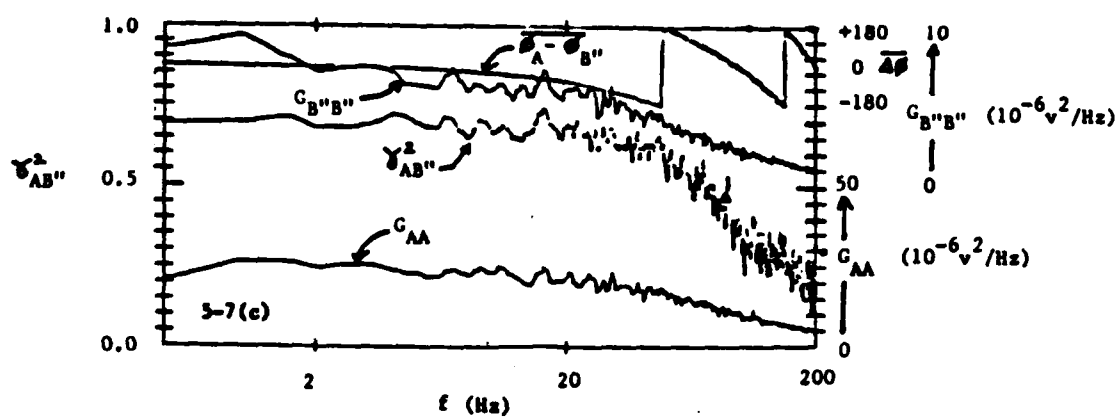
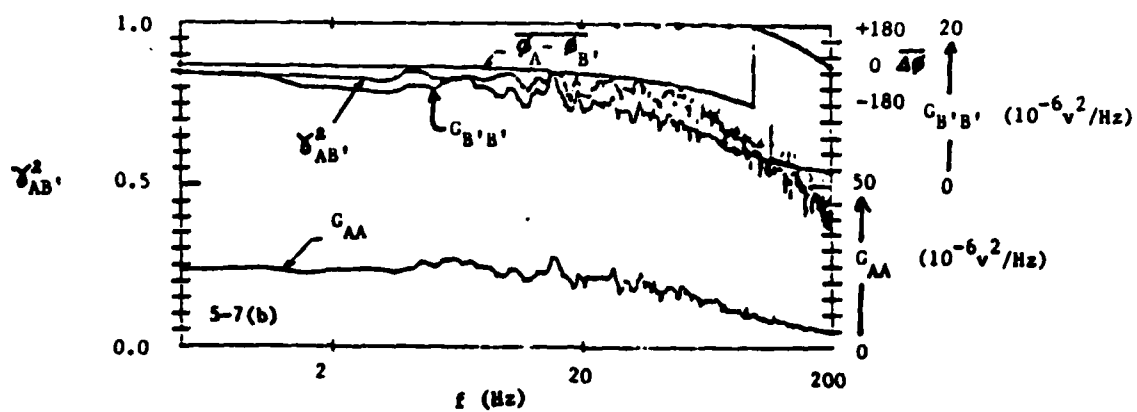


Figure 5-7: The Dependency of Relative Phase on Upstream Position of Second Probe



downstream (as explained above  $\phi_{\text{ref}} - \phi_{\text{moving}} = \phi_A - \phi_B$  decreased as  $Ax$  increased). The correlation distance was equivalent to at least six boundary layer thicknesses or six wing thicknesses, and is a distance on the order of the distance over which the pressure ridge produced by the stagnation pressure at the wing leading edge extended upstream. The autospectral density fell to one-third of its value at  $x/t = -0.25$  over the same distance.

Although the pressure ridge extended well upstream, it was not the source for the out-of-phase flow structure upstream from the wing leading edge in this case. Measurements made subsequent to this preliminary study indicated that the far upstream velocity correlations measured here were actually inherent to the boundary layer (see Section 6.2). The pressure ridge provided a physical reference separating out-of-phase structures, however. This will be discussed later.

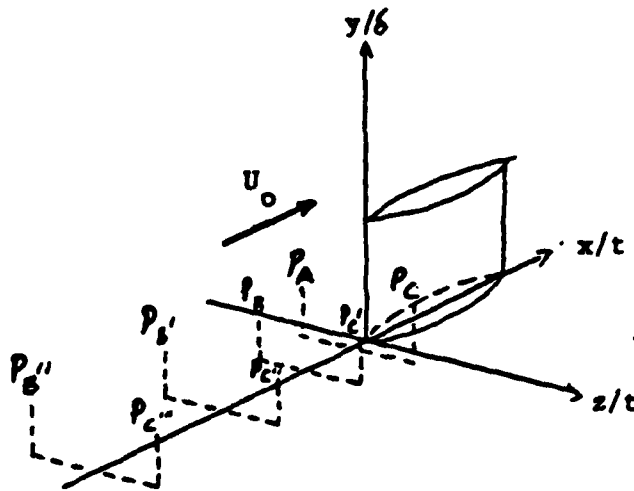
Figure 5-8 shows results for the moving probe at  $z = +0.25$ , similar to those obtained at  $z = -0.25$ , after an adjustment is made to account for the 180 deg phase shift that occurred as the probe was moved from one side of the plane of symmetry to the other. (The phase shift occurred because of the flow antisymmetry described above.)

It is concluded that the large scale temporal flow originated well upstream of the leading edge region and was perhaps associated with a wave that traveled along the pressure ridge. The disturbance bandwidth was 2-200 Hz and was antisymmetric about the plane of symmetry for the specific correlation positions investigated.

### 5.7.3 Mid-Wing Correlations

The disturbance's downstream progress was tracked by placing one probe at  $x/t = -0.12$  and the other at  $x/t = 3.0$ , and then correlating the measured outputs. The probe at  $x/t = 3.0$  was located where the wing profile changed from elliptic to circular arc; it was also the location of the wing maximum thickness. Therefore, the correlations were roughly between leading edge and mid-wing flow velocities. The results are shown in Figure 5-9, which shows that velocities at  $P_A$  ( $-0.12, 0.25, -0.25$ ) were

Note: scales distorted



$$P_A (-0.12, 0.25, -0.25)$$

$$P_C (-0.12, 0.25, 0.25)$$

$$P'_C (-1.00, 0.25, 0.25)$$

$$P''_C (-3.00, 0.25, 0.25)$$

$$P'''_C (-6.00, 0.25, 0.25)$$

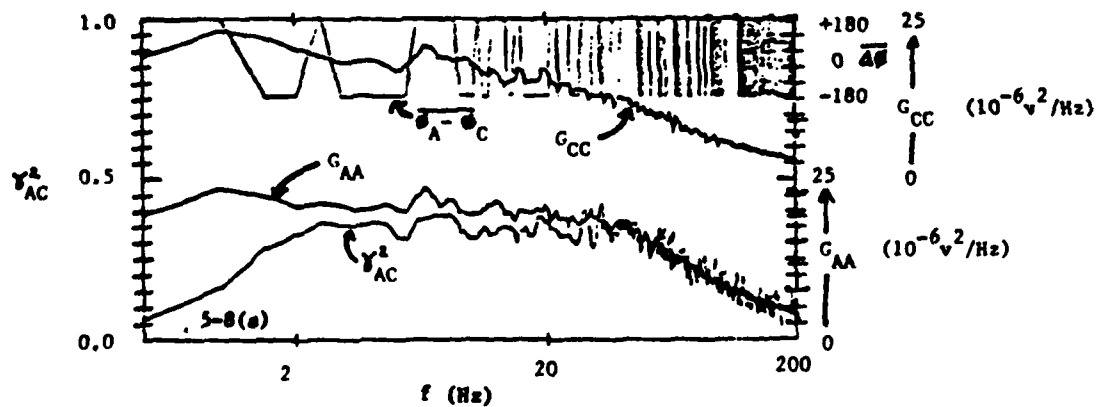
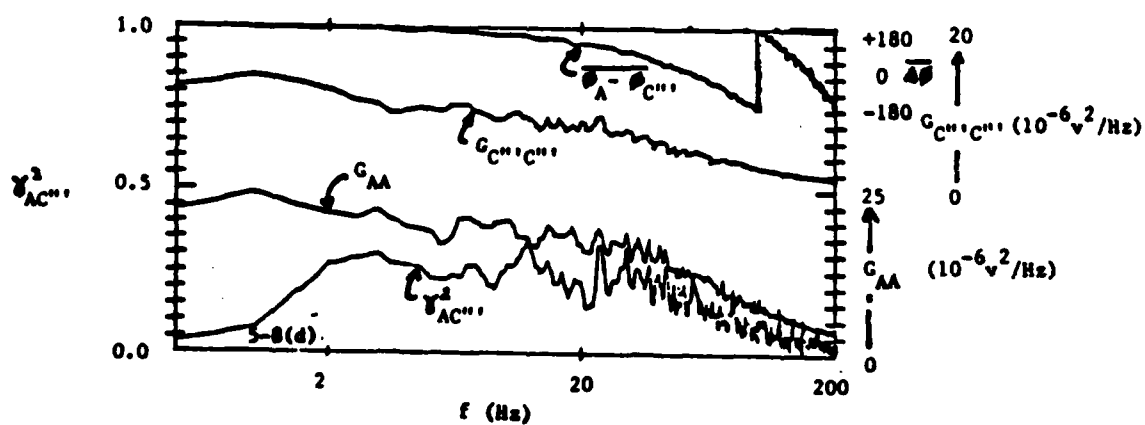
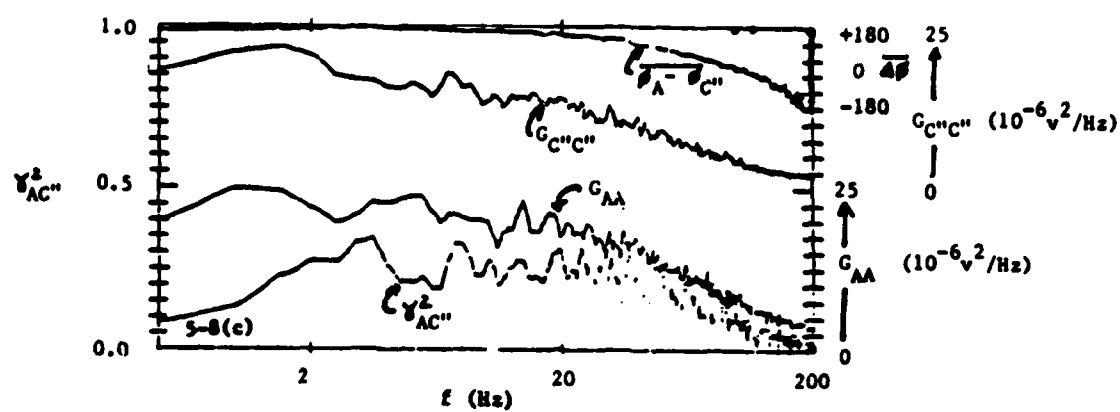
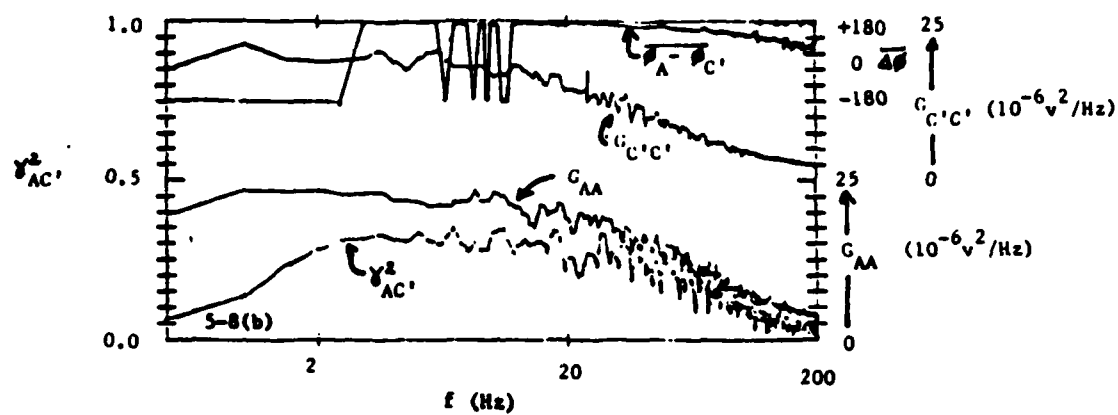
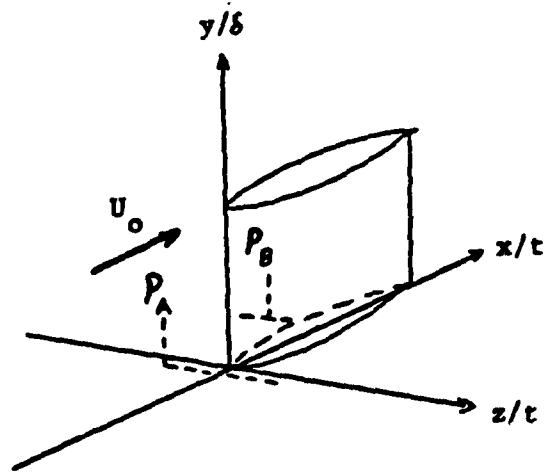


Figure 5-8: The Effect of Flow Antisymmetry on the Upstream Correlations



Note: scales distorted



$$P_A (-0.12, 0.25, -0.25)$$

$$P_B (3.00, 0.25, -0.12)$$

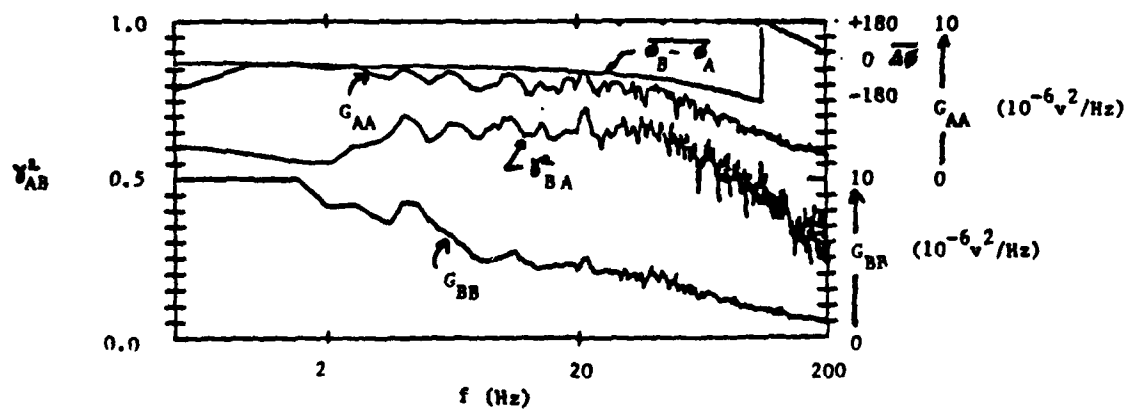


Figure 5-9: Correlation Measurements for Mid-Wing and Leading Edge Velocities

strongly correlated with those downstream at  $P_B$  (3.0, 0.25, -0.12). Furthermore, the phase for the velocities in the mid-wing region relative to the phase for the velocities in the leading edge region decreased as the frequency increased. As discussed earlier, this negative relative phase implies that events occurred at the leading edge before they occurred at mid-wing. (Note that in this case the relative phase is  $(\phi_{\text{moving}} - \phi_{\text{ref}})$ ). It is concluded that there is a disturbance that is traveling downstream from the leading edge to the mid-wing. Furthermore, that disturbance has most of its energy in a bandwidth at frequencies less than 200 Hz.

To prevent confusion it should be mentioned here that the power spectral density in Figure 5-9 is smaller than that for Figure 5-2 for the same position  $P_A$  (-0.12, 0.25, -0.25). This is because different probes with slightly different flow orientations and substantially different electronic sensitivities were used for the two measurements. This should not have affected the phase and coherence measurements, nor the relative distribution of the autospectral density as a function of frequency.

Additional correlation measurements were made in the plane  $x/t = 3.0$  (at the mid-wing) to assess the spatial extent of the temporal organized flow. Specifically, a systematic plane of symmetry correlation study was conducted, and the results indicated that two-point mirror-image positions  $P_{\pm}(3.0, y/\delta, \pm |z/t|)$  produced correlated velocities only for  $|z/t| < 0.5$ . Figure 5-10 shows the measurement results for  $P_{\pm}(3.0, 0.12, \pm 0.5)$  and  $P_{\pm}(3.0, 0.25, \pm 0.5)$ . For these positions, and for all positions with  $|z/t| > 0.5$  the coherence between the probe outputs was essentially zero. However, these observations apply strictly to mirror-image positions.

Figure 5-11 shows correlation results for  $|z/t| < 0.5$  and  $|y/\delta| \leq 0.5$  for mirror-image positions across the plane of symmetry. Figure 5-11(a) shows moderate coherence for the positions  $P_{\pm}(3.0, 0.25, \pm 0.25)$ , which were mirror image positions closer to the wing-body junction than the positions ( $z/t = \pm 0.5$ ) described above, for which the velocities were essentially uncorrelated. Subsequent repositioning of the probes even closer to the wing pro-

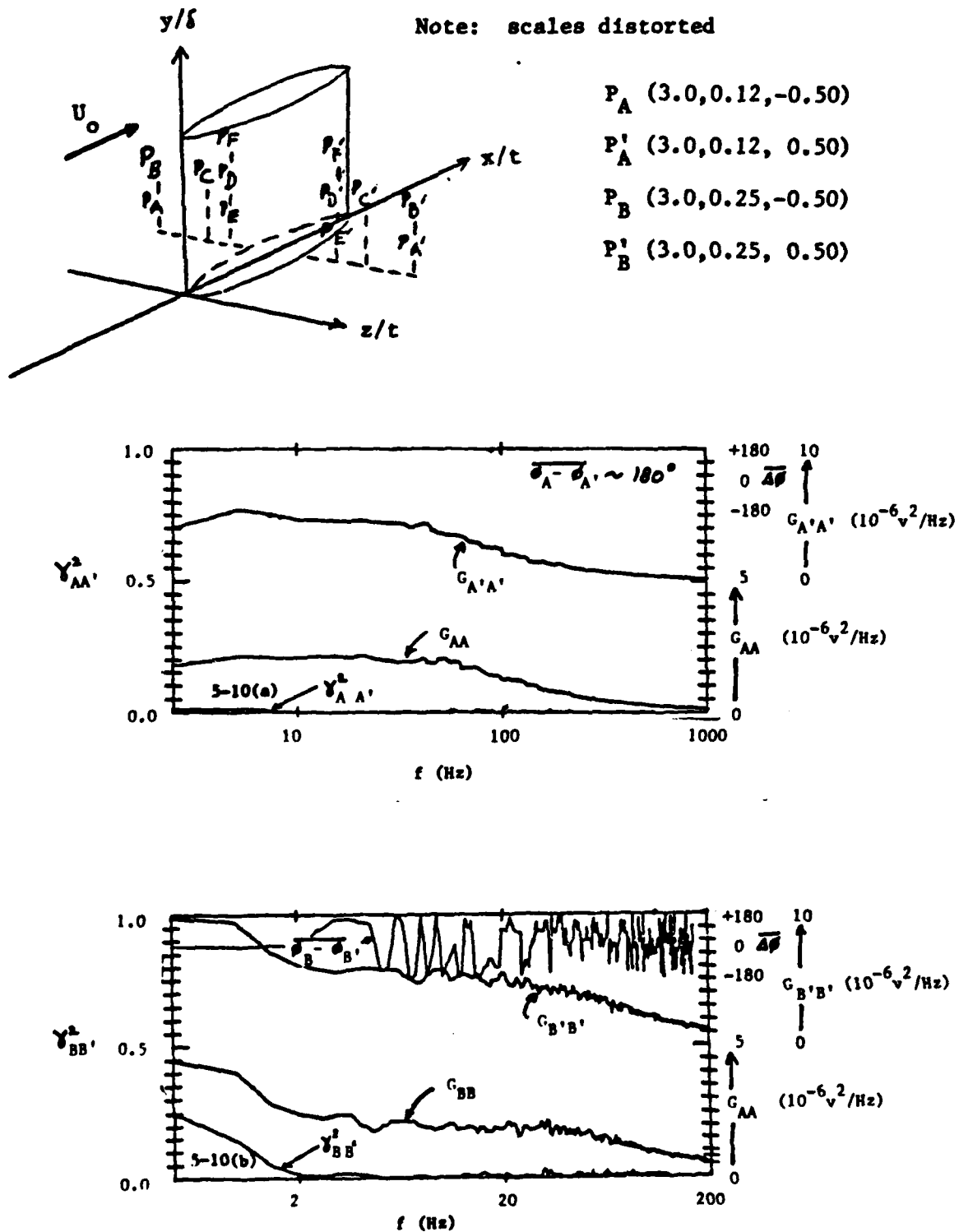
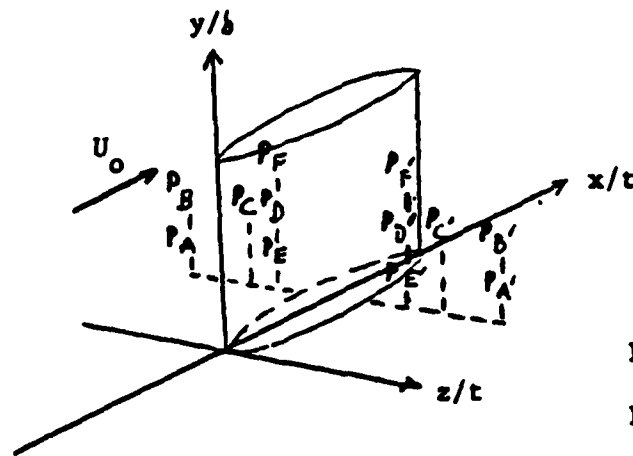
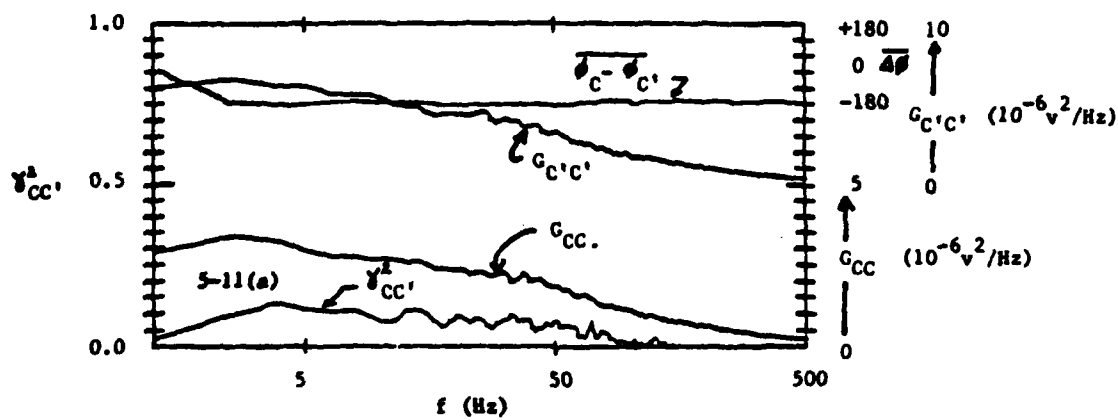
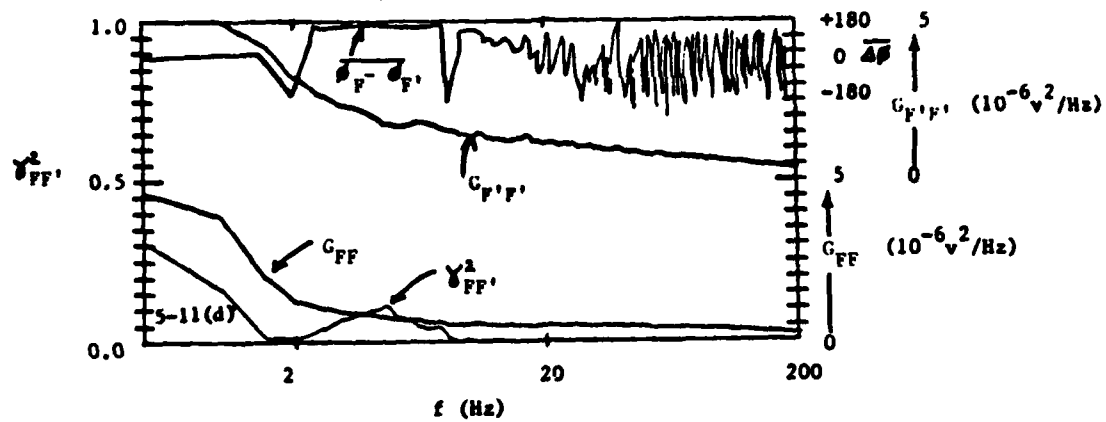
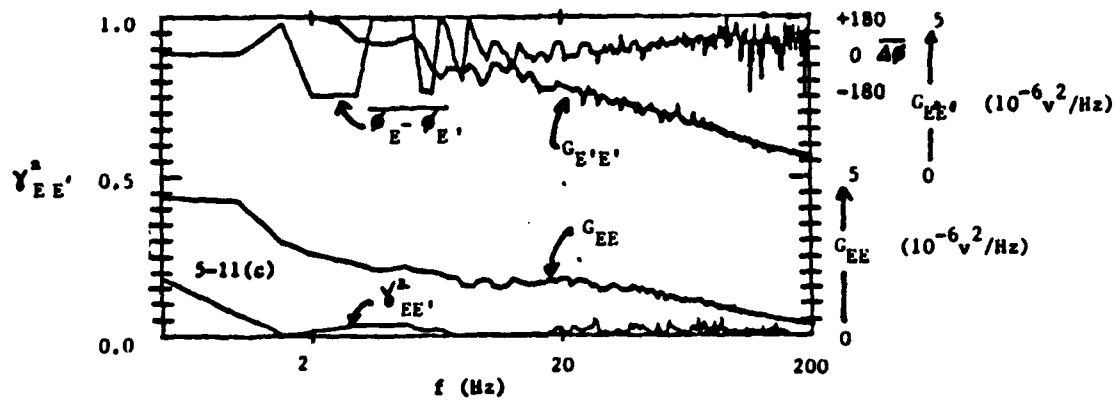
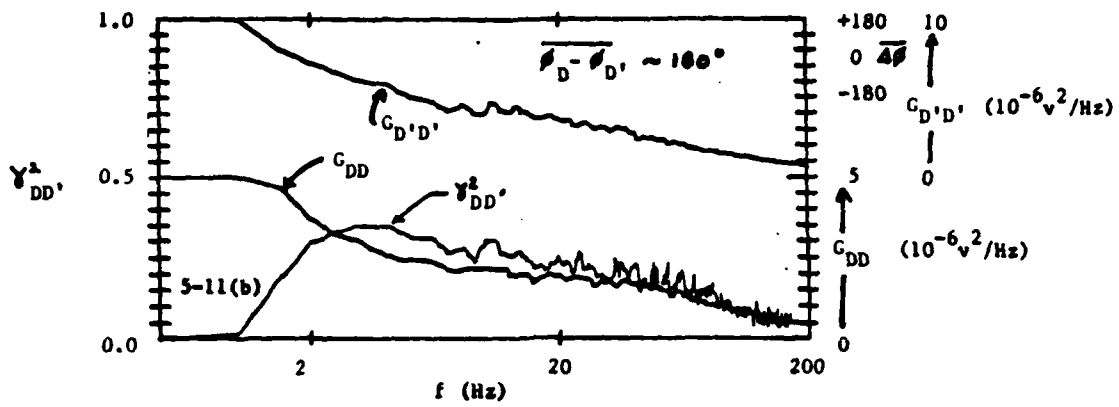


Figure 5-10: Mid-Wing Plane-of-Symmetry Correlations for  $|z/t| = 0.5$



Note: scales distorted

 $P_C (3.0, 0.25, -0.25)$  $P'_C (3.0, 0.25, 0.25)$  $P_D (3.0, 0.25, -0.12)$  $P'_D (3.0, 0.25, 0.12)$  $P_E (3.0, 0.12, -0.12)$  $P'_E (3.0, 0.12, 0.12)$  $P_F (3.0, 0.50, -0.12)$  $P'_F (3.0, 0.50, 0.12)$ Figure 5-11: Mid-Wing Plane-of-Symmetry Correlations for  $|z/t| < 0.5$



duced significant changes in the correlation features as shown in Figure 5-11(b). The figure shows large coherence for the positions  $P_{\pm}$  (3.0, 0.25,  $\pm 0.12$ ), which were very near to the wing. The relative phase between the velocity on the two sides of the wing was 180 deg.

Figure 5-11(c) shows significant changes in the correlation as the probes were maintained close to the wing ( $z/t = \pm 0.12$ ) but were positioned closer to the wall. The coherence was greatly diminished, but there appear to have been two bandwidths of correlated flow: an out-of-phase range from 2 to 4 Hz, and an in-phase range from 20 to 100 Hz. Either range is considered "low frequency" in the context of this study. But for identification purposes they will be referred to in this preliminary study as the low and high frequency bandwidths.

The correlated velocities had different spatial extent for the two bandwidths, at least for positions near the wing but relatively far from the wall. The correlations further from the wall, but at positions maintained close to the wing, were significant for the low frequency bandwidth (2-7 Hz), as shown in Figure 5-11(d) for  $P_{\pm}$  (3.00, 0.5,  $\pm 0.12$ ). On the other hand, the high frequency bandwidth (20-100 Hz) was uncorrelated.

It appears, then, that the correlated flow for mirror-image positions at  $x = 3$  is bound by  $|z/t| < 0.5$  and  $|y/\delta| \geq 0.12$ , and for the high frequency structure ( $f > 20$  Hz), the additional limitation  $|y/\delta| < 0.5$  is imposed.

It is significant that the disturbance bandwidth for the wing-body junction flow was different than that for the far upstream flow. Either new disturbances were created or only a sub-band of onset boundary layer frequencies passed through the junction while the remainder were suppressed.

The spatial extent of the flow temporal structure was further investigated by placing a reference probe at  $P_A$  (3.0, 0.25, -0.12) and moving a second probe to positions  $P_B$  (3.0,  $y/\delta$ , 0.12) on the opposite side of the wing. This correlation was different than that described above because the probes in this case (except for the

obvious exception) were not at mirror-image positions.

Figure 5-12 shows the results for positions varying from  $y/\delta = 0.3$  to  $y/\delta = 2.5$ . As  $y/\delta$  increased, the high frequency ( $f > 20$  Hz) coherence rapidly approached zero. The low frequency coherence centered on  $f = 4$  Hz as  $y/\delta$  increased, and, although diminished, was not zero for  $y/\delta = 2.5$ . This position was greater than two nominal boundary layer thicknesses from the wall. It appears, then, that the low frequency temporal flow, that traveled along the pressure ridge upstream from the wing, had effects on the wing flow well outside the nominal boundary layer. It is not clear if this effect was produced by intermediate fluctuations of the wing boundary layer, or directly by potential flow reactions to the temporal wing-body junction flow.

It is reasonable to conjecture, because of the mean root vortex transport that the flow in the outer boundary layer would be correlated with the inner boundary layer flow on the other side of the wing, although not correlated with the outer boundary layer flow on the other side. Figure 5-12(c) shows this strong "inverted boundary layer" correlation. The coherence between velocities at  $y/\delta = 0.5$  and  $y/\delta = 0.25$  on opposite sides of the wing was larger than for the mirror-image positions  $y/\delta = \pm 0.5$  (Figure 5-11(d)) and it was comparable to the coherence for  $y/\delta = \pm 0.25$  (Figure 5-11(b)) for the low frequency bandwidth.

The high frequency bandwidth was not correlated for the "inverted boundary layer" correlation, although it was for the mirror image correlation  $y/\delta = \pm 0.25$ . Therefore, the inverted boundary layer correlation seems to apply only to the low frequency bandwidth.

The cross-stream spatial extent of the low frequency structure outside the nominal boundary layer beginning at  $P_B$  (3.0, 2.5, 0.12) and extending in the z-direction is shown in Figure 5-13. The correlations with  $P_A$  (3.0, 0.25, -0.12) were extended to  $P_B$  (3.0, 2.5, 2.0) in the z-direction, where the correlation seemed to approach zero. It is concluded that the temporal flow structure, initiated upstream wholly within the boundary layer, had velocity

Note: scales distorted

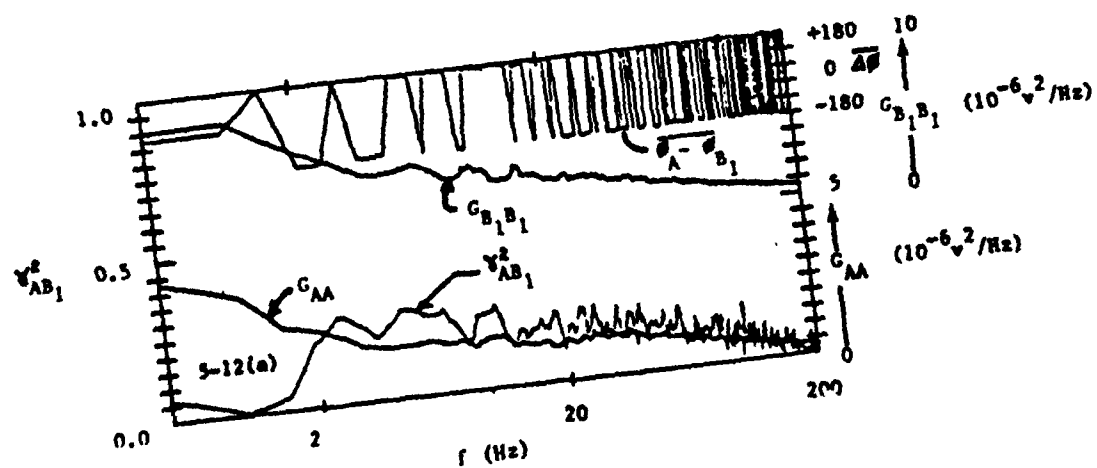
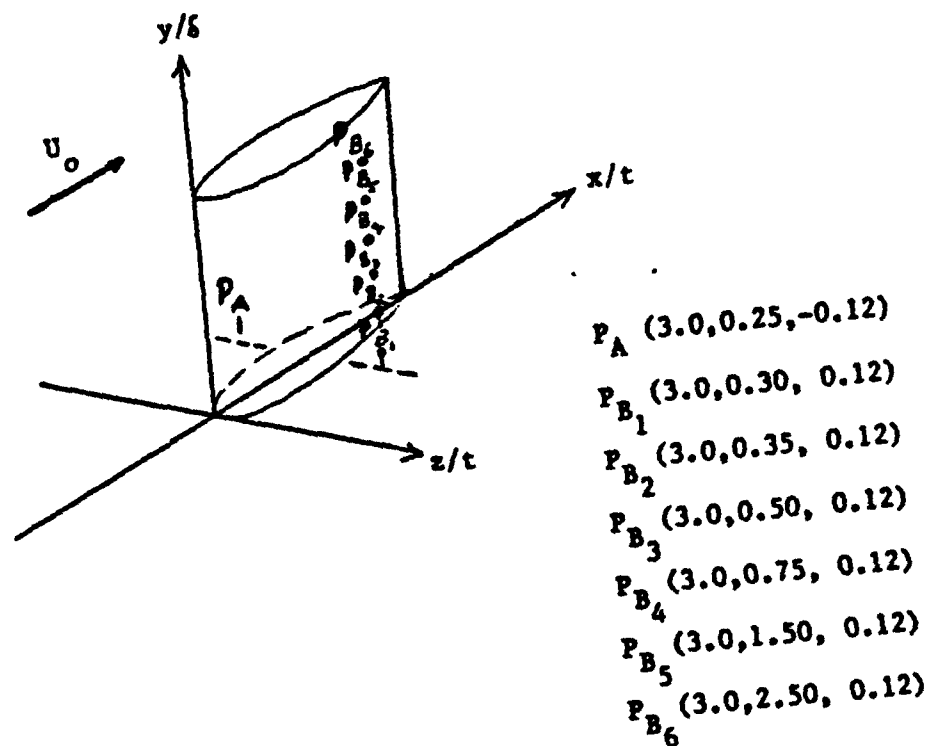
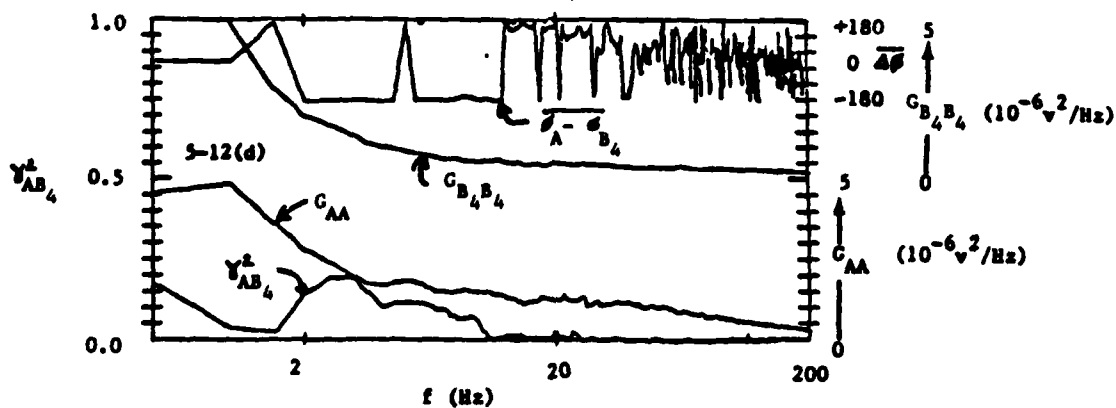
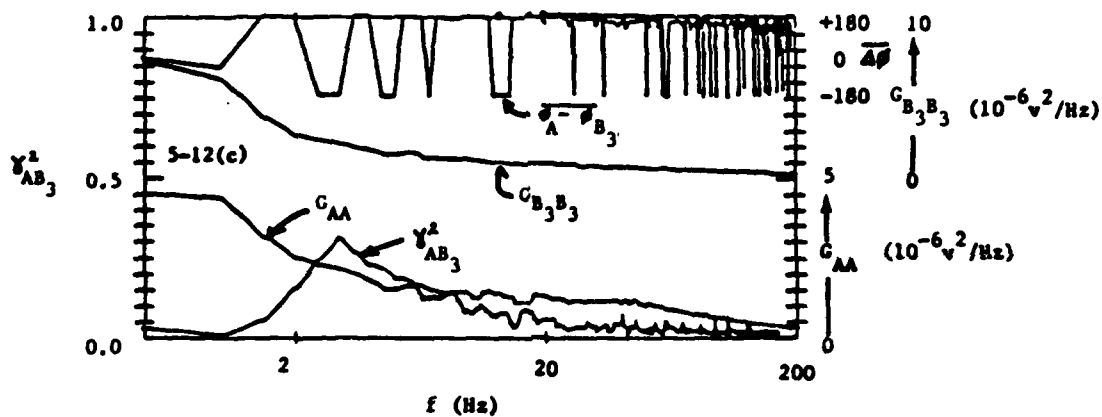
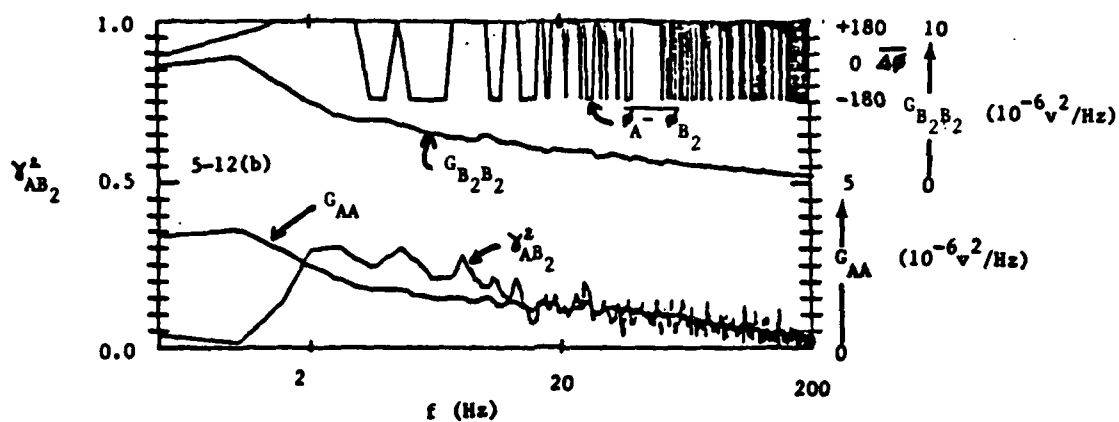
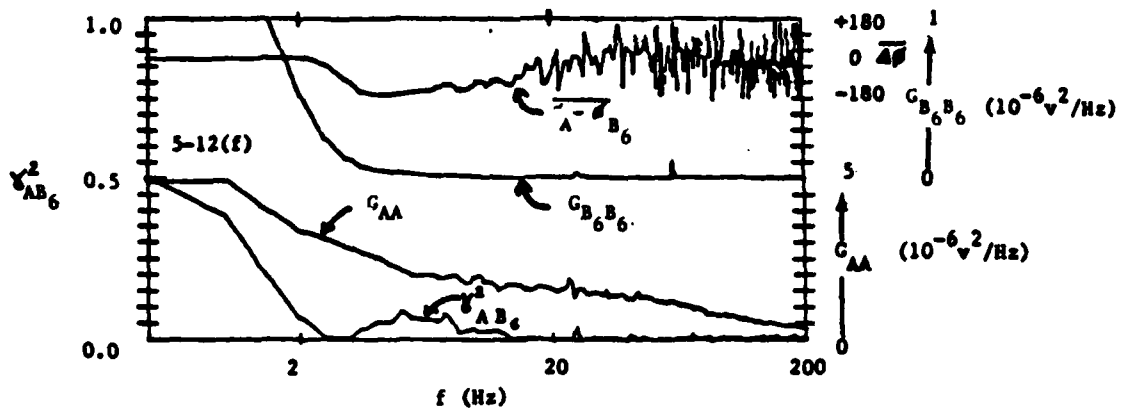
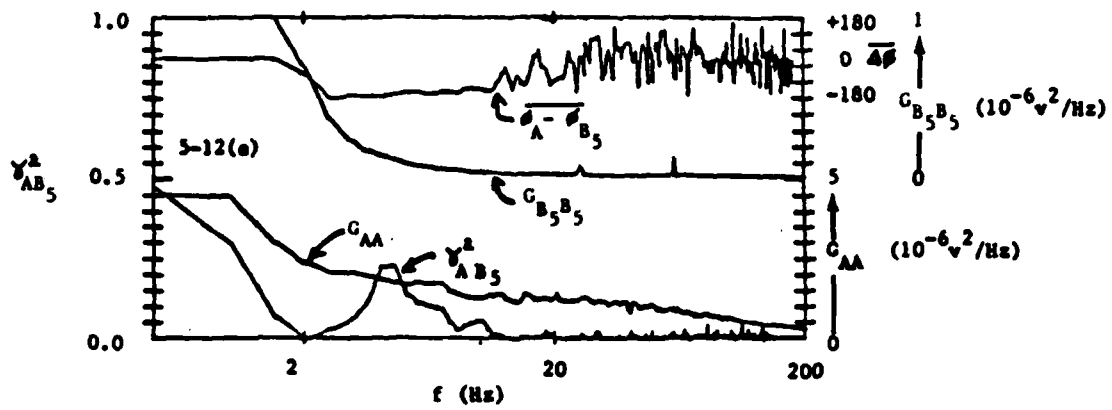


Figure 5-12: Plane-of-Symmetry Correlations With Reference Probe Well Inside Boundary Layer and Near the Wing





Note: scales distorted

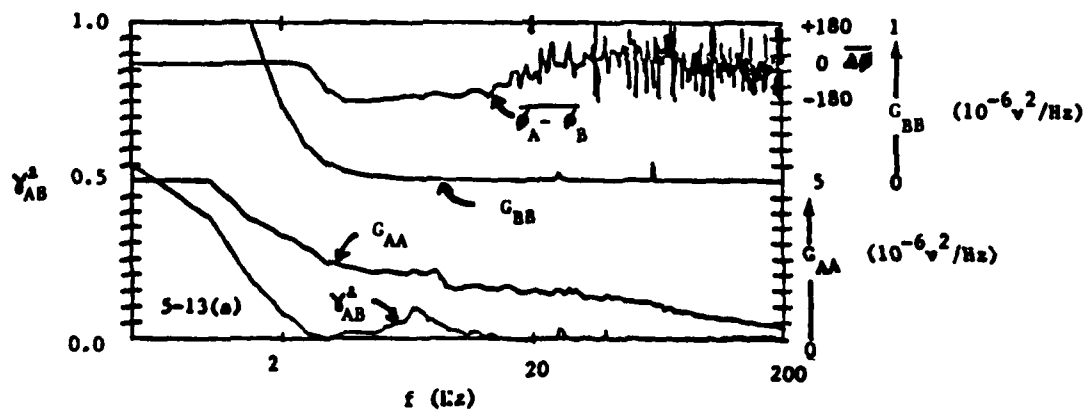
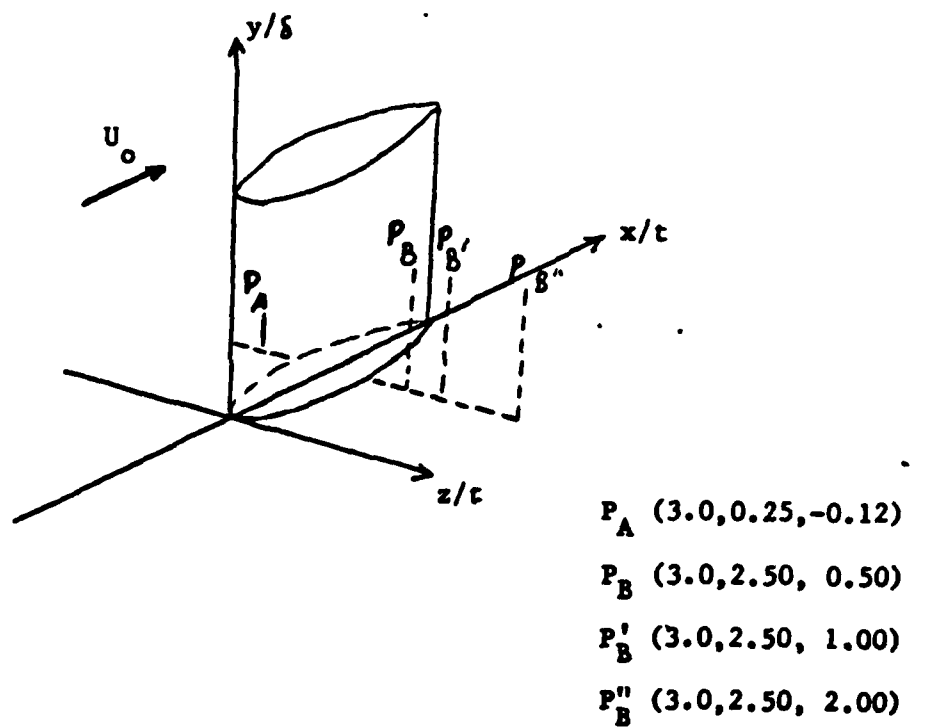
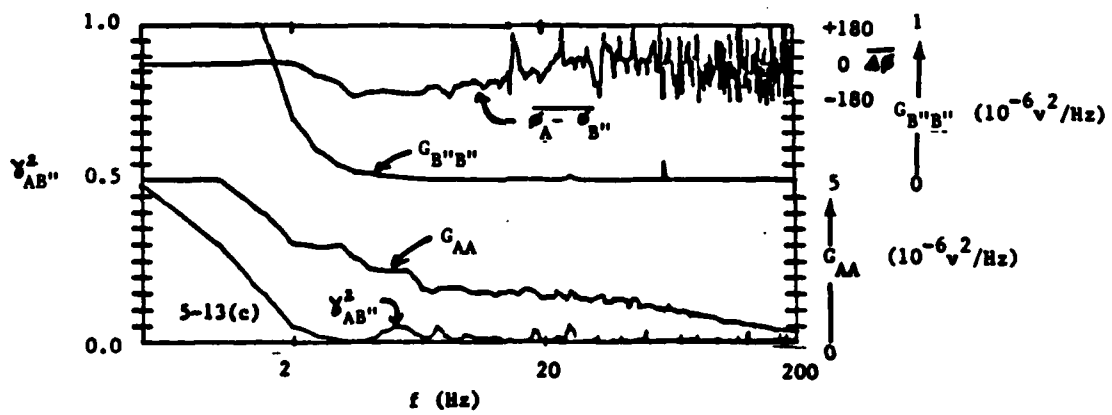
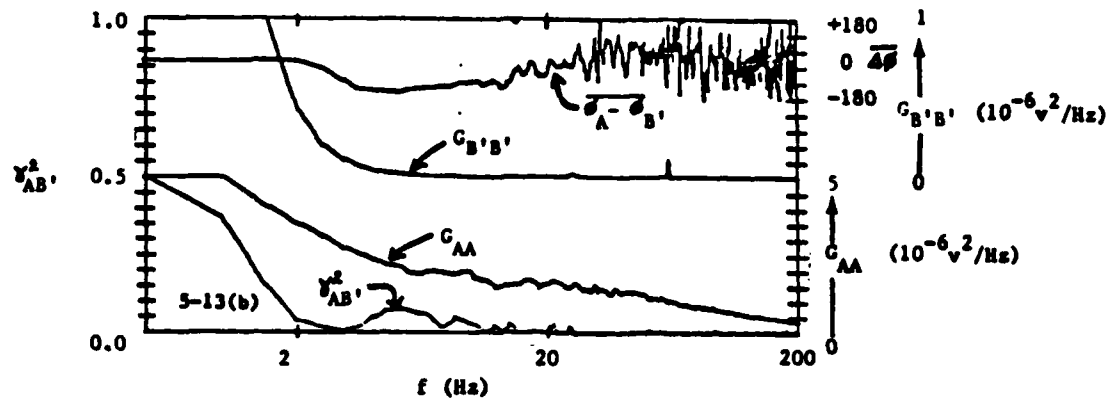


Figure 5-13: Plane-of-Symmetry Correlations Showing Cross-Stream Spatial Extent Well Outside Nominal Boundary Layer





perturbation effects well outside the boundary layer in the flow around the wing. It is not clear from the measurements if these effects were potential flow responses to the temporal flow in the boundary layer. It is clear that the velocity correlations for these positions were zero when the wing was removed and that the velocity fluctuations are not produced by mechanical oscillation of the wing as evidenced by accelerometer correlations. The certainty of these statements is argued in Section 5.8.

Further substantiation of the structure's extent is shown in Figure 5-14 for the position  $P_B$  (3.0, 1.5, 2.0) which is closer to the boundary layer edge than the outermost position of Figure 5-13. The coherence at this position was also non-zero.

The outer boundary layer correlations were further studied by moving the reference probe away from the wall to the position  $P_A$  (3.0, 0.75, -0.25), which is in the outer part of the boundary layer, and correlating its output with that from a probe placed at the positions  $P(3.0, y/\delta, 0.25)$ . This procedure permitted plane-of-symmetry correlations with the reference probe in the outer boundary layer to be compared with those described above with the reference probe further inside the inner boundary layer. Figure 5-15(a) shows a small non-zero correlation at low frequency for the mirror image position. Figures 5-15(b) and 5-15(c) show an increase in the coherence as the probe was moved toward the wall. This is consistent with the above description of the "inverted boundary layer" correlation.

It appears that the strongest correlations across the plane of symmetry for the low frequency bandwidth disturbance are for positions such that one is in the inner boundary layer on one side of the wing and the other anywhere in the (inner or outer parts) boundary layer on the other side of the wing. The correlation between the outer boundary layer velocities across the plane of symmetry are small. All of the correlations show an out-of-phase relationship across the plane of symmetry.

It is here noted, in preparation for the following presentation of the correlated flow downstream of the wing, that the

Note: scales distorted

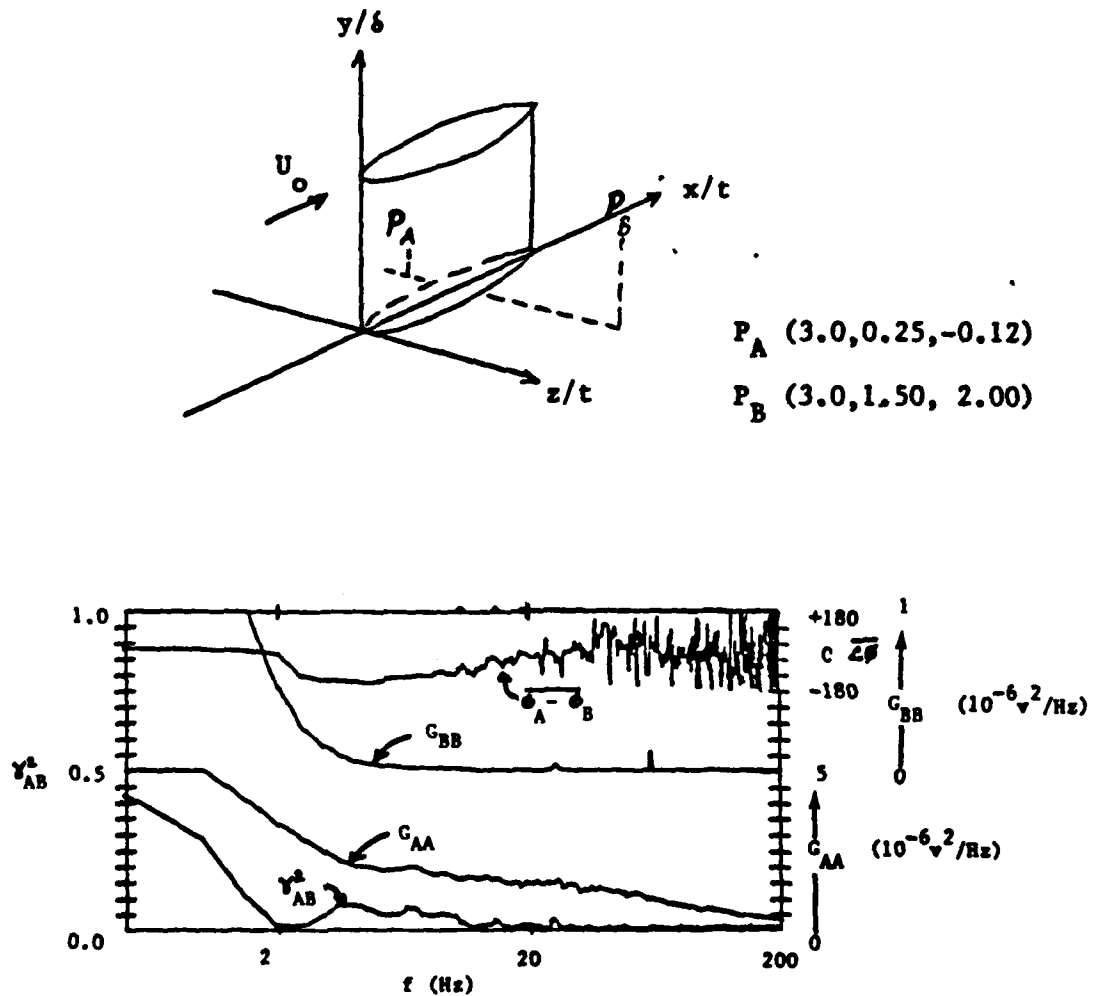


Figure 5-14: Plane-of-Symmetry Velocity Correlations Showing Non-Zero Coherence Outside Nominal Boundary Layer and Relatively Far From Wing

Note: scales distorted

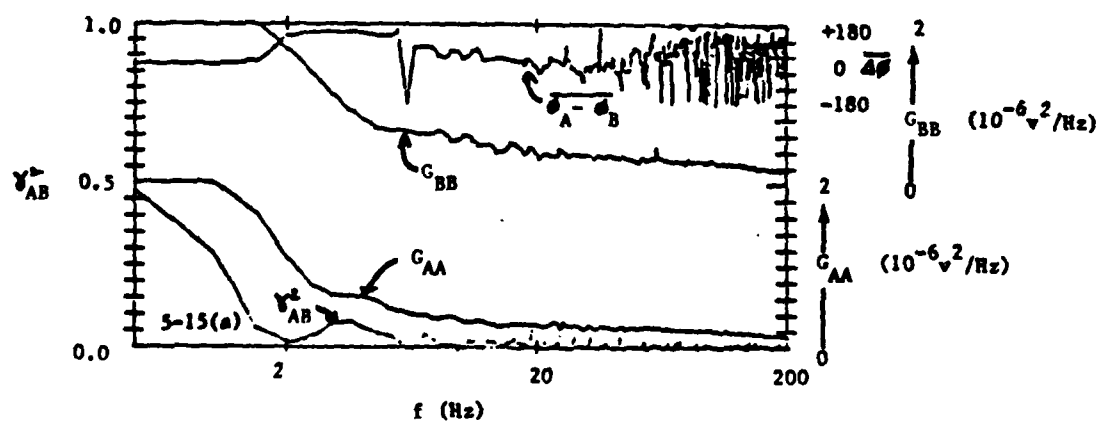
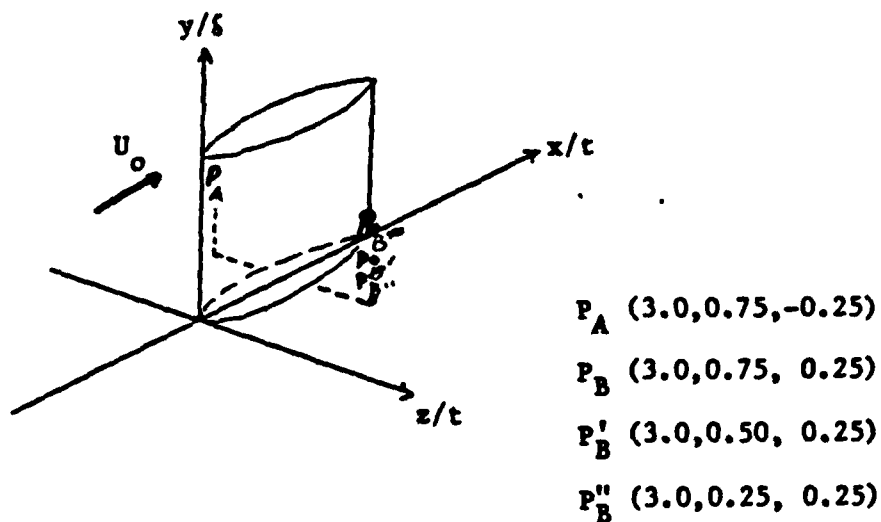
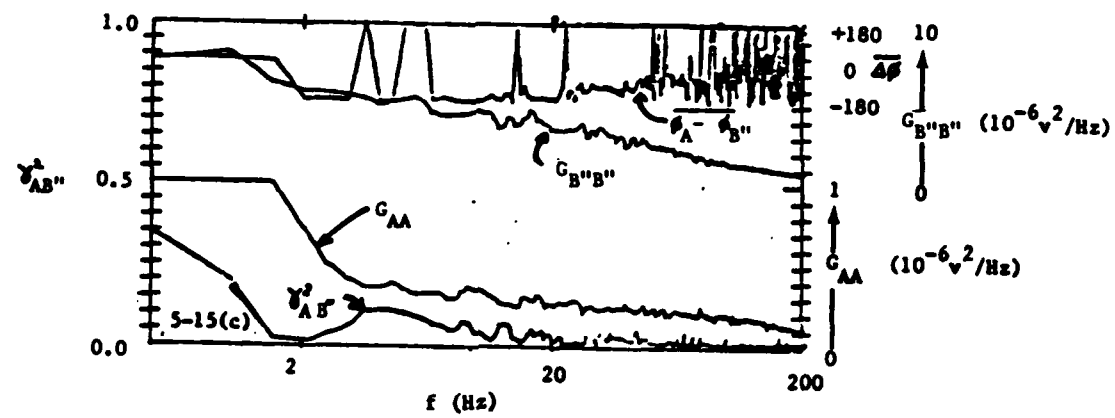
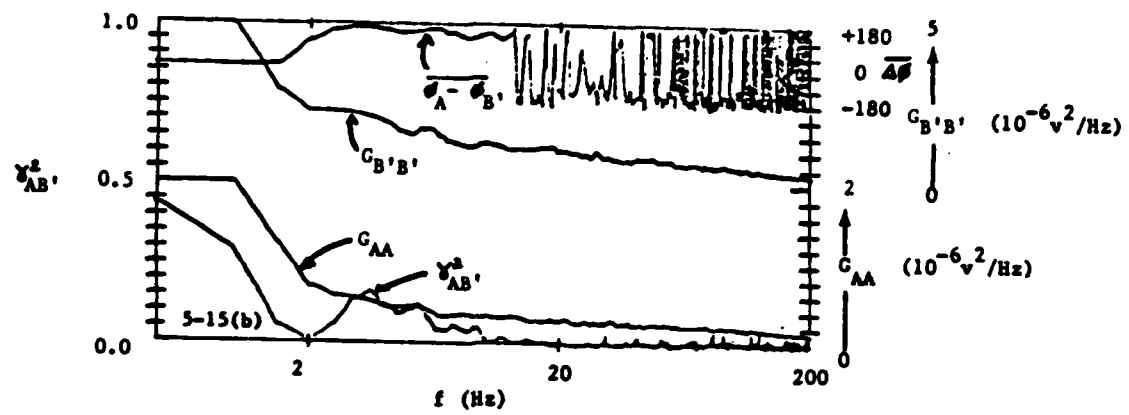


Figure 5-15: Plane-of-Symmetry Correlations Showing Strong Outer-Inner Boundary Layer Coherence



angle of incidence ( $\alpha = 2.4$  deg) of the wing did have global measurable effects on the mean velocity. Mean velocity profiles shown in Figure 5-16 for  $z/t > 0$  show a trough associated with the vortex driven outflow of low energy boundary layer fluid, while profiles for  $z/t < 0$  do not show a definite trough. The reason is that the vortex leg on the  $z/t < 0$  side of the wing was spatially expanded by the high pressure so that the outflow was spread over a larger area, producing a shallower trough. An investigation of the effects of incidence is discussed in Section 5.7.5.

#### 5.7.4 Trailing Edge and Downstream Correlations

The low frequency disturbance was tracked in its downstream movement by positioning the reference probe at the mid-wing position  $P_A(3.0, 0.25, -0.12)$  and the second probe at a position immediately downstream from the trailing edge,  $P_B(5.12, 0.25, -0.18)$ . Figure 5-17 shows significant coherence, centered on the frequency 4 Hz, between the velocity measurements at the two positions. The relative phase is a small positive angle. This result is expected because the low frequency (4 Hz) is associated with large wavelengths such that the velocities were nearly in-phase except that the peak should have occurred in time at the upstream mid-wing position before it occurred at the trailing edge. Using a nominal flow speed,  $U = 30.5$  m/s, a separation distance from the mid-wing position to the trailing edge position,  $l = 10$  cm, and a peak coherence at a frequency,  $f = 4$  Hz, the expected relative phase is  $\phi_A - \phi_B = l/(U/f) 360$  deg = 5 deg. This is consistent with the observed measurements. Furthermore, the positive slope of the relative phase as a function of the frequency indicates downstream convection (in this case  $\Delta x < 0$ ). It is concluded that low frequency organized motion of the flow, most likely as convected spatial structure, passed from the mid-wing to the trailing edge.

Two point velocity correlations were then obtained to form a quantitative measure of the spatial distribution of relative phase within one leg of the horseshoe vortex. Figure 5-18 is a compilation of those measured two-point velocity correlations, which were obtained immediately downstream from the wing trailing

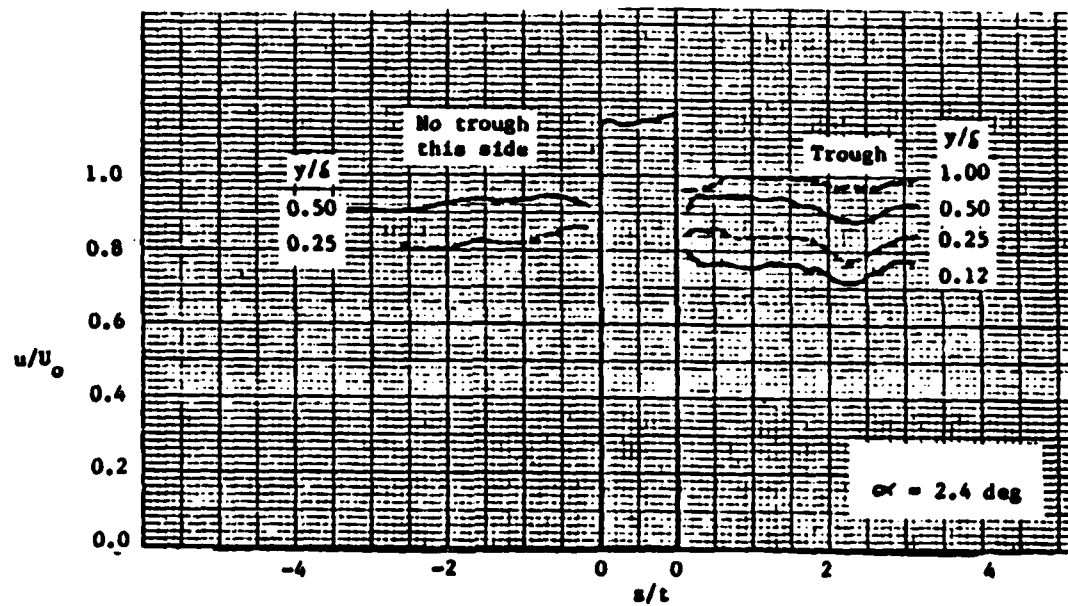


Figure 5-16: Mean Velocity Profiles for  $x/t = 3.0$  Showing Asymmetry Produced By Wing at Small Incidence Angle

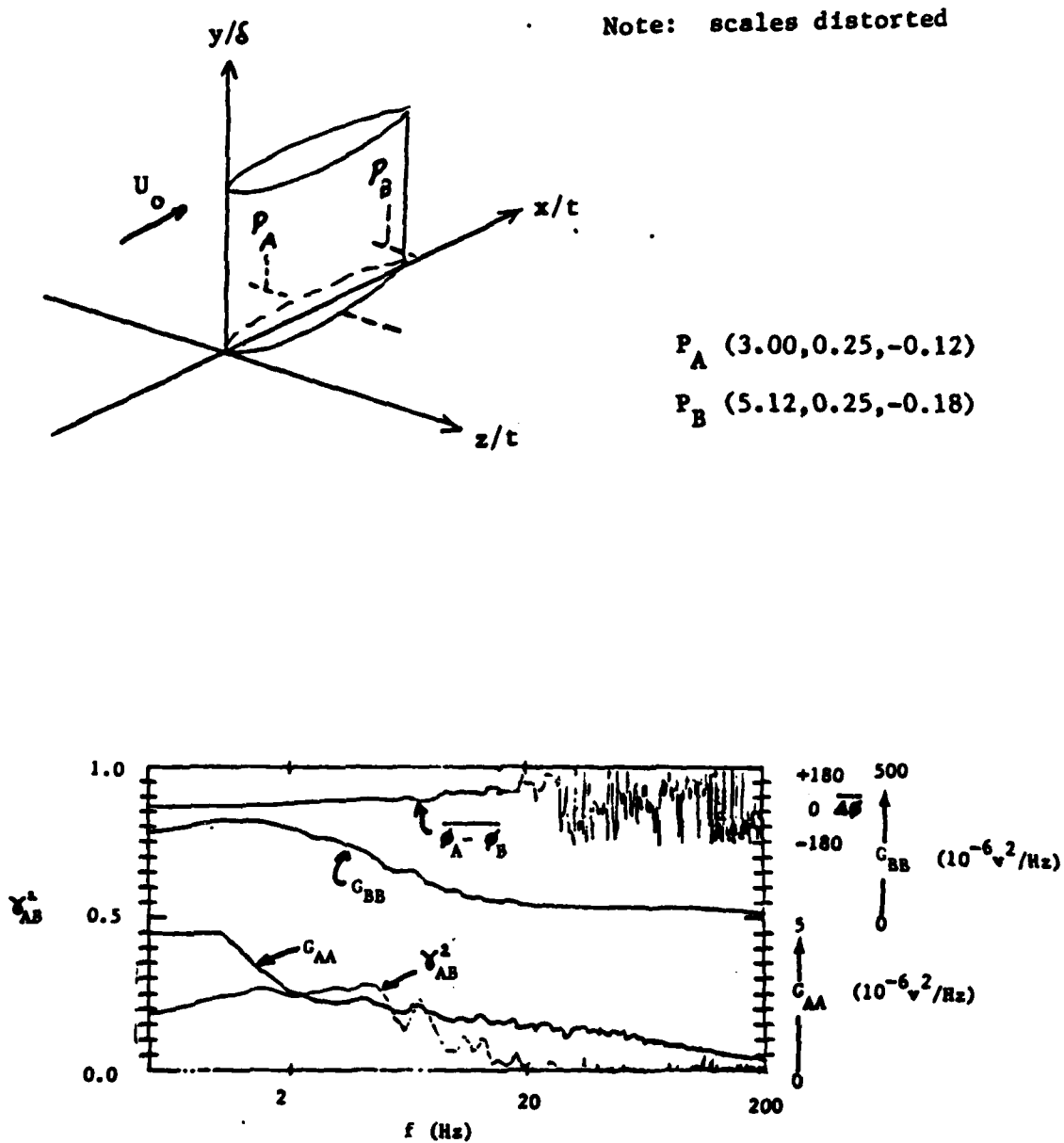


Figure 5-17: Correlations Between Mid-Wing and Trailing Edge Regions



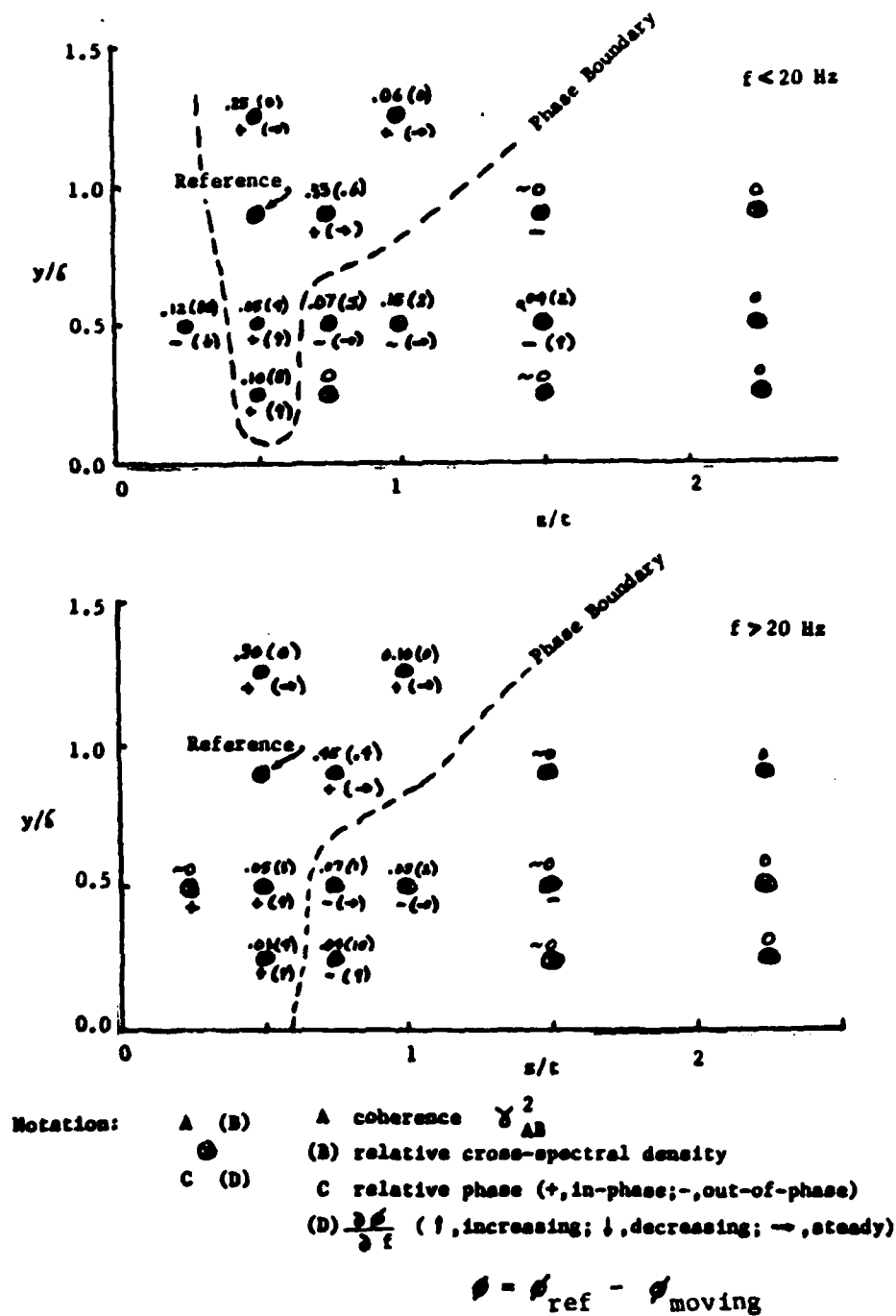


Figure 5-18: Two-Point Velocity Correlations in One Leg of Root Vortex at Trailing Edge ( $x/t = 5.12$ )

edge. The reference probe was maintained at  $P_A$  (5.12, 0.90, 0.50), while the survey probe was positioned, as shown in the figure, within the same vortex leg as the reference probe. This procedure was different than that for most of the correlations presented so far, in which the probes were on opposite sides of the wing and hence in separate vortex legs (although always within the same vortex "tube" wrapped around the wing leading edge).

Considerable information is presented in Figure 5-18 concerning coherence, cross-spectral density, and phase. The figure is presented in two parts representing the two frequency bandwidths discussed previously for the disturbances.

The most relevant features of the figure are the phase boundaries separating in-phase fluctuations from out-of-phase fluctuations. The noticeable difference between the two frequency bandwidths is for the relative phase for  $z/t < 0.5$ ; the relationship is out-of-phase for  $f < 20$  Hz and in-phase for  $f > 20$  Hz. The determination of this difference in fact was made from the one measurement shown in detail in Figure 5-19. Clearly the lower frequency bandwidth had significant coherence with an out-of-phase relationship between the velocities. On the other hand, the coherence for the higher frequency was almost zero and the phase was more nearly in-phase than out-of-phase.

A previous hint that the two bandwidth frequencies are associated with different structures was presented in Figure 5-11(c) where they had different phase relationships for plane-of-symmetry correlations at mid-wing ( $x/t = 3.0$ ). The lower frequency bandwidth disturbance was out-of-phase and the higher frequency bandwidth disturbance was nearly in-phase. Admittedly these observations involve correlations with low values of coherence and hence additional measurements are required to confirm the phase boundary location.

Figure 5-18 also shows, for both bandwidth disturbances, that the relative phase ( $\phi_{\text{reference}} - \phi_{\text{moving}}$ ) increased with frequency, except for one instance. Assuming that the fluctuations at the trailing edge result from a common upstream disturbance eventually passing through the two measurement positions, the change in

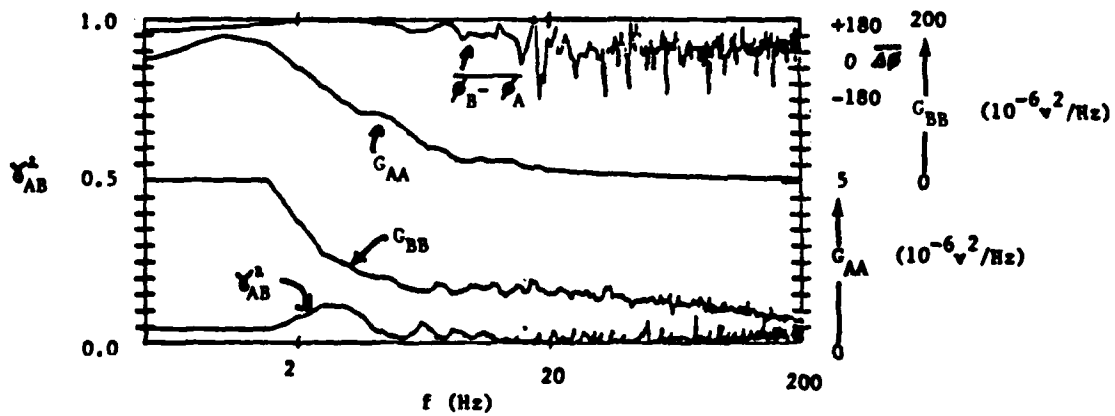
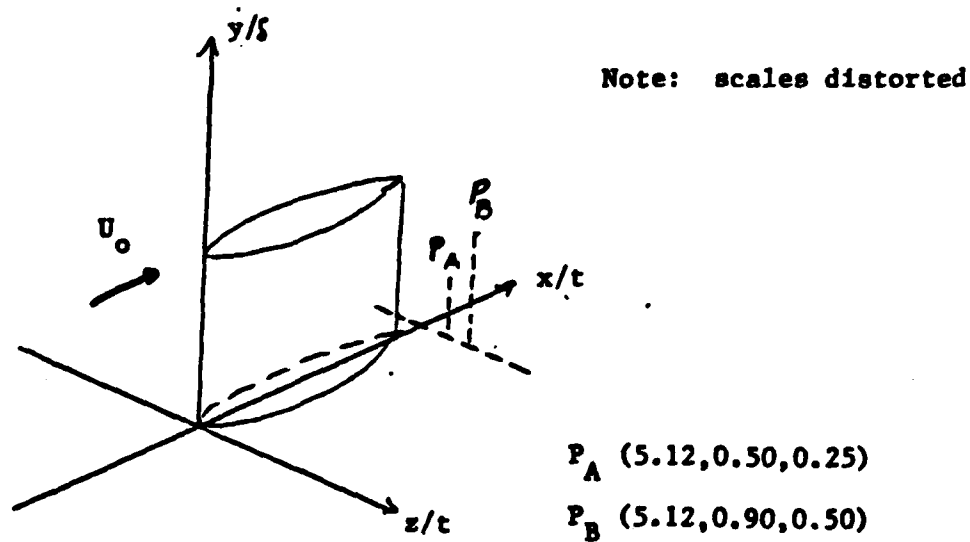


Figure 5-19: Low Frequency Out-of-Phase Correlations for One Side of Plane-of-Symmetry

relative phase with frequency must be attributable to different flow velocities for the two pathlines passing through the measurement positions. Since,  $[(\phi_{\text{ref}} - \phi_{\text{moving}})/f] \sim (-x)/U_{\text{ref}} - (-x)/U_{\text{moving}}$  where  $x$  is the distance along the pathline from the origin of the disturbance, the implication is that the disturbance inside the nominal boundary layer had a smaller average velocity than that for the outer part of the nominal boundary layer, where the reference probe was located.

Figure 5-20 adds credibility to the phase boundary presented in Figure 5-18 by showing measurement results for two additional positions. One position is inside the phase "trough" in the  $z/t = 0.5$  neighborhood for  $f < 20$  Hz shown in Figure 18, and the other is outside the trough (larger value for  $z/t$ ). Figure 5-20 demonstrates that the relative phase changed as the phase boundary was crossed.

#### 5.7.5 Downstream Correlations

Two-point velocity correlations were measured in the plane  $(18.0, y/\delta, z/t)$  located 2.5 chordlengths downstream from the wing trailing edge. The purpose of the measurements was to obtain information about the growth of the large scale low frequency organized motion of the flow originating in the wing-body junction. Specifically, it was determined that there was dramatic growth of the fluctuations described above as they were convected downstream. Far downstream from the wing, as in the present case, the flow was a wing wake-vortex-boundary layer interaction problem.

Figure 5-4 schematically shows the measurement plane at  $x/t = 18$  relative to the wing position and the free stream velocity. As shown in the figure, the onset boundary layer was at small incidence to the wing. The small incidence produced dramatic changes in the relative sizes of the two vortex legs far downstream from the trailing edge. The leg on the high pressure side of the wing was spatially enlarged relative to the leg on the low pressure side. Some evidence for this feature was shown in Figure 5-16, where it is shown that the peaks and troughs of the velocity profile were not symmetric about the wing at incidence. The accelerated flow

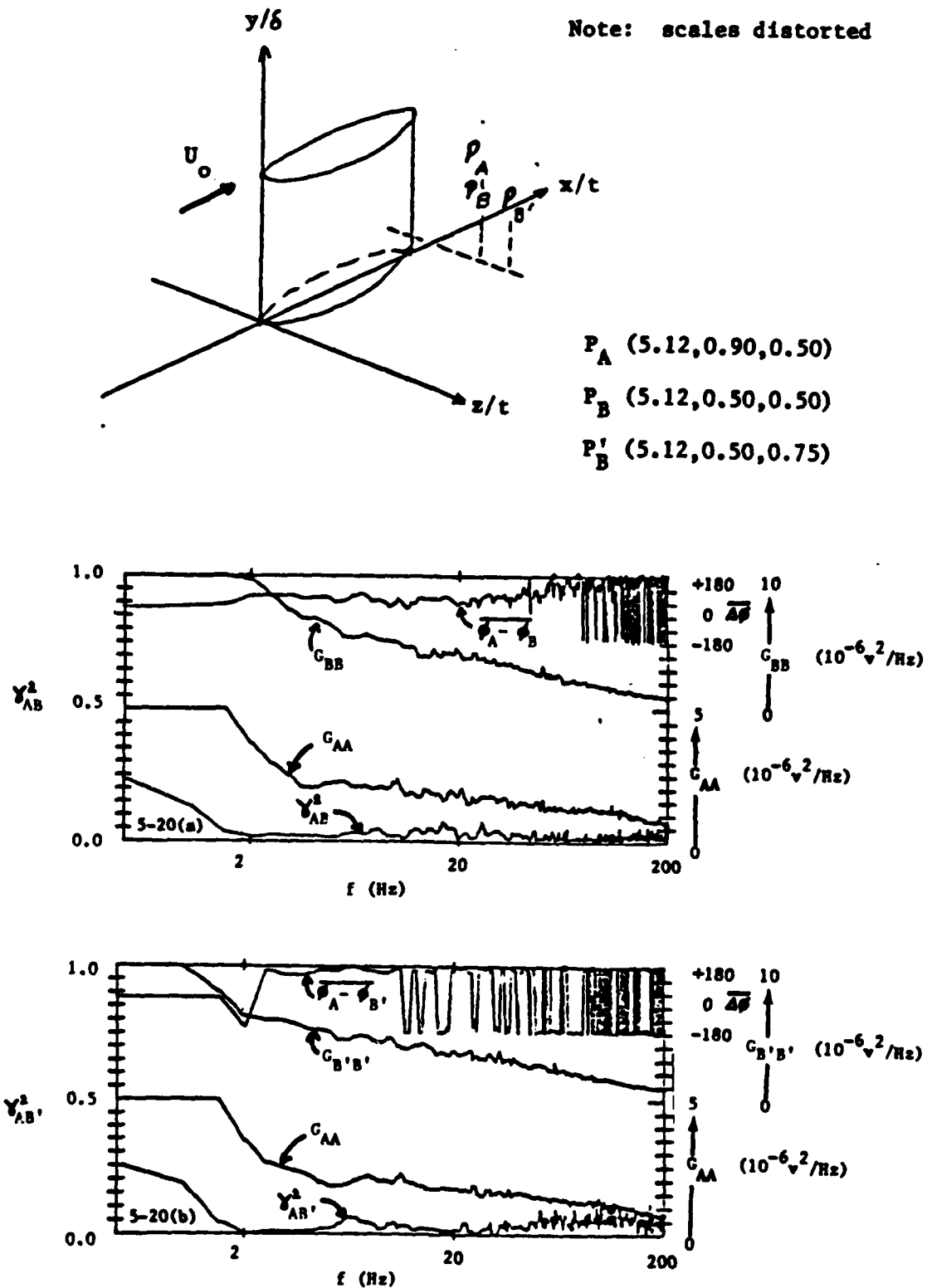


Figure 5-20: Trailing Edge Correlations Showing Phase Shift for Increased Values of  $z/t$

on the low pressure side of the wing stretched and intensified the root vortex leg on that side, while the root vortex leg on the high pressure side of the wing was compressed and enlarged in spatial extent. The legs therefore transported axial momentum into the wing-body junction with different results. Furthermore, the vortices did not appear to recover, or relax, to equal sizes even far downstream from the wing trailing edge, as discussed below.

Figure 5-21 shows the mean velocity profiles at  $x/t = 18$  as a function of  $z/t$  for various positions  $y/\delta$ . The profiles show the expected trough for large  $y/\delta$  due to the wing wake momentum deficit, and the peak for small values for  $y/\delta$  due to root vortex transport of high momentum fluid into the wing wake. The asymmetry of the profiles is attributed to the differences in size of the root vortex legs. The larger vortex, on the high pressure side, dominated the flow. The trough on the low pressure side is produced by the transport of low momentum fluid by the spatially smaller, but more intense, other vortex leg. This feature is different than the trough at  $y = 4.0$ , which is produced by the momentum deficient wing wake. Although the larger vortex also displaced low momentum fluid, it was spread over a much larger area to produce a shallow dip in the profile rather than a distinct trough.

Two-point velocity correlations were measured in this asymmetric wake. The phase distributions between measurement positions confirm that the temporal flow associated with the larger vortex spatially dominated the flow. Figure 5-22 presents the measurement positions for two placements of the reference probe. The figure also shows the locus of positions for the profile troughs shown in Figure 5-21. Because the trough is postulated to have been an effect of low momentum fluid transport by the smaller vortex leg, it is surmised that the smaller vortex core is to the left of the locus. The dashed line is a possible representation of the division between large vortex dominated flow, and small vortex dominated flow. Specifically, in-phase fluctuations occur to the left, and out-of-phase fluctuations occur to the right, of the dashed line.

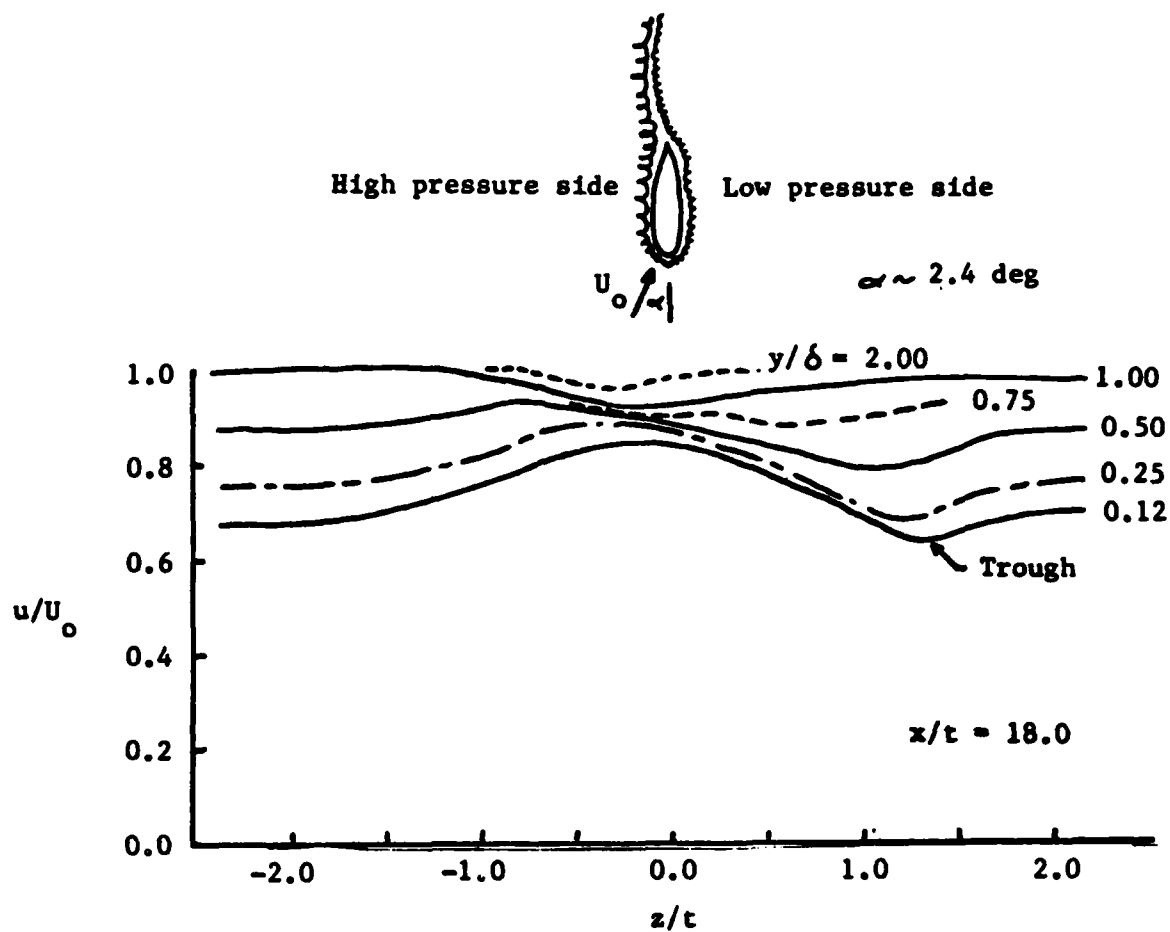


Figure 5-21: Asymmetric Wake Profiles Produced by Spatially Unequal Vortex Legs for Wing at Incidence

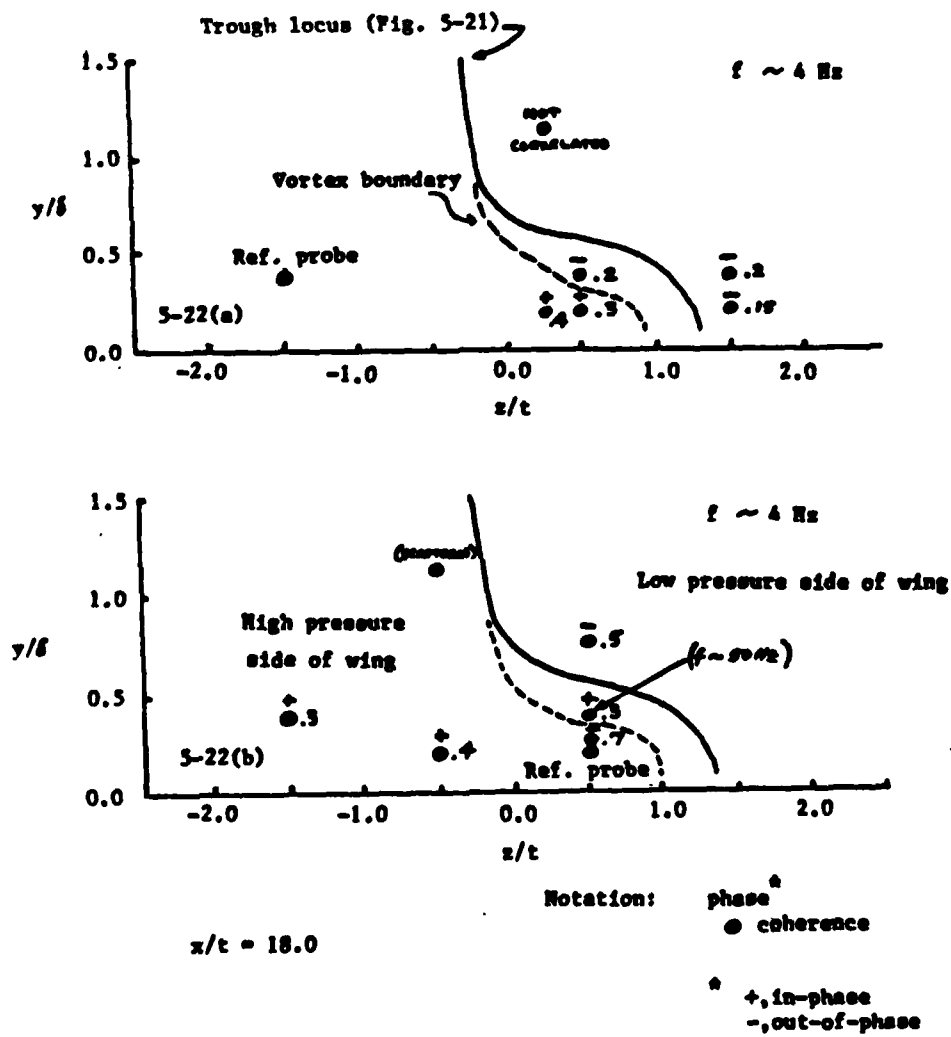


Figure 5-22: Two-Point Velocity Correlations Downstream from Wing



All the measurements for Figure 5-22 exhibited correlation bandwidths centered on approximately 4 Hz with one exception, those for the position  $P_B$  (18.0, 0.5, 0.50, 0.50) in Figure 22(b), which was centered on 50 Hz. Figure 5-23 shows results for the correlations at 4 Hz that support the thesis that the large vortex spatially dominated the flow.

Representative measurements of the coherence bandwidths are shown in Figure 5-23 for the reference position  $P_B$  (18.0, 0.50, -1.50) shown in Figure 5-22 (a). Results are shown for the out-of-phase correlations  $P_B$  (18.0, 0.50, + 1.50) and the in-phase correlations at  $P_B$  (18.0, 0.25, + 0.50).

As noted above, the correlation for  $P_B$  (18.0, 0.50, 0.50) shown in Figure 5-22 (b) indicates a correlation across the dashed line for a frequency bandwidth centered on 50 Hz. Figure 5-24 shows the measured coherence for this correlation. This result is consistent with measurements made for  $x/t = 3$ , which indicated two non-zero correlation bandwidths for mirror-image positions on either side of the wing. Figure 5-11 (c) shows the two bandwidths. The higher frequency is from 20 to 100 Hz and is in-phase across the wing. It was shown that this higher frequency bandwidth is not spatially correlated for a very large distance. It is likely that this higher frequency motion is also evident in Figure 5-22 (b), appearing as the in-phase correlation across the dashed line.

For contrast, Figure 5-25 shows the correlation bandwidths for the position  $P_A$  (18.0, 1.00, 0.50) which is centered on the lower frequency 4 Hz and is out-of-phase with the reference  $P_A$  (18.0, 0.25, 0.50). The higher frequency correlation for this case is zero, consistent with the small spatial extent observed at  $x/t = 3$  for the higher frequency disturbance.

Of special significance is the very narrow frequency bandwidth in Figure 5-25. The velocity correlations were non-zero within a 2-11 Hz bandwidth, which is dramatically smaller than the 2-200 Hz bandwidth in the onset boundary layer. However, it is difficult to distinguish the physics governing the two frequency bandwidths because they overlap for this particular wing.

Note: scales distorted

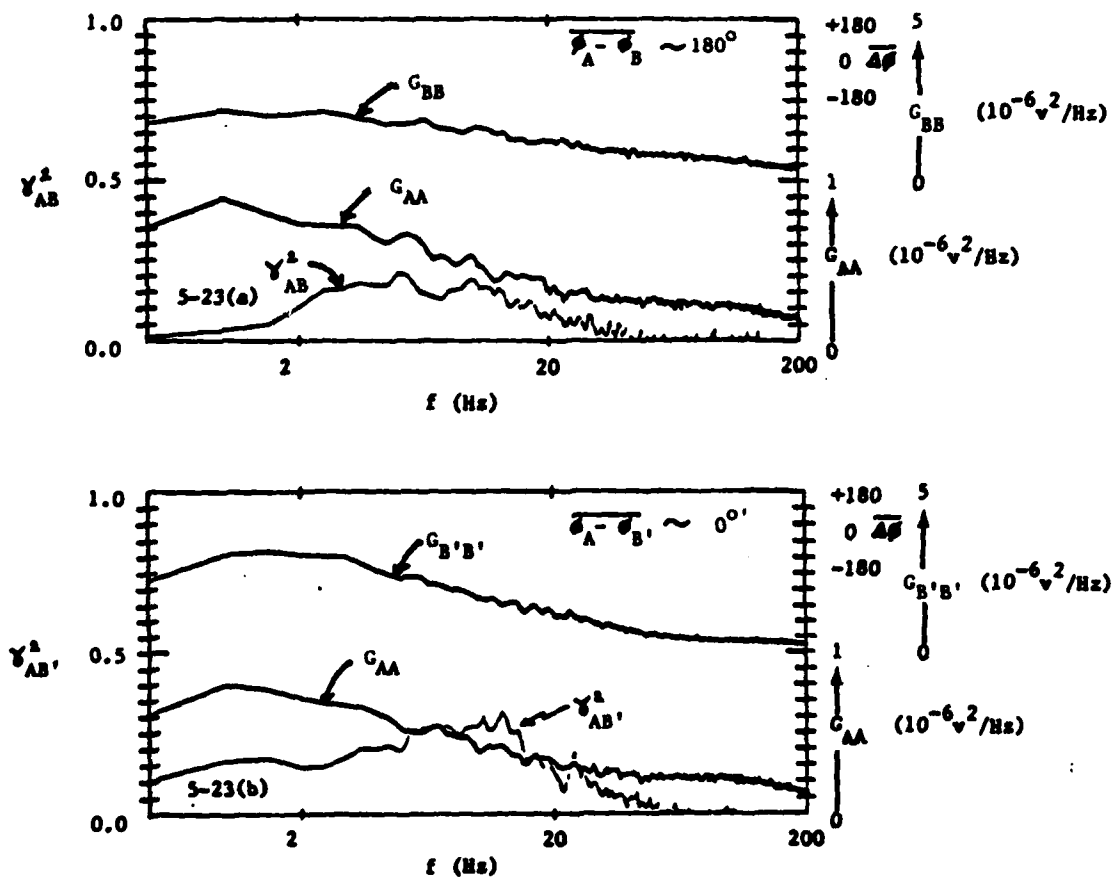
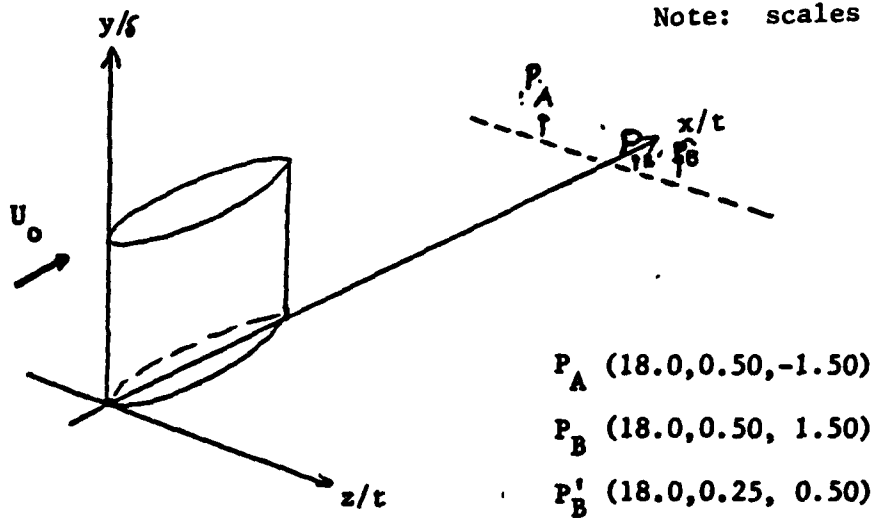


Figure 5-23: Representative Downstream Correlations

Note: scales distorted

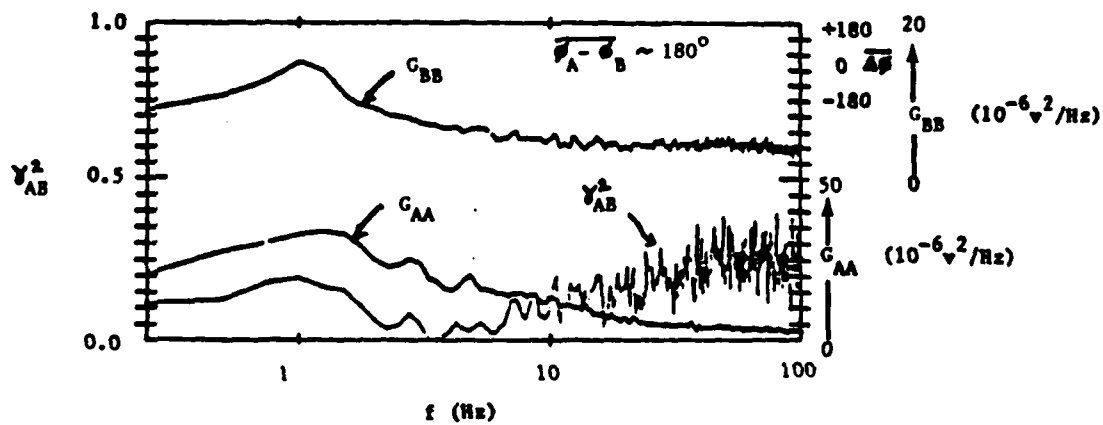
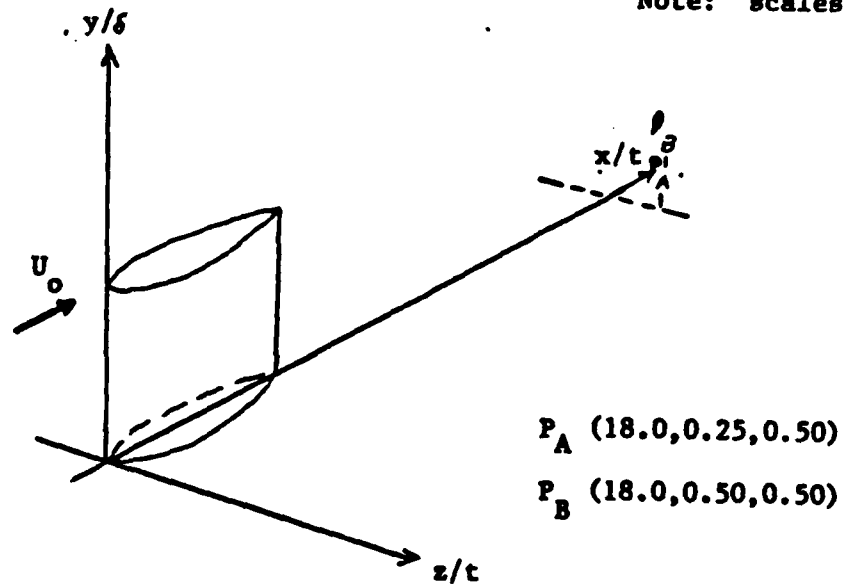


Figure 5-24: Correlations Across Vortex Boundary for Higher Frequency 50 Hz Temporal Flow

Note: scales distorted

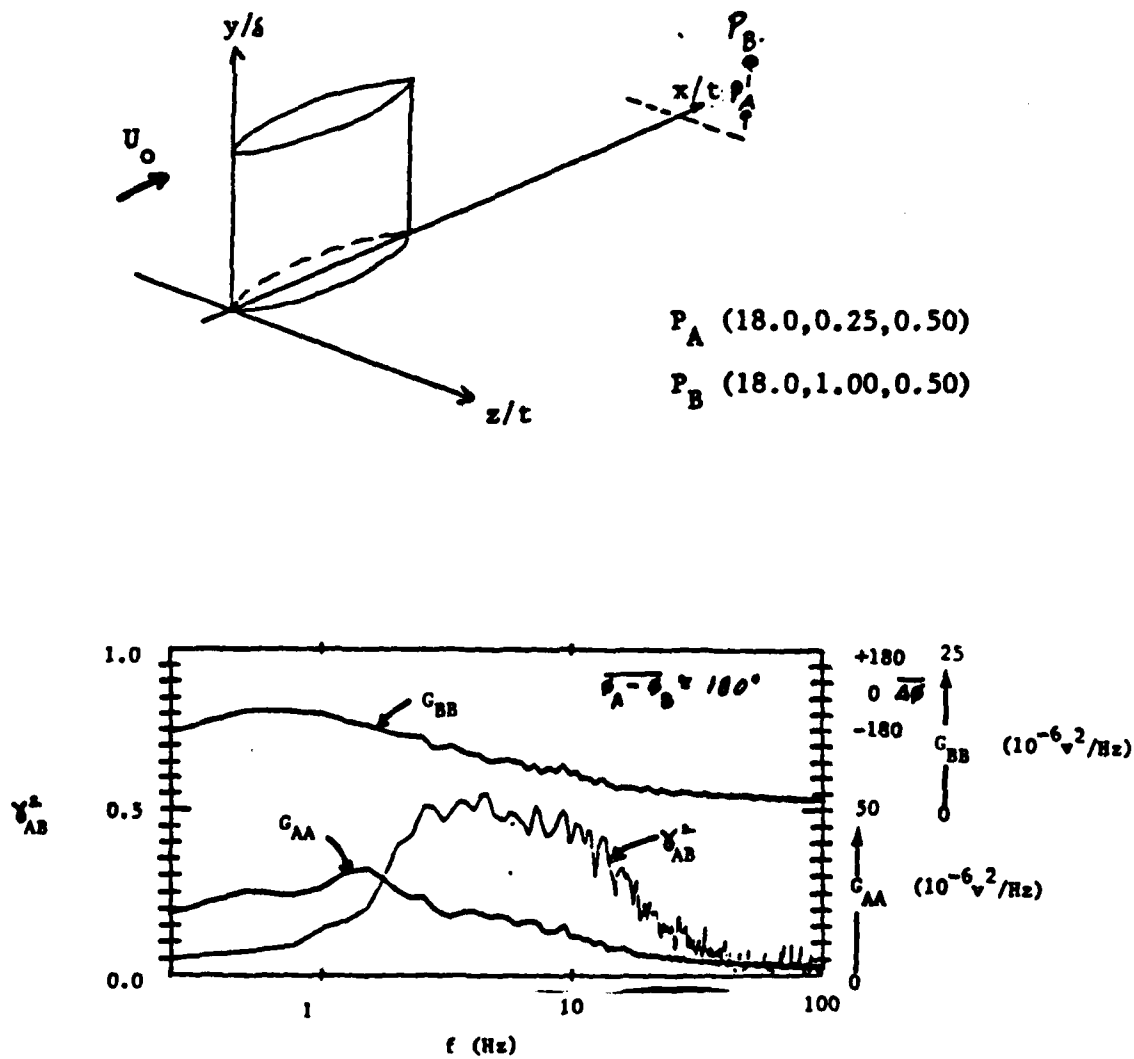


Figure 5-25: Correlations Across Vortex Boundary for Lower Frequency 4 Hz Temporal Flow

The subsequent detailed correlation studies were made with the blunter  $a/b = 1.5$  nose profile, and the frequency bandwidths were observed to be separated.

#### 5.7.6 Significant Conclusions

Several significant conclusions were made from the exploratory results, and they provided the motivation for the detailed study that followed. Those conclusions were:

1. Large scale time dependent flow does exist in the wing-body junction.
2. There are at least two relatively narrow low frequency bandwidth disturbances present, one from the onset boundary layer structure and another produced by the presence of the wing.
3. The flow structure is convected downstream, and appears to grow in spatial extent in the wing wake.
4. Two-point velocity correlation techniques employing the spectrally distributed coherence appear to separate the flow structure from the ambient turbulence even where the structure velocities are on the order of the ambient values.

#### 5.8 Tests to Verify Fluid Dynamic Origin of Temporal Flow

The large scale time dependent flow measured in the wing-body junction was of low level and had subtle characteristics. It was prudent to perform several tests to rule out instrumentation or facility related noise origins for the measured temporal features. The following tests were conducted:

1. Sequential tests with and without the wing present to demonstrate the absolute requirement that the wing be present to establish the flow.
2. Free stream velocity and acoustic pressure correlations with the boundary layer velocities to rule out possibility of external flow driven phenomena.
3. Accelerometer/anemometer output correlations to rule out mechanical vibrations as causes for the flow.
4. Velocity correlations for probes in close proximity

(single point two probe correlations) to rule out the possibility of instrument hook-up error, such as an improperly set inversion (sign) switch.

5. Variations in the velocity to test if the velocity correlations were functions of velocity to demonstrate the fundamental fluid dynamic origin of the time-dependent flow.

The above tests were conducted during the preliminary exploratory measurements of the wing-body flow. Consequently, they were performed at different times and with different experimental set-ups, such as different nose shapes for the wing. However, it is believed that the results in each case are applicable to the experiment in general. None of the tests above produced evidence of non-fluid dynamic sources for the temporal measurements. Example results from the tests are presented below.

The tests consistently showed that the large scale time dependent flow in the wing-body junction is an inherent, naturally occurring feature of the flow. It is not a product of the particular experimental arrangement.

#### 5.8.1 Sequential Measurements With and Without Wing

Sequential velocity correlations were made with and without the wing to show the presence of the large scale time dependent flow only in the presence of the wing. An example of the results is shown in Figure 5-26, which compares correlation data on two sides of the wing at midchord with data at the same measurement positions but with the wing removed. Clearly the relative phase between the correlated velocity measurements is 180 degrees with the wing present. With the wing removed the data are uncorrelated. This test showed that the wing produces the large scale time-dependent flow. It does not, however, discern if the wing mechanically amplifies flow structure inherent to the boundary layer, or if it "creates" the flow.

#### 5.8.2 Acoustic Pressure and Free Stream Velocity Fluctuations

Acoustic pressure and flow velocity measurements in the free stream flow were correlated with hot wire anemometer outputs

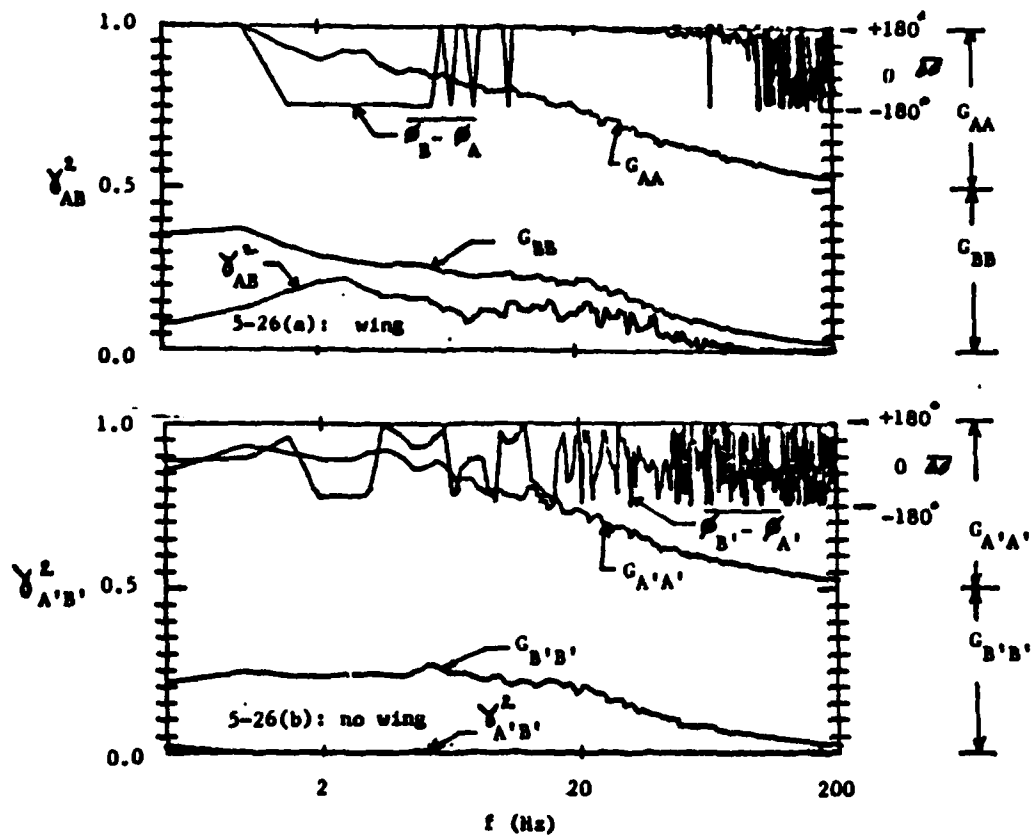
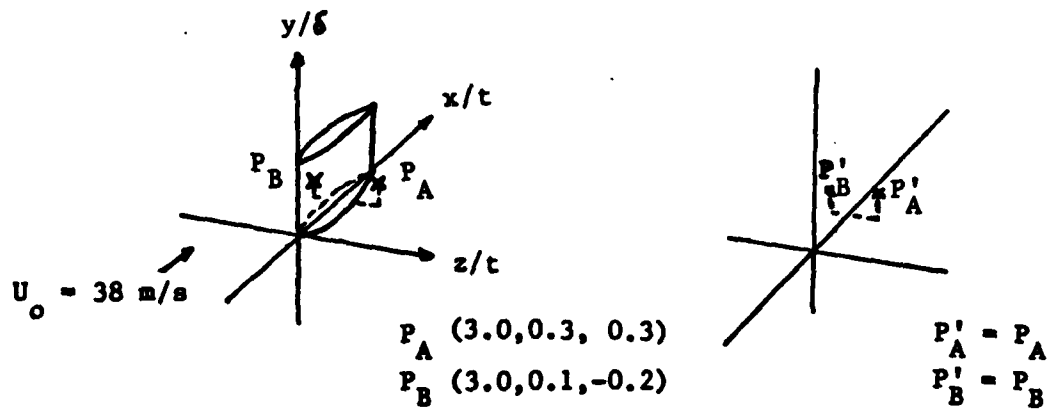


Figure 5-26: Comparison of Velocity Correlations With and Without the Wing Present

from the undisturbed boundary layer. The correlations were zero, indicating that the external flow was not temporally forcing the boundary layer.

An example of the measured acoustic correlations is shown in Figure 5-27. The data were obtained with no wing present. There is no correlation between the boundary layer velocity fluctuations and the acoustic pressure. Two of the peaks in the acoustic pressure spectrum shown in the figure are identified with the rotation of the downstream propeller of the wind tunnel. The data were obtained with a nominal propeller rotation speed equal to 25 rps; the propeller had four blades. The shaft frequency of 25 Hz and the propeller blade frequency of 100 Hz are both clearly seen as peaks in the pressure spectrum. Neither of those peaks is measured as driving the boundary layer velocity fluctuations. The tests, therefore, showed that the acoustic pressure in the free stream was not the source for any velocity fluctuations in the boundary layer, and it is reasoned that it is not the source for the wing-body junction time dependent flow.

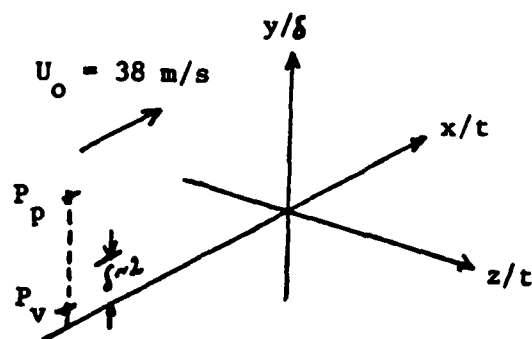
Additional measurements showed that the time dependent flow is not correlated with the very small essentially unmeasurable free stream velocity spectrum.

It is concluded that the time dependent flow in the wing-body junction is created by the interaction between the wing and the upstream boundary layer and not by free stream velocity or acoustic pressure fluctuations.

### 5.8.3 Mechanical Vibration Tests

Mechanical vibration tests were performed by correlating accelerometer output with the hot wire anemometer output. The accelerometer was placed at many locations throughout the experimental set-up. In no case was there a correlation between the accelerometer and the anemometer outputs. An example measurement is shown in Figure 5-28. The accelerometer output shows sharp spectral peaks at 49 Hz and at 101 Hz, with the accelerometer placed to be sensitive to wing "flapping." For the preliminary two point velocity correlation measurements one of the frequency bands





acoustic pressure at  $P_p (-20, 3, 0)$   
 velocity at  $P_v (-20, 0.3, 0)$

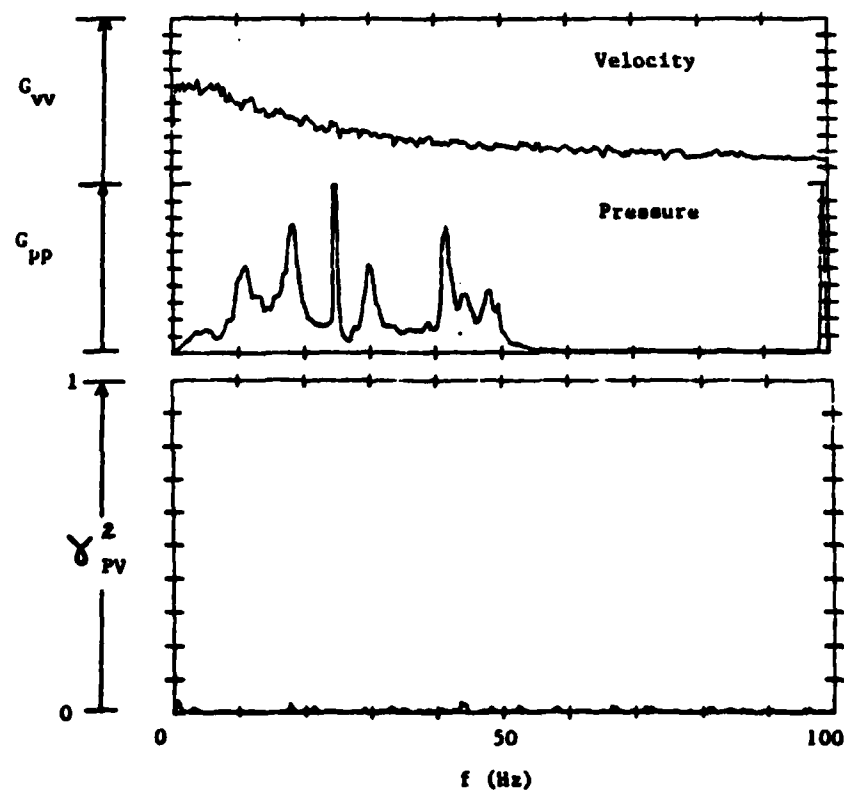


Figure 5-27: Example Acoustic Pressure-Boundary Layer Velocity Correlations

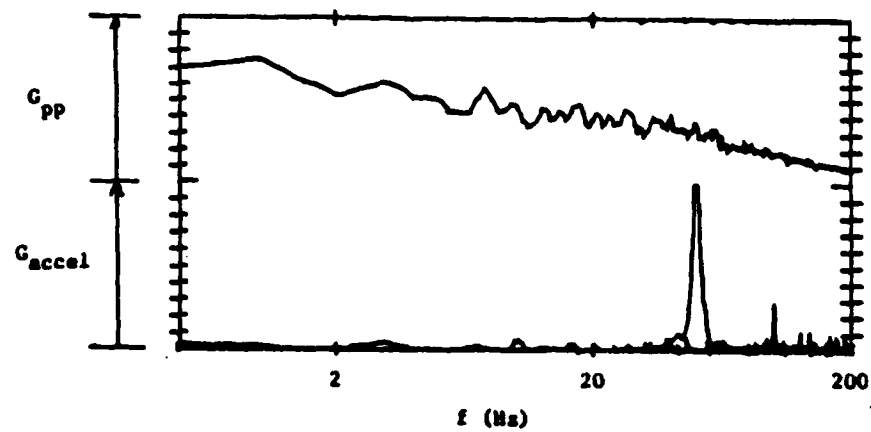
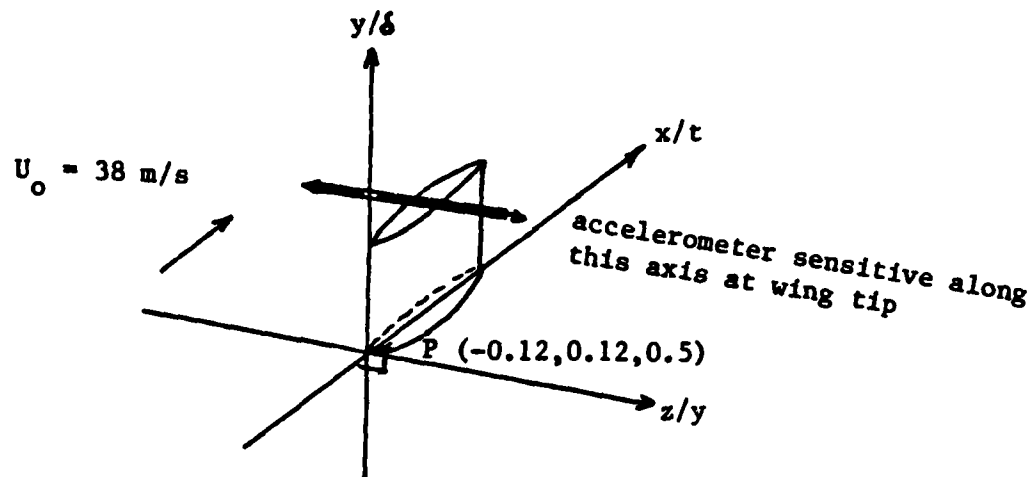


Figure 5-28: Example Mechanical Vibration Test Results for Correlations of Structural Acceleration With Flow Velocity in Wing-Body Junction

produced by the presence of the wing (20-100 Hz) did have a maximum coherence at approximately 50 Hz. However, the spatial region in which this frequency band was evident was very small which indicated that it was not produced solely by wing oscillations. For the detailed measurements, neither natural frequency was in the range of the measured time dependent flow frequencies produced by the presence of the wing. It is concluded that the large scale time dependent flow is not produced by mechanical oscillation of the test arrangement apparatus.

#### 5.8.4 Single-Point Two Probe Correlations

Several times throughout the course of the investigation the two hot wire probes used for the velocity correlations were placed next to each other to verify that the outputs were nearly identical, correlated, and in-phase. This test showed that the subtle features observed for the large scale time dependent flow, such as the out-of-phase phenomenon, were not products of error instrumentation hook-ups. Figure 5-29 is an example comparison for two probes first placed on opposite sides of then wing placed in close proximity. The spectra are in-phase for the latter case although out-of-phase for the former case. The fall-off of the coherence for the larger frequencies with the probes in close proximity is expected as the wavelengths become less than the separation distance between the probes.

#### 5.8.5 Effects of Varying Velocity

If the flow fluctuations were fluid dynamic in origin then they should have been functions of the free stream velocity. A simple test was made by observing the peak frequency for the coherence as a function of speed. An example of the results is shown in Figure 5-30 for a selected wing. In this particular case there were two peaks in the coherence. As shown in the figure, both peak frequencies are nearly proportional to the free stream velocity.

### 5.9 Identification and Isolation of Trailing Edge Shedding Frequencies

Measurements were made at the trailing edge of the wing to

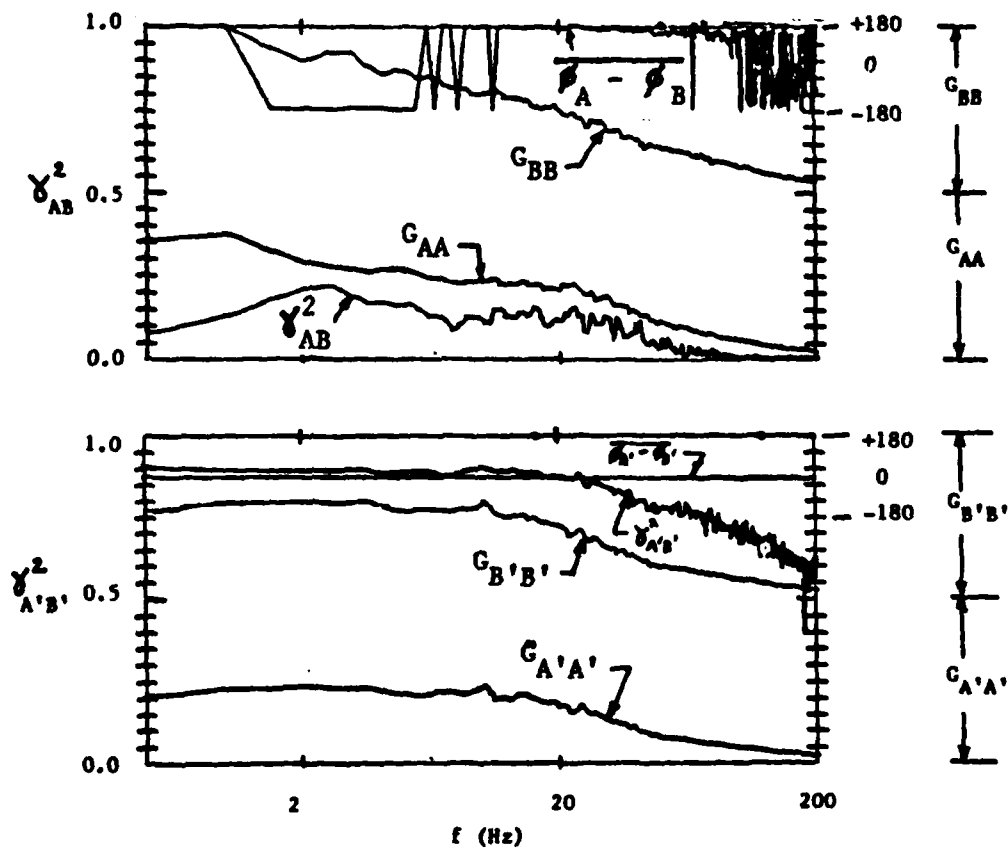
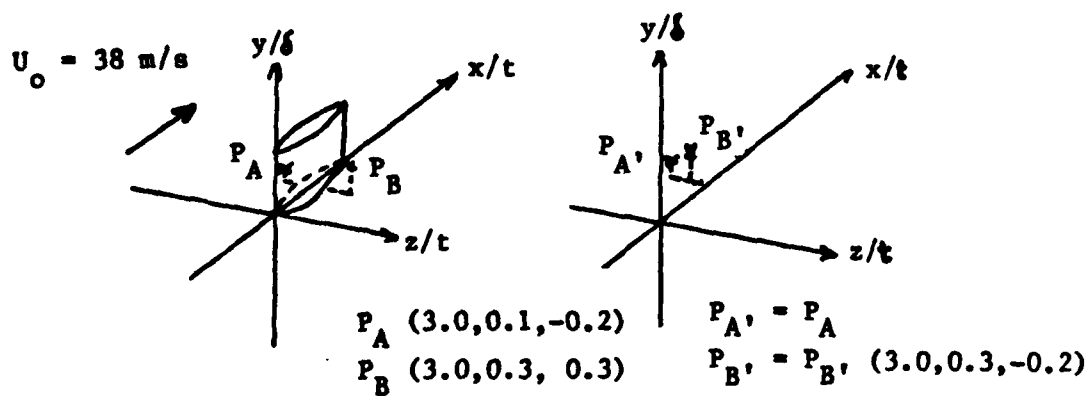


Figure 5-29: Example Test Results Showing Nearly Identical Output When Probes Placed in Close Proximity

Note: scales distorted

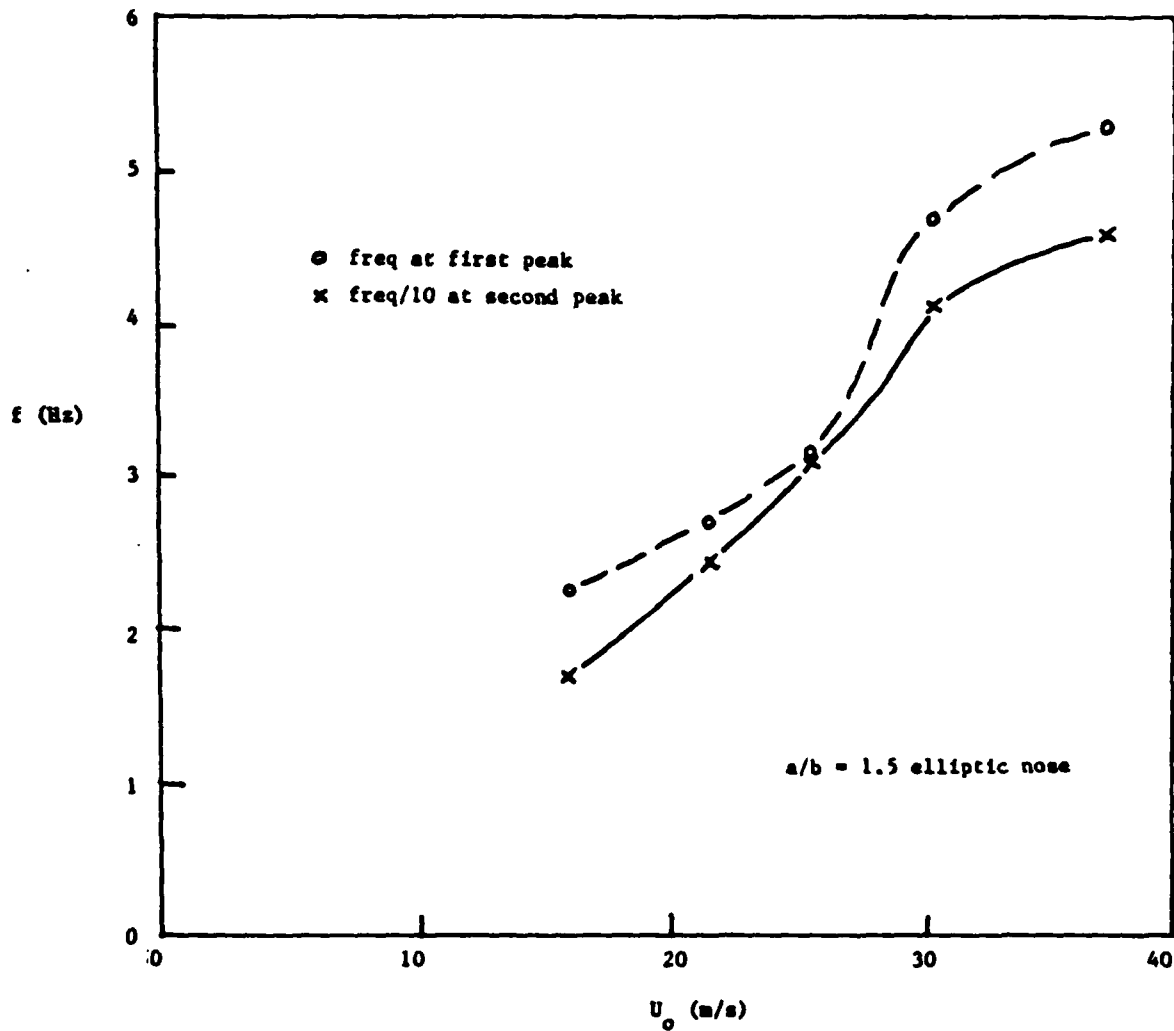
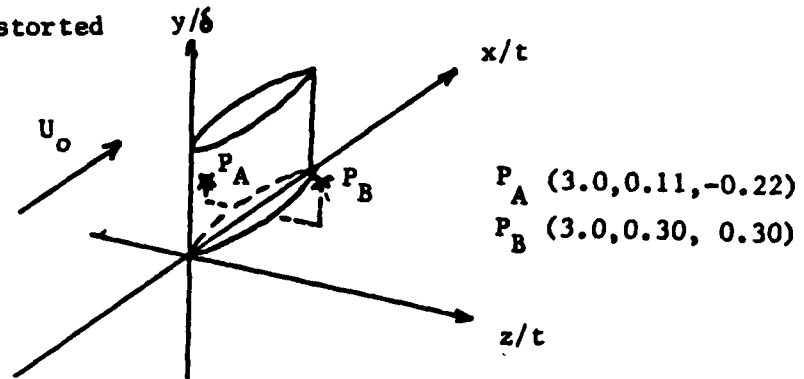


Figure 5-30: Measurements of the Peak Coherence Frequency as a Function of Velocity

identify the shedding frequency. The measured frequencies outside the boundary layer were much larger than those for the large-scale structure investigated inside the boundary layer. The frequencies increased with increasing distance from the wall as would be expected for constant Strouhal number  $fr/U$  as the velocity increases, where  $r$  is the effective radius of curvature. However, the frequency, or at least the shedding phenomena, is absent from the inner half of the boundary layer. Figure 5-31 shows an example set of measurements obtained at the wing trailing edge for the  $a/b = 6$  nose profile. As the distance from the wall increased the large shedding frequency first becomes noticeable for  $y/\delta = 0.5$ . Outside the boundary layer the prominent shedding frequency is 400 Hz. Figure 5-32 shows similar results for the  $a/b = 1.5$  nose profile.

It is concluded that the measurements have isolated the shedding frequency, and that it is not the cause for the low frequency flow in the wing-body junction.

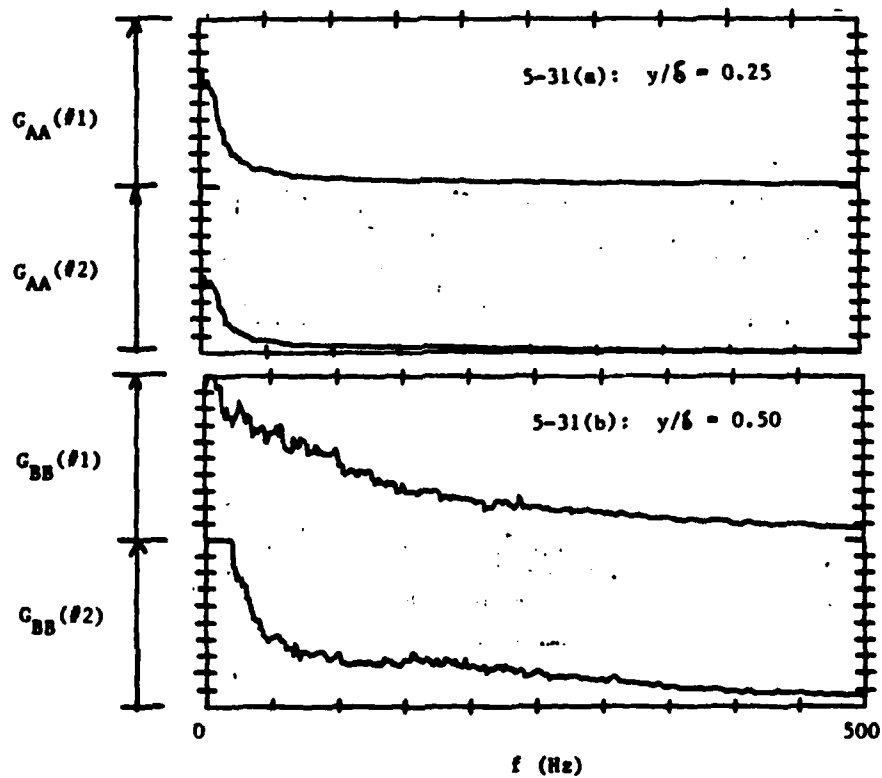
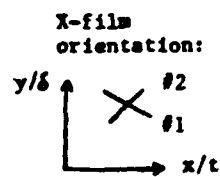
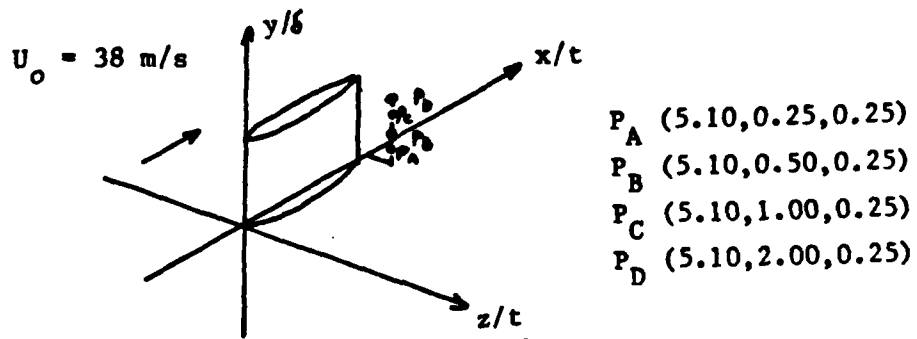
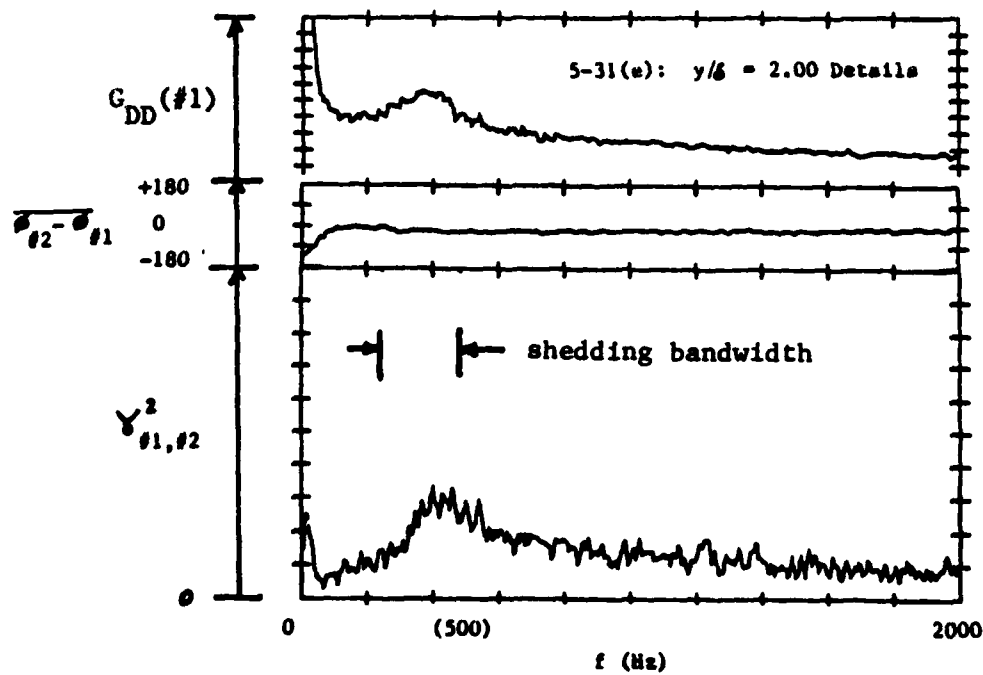
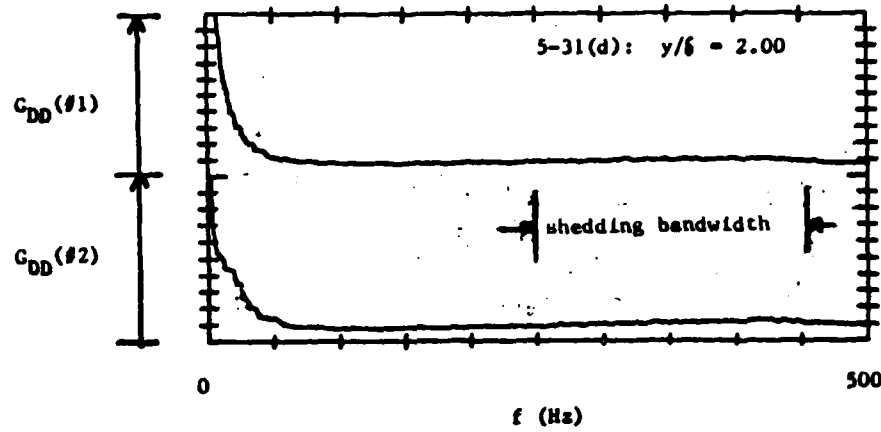
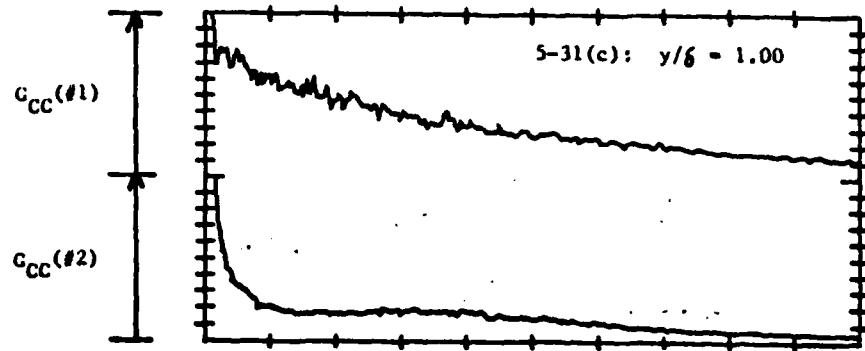


Figure 5-31: Data Showing Shedding Frequency at Trailing Edge of  $a/b = 6.0$  Elliptic Nose Wing





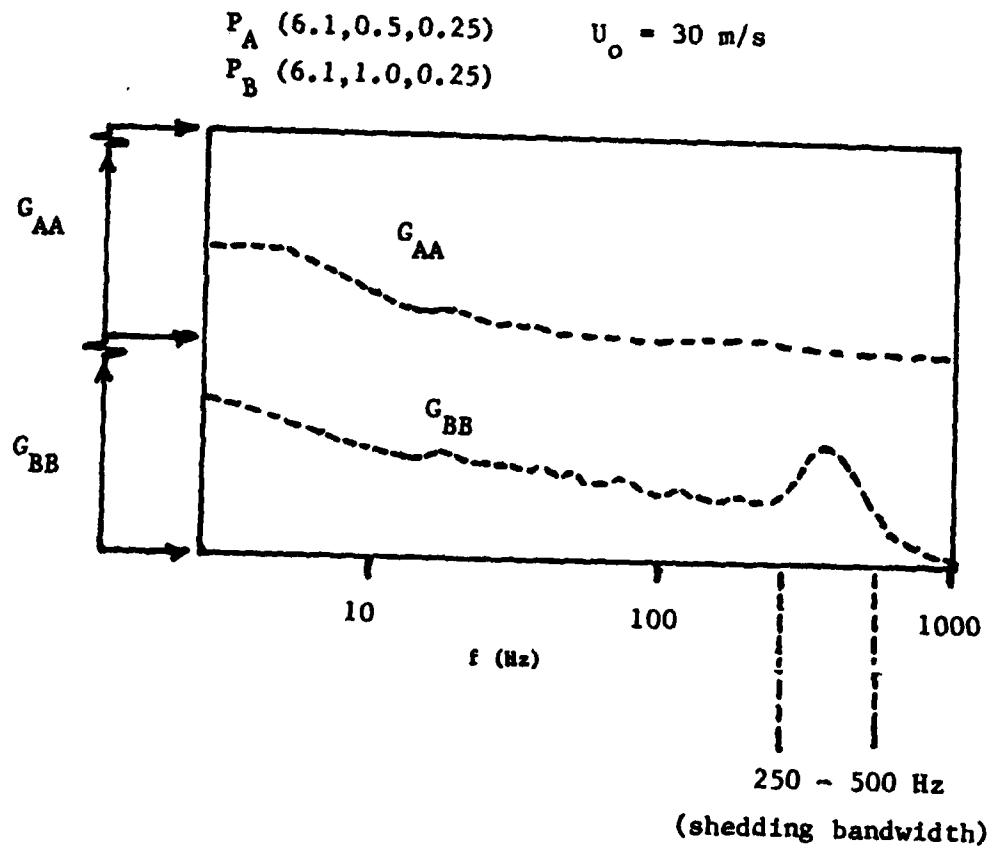


Figure 5-32: Data Showing Shedding Frequency at Trailing Edge of  $a/b = 1.5$  Elliptic Nose Wing

## CHAPTER 6

### LARGE SCALE TEMPORAL FLOW MEASUREMENT RESULTS ( $a/b = 1.5$ ELLIPTIC NOSE)

#### 6.1 Method for Presentation

##### 6.1.1 Correlation Contours

A method was needed to present the data in a way that the temporal flow structure over a substantial portion of the flow could be depicted in a single graphical display. The method that evolved produces correlation contours in the  $(y/t, z/t)$  plane normal to the free stream flow direction. The contours are of the contrived quantity  $S\gamma$ , which is similar to the linear correlation coefficient.  $S\gamma$  numerically describes the correlations between the velocity at a fixed probe  $P_A$  and the velocity at a traversing probe  $P_B$ . The quantity  $S\gamma$  is defined to be the square root of the nominal peak value of the coherence multiplied by the cosine of the relative phase between the velocities at the two probe positions;  $S\gamma \equiv \cos(\overline{\phi_B - \phi_A}) \sqrt{\gamma_{AB}^2}$ . For the low frequency motions investigated in this experiment,  $\cos(\overline{\phi_B - \phi_A})$  is approximately +1 or -1 for probes at the same longitudinal position in the flow.

Therefore  $S_\gamma \approx \pm \gamma_{AB}$  where the sign is determined by the relative phase of the velocities; in-phase implies +1, and out-of-phase implies -1.

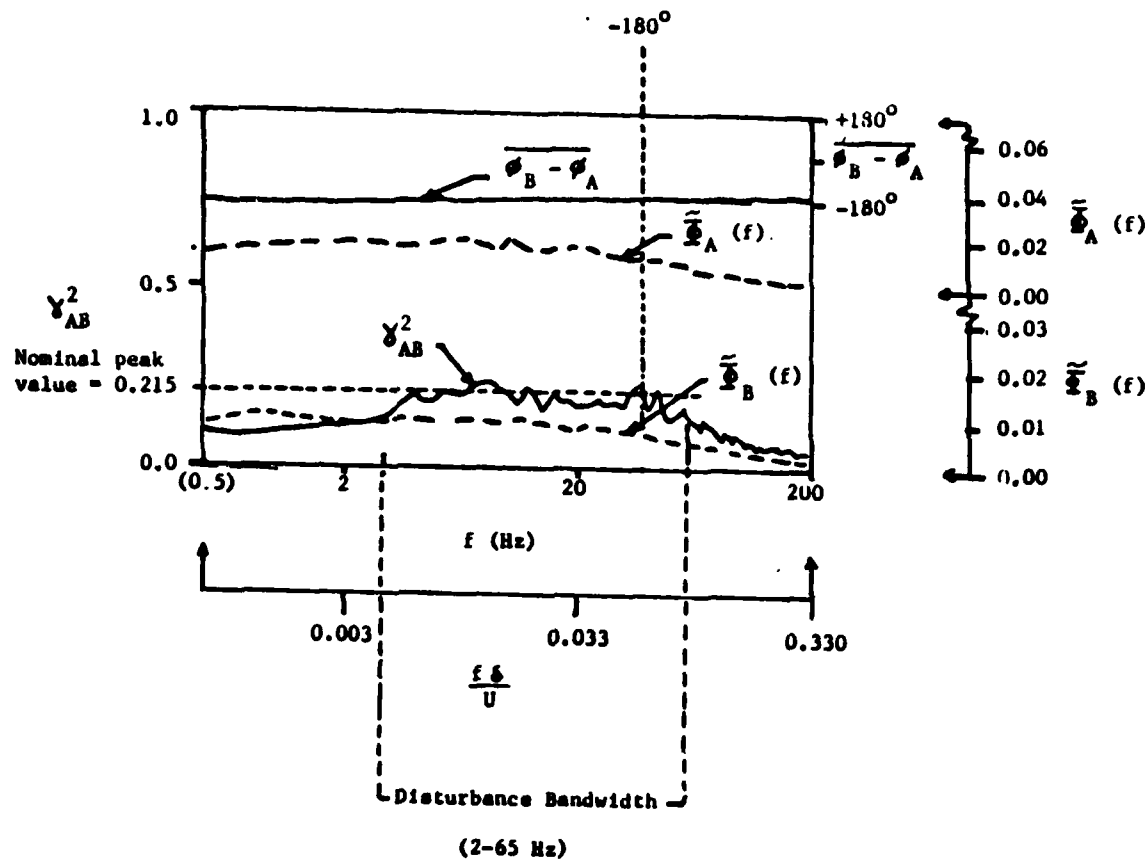
The justification for equating  $\gamma_{AB}$  to the linear correlation coefficient was described in Section 5-4. In that section  $\gamma_{AB}^2$  was described as the square of the linear correlation coefficient for each frequency.

The magnitude of the contour value for  $\gamma_{AB}^2$  was obtained in the following manner for each pair of correlation measurement positions,  $P_A (x_0/t, y_0/t, z_0/t)$  (fixed position) and  $P_B (x_0/t, y/t, z/t)$  (variable position). The nominal peak value of the coherence was observed to occur within a band of frequencies characterizing the disturbance, as shown in Figure 6-1. The fluctuations of the coherence with frequency about the nominal peak value were taken as manifestations of the statistical uncertainty in the measurement of the signal. Therefore, a line was drawn through the nominal mean value for the coherence, and projected to obtain the value  $\gamma_{AB}^2$  for calculation of  $S_\gamma$ . The sign for  $S_\gamma$  was obtained directly from the phase relationship at the nominal peak value of the coherence. This procedure is illustrated in Figure 6-1.

The band of frequencies for the non-zero coherence was not identical for all the measurements. In general there were three frequency bands, and a notation as to which bandwidth  $S_\gamma$  applies is made for each presentation of results. The three frequency bandwidths, and the flow regions in which they appear to originate are as follows:

- Bandwidth I: 2-65 Hz; onset boundary layer (characteristic center frequency  $f_o$ )
- Bandwidth II: 25-80 Hz; wing-body junction flow (characteristic center frequency  $f_b$ )
- Bandwidth III: 0.5-10 Hz; wing-body junction wake flow (characteristic center frequency  $f_{wb}$ )

Although the numerical values of the frequency bandwidths overlap, they usually do not all appear simultaneously in the measurements and are distinguishable in the data.



EXAMPLE:

$$\begin{aligned}
 S_Y &= \cos(\phi_B - \phi_A) \sqrt{Y_{AB}^2} \\
 &= (-1.0) (0.215)^{1/2} \\
 &= -0.47
 \end{aligned}$$

Figure 6-1: Example Calculation of  $S_Y$  from Measurement Data

The contours for  $S_y$  were obtained by plotting the measured data at the  $y/t$  and  $z/t$  positions of the traversing probe,  $P_B$  ( $x_0/t$ ,  $y/t$ ,  $z/t$ ).

Caution should be exercised when interpreting the contours of  $S_y$ : they apply specifically to correlations relative to velocities at the fixed probe position,  $P_A$  ( $x_0/t$ ,  $y_0/t$ ,  $z_0/t$ ), and are not necessarily appropriate for other positions. Specifically, correlations between velocities at two arbitrary positions of the traversed probe cannot be deduced from correlations at each of those positions relative to the fixed probe. This will be discussed in detail in Chapter 7.

### 6.1.2 Scaling Quantities

This section describes the reasoning behind a rational choice for scaling parameters. The dimensionless frequency is defined as  $f\delta/U_0$  where  $\delta$  is the onset boundary layer thickness and  $U_0$  is the free stream velocity; and the dimensionless velocity fluctuation is  $u'/U_0$ . Correspondingly, the power spectra density  $\phi(f) = u'^2(f)/\Delta f$  of the velocity fluctuations  $u'$  is made dimensionless by forming

$$\frac{\phi(f)}{\delta U_0} = \frac{\overline{u'^2(f)}}{\Delta f \delta U_0} \equiv \tilde{\phi}(f). \text{ It is reasonable to}$$

expect that the frequency band of the large scale temporal flow in the wake region is physically governed by the non-dimensional set of numbers:

$$\frac{\delta f_{wb}}{U_0} = (\delta/t, a/b, c/t, \alpha, \beta, C_f, R_\delta, f_0\delta/U_0, l_z/\delta)$$

where  $c$  = wing chord length

$\alpha$  = wing incidence angle

$\beta$  = included angle of circular arc tail

$R_\delta$  = boundary layer thickness Reynolds number

$l_z$  = lateral extent of flow structure in onset boundary layer

The independent variables from the onset boundary layer are  $C_f$ ,  $R_\delta$ ,  $f_0\delta/U_0$ , and  $l_z/\delta$ . Because test data were obtained for a fixed tunnel geometry and free stream velocity (30.5 m/s) those independent variables were fixed as follows:

$$C_f = 0.00225 (= d\theta/dx)$$

$$R_\delta = 10^4 \quad (R_\theta = 10^5)$$

$$f_o \delta / U_o = 0.05 \text{ (where the center frequency } f_o \text{ was chosen from bandwidth I)}$$

$$l_z / \delta = 1.0 \text{ (where the characteristic length was chosen to be the width of the positive correlation region in the onset boundary layer)}$$

Similarly, the wing geometry independent variables ( $\delta/t$ ,  $a/b$ ,  $c/t$ ,  $\alpha$  and  $\beta$ ) were

$$\delta/t = 1.0 \text{ (onset boundary layer thickness/wing thickness ratio)}$$

$$a/b = 1.5 \text{ (ratio of major/minor axis of semi-elliptical nose)}$$

$$c/t = 5 \text{ and } 19.5 \text{ (chord length/wing thickness ratio)}$$

$$\alpha = 0 \text{ radians (wing angle of incidence)}$$

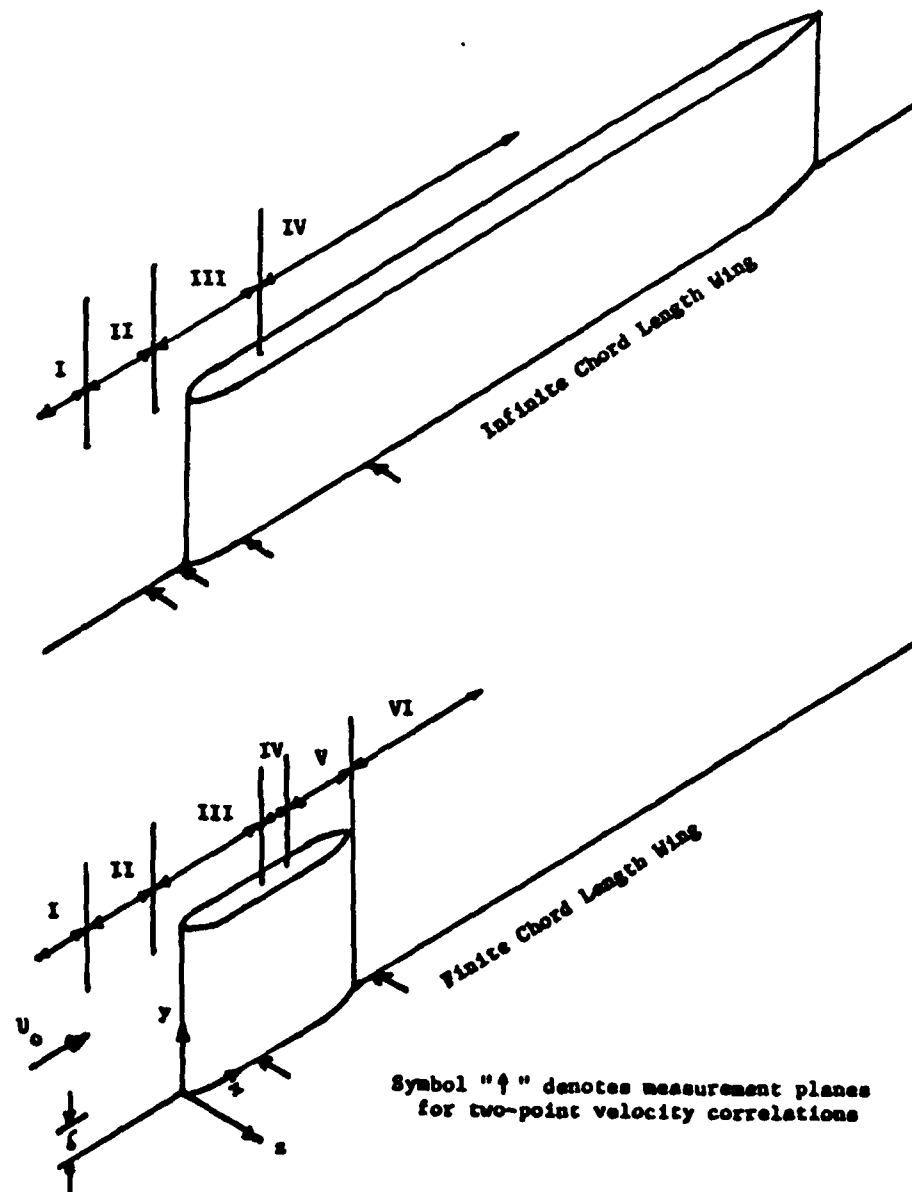
$$\beta = 0.49 \text{ radians (28 deg) (trailing edge angle)}$$

### 6.1.3 The Investigated Flow Regions

The large scale temporal flow structure was investigated in Regions I, II, III, IV, and VI, which were defined in Section 2.2. The investigations were performed with two geometrical chord lengths for the wing, described in Section 3.2 and shown in Figure 6-2. In the first case, the chord length to wing thickness ratio  $c/t$  was 19.5. This configuration was designated the infinite chord length wing, and was used to eliminate trailing edge effects on the flow in the wing-body junction. It was assumed that the relatively large distance between the nose and the tail would allow this assumption. In the second case, the value of  $c/t$  was 5, and the effects of the trailing edge were studied both upstream along the side of the wing and in the downstream wing-body junction wake flow. This configuration is designated the finite chord length wing. The streamwise locations  $x_o$  of the planes ( $y/t$ ,  $z/t$ ) in which the two point velocity correlations were measured for each configuration are identified in Figure 6-2 by the arrow symbols.

### 6.2 Spatial Structure of Onset Boundary Layer (Region I)

Measurements of the two-point velocity correlations for lateral ( $z/t$ ) and transverse ( $y/\delta$ ) separations of the probes were



- |                                      |                                |
|--------------------------------------|--------------------------------|
| Region I - Onset Boundary Layer      |                                |
| II - Pressure Driven Boundary Layer  | } Wing-Body Junction Flow      |
| III - Leading Edge Separation Region |                                |
| IV - Developed Secondary Flow        | } Wing-Body Junction Wake Flow |
| V - Trailing Edge Separation Region  |                                |
| VI - Wake-Boundary Layer Region      |                                |

Figure 6-2: Schematic Showing Locations of Measurement Planes for the Infinite and Finite Chord Length Wings

made with the wing removed to characterize the inherent spatial flow structure of the onset boundary layer (Region I).

The correlations were made with the fixed probe at a transverse location within the onset boundary layer ( $y/\delta = \text{constant}$ ) but at two different locations on the wall. Measurements were made at the two locations in order to show that the results were independent of wall position and therefore representative of classical flat plate data. The results for  $P_A$  (-1.00, 0.22, -0.25) are shown in Figure 6-3, and the results for  $P_A$  (-0.45, 0.22, 0.30) are shown in Figure 6-4. The correlation contours in the two figures are in substantial agreement; most importantly, the widths of the positive and negative correlation regions are similar. The data clearly show a lateral spatial structure in the flow that is consistent with the notion of adjacent regions of flow acceleration and deceleration. For the reasons given in Section 5.6 the region of negative correlation is believed to have been the result of fluid dynamic phenomena, and not of instrumentation limitations or endwall boundaries of the wind tunnel.

An example of the frequency distribution of the velocity power spectra  $\phi_A(f)$  and  $\phi_B(f)$ , the coherence  $\gamma_{AB}^2$ , and relative phase  $\phi_B - \phi_A$  are shown in Figure 6-5 for velocity correlations at  $P_A$  (-1.0, 0.22, -0.25) and  $P_B$  (-1.0, 0.25, +0.25). These positions were negatively correlated with  $\gamma_{AB}^2 > 0.10$  over the coherent frequency range 2-65 Hz. Note that the coherent structure is not immediately evident with a large peak in the power spectra  $\phi_A(f)$  and  $\phi_B(f)$ .

Additional frequency distributions of velocity correlation information are presented in Figure 6-6 where similar information to that described above is shown for  $P_A$  (-0.45, 0.22, 0.30) and  $P_B$  (-0.45, 0.35, 0.80) at two speeds  $U_0 = 30.5$  m/s and  $U_0 = 15.2$  m/s. The noteworthy feature is the shift in the frequency band of the coherent fluctuations to lower values in proportion to the lower velocity; this result indicates a fluid dynamic source for the measured fluctuations.

The effect of the transverse position ( $y/\delta$ ) of the fixed



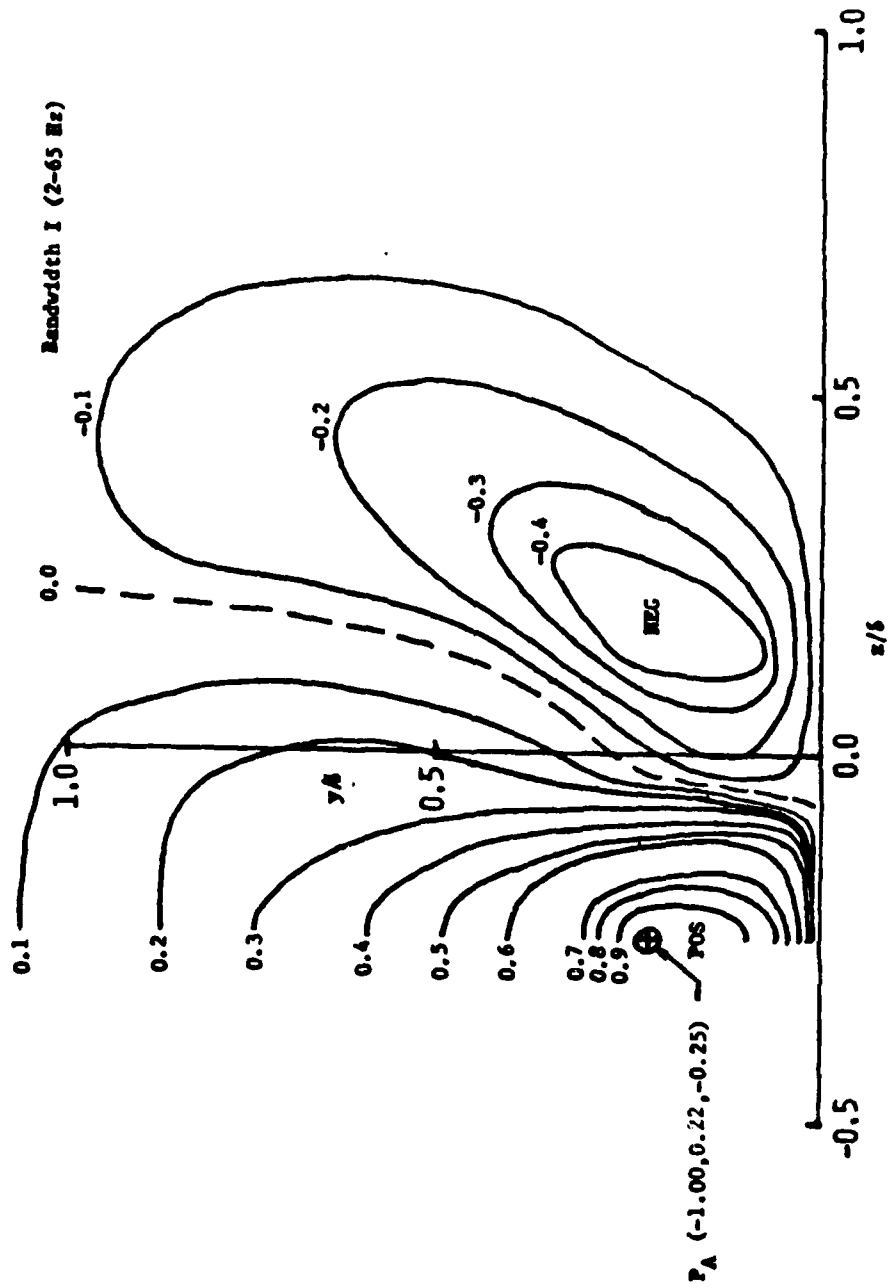


Figure 6-3: Contours of Constant  $S_y$  for the Onset Boundary Layer for the First Wall Location

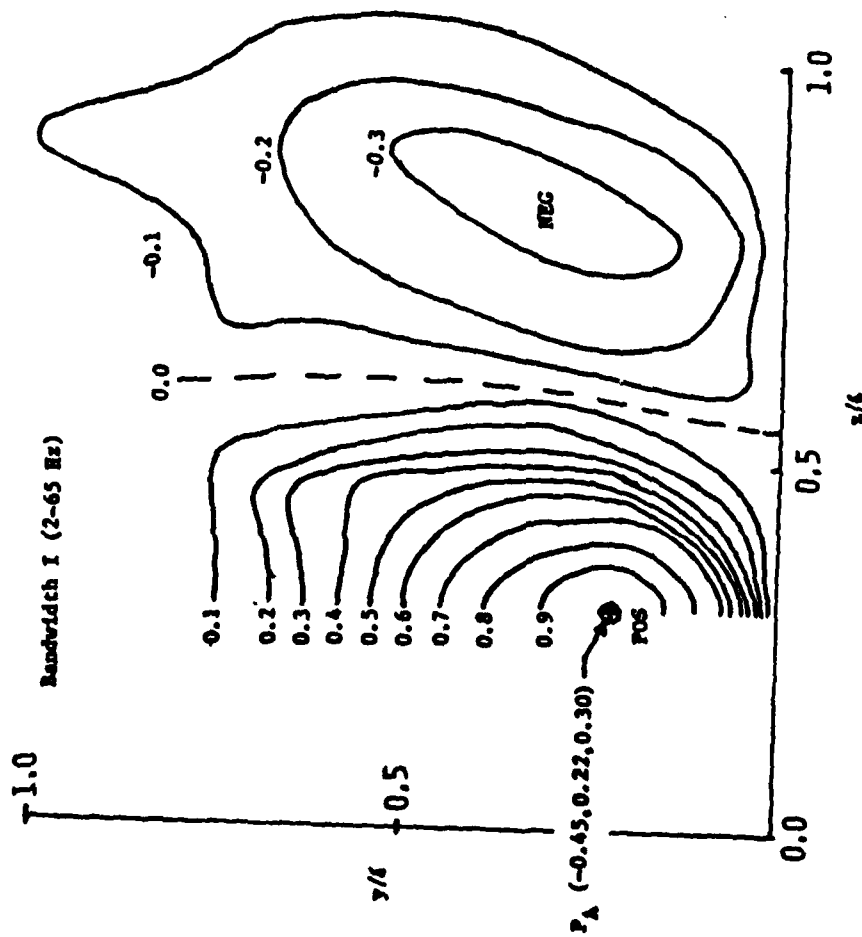
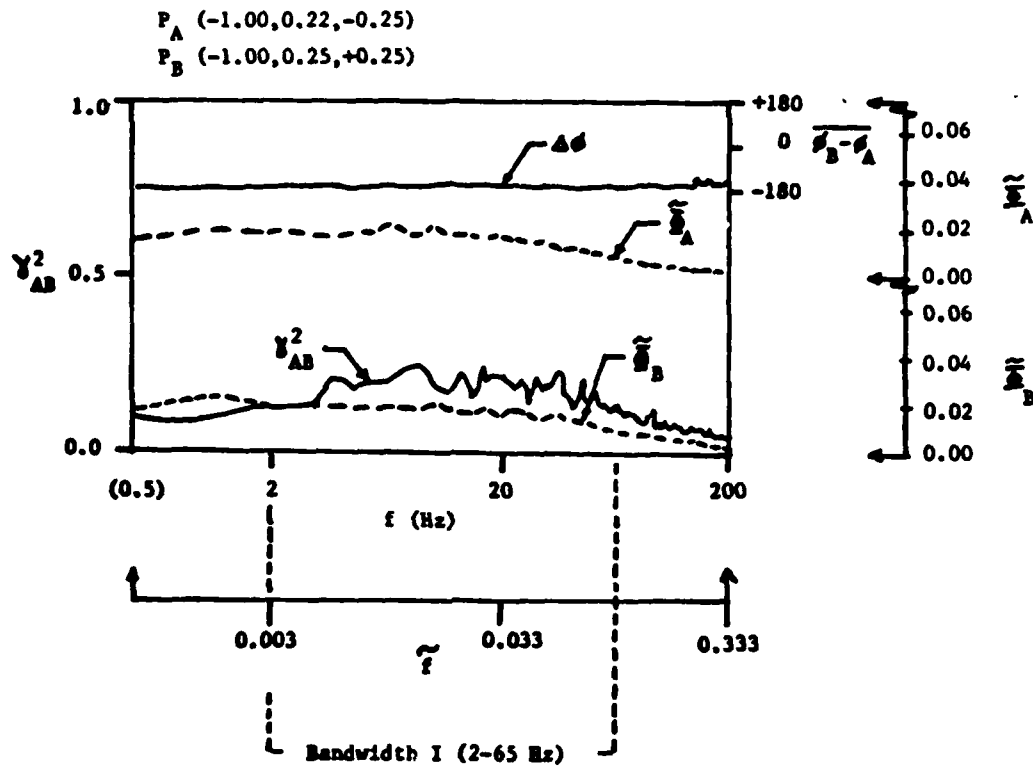
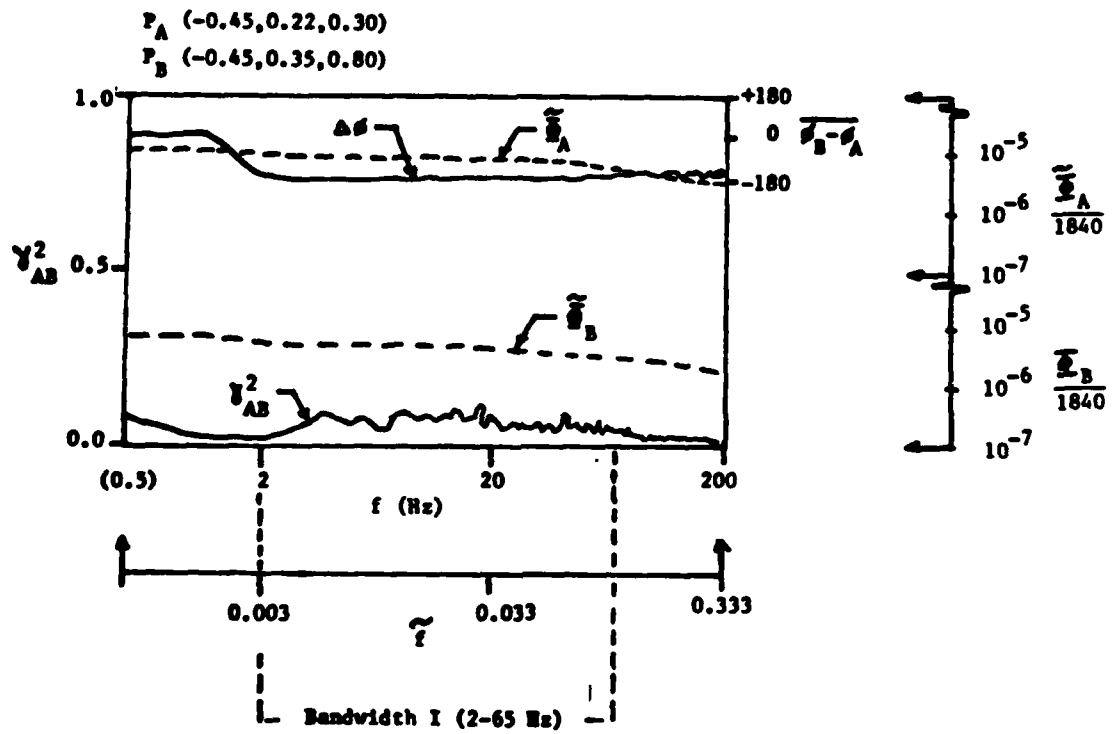


Figure 6-4: Contours of Constant  $S_v$  for the Onset Boundary Layer for the Second Wall Location

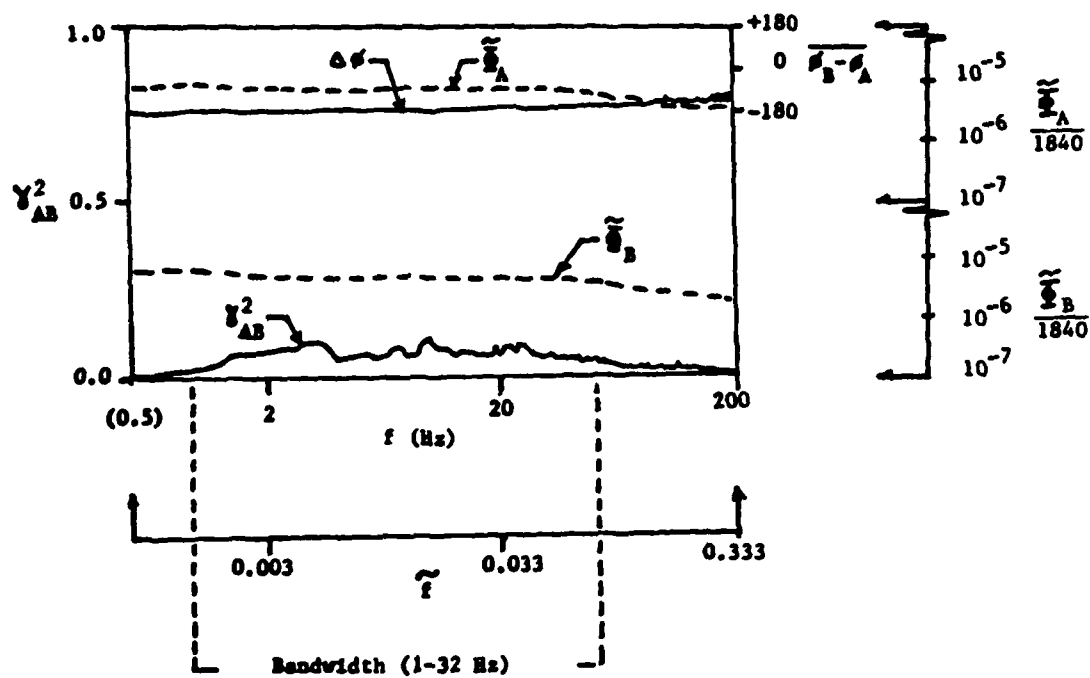


**Figure 6-5: Example Spectral Distribution of Correlation Measurement Data for the Onset Boundary Layer**



6-6(a):  $U_0 = 30.5$  m/s

Figure 6-6: Example Spectral Distribution of Correlation Measurement Data as Functions of Free Stream Speed



6-6(b):  $U_0 = 15.2$  m/s

probe  $P_A$  on the correlation contours is shown in Figures 6-7 and 6-8 with  $P_A$   $(-0.45, \underline{0.40}, 0.30)$  and  $P_A$   $(-0.45, \underline{0.60}, 0.30)$ . These figures, in conjunction with the above presented Figure 6-4 with  $P_A$   $(-0.45, \underline{0.22}, 0.30)$ , show two features. First, the lateral correlations were strongest for position  $P_A$  at  $y/\delta < 0.5$ . And, second, non-zero correlations were obtained outside the boundary layer for positions  $P_A$  at  $y/\delta > 0.5$ . This result most likely reflects the intermittancy of the edge of the boundary layer.

### 6.3 Spatial Structure of Wing-Body Junction Flow

#### 6.3.1 Infinite Chord Length Wing

The spatial structure of the wing-body junction flow was investigated using the infinite chord length wing. Measurements were made in the planes indicated in Figure 6-2 for Regions II, III, and IV.

##### 6.3.1.1 Region II (Pressure Driven Boundary Layer) $(-10 \lesssim x/t \lesssim -0.8)$

Figure 6-9 shows the correlation contours in Region II for the fixed probe at  $P_A$   $(-1.00, 0.25, -0.25)$  and the traversed probe at  $P_B$   $(-1.00, y/\delta, z/t)$ . The measurement plane was immediately upstream from the location of the mean flow leading edge separation. The correlation contours in Figure 6-9 are similar to the correlation contours for the onset boundary layer, Figures 6-3 and 6-4. The noticeable difference is that the regions of positive and negative phase are extended in the lateral dimension because the flow slowed and spread out to pass around the wing. Figure 6-10 shows example spectral distributions of the power spectral densities, the coherence, and the relative phase for the traversed probe at  $P_B$   $(-1.00, 0.25, 0.25)$ . The distributions are similar to those obtained for the onset boundary layer shown in Figure 6-5.

##### 6.3.1.2 Region III (Leading Edge Separation Region) $(-0.8 \lesssim x/t \lesssim 4)$

Figure 6-11 presents the correlation contours in Region III with the fixed probe at  $P_A$   $(-0.12, 0.25, -0.50)$ . This position was immediately downstream from the leading edge mean flow separation but upstream from the wing leading edge. The positive and nega-

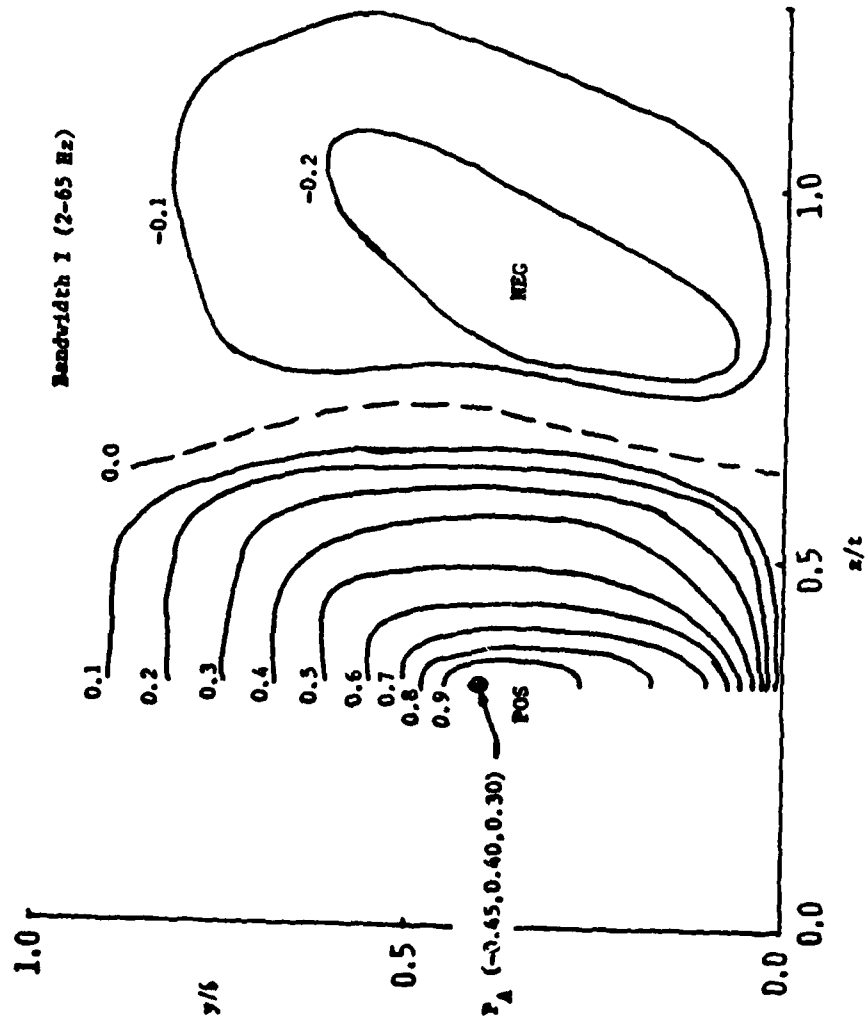


Figure 6-7: Contours of Constant  $S_y$  for the Fixed Probe at  $y_0/b = 0.40$

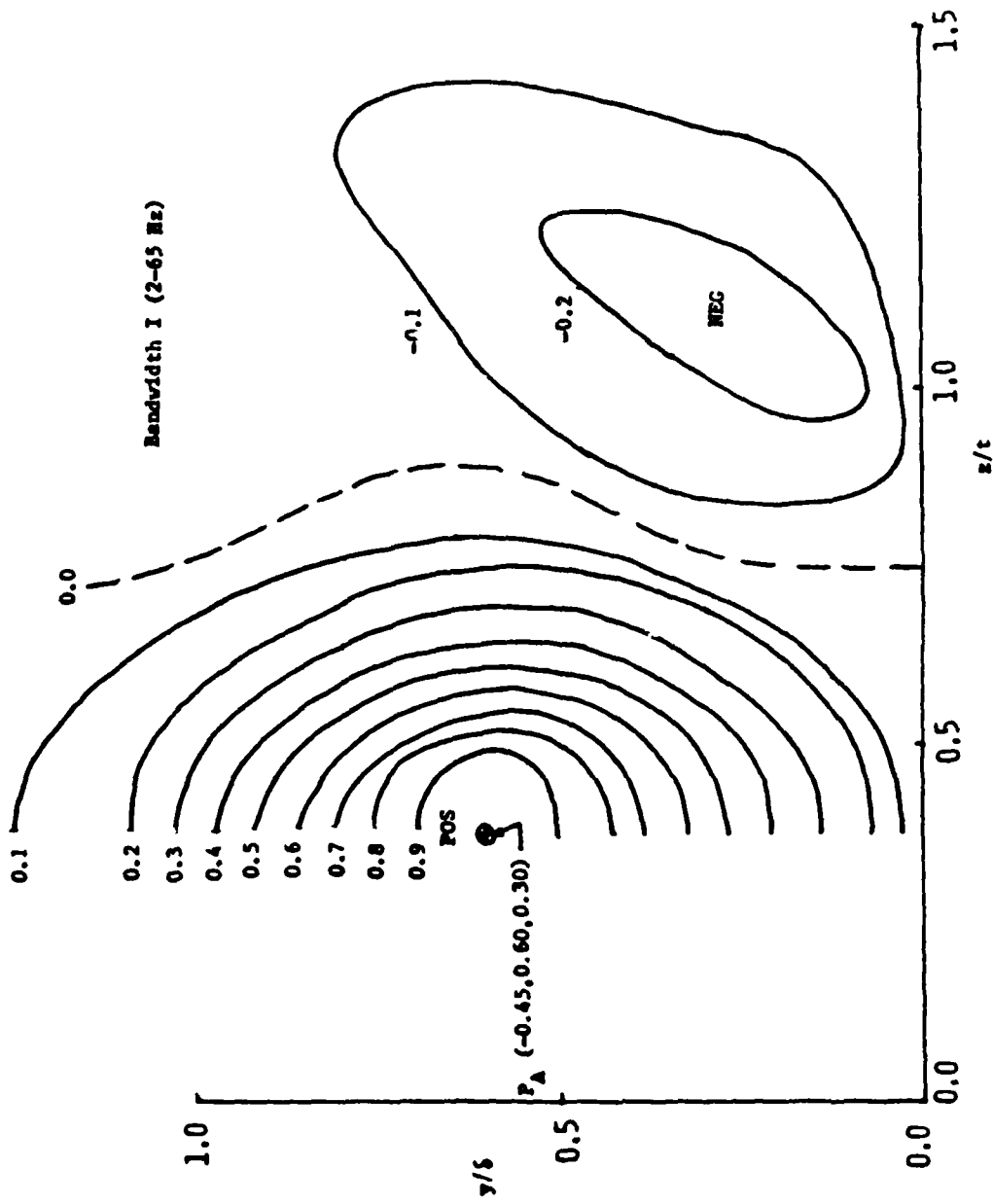


Figure 6-8: Contours of Constant  $S_y$  for the Fixed Probe at  $y_0/s = 0.60$



AD-A139 836

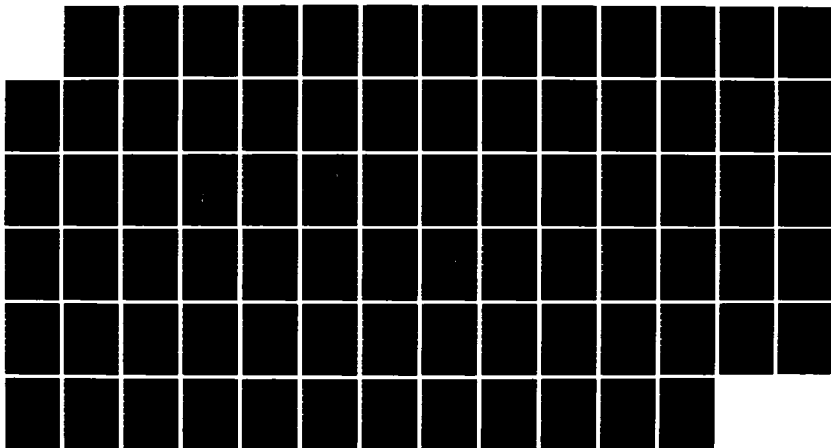
EXPERIMENTAL INVESTIGATION OF THE TURBULENT LARGE SCALE  
TEMPORAL FLOW IN T. (U) CATHOLIC UNIV OF AMERICA 3/3  
WASHINGTON DC SCHOOL OF ENGINEERING A. E P ROOD

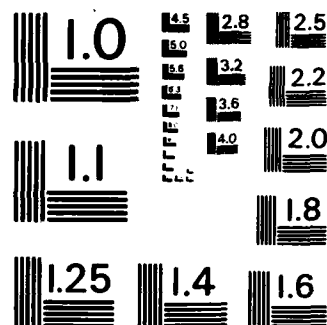
UNCLASSIFIED

MAR 84 DTNSRDC-HA84-1

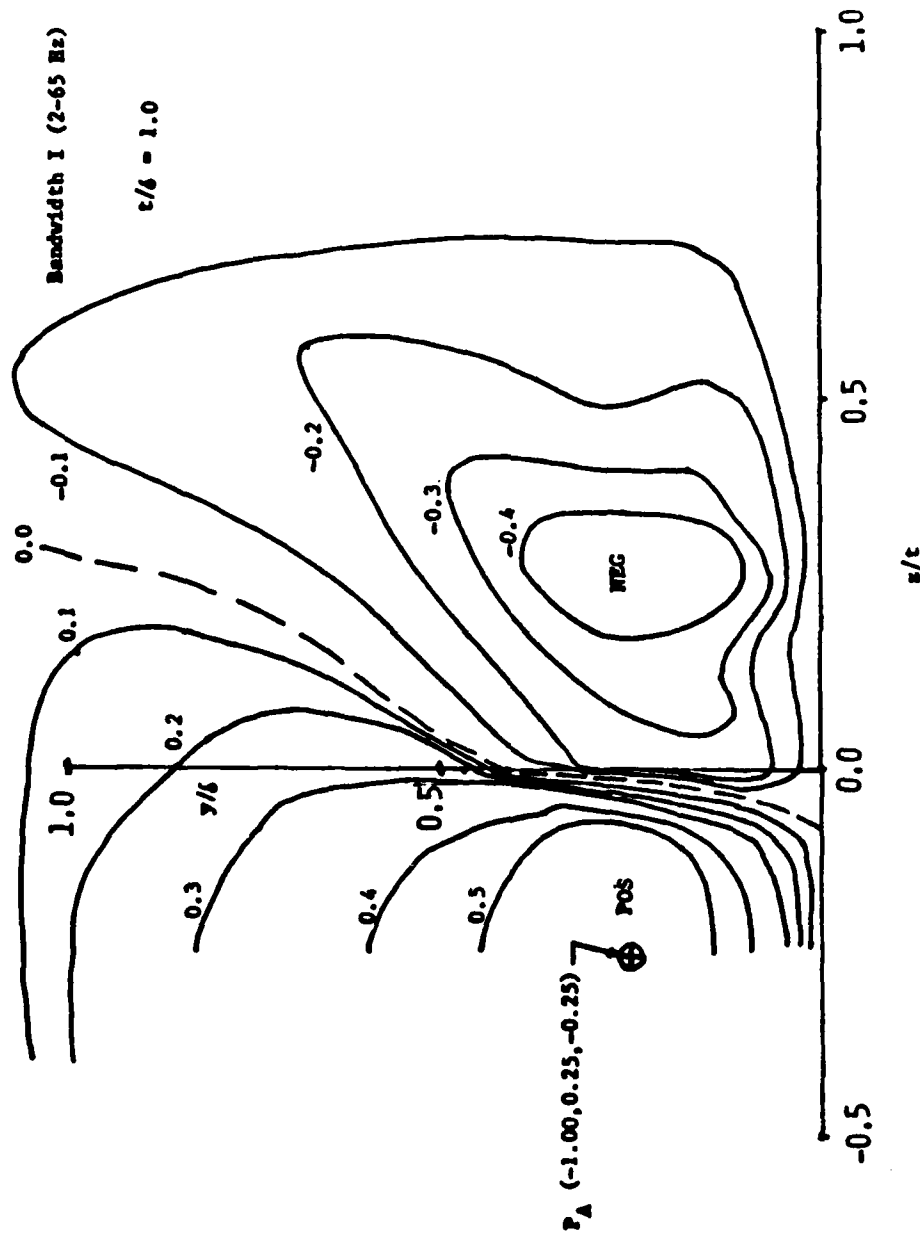
F/G 20/4

NL





MICROCOPY RESOLUTION TEST CHART  
NATIONAL BUREAU OF STANDARDS-1963-A

Figure 6-9: Contours of Constant  $S_y$  in Region II

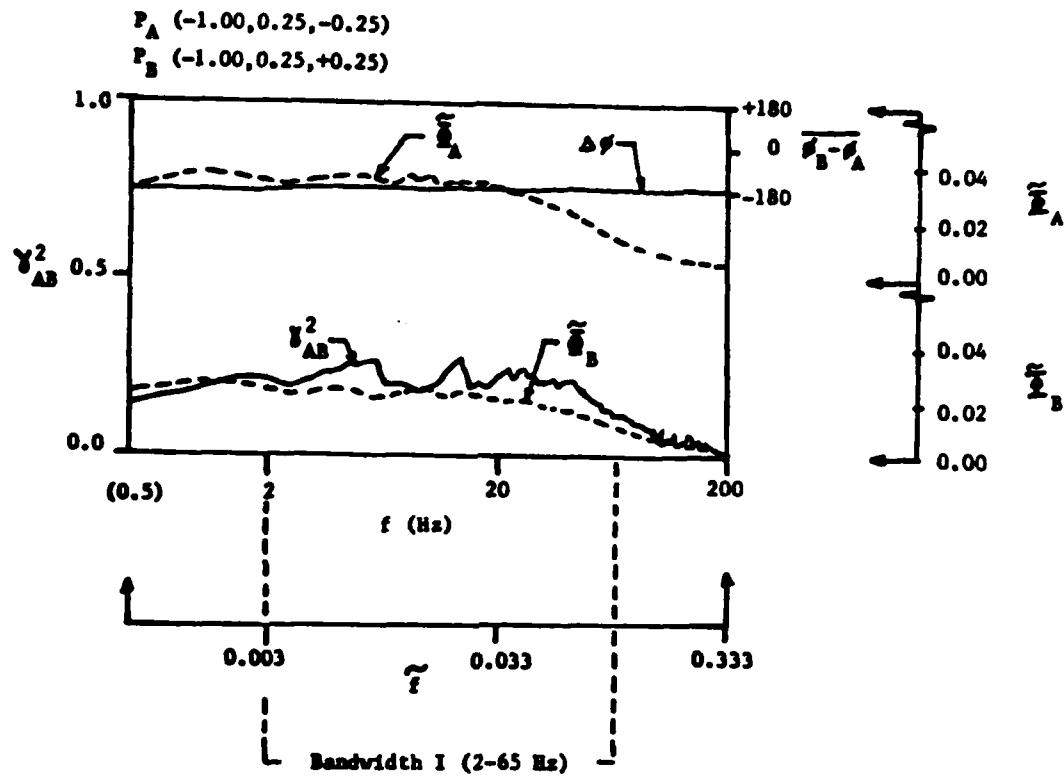


Figure 6-10: Example Spectral Distributions of Correlation Measurement Data for Region II

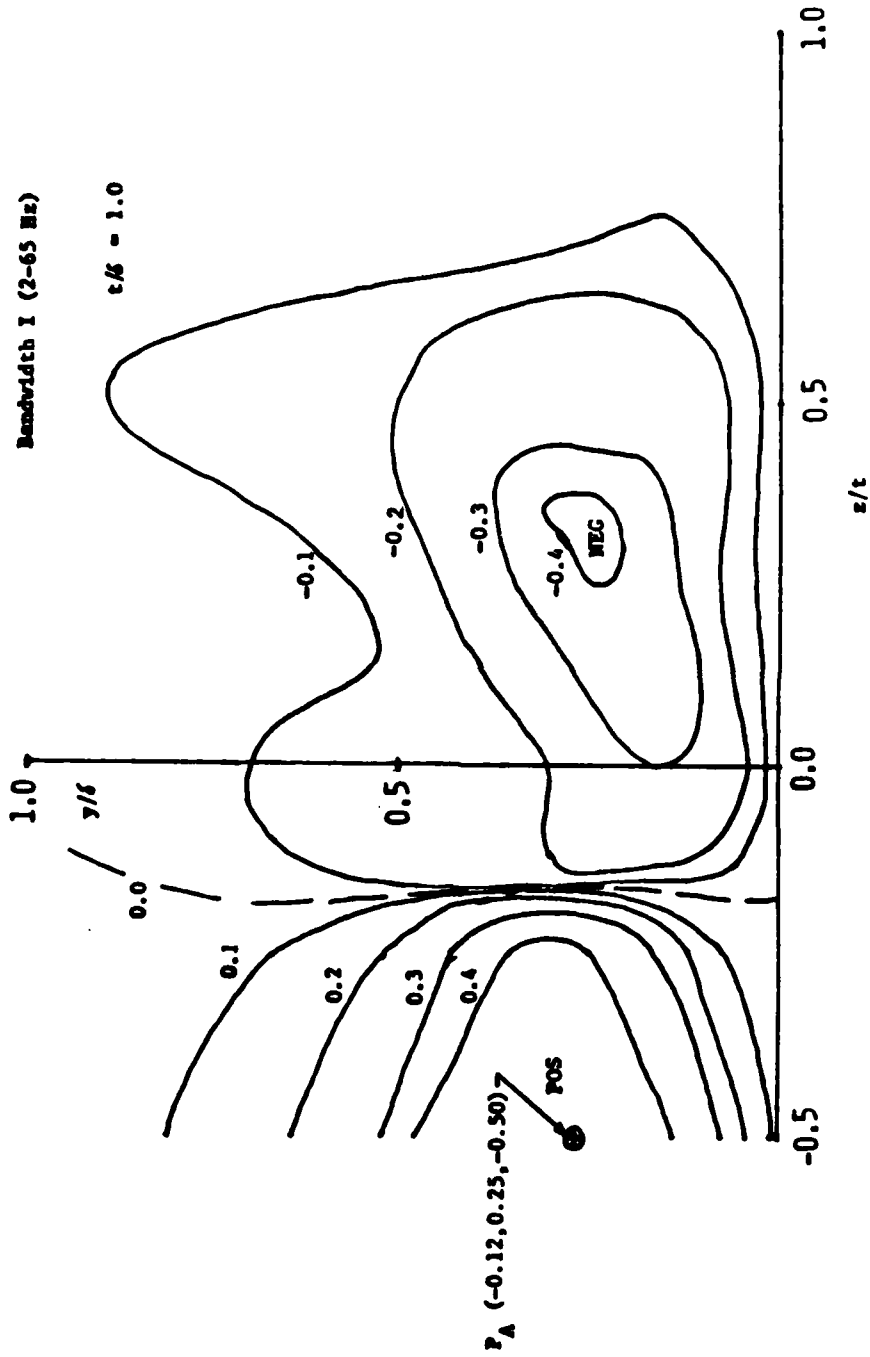


Figure 6-11: Contours of Constant  $S_y$  in Region III Upstream from the Wing Leading Edge

tive correlation regions were extended even further in the lateral direction than they were in Region II. The extension is about 50 percent of the lateral distance for the onset boundary layer in Region I (Figures 6-3 and 6-4). By comparing Figures 6-9 and 6-11 it is seen that there was no abrupt distortion of the correlation contours as the flow passed through the leading edge separation where the horseshoe vortex was formed. It is tentatively concluded that the horseshoe vortex introduced no new frequencies or magnified amplitudes at its origin in the flow separation immediately upstream from the wing leading edge.

Although the leading edge separation did not immediately produce gross distortion of the correlation contours, the coexisting horseshoe vortex did eventually distort the contours downstream but still inside Region III. As the relatively undisturbed flow passed around the wing leading edge, the flow was inverted by the lateral and transverse velocities of the vortex to produce the contours shown in Figures 6-12 and 6-13. In these figures, the correlations are for both the fixed and the traversing probes on the same side of the wing. Figure 6-12 shows the results obtained for the fixed probe near the wing,  $P_A$  (2.00, 0.15, 0.15), and Figure 6-13 for the probe further from the wing,  $P_A$  (2.00, 0.20, 0.80). Notable in the figures is the absence of the nearly vertical division between the regions of positive and negative correlation that was observed for the onset boundary layer. Evident in both figures is the effect of the "jetting" flow produced by the streamwise vorticity as it circulated axial momentum. From a comparison of the correlation contours in Figures 6-12 and 6-13 with the velocity contours shown in Figure 4-15, it is observed that there was a "jetting" of both the correlation and velocity contours from the high momentum (velocity) region into the contours for the lower momentum (velocity). It is tentatively concluded that the distortions of the correlation contours were produced by vortical transport of the fluid by the horseshoe root vortex.

A new feature of the flow was observed for the correlations shown in Figure 6-12: the "finger" of the positively correlated

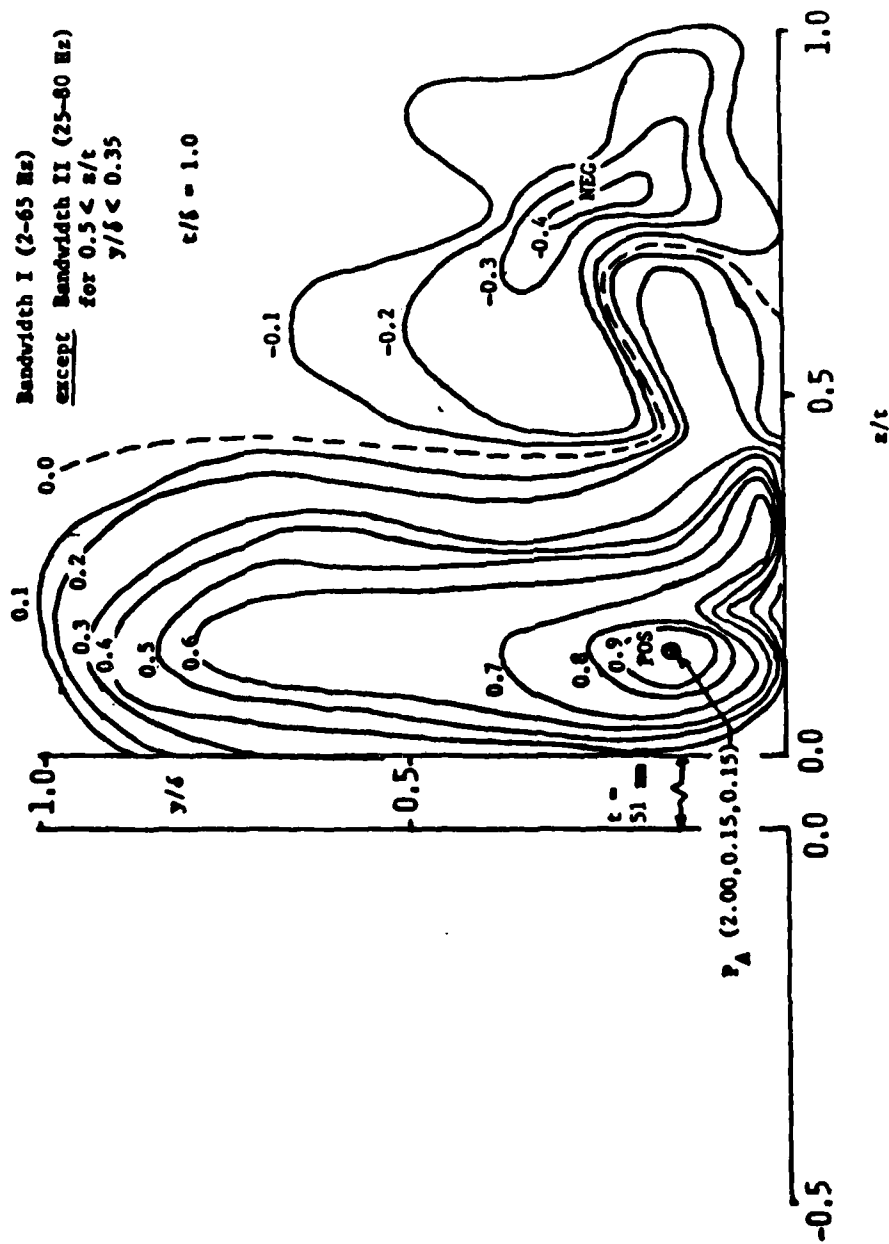


Figure 6-12: Contours of Constant  $S_y$  in Region III Downstream from Wing Leading Edge ( $P_A$  Close to Wing)

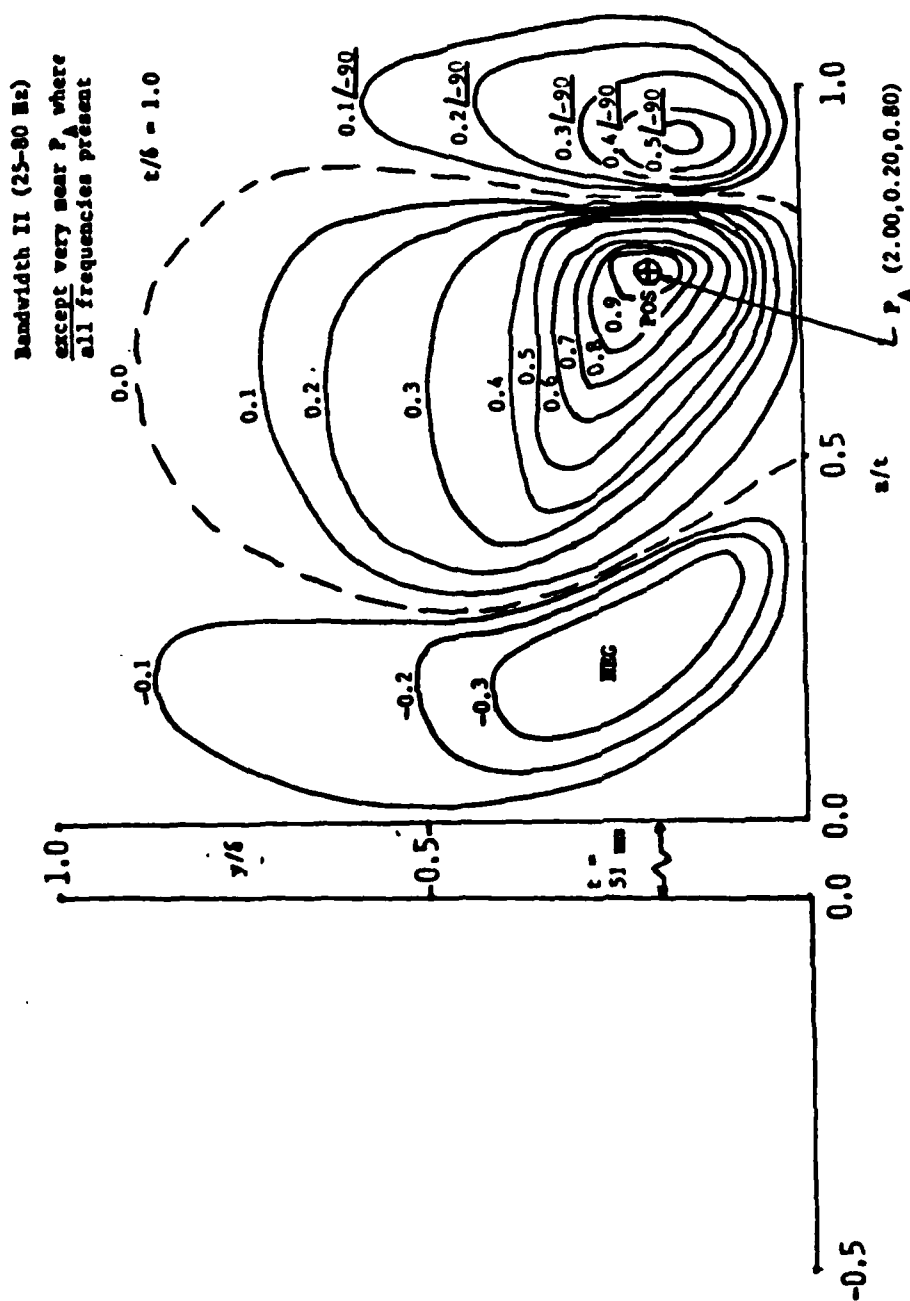


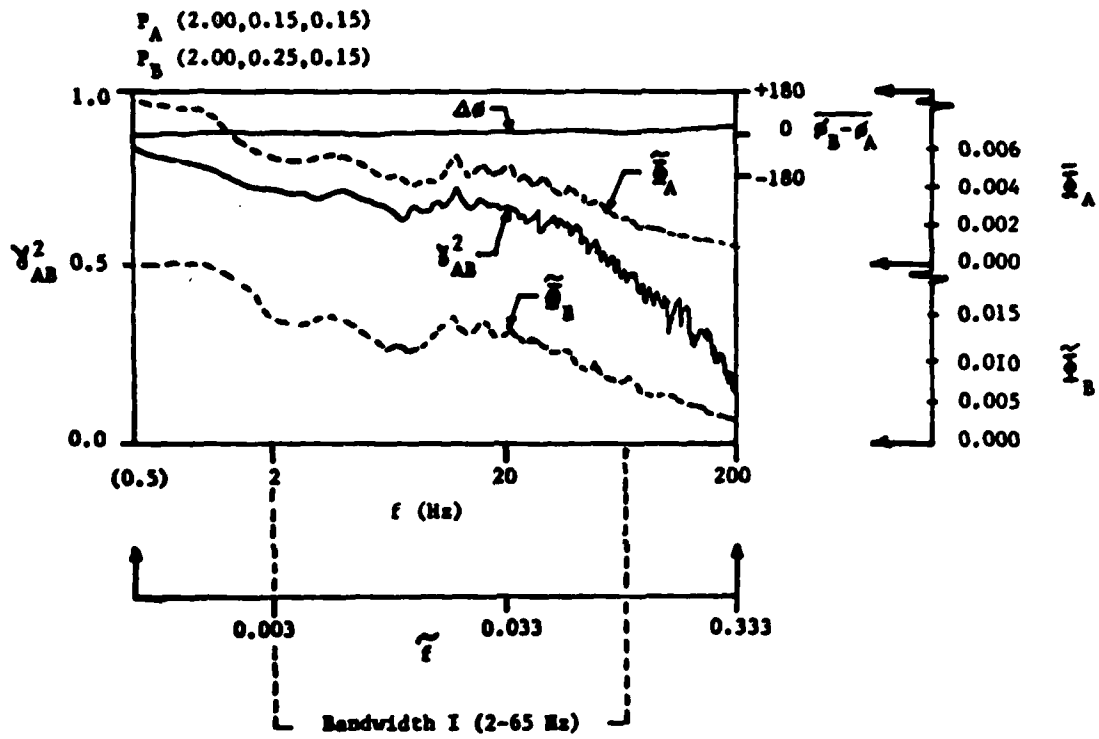
Figure 6-13: Contours of Constant  $S_y$  in Region III Downstream from Wing Leading Edge ( $P_A$  Far from Wing)



region jetting up into the negative correlation region exhibited a frequency bandwidth different from that in the rest of the measurement plane. Figure 6-14 shows spectral measurement results for the two frequency bandwidths. The spectrum in Figure 14(a) for the positively correlated region with  $P_B$  (2.00, 0.25, 0.15) is similar to that for the onset boundary layer with Bandwidth I (2-65 Hz). The spectrum shown in Figure 14(b) from the region of the jetting "finger" at  $P_B$  (2.00, 0.25, 0.75) in the negatively correlated region exhibits a new frequency bandwidth (25-80 Hz) which is denoted as Bandwidth II. It is not clear from the measurements if the origin of this higher frequency bandwidth was in fact a result of the presence of the wing in the wall boundary layer. It is possible that it was a flow structure inherent in the onset boundary layer inner wall region that was displaced away from the wall by the horseshoe vortex transport. In either case, it was a newly created frequency band in the flow structure observed at positions away from the wall, and, is a consequence of the interaction of the flow in the wing-body junction region.

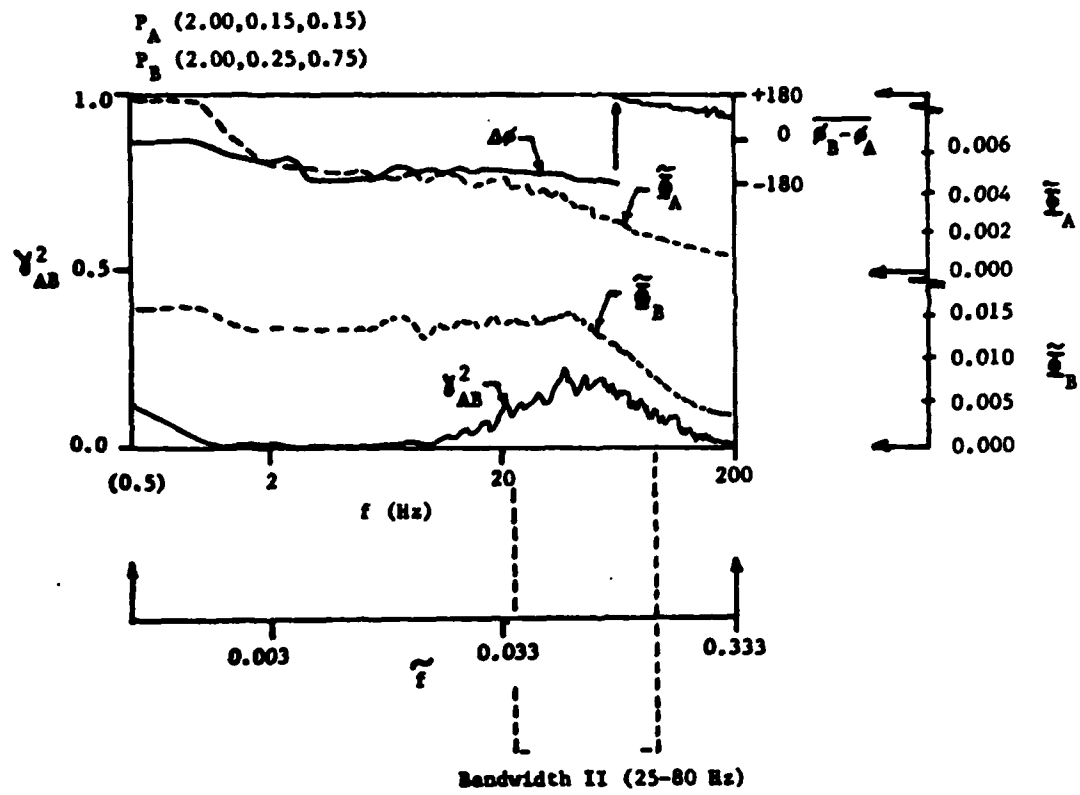
The meaning of the negative relative phase less than  $-180$  degrees for the correlation contours at positions  $z/t > 0.8$  in Figure 6-13 may be that there was a difference in the mean velocities or convection paths for parts of flow structure originating upstream and traveling to positions  $P_A$  and  $P_B$ . The structure parts could then have passed  $P_B$  after first passing  $P_A$  (the fixed probe position). This explanation is reasonable if the flow at  $P_B$  was either at a slower speed or a longer distance in its convection from the origin of the disturbance.

In addition to the above correlation measurements made with the two probes on the same side of the wing, a series of correlation contours were measured at positions  $P_B$  (2.00,  $y/t$ ,  $z/t$ ) in Region III with the fixed probe on the other side of the wing at six positions inside the spatial zone ( $-0.75 \leq z/t \leq -0.15$ ) and ( $0.15 \leq y/\delta \leq 0.60$ ). The results for these "across-wing" correlations are presented in Figures 16-15 through 6-22. The figures show that the flow was correlated for positions of the traversing



6-14(a): Bandwidth I

Figure 6-14: Example Spectral Distributions of Correlation Measurement Data for Region III



6-14(b): Bandwidth II

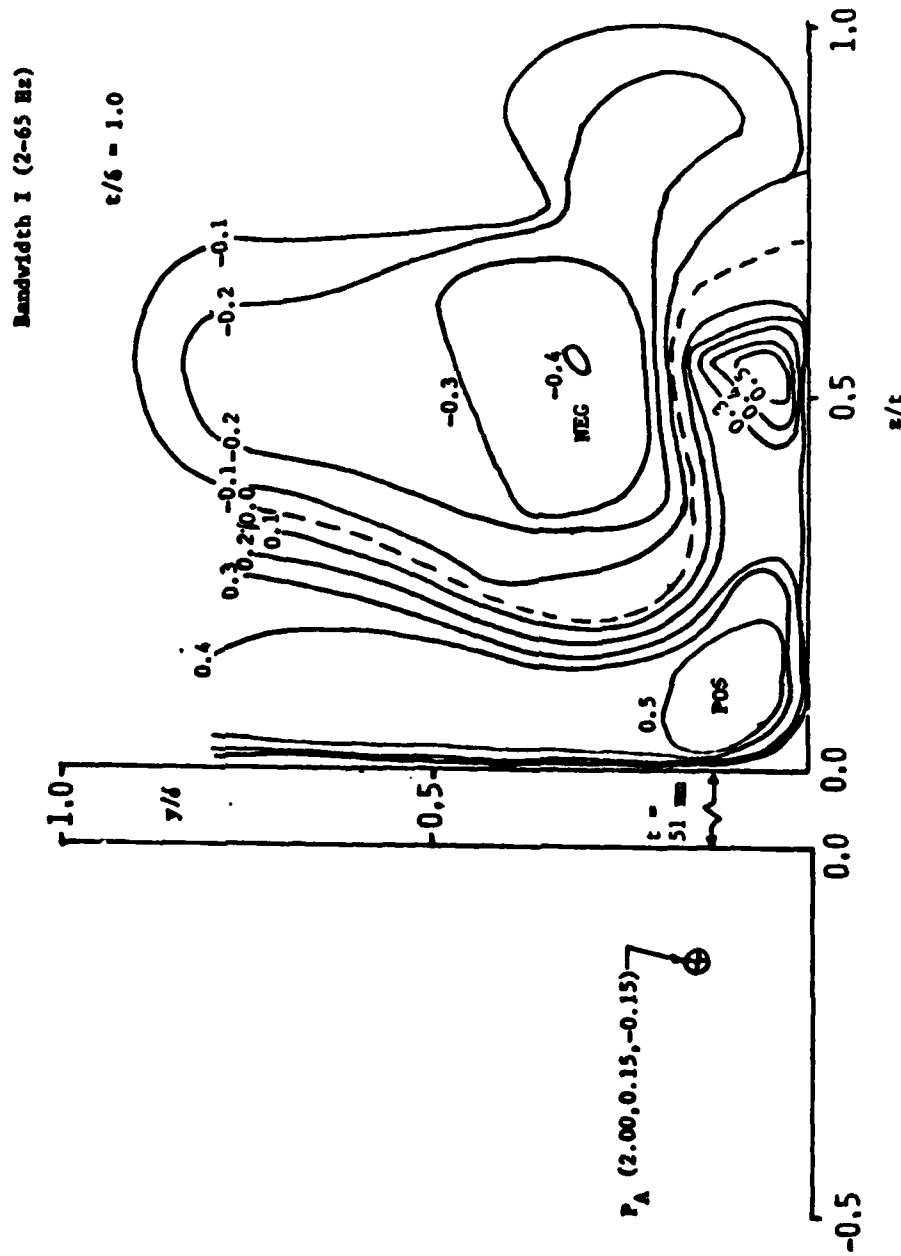
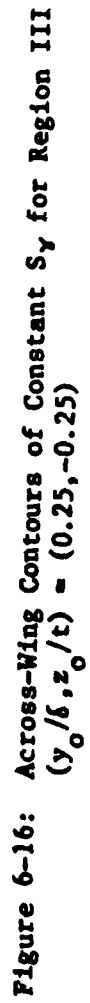


Figure 6-15: Across-Wing Contours of Constant  $S_y$  for Region III  
 $(y_0/\delta, z_0/\delta) = (0.15, -0.15)$



**Figure 6-16: Across-Wing Contours of Constant  $S_y$  for Region III  
( $y/\delta, z/t$ ) = (0.25, -0.25)**

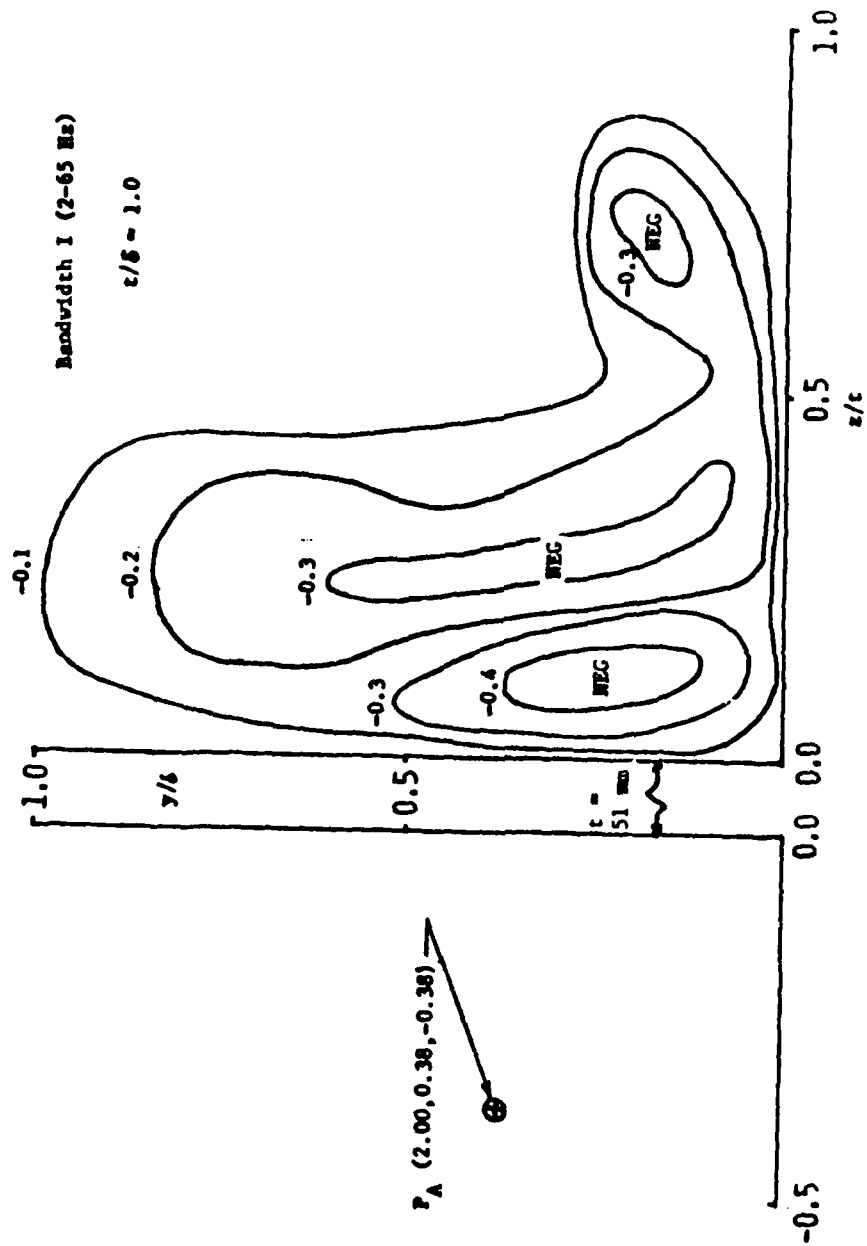


Figure 6-17: Across-Wing Contours of Constant  $S_y$  for Region III  
 $(y_0/b, z_0/t) = (0.38, -0.38)$

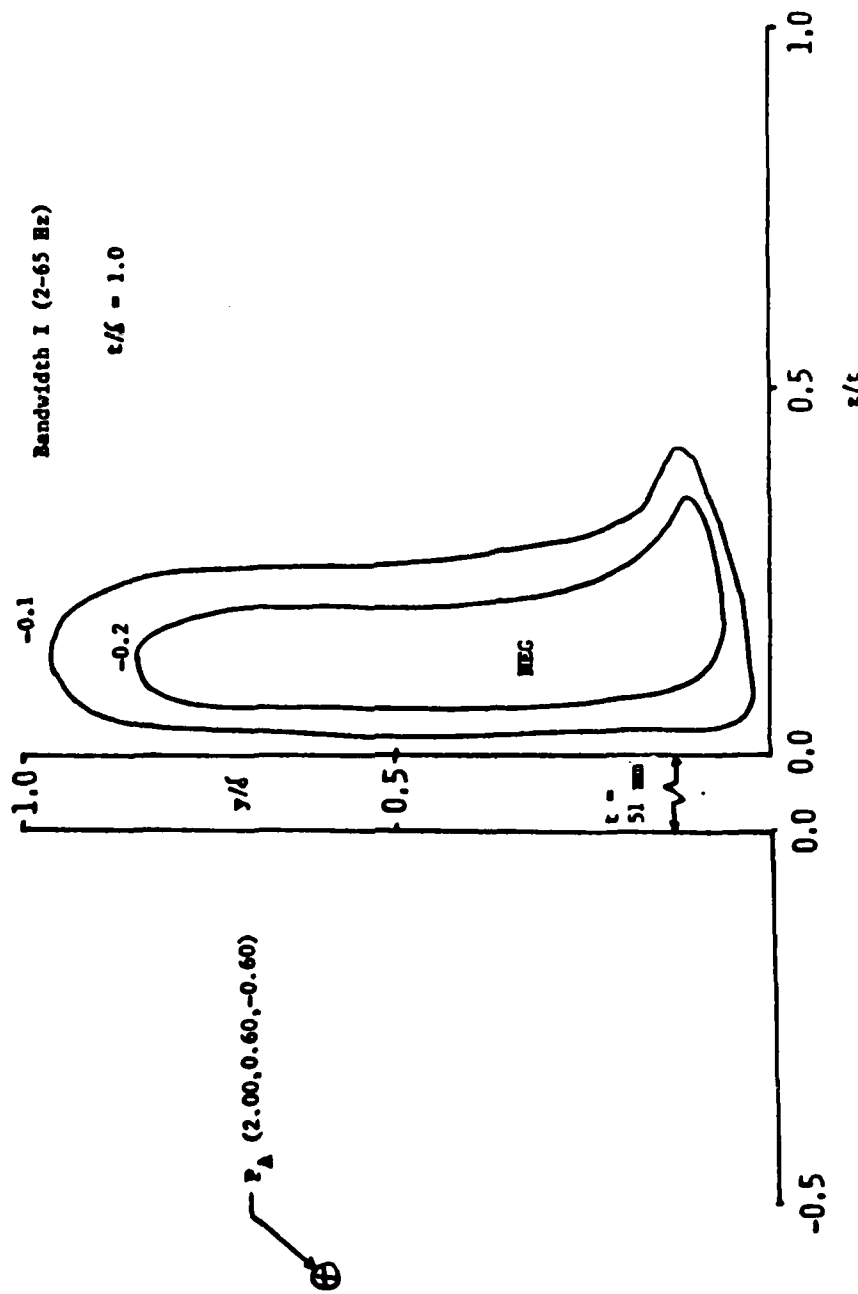


Figure 6-18: Across-Wing Contours of Constant  $S_Y$  for Region III  
 $(y_0/b, z_0/t) = (0.60, -0.60)$

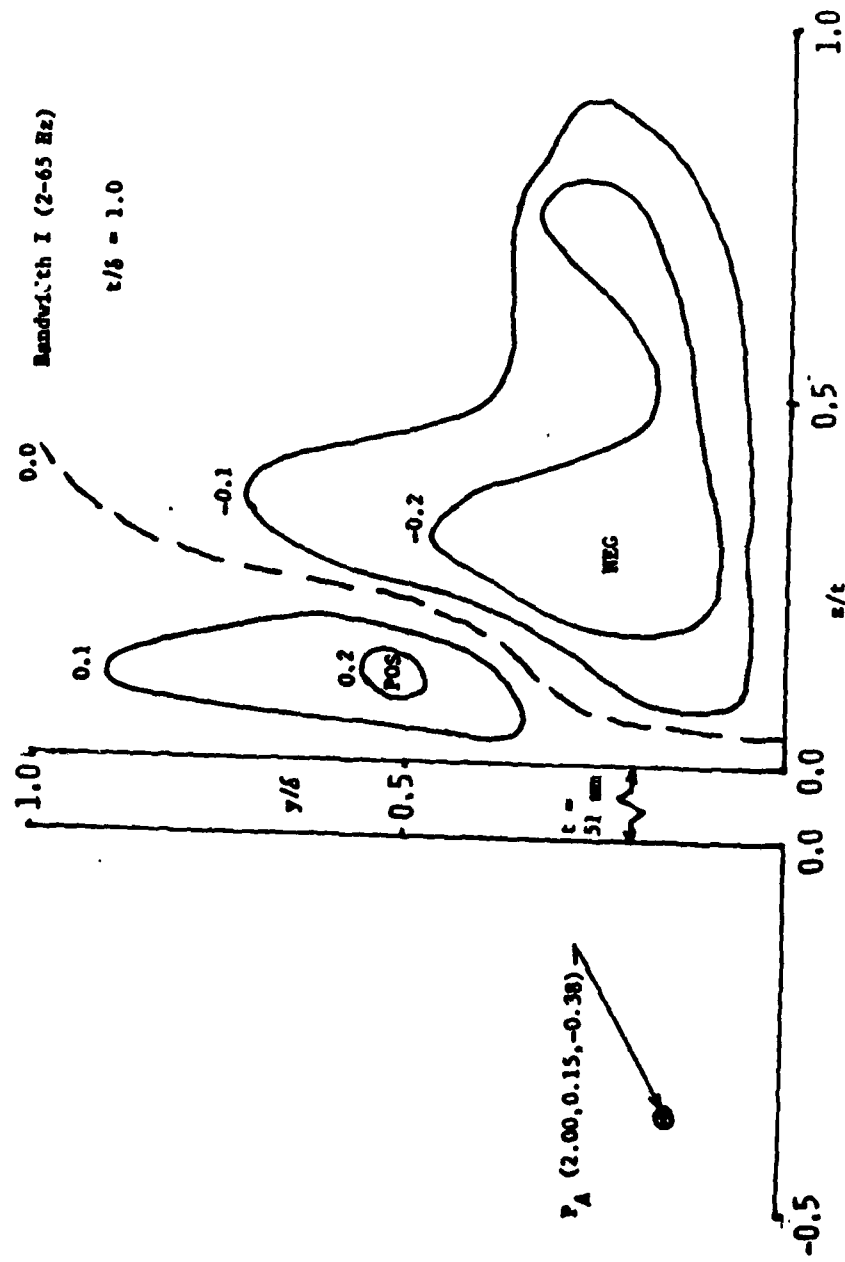


Figure 6-19: Across-Wing Contours of Constant  $S_y$  for Region III  
 $(y_0/b, z_0/t) = (0.15, -0.38)$



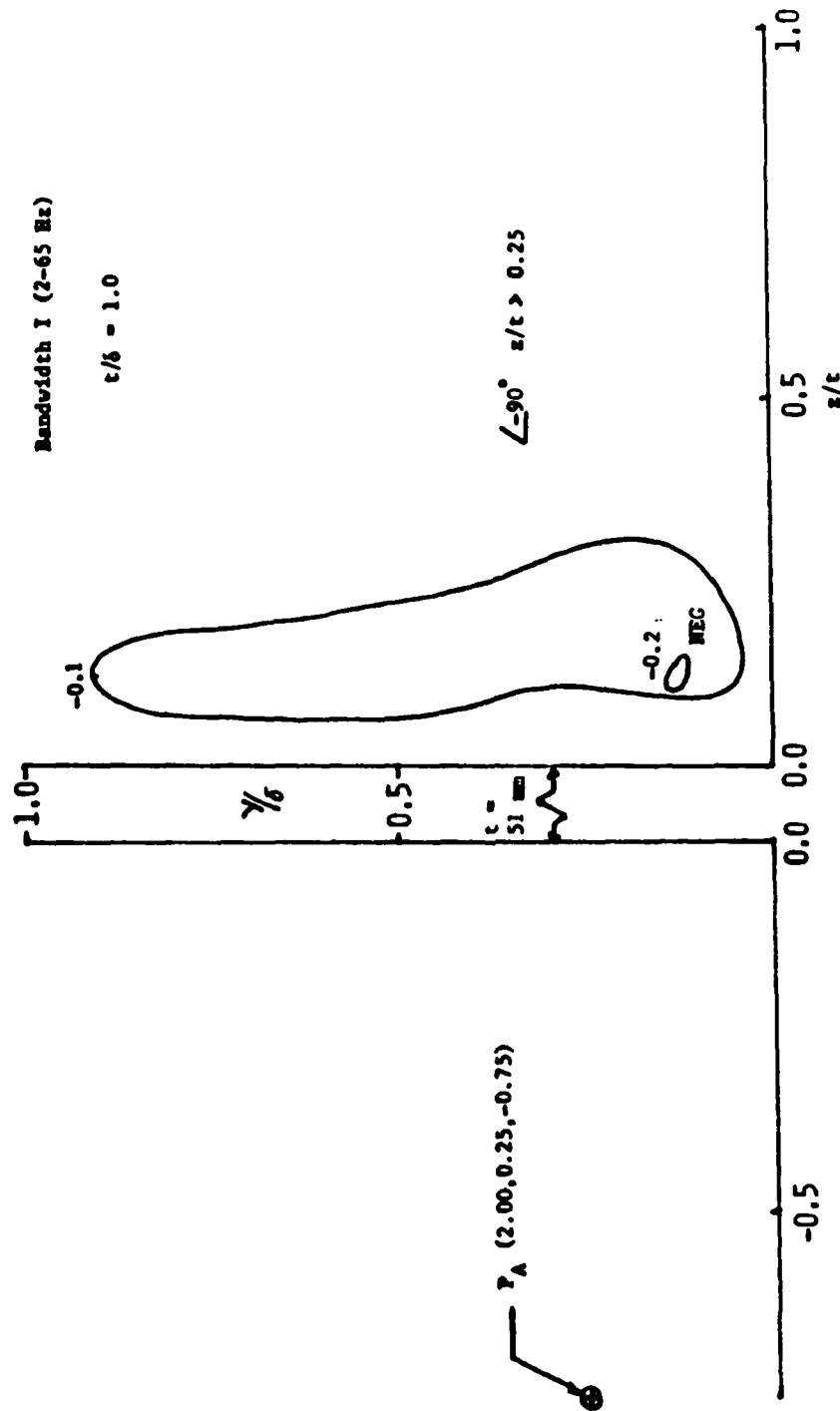


Figure 6-20: Across-Wing Contours of Constant  $S_1$  for Region III  
 $(\gamma_0/\delta, z_0/\tau) = (0.25, -0.75)$

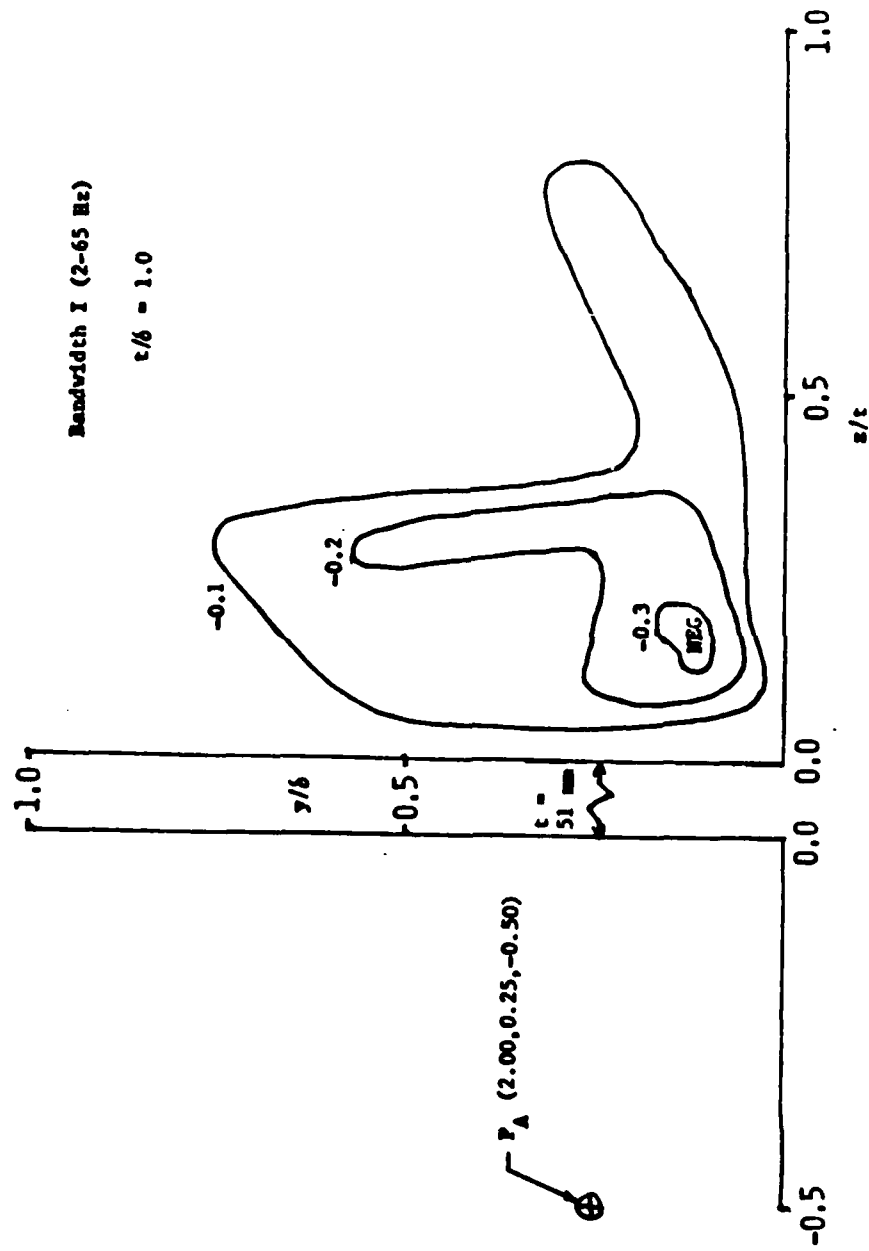
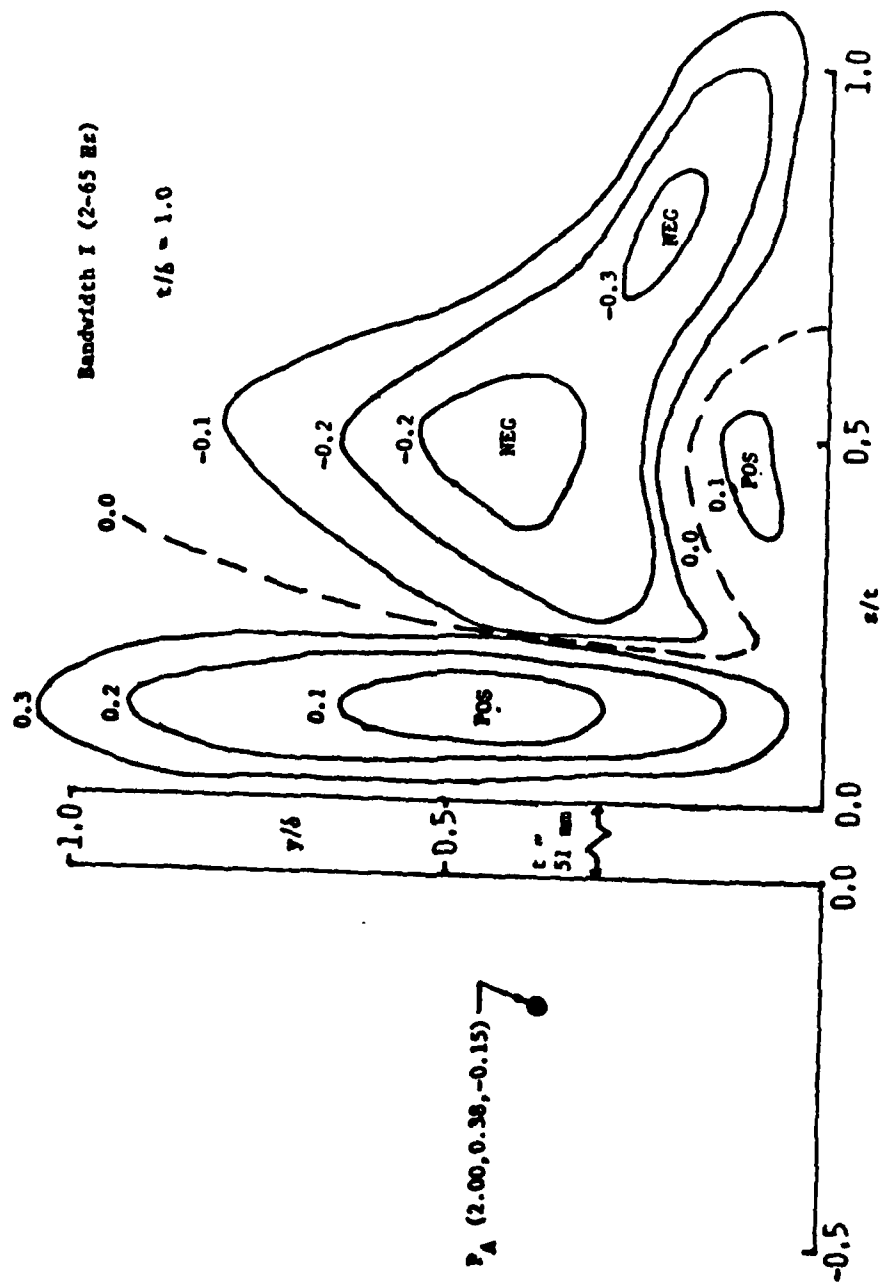


Figure 6-21: Across-Wing Contours of Constant  $S_y$  for Region III  
 $(y_o/\delta, z_o/t) = (0.25, -0.50)$



**Figure 6-22: Across-Wing Contours of Constant  $S_q$  for Region III  
( $y_0/6, z_0/t$ ) = (0.38, -0.15)**

probe as far from the wing as  $z/t = 0.75$ . The correlation contours show the distortion effect of the vorticity transport described above, where the correlations were swept out from the intersection of the wing and wall in a direction along the wall, followed by a lifting away from the wall. The correlations were greatest in magnitude and spatial extent for the fixed probe near the wing and wall intersection, and decreased as the fixed probe was moved in the transverse or lateral directions.

Examples of the "across-wing" spectral distributions of the power spectral density, the coherence, and the relative phase are given in Figures 6-23 and 6-24. The fixed and traversed probes were at symmetric positions relative to the wing for the measurements presented in Figure 6-23,  $P_A (2.0, 0.15, -0.15)$  and  $P_B (2.0, 0.15, +0.15)$ . The correlations are in-phase and within the Bandwidth I (2-65 Hz). In Figures 6-24 the probe positions were located at non-symmetric positions with  $P_B$  further away from the wing and near the boundary between the positive and negative correlations. These locations were  $P_A (2.00, 0.15, -0.15)$  for the fixed probe and both  $P_B (2.00, 0.10, 0.55)$  (Figure 6-24(a)) and  $P_B (2.00, 0.20, 0.55)$  (Figure 6-24(b)) for the traversed probe. In Figure 6-24(a), the correlations were in Bandwidth I (2-65 Hz) similar to the symmetric condition. Figure 6-24(b) presents evidence that Bandwidth II (25-80 Hz) was present with small coherence. This was the only measurement in which Bandwidth II was observed for the "across-wing" correlations in Region III.

#### 6.3.1.3 Region IV (Developed Secondary Flow) ( $4 \lesssim x/t < \infty$ )

Additional two-point velocity correlations were measured in the plane at the streamwise location at  $x_0 = 6.05$  in Region IV. The "across-wing" correlation contours for the traversing probe are presented in Figure 6-25 for  $P_A (6.05, 0.15, -0.15)$ , in Figure 6-26 for  $P_A (6.05, 0.40, -0.40)$ , and in Figure 6-27 for  $P_A (6.05, 0.15, -0.40)$ . The correlations were substantially diminished in magnitude, but the effective displacement of the correlation regions by the vorticity transport was greater, than for the contours in the upstream Region III for  $P_A (2.00, y/\delta, z/t)$ . This observation is

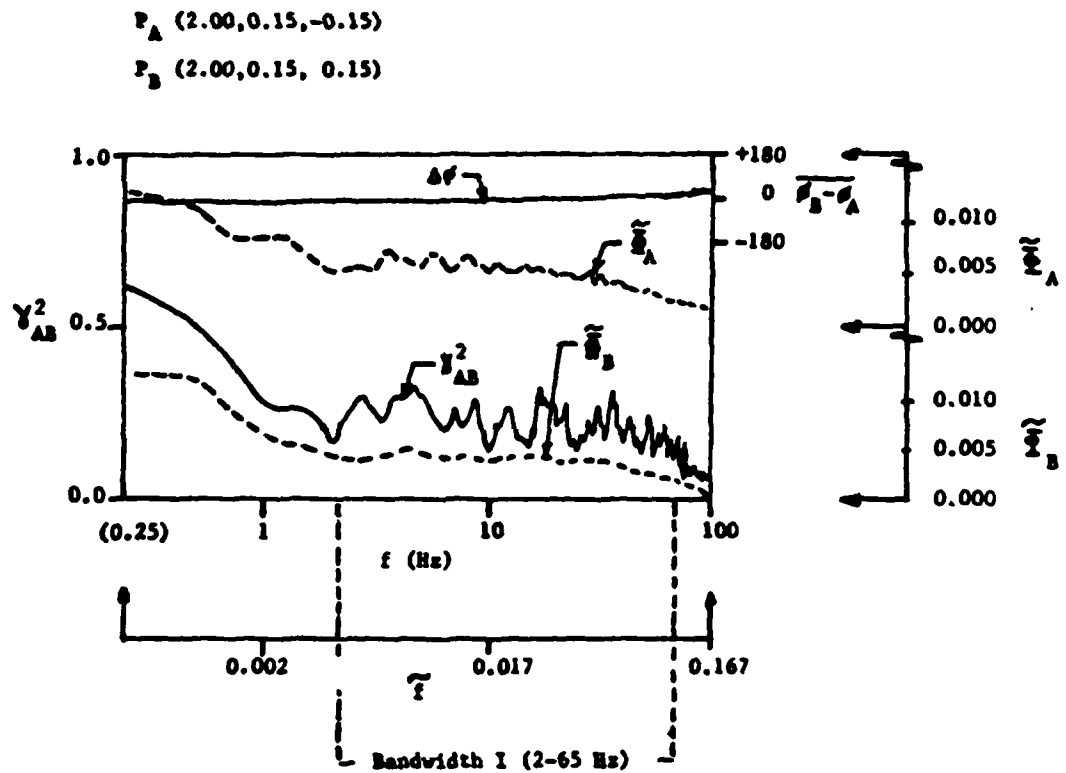
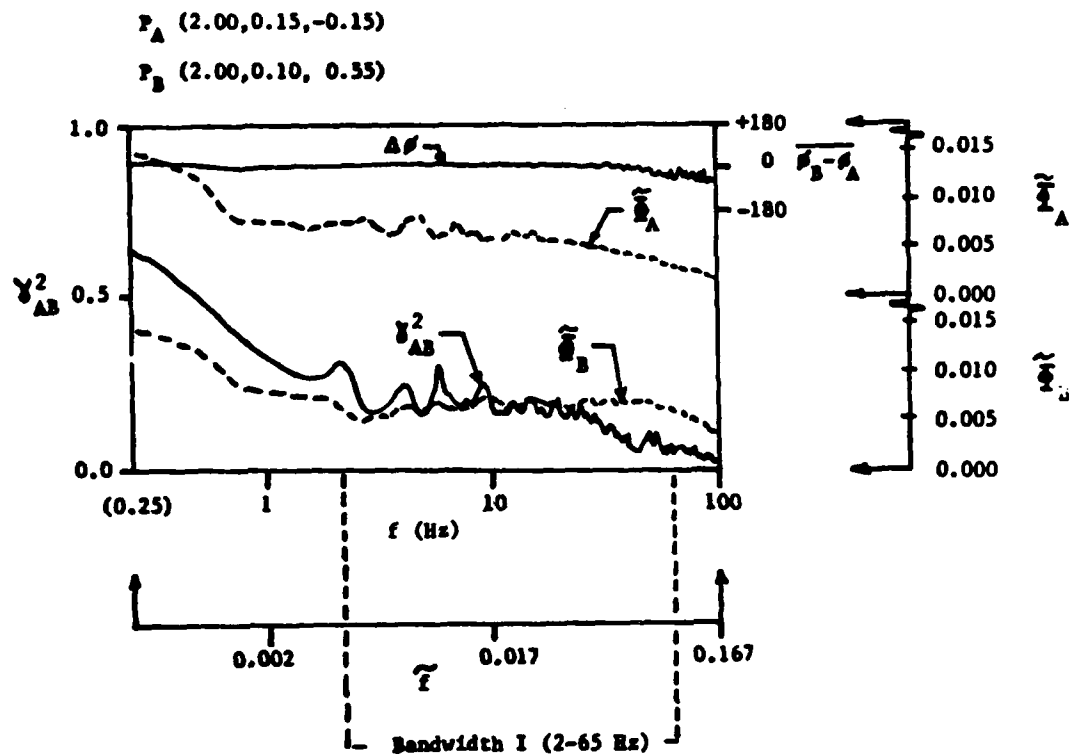
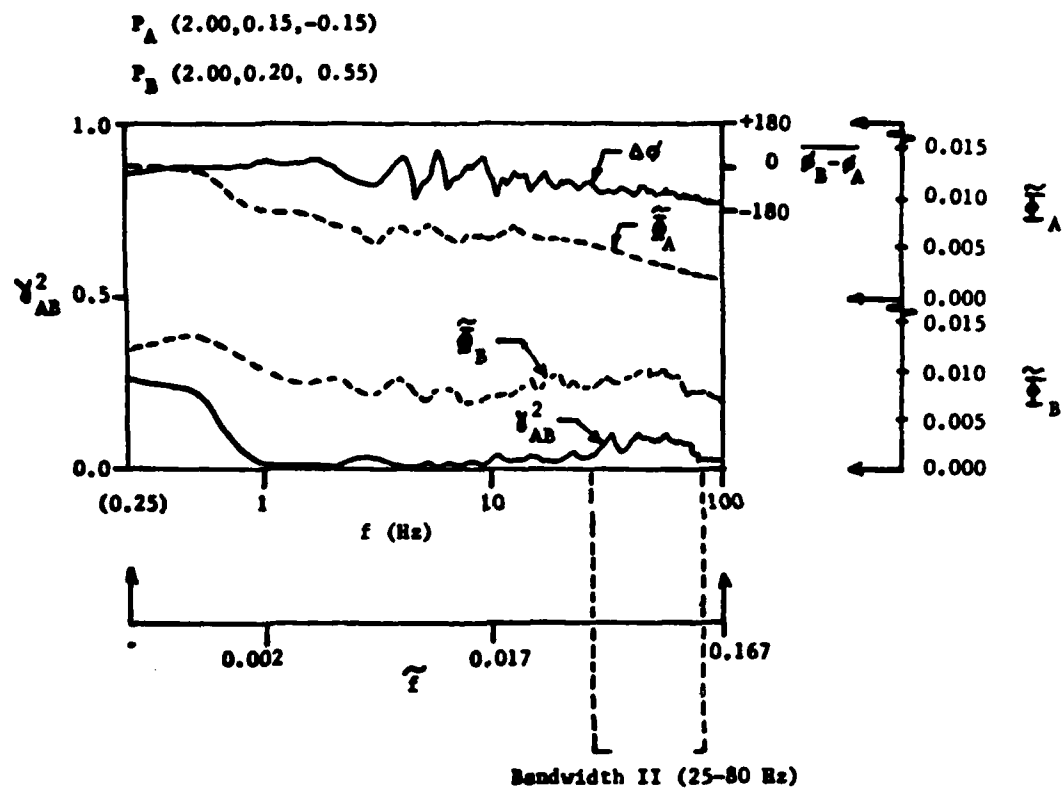


Figure 6-23: Example Across-Wing Spectral Distributions of Correlation Measurement Data for Symmetric Probe Positions in Region III



6-24(a): Bandwidth I

Figure 6-24: Example Across-Wing Spectral Distributions of Correlation Measurement Data for Non-Symmetric Probe Positions in Region III



6-24(b): Bandwidth II

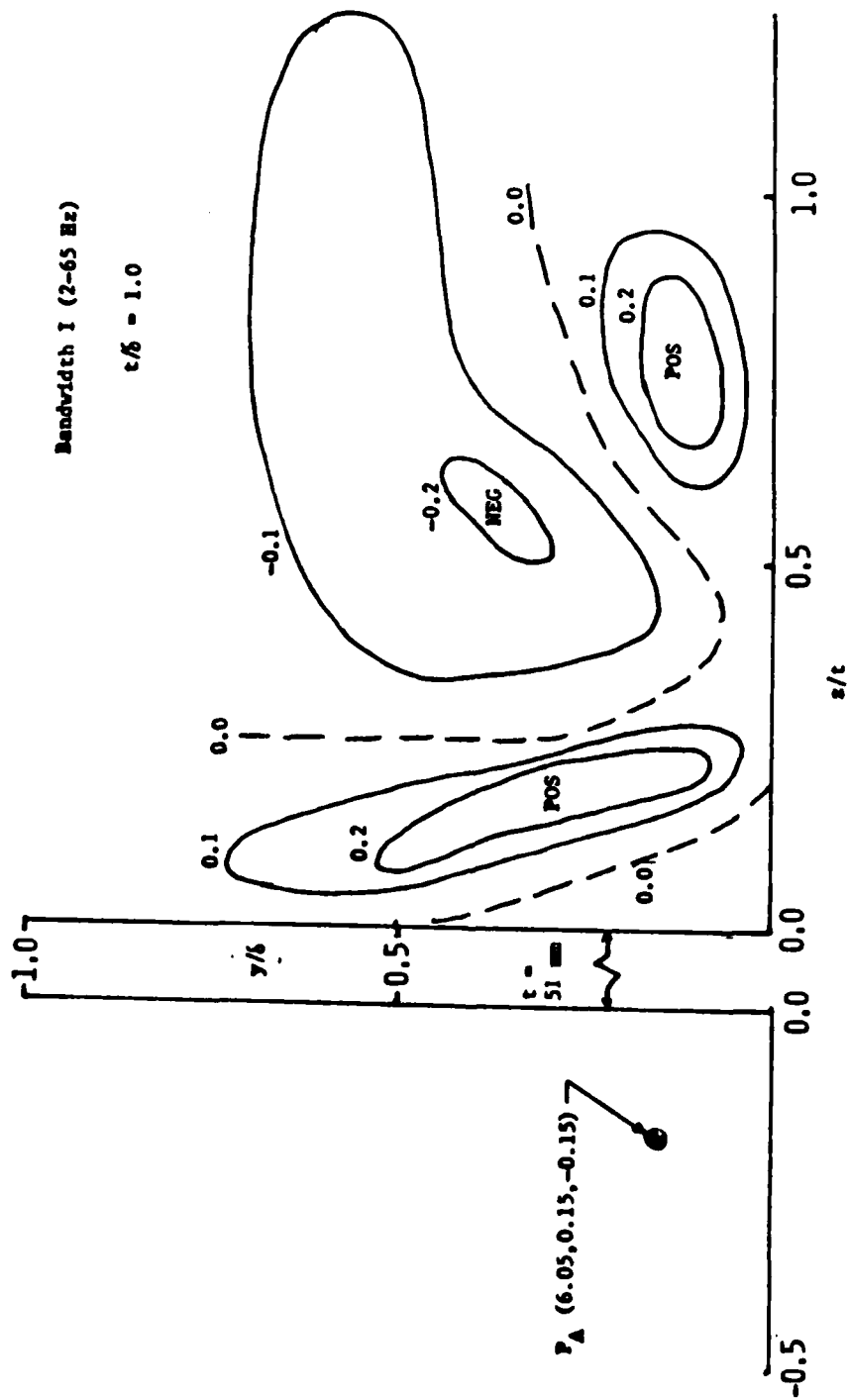


Figure 6-25: Across-Wing Contours of Constant  $S_y$  for Region IV  
 $(y_0/\delta, z_0/t) = (0.15, -0.15)$



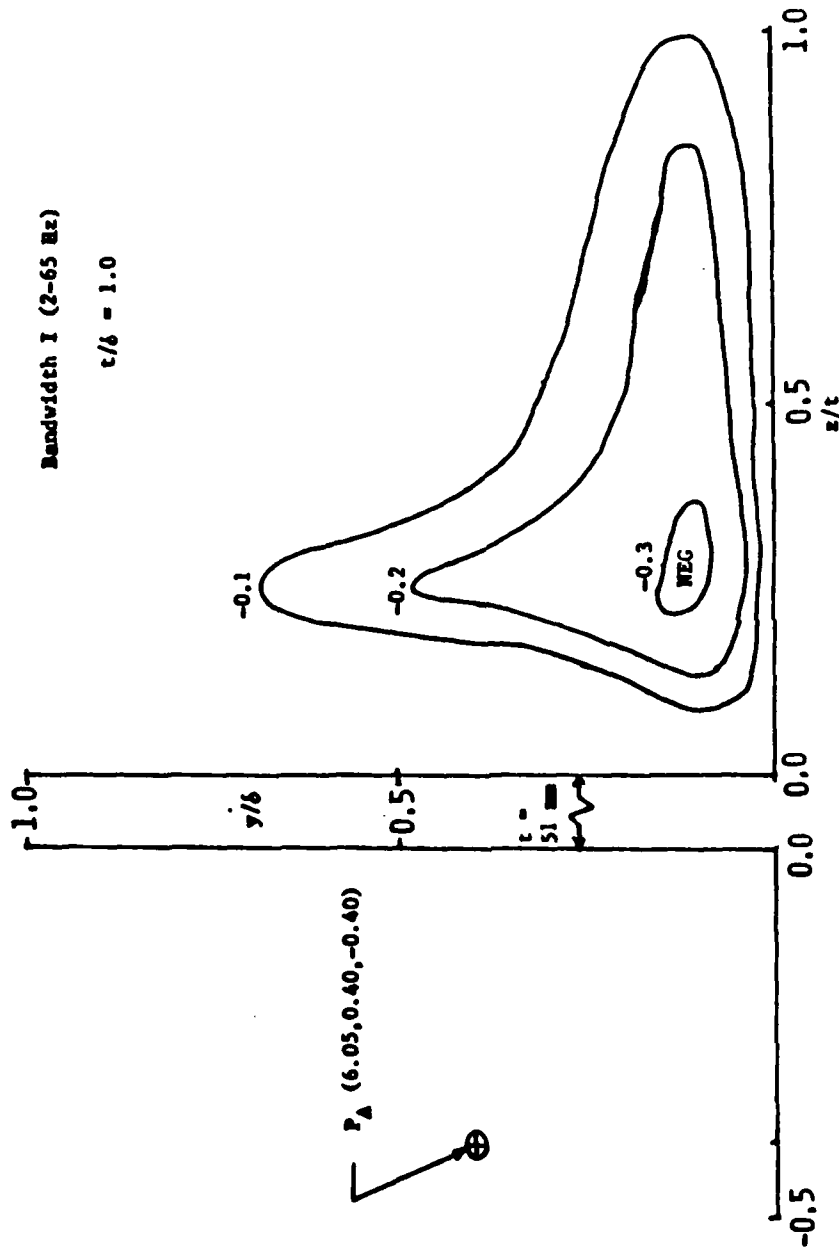


Figure 6-26: Across-Wing Contours of Constant  $S_y$  for Region IV  
 $(y_0/b, z_0/t) = (0.40, -0.40)$

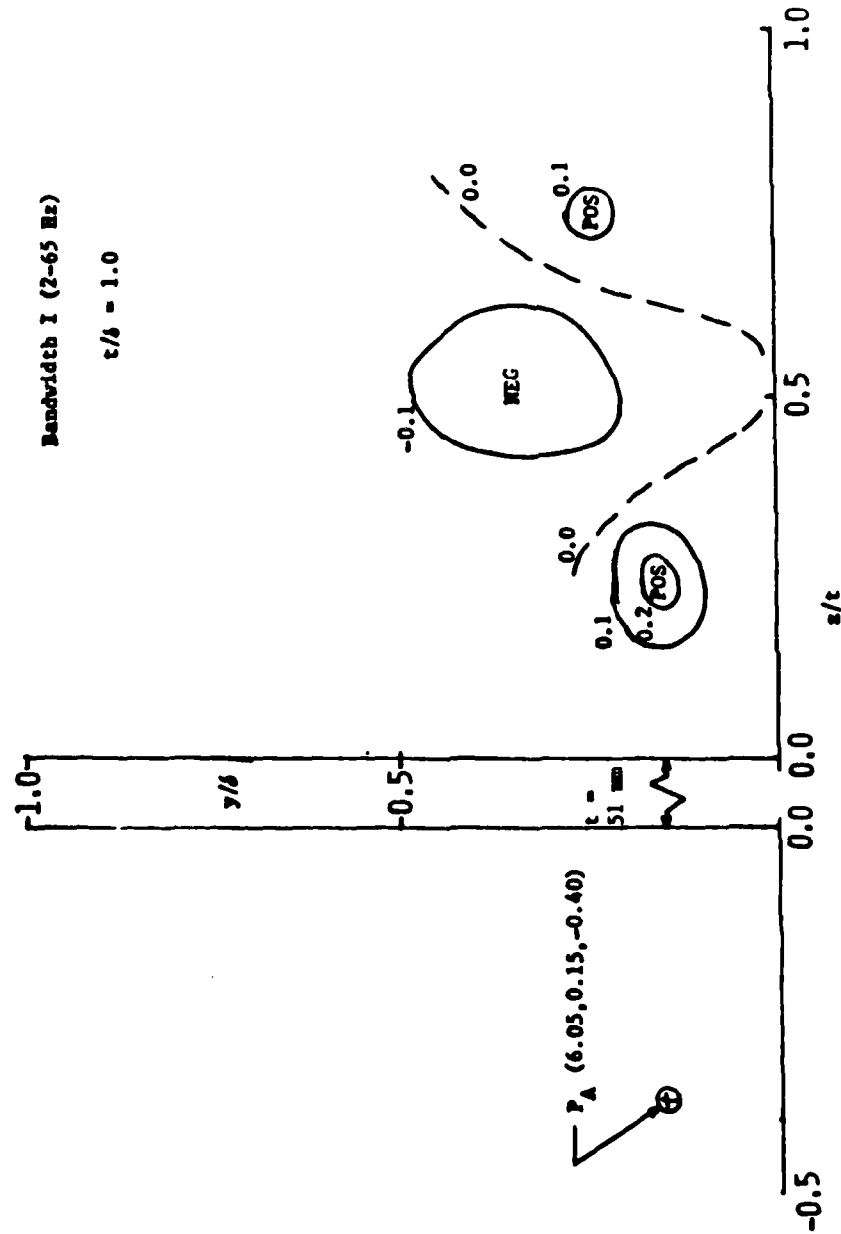


Figure 6-27: Across-Wing Contours of Constant  $S_y$  for Region IV  
 $(y_0/\delta, z_0/\tau) = (0.15, -0.40)$

made by comparing Figures 6-25, 6-26, and 6-27 with Figures 6-15, 6-17, 6-19, respectively. These results are not surprising; the diminished correlation magnitudes were a consequence of the shear and the diffusive forces produced by the vorticity as it jetted high axial momentum flow into the low momentum region of the flow.

#### 6.3.1.4 Summary Comments

Summary comments drawn from the observations of the flow in the wing-body junction are first, that the vortical motion caused by the horseshoe vortex effectively displaced the correlation contours in the lateral and transverse directions; second, that the jetting of high axial momentum fluid into the low momentum boundary layer resulted in partial destruction of the flow structure; and finally, that the onset boundary layer frequency Bandwidth I was preserved in the junction flow although at positions away from the wall a new higher frequency Bandwidth II evolved.

#### 6.3.2 Finite Chord Length Wing

Measurements were made with the finite chord length wing to establish the effect of the trailing edge condition on the wing-body junction flow and to observe the temporal flow structure in the wing-body junction wake flow.

##### 6.3.2.1 Region III (Leading Edge Separation Region) ( $-0.8 < x/t \lesssim 4$ )

Two-point velocity correlations were repeated at the downstream end of Region III at the plane location  $x_0/t = 2.0$  with the finite chord length wing. The purpose was to examine the effect of the trailing edge condition on the upstream flow structure. "Across-wing" correlation contours are presented in Figure 6-28 for the fixed probe at  $P_A$  (2.00, 0.15, -0.15) and in Figure 6-29 at  $P_A$  (2.00, 0.25, -0.25). The fixed probe  $P_A$  was located on one side of the wing while the traversing probe  $P_B$  was located on the other side. A direct comparison can be made between the contours in Figures 6-28 and 6-29 with those in Figures 6-15 and 6-16 for the infinite chord length wing. The comparison shows that the positive and negative correlation regions for the finite chord length wing were smaller in spatial extent and magnitude than those for the infinite chord length wing. This result was expected

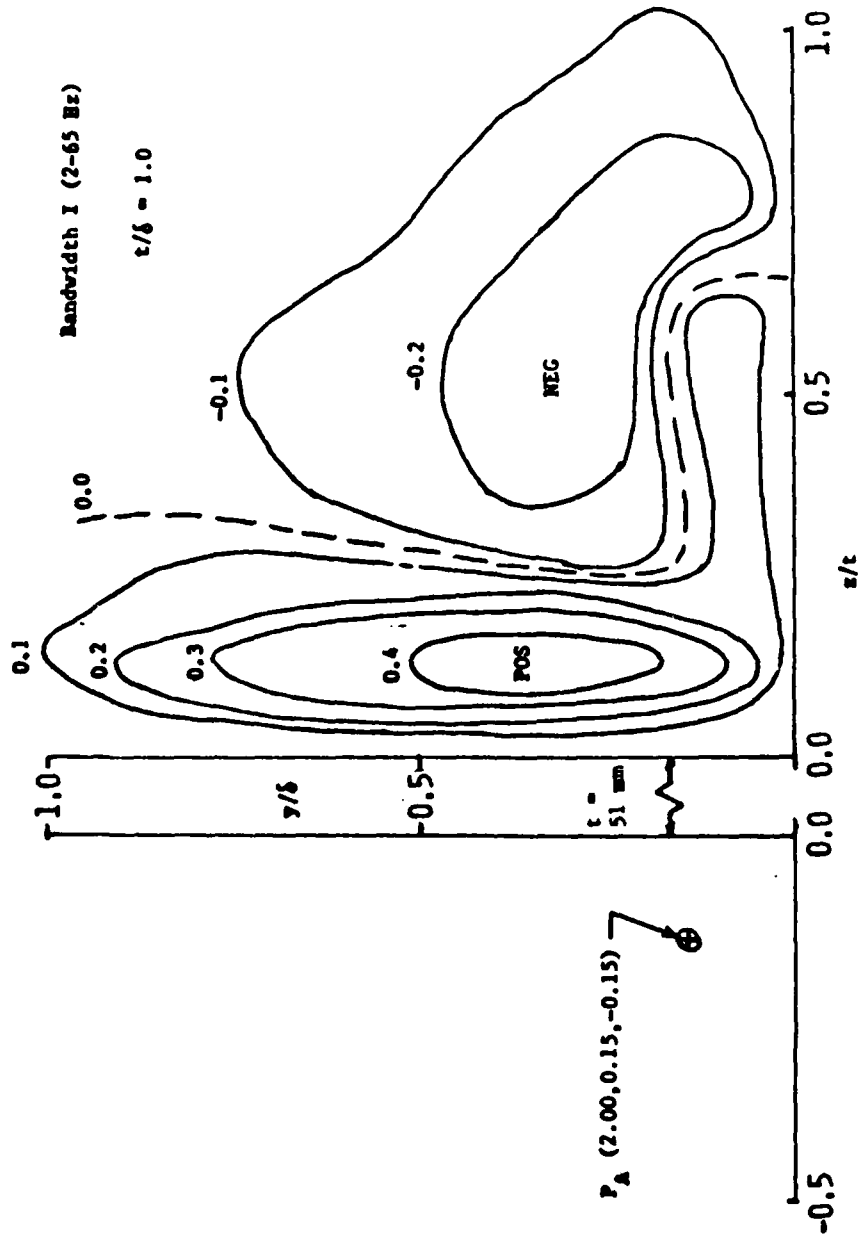


Figure 6-28: Across-Wing Contours of Constant  $S_y$  for Region III  
for Finite Chord Length Wing  
( $y_o/\delta, z_o/t$ ) = (0.15, -0.15)

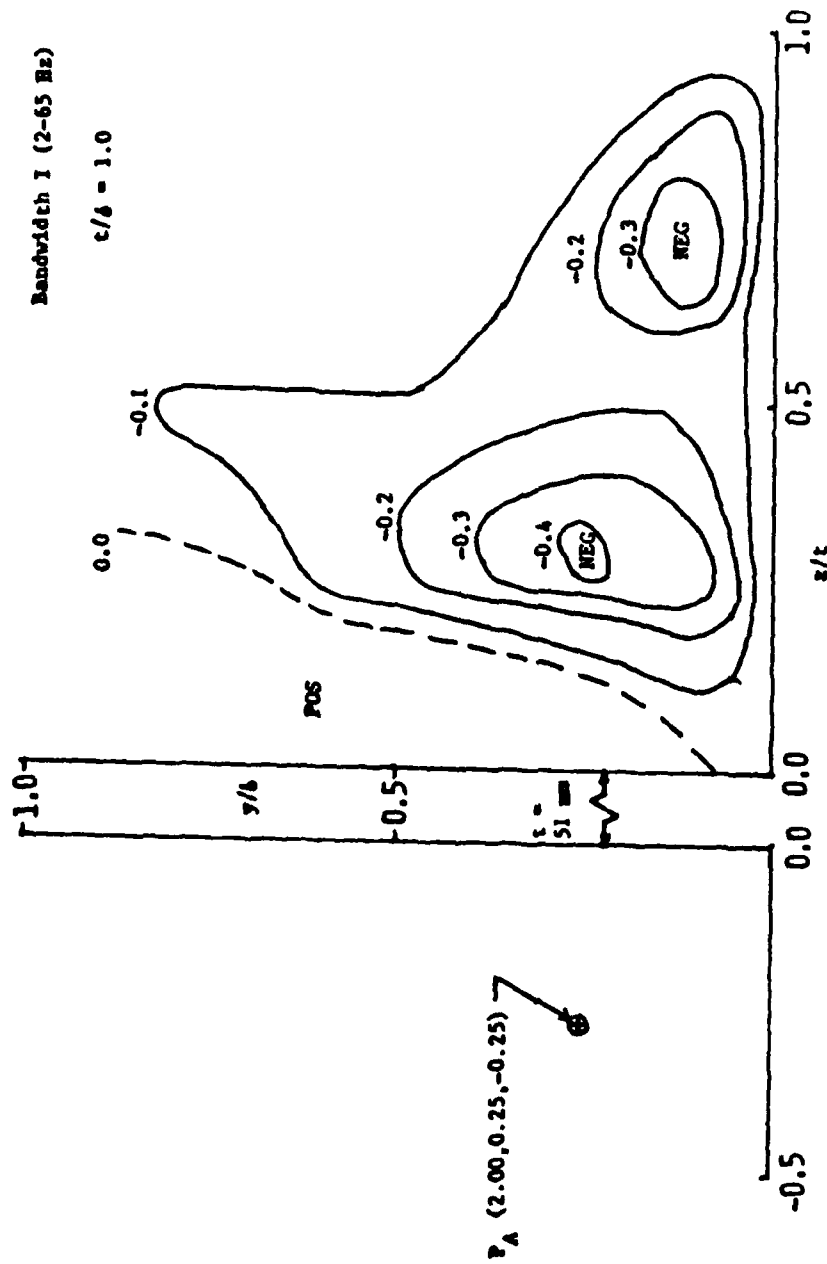


Figure 6-29: Across-Wing Contours of Constant  $S_y$  for Region III  
for Finite Chord Length Wing  
( $y_0/b, z_0/t$ ) = (0.25, -0.25)

because the finite chord length wing experienced flow acceleration along its side that was not present for the infinite chord length wing. This aspect of the flow will be discussed in greater detail in Chapter 7. Another observation from the comparison is that, in general, the effect of the finite chord length was to suppress positive correlations or to enhance negative correlations perhaps because of a change in the mean flow for the horseshoe vortex.

Although no measurements were obtained showing a disturbance in Bandwidth II (25-80 Hz), it is believed that this result was because of the limited number and locations for the probe positions. It is likely that a more complete mapping would show Bandwidth II, which did reappear in measurements downstream to be discussed in Section 6-4.

No other new features were apparent in the spectral distribution of the correlation data. It is tentatively concluded that the flow in Region III was slightly modified by the change in the mean flow, and that the temporal structure in this region was basically unchanged by the trailing edge conditions of the wing.

#### 6.4 Spatial Structure of Wing-Body Junction Wake Flow (Region VI)

Measurements were continued with the finite chord length wing at positions in a plane downstream from the wing trailing edge. Those measurements were made in Region VI, which is part of the wing-body junction wake flow and clearly the most complex region. The results obtained in this region must be considered exploratory since more systematic measurements are required to clarify the complex nature of the flow. It is shown that the wing-body junction wake flow is distinguished from the upstream wing-body junction flow both in the spatial distribution and frequency content of the large scale temporal flow. The active ingredient producing the new features in the flow was the adverse pressure gradient in the trailing edge region of the wing. The spatial structure and frequency of the wake flow were distinctly different inside the boundary layer than outside the boundary layer, where for the latter condition ordinary Strouhal-type shedding occurred with a much higher frequency (See Section 5.9). The spatial structure of this complex flow is shown by the correlation contours in

Figure 6-30 for the fixed probe at  $P_A$  (6.10, 0.25, -0.38) and the traversing probe at  $P_B$  (6.10,  $y/\delta$ ,  $z/t$ ).

The correlation contours show that the flow fluctuations were antisymmetric about the wing plane-of-symmetry. That is, the velocity increased on one side of the wing as it decreased at the reflected position on the other side. This result is in contrast to the correlation contours obtained for Regions I-IV, where the flow was apparently symmetric although positively and negatively correlated.

Example spectral distributions of the power spectral densities, coherences, and relative phases are shown in Figures 6-31 (a), (b), and (c) for three positions of the traversing probe:  $P_B$  (6.10, 1.25, -0.25),  $P_B$  (6.10, 1.50, 0.25), and  $P_B$  (6.10, 0.25, 0.25). These positions as well as the fixed probe position  $P_A$  (6.10, 0.25, -0.38), were in the wing "shadow" in the downstream direction. The results for these positions  $P_B$  represent measurements in three correlation regions. As shown in Figure 6-30, there were at least two additional correlation regions distinguished by relative phase, one of which was outside the wing "shadow", another of which extended from inside the "shadow" to outside the "shadow." A third Bandwidth III (0.5-10 Hz) was observed in these measurements and was lower than either of the two bandwidths observed in Regions I-IV. Those two were the onset boundary layer Bandwidth I (2-65 Hz), and the high frequency Bandwidth II (25-80 Hz) that appeared in the wing-body junction flow. Apparently the trailing edge condition introduced a "natural frequency" into the spectral distribution of large-scale temporal flow structure that gave rise to Bandwidth III. It is interesting that neither the onset boundary layer frequency Bandwidth I nor the wing-body Bandwidth II appeared in the correlations for the fixed probe at  $P_A$  (6.10, 0.25, -0.38) shown in Figure 6-30; only the frequency Bandwidth III (0.5-10 Hz) was observed. Except in the vicinity of the wake centerline where values of the power spectral density were large, the power spectral density for Bandwidth III (0.5-10 Hz) was comparable in magnitude to the previous measurements for Bandwidth I (2-65 Hz)

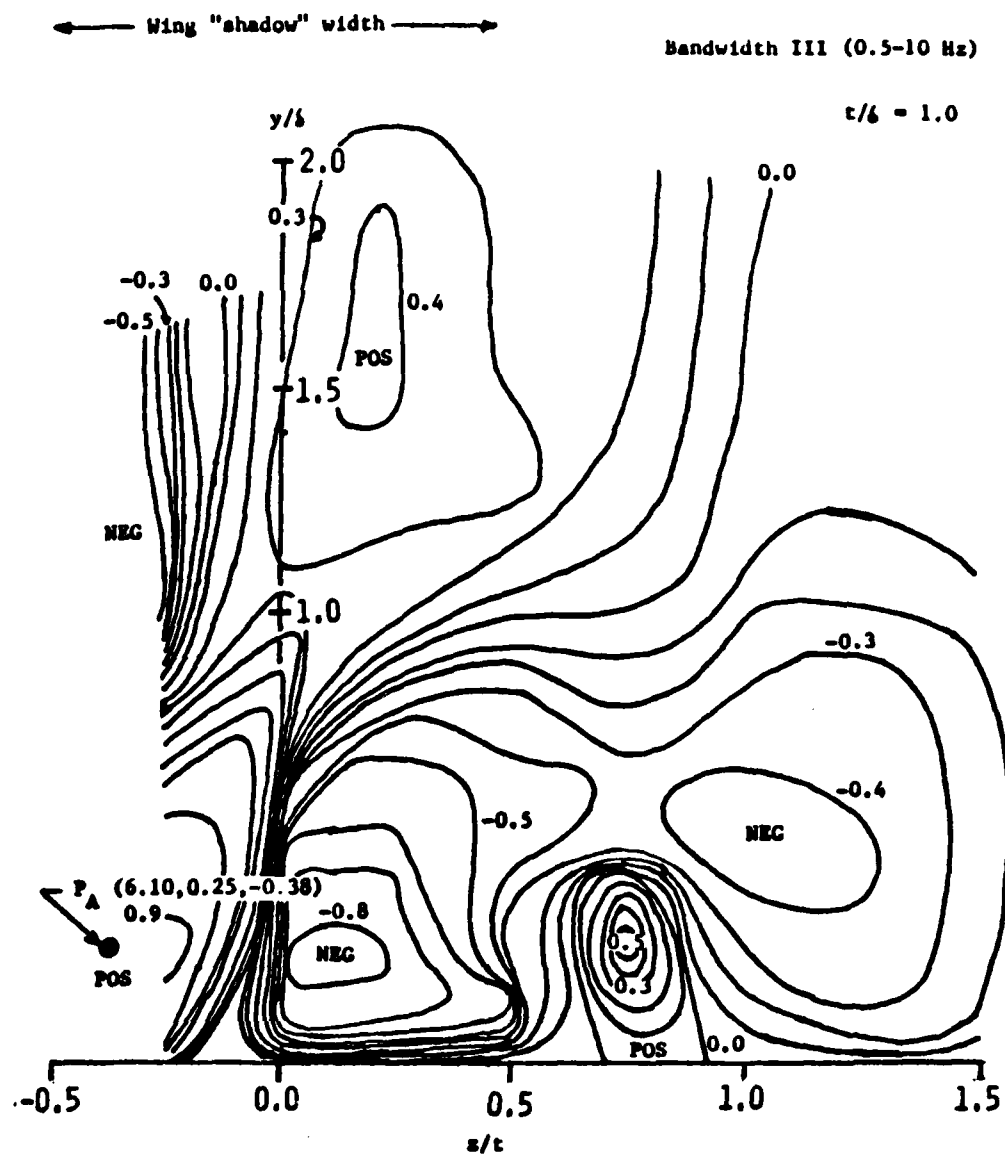
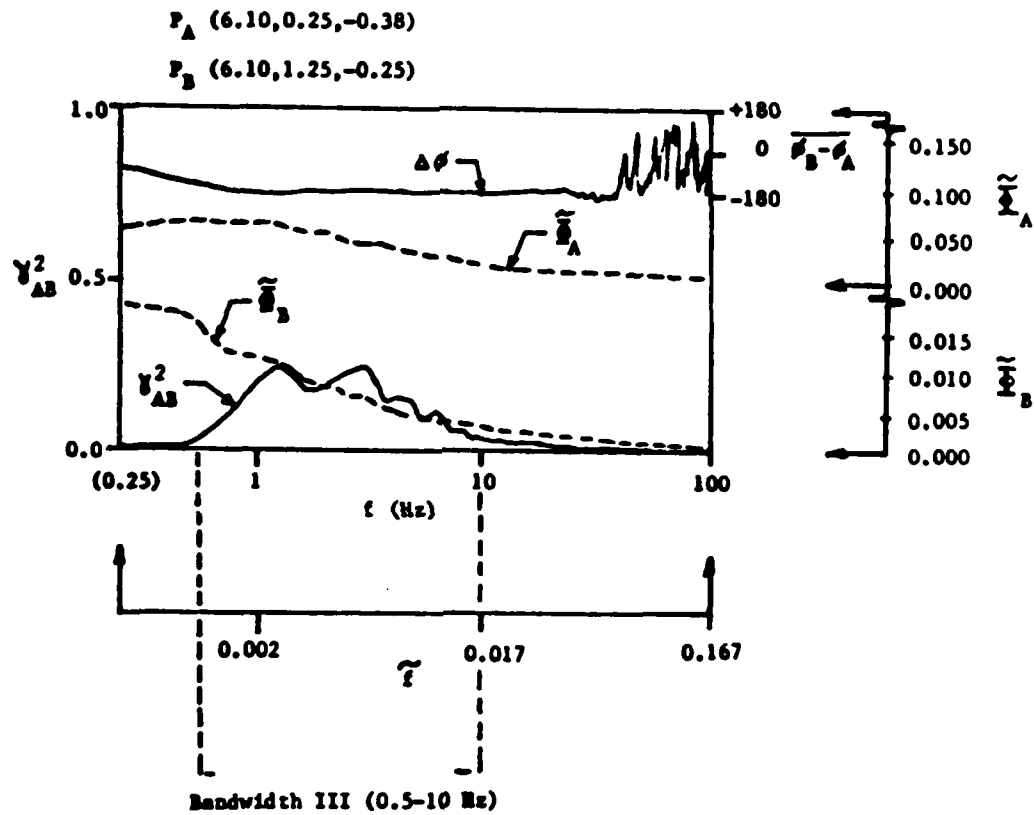


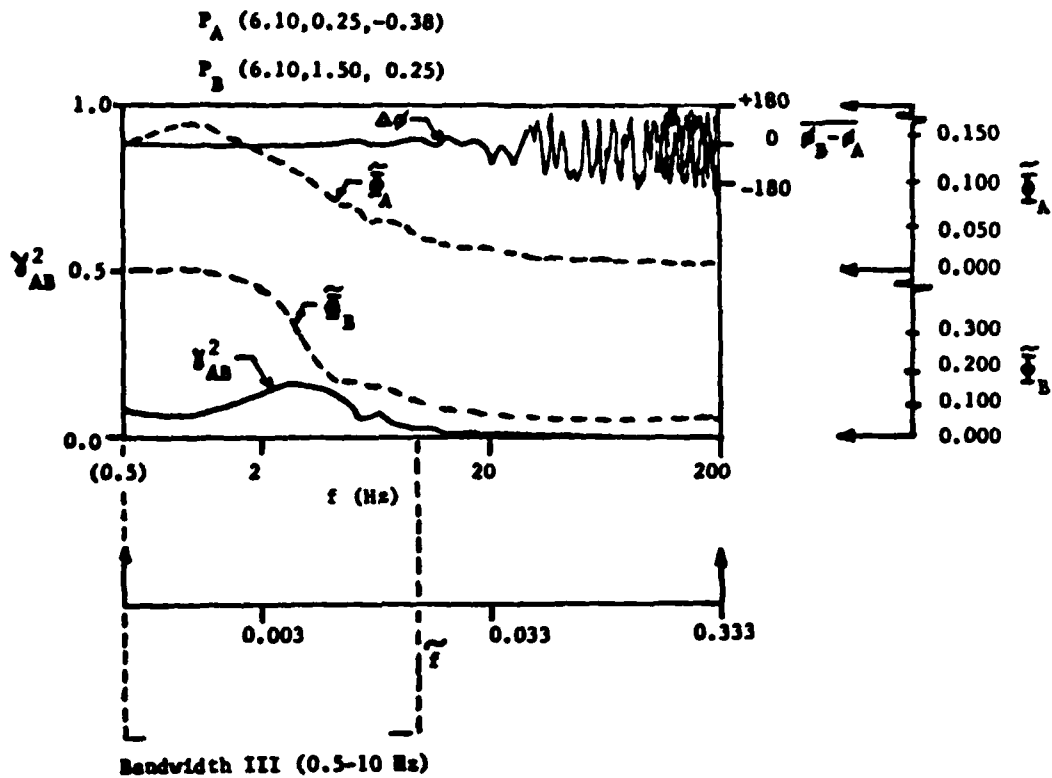
Figure 6-30: Contours of Constant  $S_y$  for Region VI  
( $P_A$  in Wing Shadow)



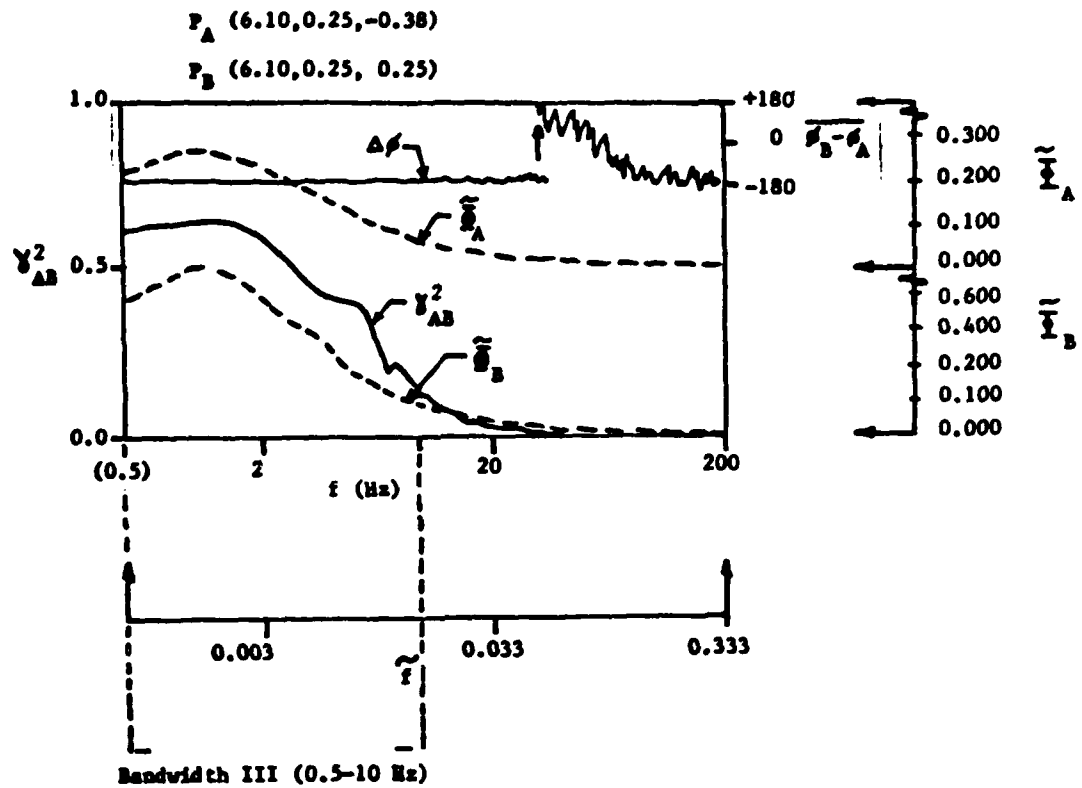


6-31(a): First Correlation Region ( $y_o/b, z_o/t$ ) = (1.25, -0.25)

Figure 6-31: Example Spectral Distributions of Correlation Measurement Data for Region VI ( $P_A$  in Wing Shadow)



6-31(b): Second Correlation Region  $(y_o/\delta, z_o/t) = (1.50, 0.25)$



6-31(c): Third Correlation Region  $(y_o/\delta, z_o/t) = (0.25, 0.25)$

and Bandwidth II (25-80 Hz). Apparently the new Bandwidth III (0.5-10 Hz) did not simply drown out the two other bands, which are apparently missing for correlations with  $P_A$  (6.10, 0.25, -0.38).

On the other hand, positioning the probe  $P_A$  further from the wing wake in the lateral direction produced correlations for Bandwidth II (25-80 Hz) as well as Bandwidth III (0.5-10 Hz). Figures 6-32 and 6-33 show the correlation contours for the fixed probe at  $P_A$  (6.1, 0.25, -0.75), which was twice as far from the nominal wake centerplane ( $z/t = 0.0$ ) as was the position for the contours presented in Figure 6-30. In fact, the position  $P_A$  (6.1, 0.25, -0.75) was outside the projected profile of the wing (thickness) onto the measurement plane.

The correlation contours shown in Figure 6-32 are for the frequency Bandwidth III (0.5-10 Hz) and can be compared to the contours shown in Figure 6-30. The comparison shows that the correlations are quite different. With the fixed probe closer to the wake centerline the correlation regions, shown in Figure 6-30, were "pockets" of positive and negative values which, for one thing, did not extend completely through the boundary layer. On the other hand, the correlations obtained with the fixed probe further from the wake centerline, shown in Figure 6-32, clearly show that both the regions of positive and negative correlation extend from the wall to the edge of the boundary layer.

The correlation contours shown in Figure 6-32 are similar to the contours shown in Figure 6-4 for the onset boundary layer. There are two distinctions however. First, the frequency Bandwidth III (0.5-10 Hz) for the wing-body junction wake flow (Figure 6-32) is different than that for frequency Bandwidth I (2-65 Hz) for the onset boundary layer (Figure 6-4). Second, there were three correlation regions measured in the direction of increasing  $z/t$  relative to the position of the fixed probe in the wing-body junction wake flow, while the onset boundary layer measurements showed only two regions.

Figure 6-33 shows the correlation contours for Bandwidth II (25-80 Hz). That frequency band was first observed in the wing-

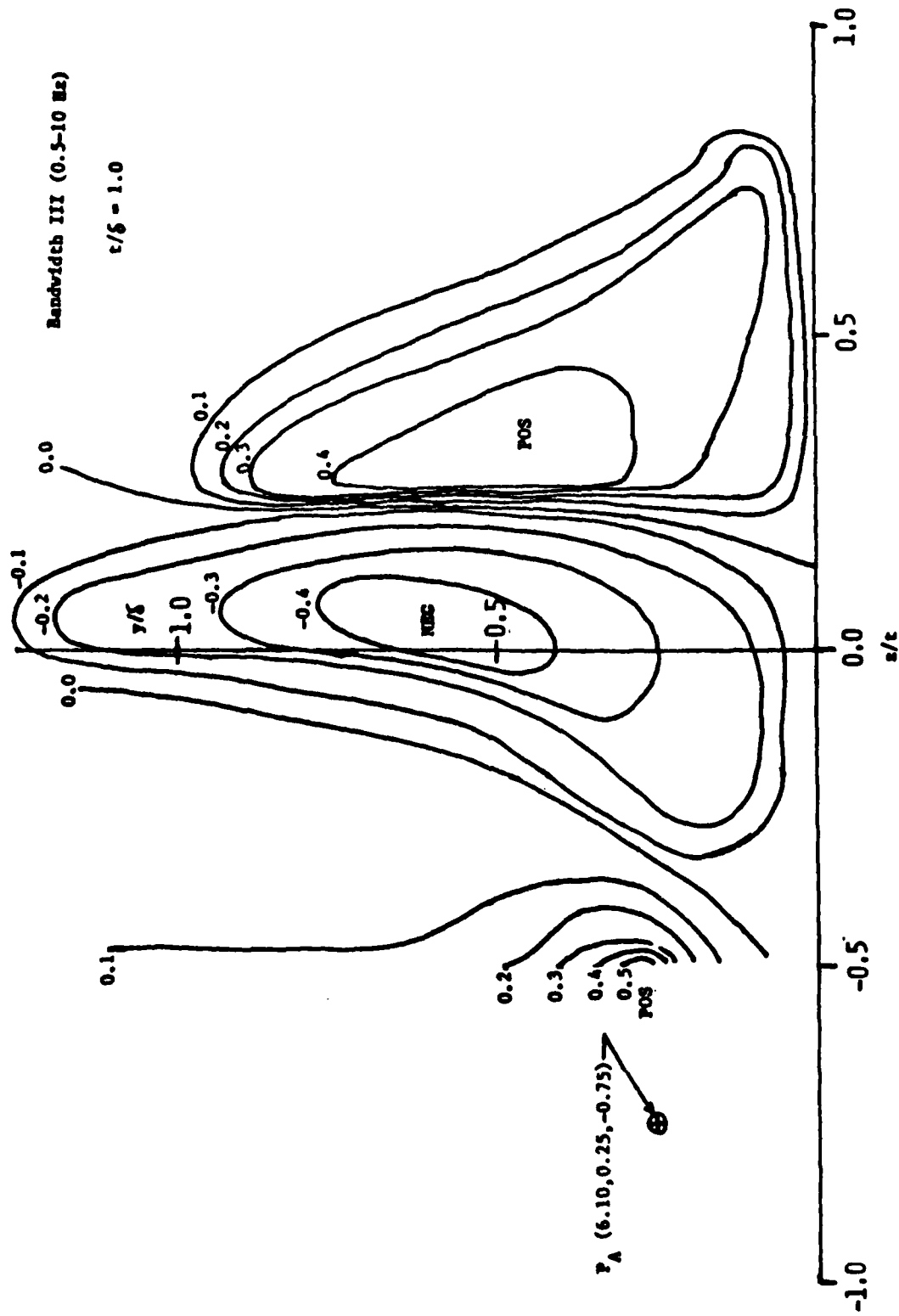


Figure 6-32: Contours of Constant  $S_y$  for Region VI for Bandwidth III  
 ( $P_A$  Outside Wing Shadow)

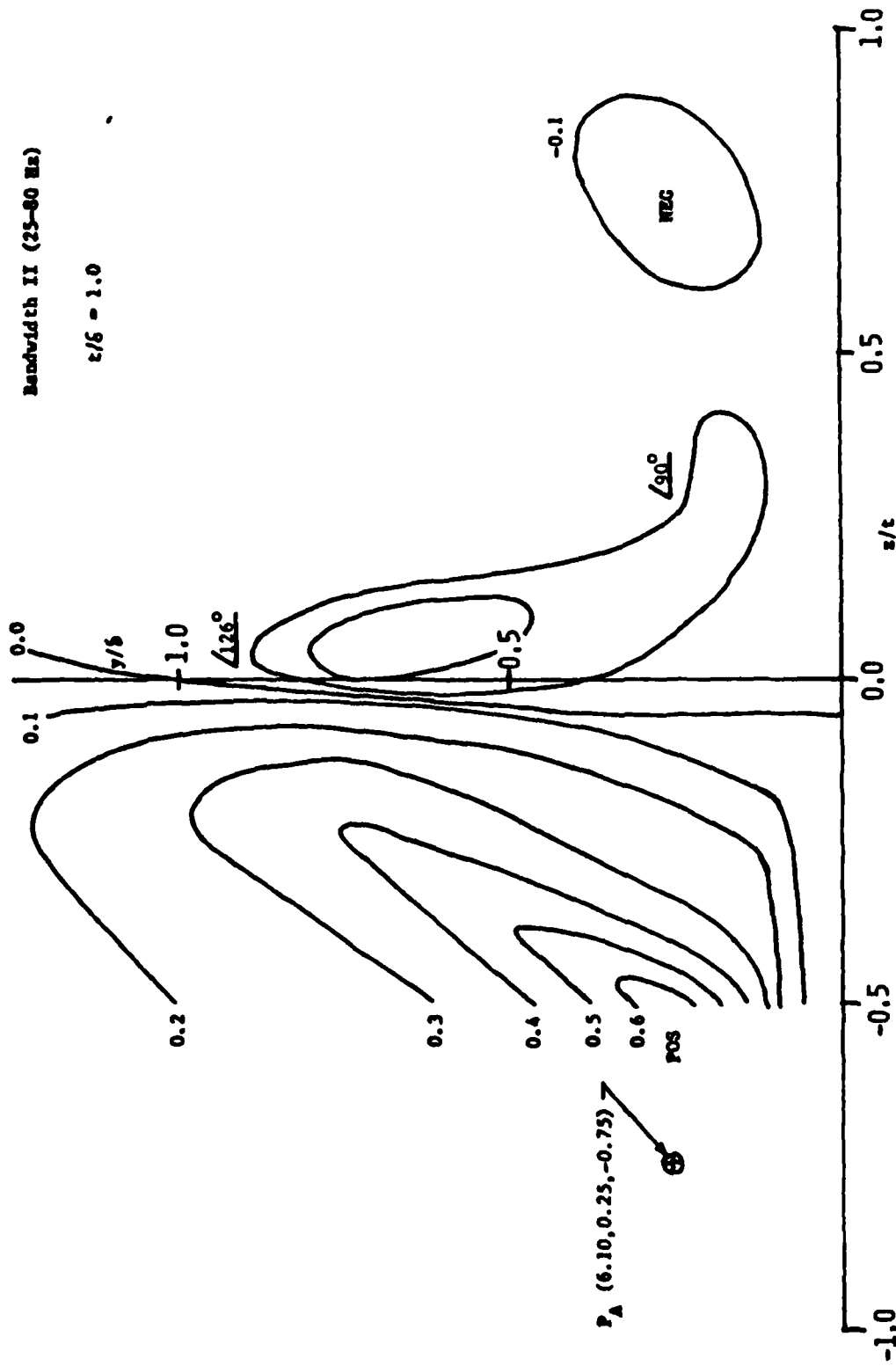
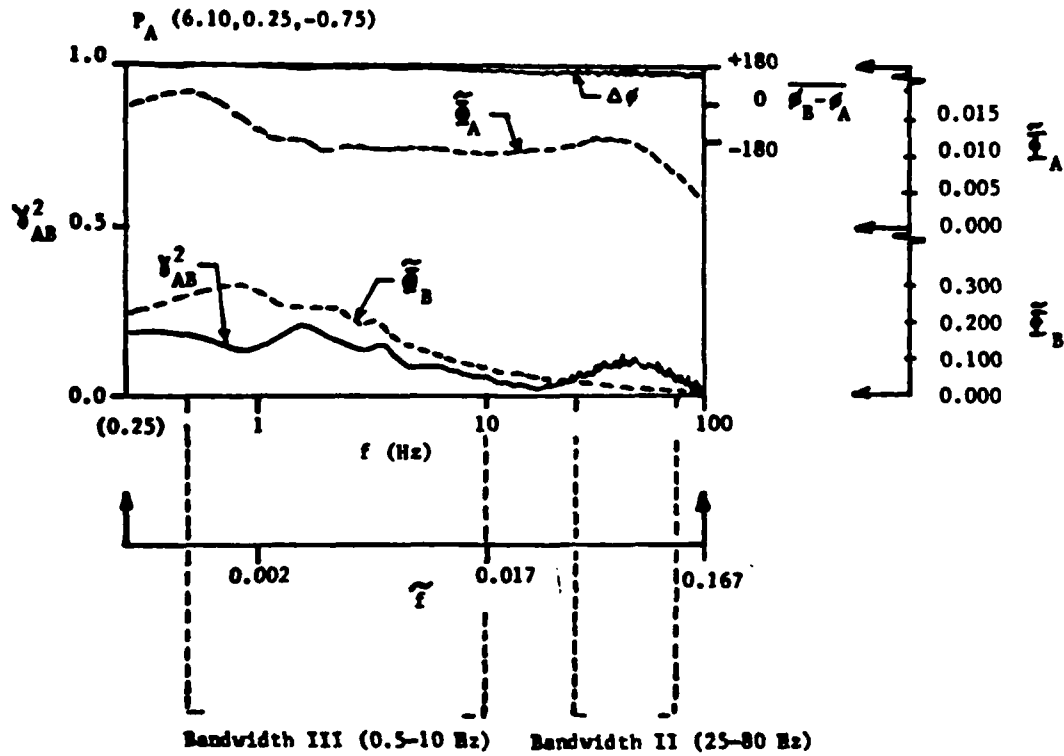


Figure 6-33: Contours of Constant  $S_y$  for Region VI for Bandwidth II  
( $P_A$  Outside Wing Shadow)

body junction flow. Apparently the disturbance associated with that frequency band persisted into the wake flow and grew in spatial extent. The contours in Figure 6-33 for Bandwidth II (25-80 Hz) are not similar to those obtained at the same location for the Bandwidth III (0.5-10 Hz). For one thing the width of the positive region surrounding the fixed probe is twice as wide. Furthermore, there is a region of gradual spatial change in the relative phase between the large region of positive phase and the small region of negative phase. There are only two, rather than three correlation regions in the direction of increasing  $z/t$ .

Figure 6-34 is an example of the measurement spectra that clearly shows that the two frequency bands described above were experimentally distinguishable.

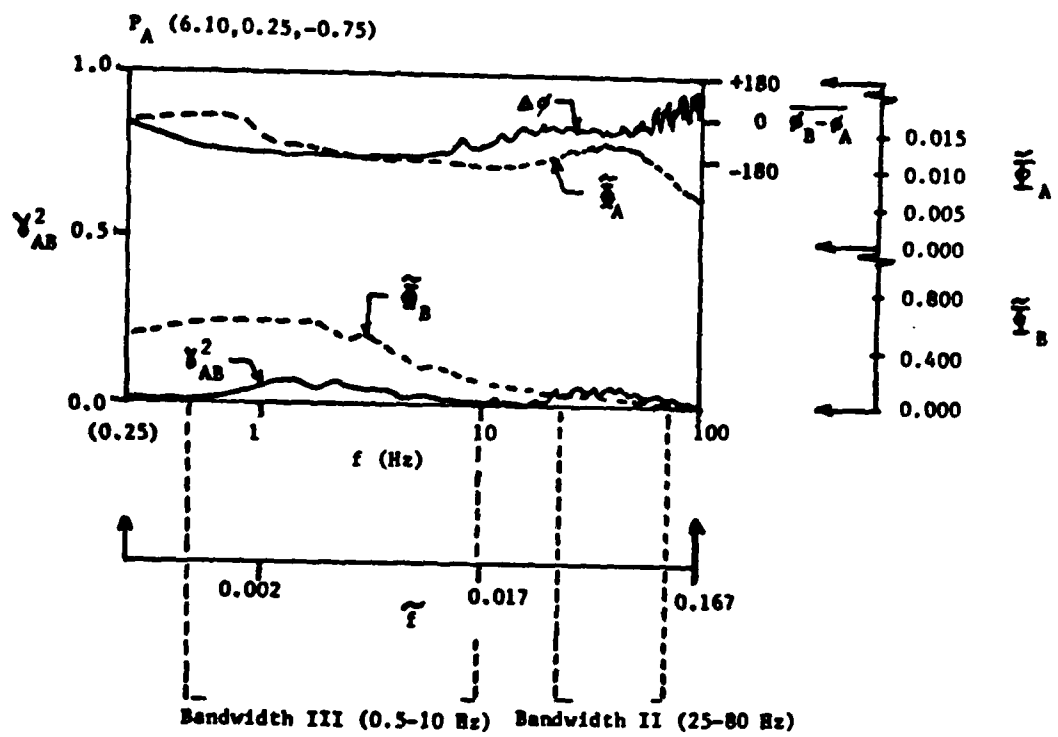
The measurements indicate that there were two kinds of flow structure in the wing-body junction wake: a vertically arranged structure outside the wing wake proper with regions of positive and negative phase each extending from the wall to the edge of the boundary layer, and an antisymmetrically arranged structure in the wake proper that was characterized by pockets of positive and negative correlation. The vertically arranged structure exhibited frequencies in Bandwidth II (25-80 Hz) and Bandwidth III (0.5-10 Hz). The spatial patterns of the correlation regions were different for the two bandwidths. On the other hand, antisymmetrically arranged structure exhibited frequencies only in Bandwidth III.



6-34(a):  $P_B (6.10, 0.50, 0.00)$

Figure 6-34: Example Spectral Distributions for Correlation Measurement Data for Region VI Showing Bandwidth Separation  
 $P_A (6.10, 0.25, -0.75)$





6-34(b):  $P_B (6.10, 0.10, -0.25)$

## CHAPTER 7

### THE MEASUREMENT RESULTS: INTERPRETATION, CONJECTURE, CONCLUSIONS

In view of the complexity of the wing-body junction flow, and the limited data available in the open literature, it was expected that this experimental investigation would raise new questions about the governing physics of the flow. This clearly has been the case. The investigation accomplished the objective of showing that the wing-body junction flow is characterized by large scale time dependent flow structure. The investigation established an orderly framework of discussion and observation around which additional research can be performed to uncover the quantitative governing physics. As shown in the results, distinct features of the flow structure are inherent in the onset boundary layer, and others are introduced by the wing-body junction flow, and still other unique features are created in the wing-body junction wake flow in the trailing edge region.

The results show that the frequency and spatial extent of the structure originated at the trailing edge is governed in part by the mean flow quantities around the wing nose geometry. The

mechanics of the structure originated in the trailing edge region, as a consequence of the wing geometry, were only broadly defined by the present investigation. Furthermore, the apparent stability observed in this investigation of the flow in the leading edge region should not be construed as a universal feature of the wing-body junction flow. Rather, the conclusion should be that the particular fixed parameters in this investigation constrained the motion of the leading edge vortex separated flow.

The author believes that variation of the defining parameters will, in some cases, produce an unstable leading edge vortex flow. There is no a priori reason that flow separation in that region should be steady; all the information at hand suggests that it should be unsteady; see, e.g. Simpson, et al. (1981) in regard to unsteady two-dimensional separation in an adverse pressure gradient. In fact, support for this statement is found in the present investigation at the trailing edge of the wing. An observed separation pattern indicative of adverse pressure gradients was associated with the production of large scale time dependent flow structures in the wing-body junction wake flow.

Inasmuch as the measurements require additional detail to determine the quantitative governing physics, the discussion of results will address only the phenomenological description of the flow. The notable contribution of the interpretation presented in this chapter is to provide a guide for future research, and to provide credibility for the present investigation by presenting a physical framework for discussion in which the measurements are mutually consistent.

The discussion is presented in three sections. The first section examines the meaning and limitations of the two-point velocity correlations and the correlation contours; the second section discusses the physical interpretation of the flow phenomena that can be made from the measurements; and finally, the third section presents a list of conclusions drawn from this investigation.

### 7.1 Interpretation of the Two-Point Correlation Contours

The measurements of velocity correlation contours presented

in this investigation require careful interpretation because of the averaging process involved, and because of the extrapolation of two-point statistics to multipoint statistics that is implied by the correlation contours. The coherence obtained between two measurement positions was the result of an averaging process that necessarily loses information. For example, it is not apparent whether the measured frequency bandwidth was produced by multi-frequency structures of constant amplitude or if it was produced by constant frequency structures with variable amplitudes. Nevertheless, the implication of non-zero coherence (the quantity from which the correlation contours were derived) is that there was mutual fluid motion at the two measurement positions. It is expected that the averaging process understated the true spatial correlation of individual flow structures.

The correlation coefficient obtained from the square root of the coherence is a measure of joint probability density under Gaussian conditions. The correlation coefficient is very simply interpreted as a measure of the fractional part of the velocity fluctuation at position B that is linearly related to the fluctuation at position A. But this interpretation must be broadened by a reference to joint probability density statistics to have physical meaning.

An understanding of the physical meaning of the concept of a correlation coefficient for each frequency can be obtained by examining the probability density associated with the two-point velocity correlations. It is developed in this section that the correlation coefficient specifies both the slope of the linear curve fit between the two velocity fluctuations and the statistical distribution of the velocities about the linear fit. The reference for the following discussion is Jenkins and Watts (1968, p.67, 74, 109). Information in that reference has been specially applied by this author to an analysis of the present measurements.

The joint probability density function for a given frequency of the velocity fluctuations  $u_A'$  and  $u_B'$  at positions  $P_A$  and  $P_B$ , respectively, is the following:

$$f_{AB}(u_A', u_B') = \frac{1}{2\pi\sigma_A\sigma_B} \left( \frac{1}{1-\rho_{AB}^2} \right)^{1/2} \exp \left\{ \frac{-1}{2(1-\rho_{AB}^2)} \left[ \left( \frac{u_A'}{\sigma_A} \right)^2 + \left( \frac{u_B'}{\sigma_B} \right)^2 - 2\rho_{AB} \left( \frac{u_A'}{\sigma_A} \right) \left( \frac{u_B'}{\sigma_B} \right) \right] \right\}$$

where  $\sigma_A$ ,  $\sigma_B$  denote the root mean square velocity fluctuations at  $P_A$  and  $P_B$  for given frequency  $f$  and  $\rho_{AB} = \frac{\overline{u_A' u_B'}}{\sigma_A \sigma_B}$  is the correlation coefficient. In the case where the fluctuations are either in-phase or out-of-phase,  $\rho_{AB} = \pm 1$ .

The argument of the exponential is the equation for an ellipse oblique to the  $u_A'$  and  $u_B'$  axis. For  $\rho_{AB} = 0$ , the equation describes a circle, and the lines of constant probability density  $f_{AB}(u_A', u_B')$  are concentric circles. For non-zero values for  $\rho_{AB}$ , the lines of constant probability density form ellipses rotated in the  $u_A'$  and  $u_B'$  plane. Figure 7-1 shows the contours  $2\pi\sigma_A\sigma_B f_{AB}(u_A', u_B') = 0.5$  for two values of  $\rho_{AB}$ , 0.0 and 0.5. The least squares linear fit of  $\frac{u_B'}{\sigma_B}$  as a function of  $\frac{u_A'}{\sigma_A}$  is also shown in the figure; the slope of the line is equal to the value of  $\rho_{AB}$ .

Figure 7-2 shows additional significance of the linear fit determined by the value of  $\rho_{AB}$ . The several shaded bars in the figure represent ranges of values for  $u_B'$  corresponding to a certain probability for occurrence. There are two ranges, or bars, presented for each of five values for  $u_A'/\sigma_A$ , (-1.0, -0.5, 0.0, +0.5, and +1.0). One of the two ranges is for  $\rho_{AB} = 0.0$ , and the other is for  $\rho_{AB} = 0.5$ ; the two ranges are noted in the figure and distinguished by the shading patterns. The ranges represent the interval, centered on the mean value of  $u_B'/\sigma_B$ , in which 70 percent of the values of  $u_B'/\sigma_B$  will lie when

$$\frac{u_A'}{\sigma_A} - \delta < \frac{u_A'}{\sigma_A} < \frac{u_A'}{\sigma_A} + \delta,$$

where  $\delta$  is an infinitesimal interval.

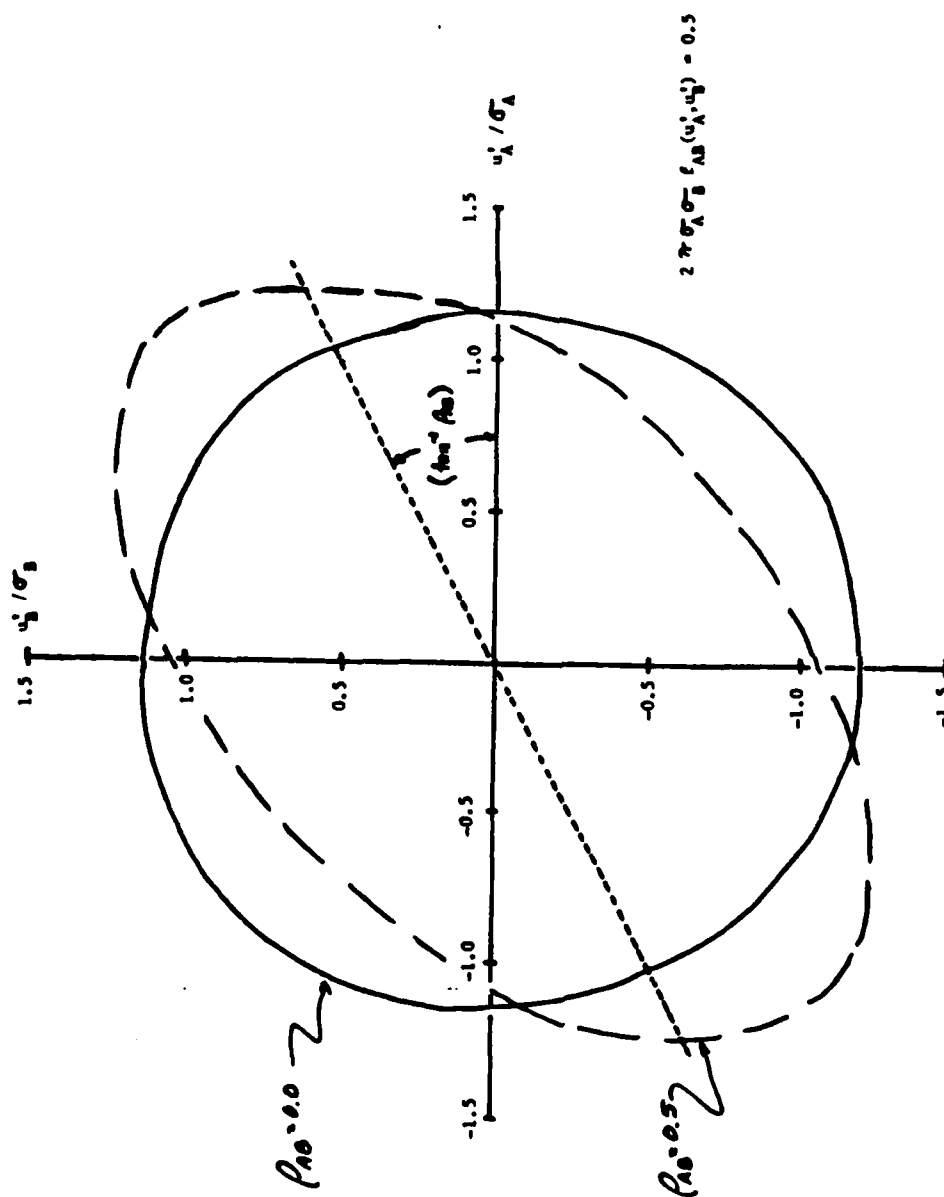


Figure 7-1: Joint Probability Density Function Contours for Two-Point Velocity Correlations



Figure 7-2 shows that increasing  $\rho_{AB}$  decreases the statistical spread as it increases the expected mean value of  $u_B'$  for a given value of  $u_A'$ . Note, however, that the figure cannot be used to make probability predictions at the different values for  $u_A'$ ; to make that comparison the joint probability along the  $u_A'$  axis would have to be examined.

A physical interpretation of the meaning of Figure 7-2 is presented in Jenkins and Watts (1974, p.74), where typical scatter diagrams for several values of  $\rho_{AB}$  are presented. The scatter diagrams show sets of discrete measured values of  $(u_A', u_B')$  that could be obtained in an actual situation. Jenkins and Watts state that data for  $\rho_{AB} = 0.5$  is weakly correlated.

To apply this statement to the present measurements will require additional experimental information. The statement is surely correct considering all the measurement data with equal weighting. However, if the flow structure is only present part of the measurement time, and absent for the remainder, the type of measurement presented in this investigation would lead to weak correlations. It would be more exact and revealing to measure correlation only while the structure was present and to separately measure the fraction of time that it is present. This technique of conditional sampling has yet to be developed for the present problem.

The correlation contours seem to imply that the flow through the measurement plane is, on the average, mutually related at arbitrary positions according to values of the contours at the specific positions. This is, in general, not correct unless certain other conditions are present because the contours are functions of the positions of the reference probe. For example, the correlations  $AB_1$  and the  $AB_2$  do not imply anything about the correlation  $B_1B_2$ . Hence, the contours cannot be used to describe mutual association between velocities at two measurement positions neither of which is at the reference position. In fact, study of the correlation contours shows quite explicitly that the numerical contours can be quite different for different reference positions.



Physical meaning in terms of large scale movement of the flow can be obtained from the correlation contours. To obtain this meaning one must have certain perceptions of the flow. These perceptions are developed below in two steps. First, the physical meaning of the contours in the onset boundary layer is presented.

#### 7.1.1 Contours in the Onset Boundary Layer

The onset boundary layer is a classical equilibrium boundary layer and the mean flow results can be compared with those in the open literature (Section 4.1).

The correlation contours obtained in this investigation are also consistent with results obtained previously by Favre, et al (1958). The measured positive correlation contours surrounding the reference probe position in this investigation are across-stream planar cuts from the streamwise elongated correlation surfaces reported by Favre, et al. These elongated surfaces can be envisioned as representing "cigar-shaped" structures.

Although three-dimensional correlation contours were not obtained in the present measurements, other information that was obtained can be used to demonstrate that the flow structure was streamwise elongated. The low frequency disturbance bandwidth for the present data implies a long correlation distance in the longitudinal direction. Example auto-correlation functions at  $P_A$   $(-1.00, 0.25, -0.25)$  and  $P_B$   $(-1.00, 0.10, 0.25)$  are shown in Figure 7-3. It is estimated from the figure that flow structure existed at each measurement position for 0.75 seconds. Invoking Taylor's frozen eddy hypothesis and estimating the local mean flow speed, 27 m/s, one arrives at a correlation distance equal to 20m. This length is two orders of magnitude larger than the lateral or transverse dimensions of the structure; hence the structure is elongated.

The present investigation elaborated on the phenomena reported by Favre by measuring the adjacent negatively correlated finite flow region adjacent to the elongated positively correlated region. The appearance of negatively correlated regions of the flow makes sense; a thrust of fluid, as in the form of a finger

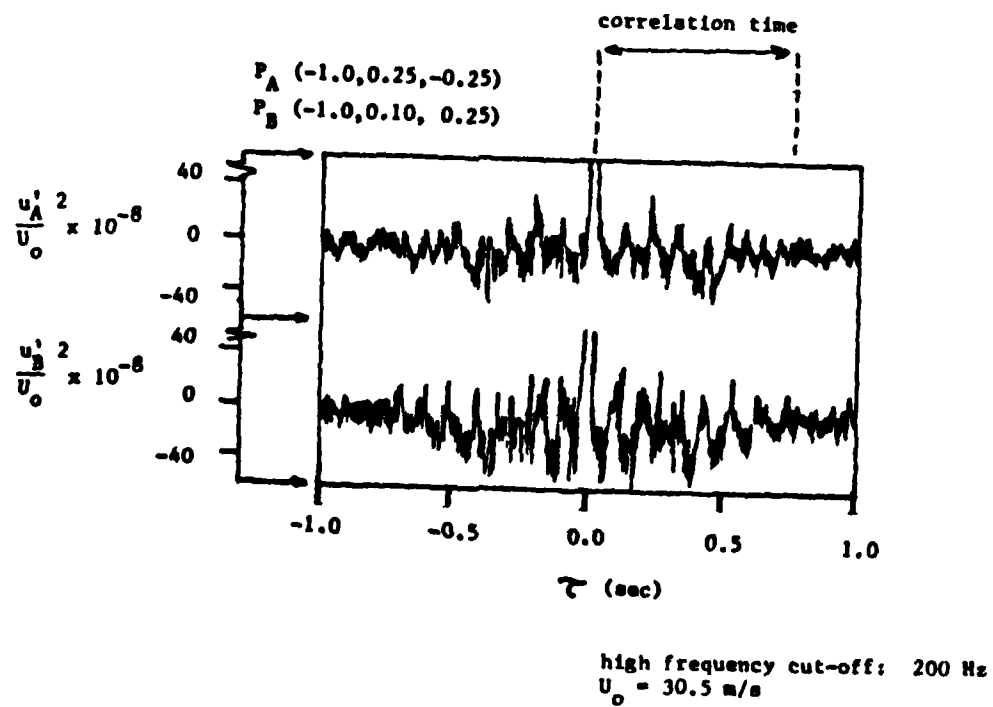


Figure 7-3: Example Auto-Correlation Functions for Onset Boundary Layer

of jetting fluid, would be expected to be accompanied by a deceleration of the fluid on either side to satisfy continuity of flow. This result is not new; Champagne, et al (1970) measured negative correlations outside the positive region, i.e., at distances beyond the first zero crossing of the correlation function, but the correlation function measurement technique employed at that time was not refined enough to produce accurate results. Furthermore, the negative correlations were observed to extend to the wall bounding the fluid. In that case it would be expected that the large-scale flow structure was representative of duct flow rather than boundary layer flow because the end wall conditions contributed to the measured flow.

In the present experiment the technique employed Fast Fourier Transforms and solid state computer micro-chip electronics to provide both nearly real time low frequency analysis and a significant improvement in accuracy. Furthermore, the observed negative correlation region was an order of magnitude smaller than the wind tunnel width. The small size of the negatively correlated region, relative to the tunnel width, satisfied one requirement of Comte-Bellot and Corrsin (1971) for separating fluid dynamic negative correlations from measurement instrumentation, or network, negative correlations (see Section 5.6 for a discussion). Furthermore, the finite lateral negative correlation region decoupled the measured flow from the tunnel end wall boundary layers. Therefore, it is believed that the measured low frequency "eddies" were not products of duct flow but rather of the flat plate boundary layer.

The specific correlation contours for these "eddies" generally depend on the location of the fixed probe. It is difficult to interpret the meaning of "superimposed" two-point correlations from two reference positions. However, certain conclusions are plausible from two-point correlations if the domain of influence of the velocity at one reference position is coexistent with the domain at another position, providing the two reference positions are correlated. Consider the correlation con-

tours for the onset boundary layer in Figures 6-4, 6-7, and 6-8. The figures show that in general the regions of positive and negative correlation are independent of the position  $y$  for reference positions  $(x_0, y, z_0)$  where  $x_0$  and  $z_0$  are points inside the boundary layer.

Under these conditions it is plausible that the flow moved as occasional (quasi-random) wholesale movements in fairly large regions defined by the signs of the correlation regions, and that this movement occurred at random positions in the boundary layer. Furthermore, the movements may have had overlapping structure.

#### 7.1.2 Contours in the Wing-Body Junction Flow

The large scale time dependent flow structure in the onset boundary layer has phenomenological description in the notion of elongated correlation surfaces. However, that description fails in the wing-body junction flow for two reasons. First, the mean vortex flow inverts the boundary layer, thereby deforming the elongated correlation surfaces in the lateral and transverse directions. Second, the inversion transports high energy fluid into the lower energy region of the boundary layer. There is a longitudinal "jetting" of high momentum fluid through the low momentum fluid. Hence, the correlation contours become distorted in the longitudinal direction.

The result is that a material line of particles coinciding with a contour of constant correlation in the measurement plane is distorted as it moves downstream. Original material planes become distorted surfaces. Hence it would be expected that correlations in  $(y, z)$  planes would decrease as  $x_0$  increases. This apparent dissipation is in addition to the shear and diffusive forces which also decrease the correlations.

In this investigation only correlation contour measurements in planes were made. However, no apologies are made for not mapping correlations in three-dimensional space because the precise manner in which the data will be used is open to speculation.

A suggested first order treatment of the data for large scale force calculations is presented in the next section.

### 7.1.3 Integrated Flow Structure

A numerical measure of the size of the large scale flow structure is needed to visualize its importance relative to the rest of the flow and in order to estimate its significance in engineering calculations. An example of engineering type calculations is the vibratory impact of the flow structure on rotating machinery downstream from the wing.

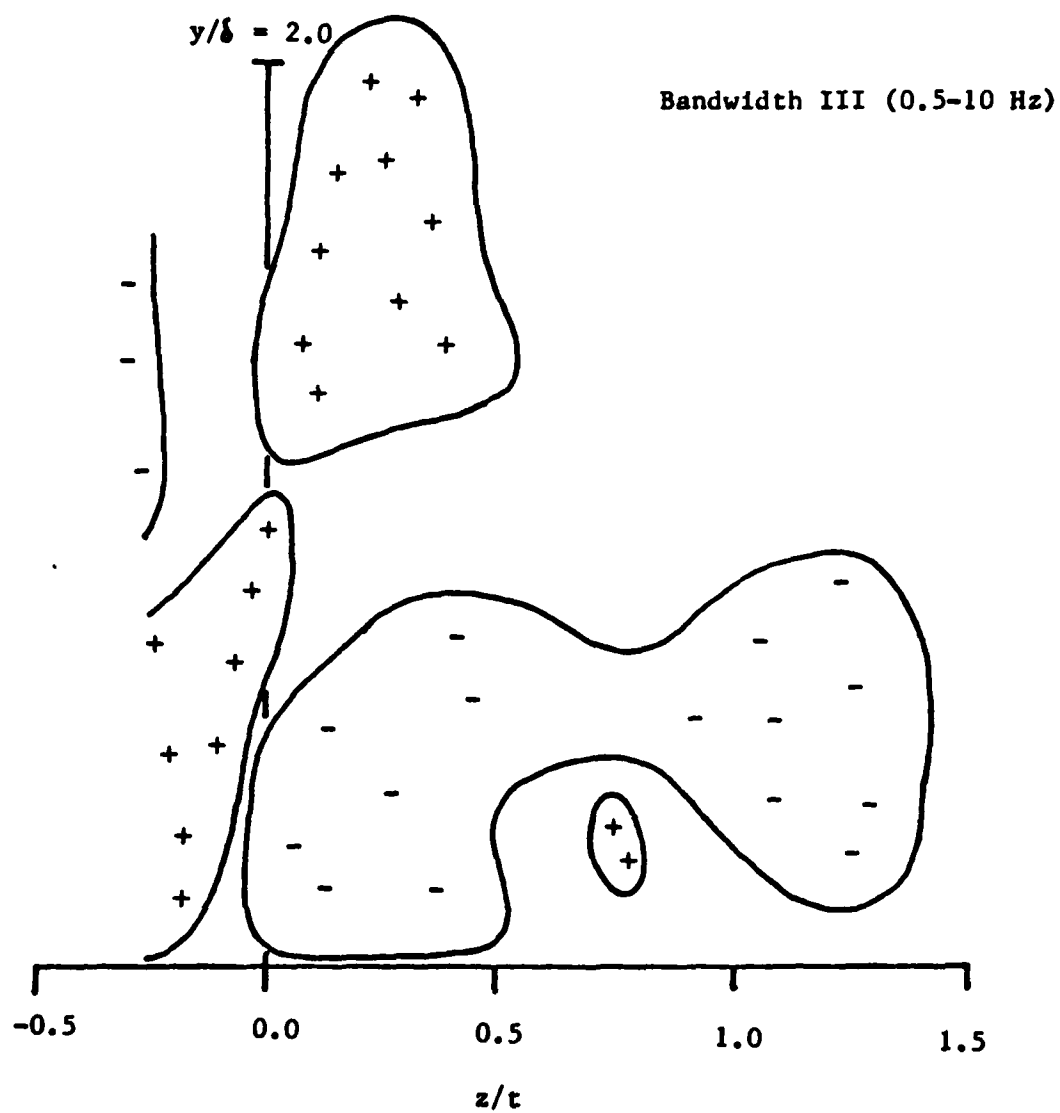
The reasoning for the numerical measure proposed below begins with the notion that the structure is elongated in the streamwise direction. The present investigation shows that in almost all cases the correlations were either almost in-phase or out-of-phase. Because the large scale structure had a wavelength much larger than either the wing chord length or the boundary layer thickness, it is estimated that the longitudinal distortion of the correlation surface produced insignificant relative phase changes in planes within a few wing chord lengths downstream from the trailing edge. This estimate may not be accurate further downstream.

It is proposed that the numerical measure of the size of the large scale flow structure be the area bounded by the  $S_y = 0.3$  correlation contour, where the reference probe is placed at a position that maximizes the area within the 0.3 correlation contour surrounding the reference probe. The wholesale coherent movement of fluid within that boundary is defined to be the integrated flow structure applicable for engineering type calculations. The choice of the 0.3 correlation contour was made from observations that the data for  $S_y < 0.3$  (coherence  $\sim 0.1$ ) were noticeably less reliable than data for  $S_y > 0.3$ .

An example application of the integrated flow structure to the data in the measurement plane ( $6.05, y/\delta, z/t$ ) is shown in Figure 7-4. In this figure, which was prepared from Figure 6-30, it is assumed that the reference probe was at the maximal position described above.

### 7.2 Conjecture About The Large Scale Time Dependent Flow Structure

This section contains speculative arguments which are



(from Fig. 6-30)

Figure 7-4: Spatial Location of Integrated Flow Structure  
Immediately Downstream from the Wing Trailing  
Edge

intended to provide a framework for further discussion of the time dependent flow in the wing-body junction. Clearly the flow is complex and a complete mapping of detailed measurements sufficient to define the entire flow over a range of parameters would be an expensive undertaking. Hence, it is desirable to establish a model flow in terms of a visual construct that can suggest additional measurements to test the validity of the model. The model must be continuously modified to be consistent with the new evolving information. At any time, a model must be considered consistent if it explains the data in hand and if it is otherwise based on fundamental fluid mechanics theory or observation.

The phenomenological description presented below is based on the measured velocity correlations, mean flow velocity and pressure, and flow separation patterns obtained during the present study. However, the results from previous studies are readily introduced where appropriate to elaborate on the flow description. In some respects the description to follow is a conjecture by the author gleaned from all the bits and pieces of information, both in the literature and from actual experiment, that were obtained throughout this investigation.

#### 7.2.1 The Onset Boundary Layer (Region I)

The observations indicate that the onset boundary layer, independent of the presence of the wing, contains large scale time dependent flow structure, or organized motion of the flow that is confined both in time and in space. The structure is convected by the mean flow and produces features similar to those expected for a longitudinal acceleration, or jetting, of fluid with flow deceleration, or reversal, on either side of the jet; see Figure 7-5. The amplitude of the fluctuating velocity in the structure is a small fraction of the mean flow speed. Hence the structure is manifested as a small perturbation of the mean flow. The structure has spatial extent with height and width on the order of the boundary layer thickness, and length an order of magnitude larger. The frequency for the structure is low ( $f\delta/U_0 = 0.04$ ), on the order of one-

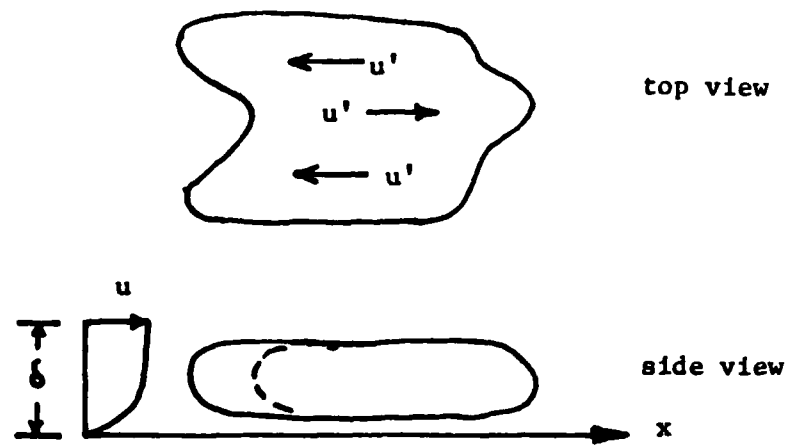


Figure 7-5: Jetting Model of Flow Structure

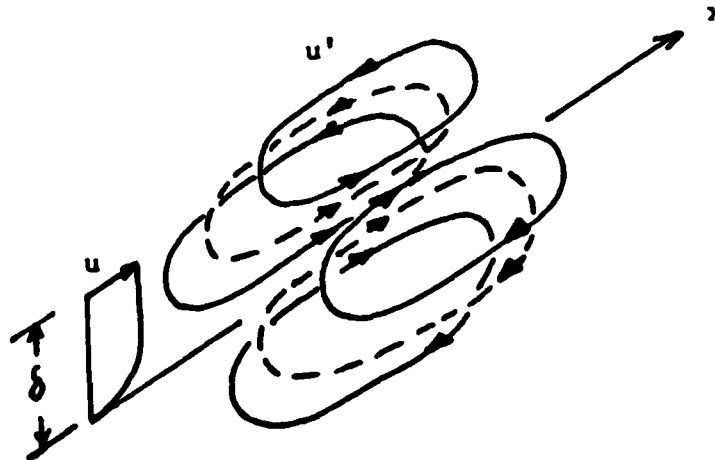


Figure 7-6: Eddy Model of Flow Structure



fifth the typical energy carrying frequencies ( $f\delta/U_0=0.2$ ); see Rao (1971).

The structure is similar to an elongated body of fluid, with parts further from the wall moving faster and with the velocity at the center of the body fluctuating in the opposite direction to that at the outer parts in the lateral directions.

The concept of a jet of fluid is possibly a too restrictive description of the structure. A more versatile model that is also consistent with the measured velocity correlations is a large eddy motion in which the structure consists of convected counterrotating eddy pairs, or even higher multiple order arrangements; see Figure 7-6.

The readily apparent difference between the two models is the degree of cross-velocity in the lateral ( $z$ ) direction. The larger the cross-velocity, the more eddy-like the structure. To assess the appropriateness of either of the jet and eddy models, detailed measurement of the spatial and temporal features of the lateral velocity component would have to be made under carefully controlled test conditions.

For both models, the fluid motion is vertically structured. That is, it has nearly constant phase in the transverse ( $y$ ) direction in the boundary layer, i.e., from the wall to the free stream. The phase is, however, a function of lateral ( $z$ ) position consistent with the observed flow reversals.

The actual motion of the fluid may be a superposition of a large number of the flow structures described above, or it may consist of a small number of structures of larger amplitude. The subsequent flow produced by the wing may depend on the "density" of the structures in the onset boundary layer.

### 7.2.2 The Effect of the Wing

#### 7.2.2.1 Region II (Pressure Driven Boundary Layer)

In the present investigation the upstream onset boundary layer structure was largely unaffected by the presence of the pressure gradient produced by the presence of the wing. In fact the structure was observed to maintain its spectral distribution even as

it passed downstream through the leading edge separation region. This observation can result from at least two possible descriptions of the flow dynamics depending on whether the flow structures are sparse or superimposed.

In the first description, the flow structure is a single organized motion that, in general, passes to one side or the other of the pressure ridge. The pressure differential across the ridge produces an oscillation of the ridge which if present in this study was not sufficient to result in a resonant motion. The second description envisions a superposition of many structures randomly positioned in space. The overlapping structures, passing to either side of the pressure ridge, are of sufficient number that the net pressure differential across the pressure ridge is almost zero.

The present measurements are not in sufficient detail to resolve which, if either, of the descriptions is appropriate. The reason is that the measurements are ensemble averages of the time dependent characteristics of the flow. It is not possible to determine if the measurements were of successive structures passing the probes, or of superimposed structures continuously passing the probes. Additional information about the structure will have to be obtained from conditional sampling techniques. It is conjecture by this investigator that the true answer is that the structure is a superposition of many structures, but not very dense or else the correlations would be nearly zero for even very small distances.

#### 7.2.2.2 Region III (Leading Edge Separation Region)

These slightly overlapping structures pass almost intact through the separation region near and upstream from the leading edge of the wing. However, the structure is stretched in the lateral direction as the mean flow passes to either side of the wing. As the structure initially passes to the side of the wing nose, it is "turned over" by the mean cross-flow, or circulation, in the root vortex. The mean flow circulation transports momentum, first from outside the boundary layer down into the wing-wall junction; secondly, out from the junction along the wall; and finally, up

into the boundary layer. Because of this transport a second structure with a bandwidth of larger frequencies than those measured in the onset boundary layer is literally pumped from the wall region and up into the middle regions of the boundary layer. It is not clear from the measurements in this study if the second disturbance is produced by the presence of the wing such as from an oscillation at the separation line produced on the wall by the root vortex. This author suspects that it is the structure present in the wall region of the onset boundary layer that is transported away from the wall by the vortical circulation. Evidence supporting this statement is the small peak in the power spectral density in this higher frequency bandwidth observed for probe positions very near the wall.

The velocity correlations are positive for positions both near to the wing and positioned symmetric to the plane-of-symmetry of the wing. In effect the wing simply divides the onset boundary layer structure in a way that does not destroy its basic correlations, except very near the wing where the velocity and hence the correlation tend to zero as a consequence of the no-slip condition. In the presence of the wing, two fluid elements maintain their original correlation though the wing forces them further apart.

The correlations on either side of the wing are arranged in positive and negative regions that are generally independent of the location of the fixed probe within a fairly large latitude. Hence the flow around the wing has large-scale structure that is in-phase along the sides of the wing and out-of-phase further from the wing. The significance of this feature is that the wing provides an absolute reference for the large-scale structure, whereas there was no reference in the onset boundary layer. The importance of this reference is that there will be definite phase relationships between the fluctuations on one side of the wing and on the other side.

In the case of an infinite wing the regions of positive correlation remain quite large on either side of the wing; they are about equal to the boundary layer thickness in width. However, the

finite chord length wing exhibits much smaller widths for the positive regions, which introduces the possibility that the flow at the two sides of the trailing edge can be out-of-phase.

If the wing chord length is finite, the flow is at higher velocity along the sides of the wing than it is for an infinite chord length wing. The velocities at the sides of finite chord length wings can be sufficiently large to maintain a relatively large vorticity intensity. This effect is that the vortical transport can be sufficient to produce out-of-phase correlations at symmetric positions about the wing plane of symmetry; whereas, in-phase correlations are obtained for the infinite chord length wing. The explanation for the negative correlations is not that flow originally in-phase suddenly becomes out-of-phase flow close to the wing. The intense vorticity associated with the finite chord length wing transports flow toward the wing that was, in the onset boundary layer, separated by a larger lateral distance. That larger distance means that the flow was, in the onset boundary layer out-of-phase (or negatively correlated). Therefore the flow along the sides of the wing exhibits out-of-phase fluctuations and appears to have antisymmetric fluctuations about the wing plane of symmetry.

#### 7.2.2.3 Region IV (Developed Secondary Flow)

The root vortex produces large variations in the axial momentum distribution that decrease the structural features in two ways. First, the vortex motions literally produce a high speed fluid jet in the boundary layer near the wing-body intersection, and a low speed jet in the outer part of the boundary layer away from the wing-body intersection. The resulting velocity gradients produce shearing forces that dissipate the structure. Second, the inversion of the boundary layer produces distortion of the structure in the lateral, transverse, and longitudinal directions. The longitudinal distortion would be expected to decrease two-point velocity correlations in the transverse and lateral directions.

### 7.2.3 The Special Effects of the Trailing Edge

#### 7.2.3.1 Region V (Trailing Edge Separation Region)

The flow apparently undergoes dramatic changes in its characteristics as it passes through the trailing edge region of the wing. In this region the mean separation line on the wing, parallel to the trailing edge outside the boundary layer, is curved toward the trailing edge for a relatively thick wing as a result of the root vortex transport of high momentum into the momentum deficient boundary layer to delay separation.

It is believed that the trailing edge separation in Region V is the cause for the radical changes in both the frequency bandwidths and the correlation patterns observed in Region VI downstream from the trailing edge. These changes may be the result of a selection process in which there is enhancement of the correlations of fluctuations at certain frequencies of the onset disturbance, and suppression of others. The enhancement is governed by the "natural frequencies" of the separations on the wing and on the wall.

A schematic of the trailing edge separated flow is shown in Figure 7-7. The schematic shows the following major features: (1) the ordinary Strouhal-type shedding phenomenon outside the boundary layer, (2) a lower frequency shedding inside the boundary layer associated with the wing separation line curvature inside the boundary layer for Region V, (3) a divergent pair of separation lines on the wall for Region VI, separating the wake proper from the high energy outer parts of the wake, and (4) the rolled over vortex sheet in Region VI associated with the wall separation.

#### 7.2.3.2 Region VI (Wake-Boundary Layer Region)

The divergent separation lines on the wall in the wing wake are dependent on the vortical transport and the wing separation lines for both their included angle and their virtual origin (see Figure 7-7). In the present investigation the separation line on the wing curved to the trailing edge, delaying separation on the wall so that the separation lines on the wall were separated by an included angle of 70 deg and had a virtual origin, from which the

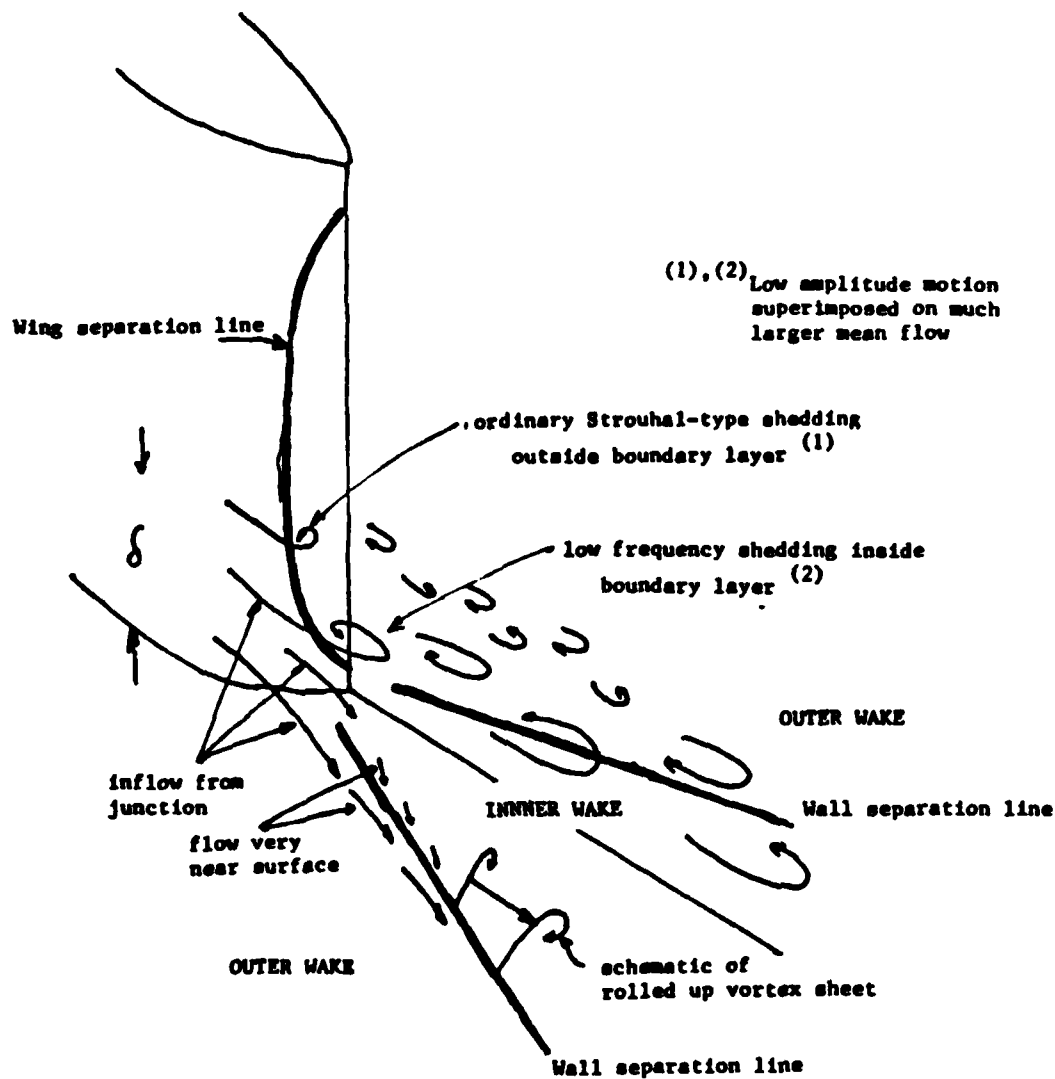
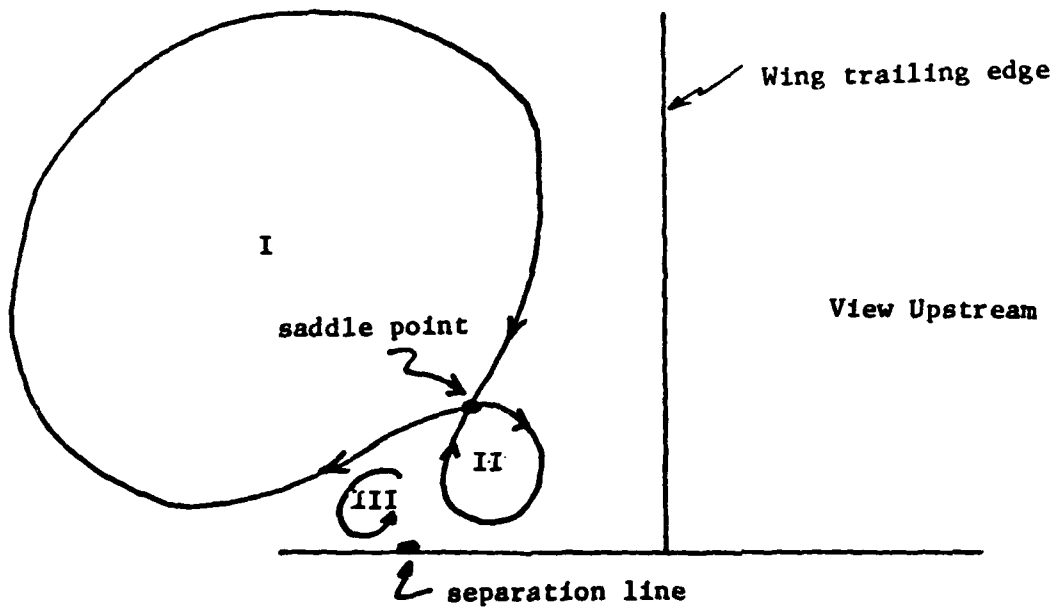
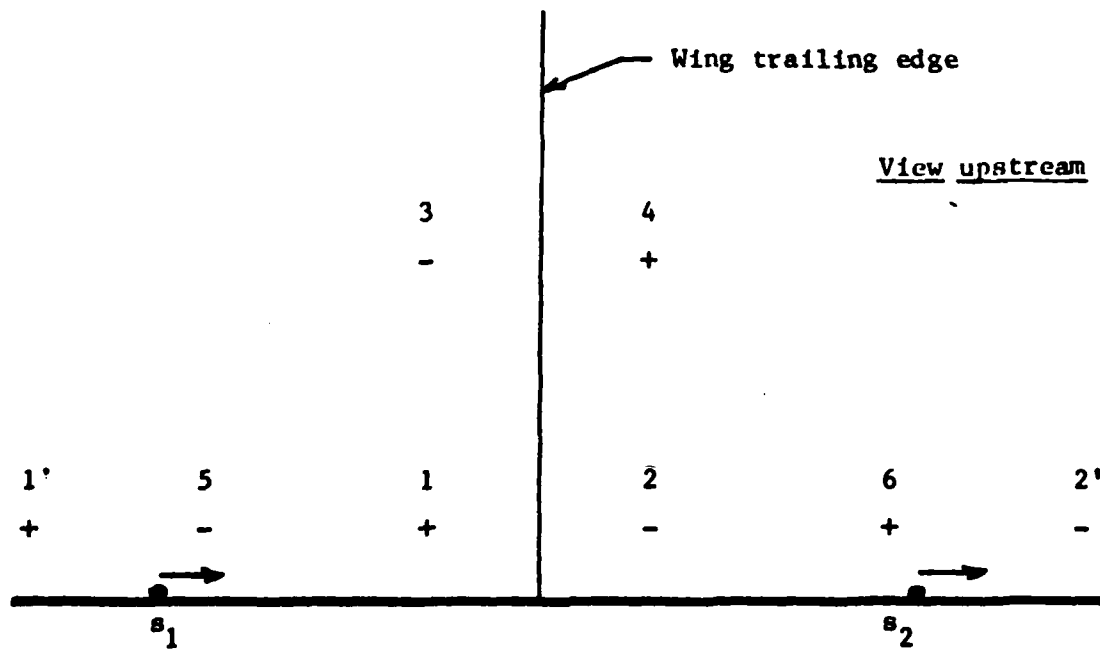


Figure 7-7: Schematic of Flow Structure and Separations at Wing Trailing Edge



- I - Root vortex
- II - Separation vortex sheet rolled up
- III - Third vortex - - low speed "pocket"

Figure 7-8: Schematic of Flow Parts in Vicinity of Rolled Up Vortex



- 1, 1' - structure jets fluid from junction and into wake, causing separation line  $s_1$  to move toward wake center
  - 2, 2' - deceleration of fluid at 2
  - 3 - " " " 3
  - 4 - acceleration " " 4
- } effects of flow continuity
- 5 - apparent deceleration of fluid as low speed vortex pocket at  $s_1$  moves toward wake center
  - 6 - apparent acceleration of fluid as low speed vortex pocket at  $s_2$  moves away from wake center

Figure 7-9: Schematic Identifying Physical Sources for Antisymmetric Pockets of Correlated Flow Fluctuations



lines appeared to radiate, a distance equal to one-half the wing thickness upstream from the wing geometric trailing edge.

Figure 7-8 shows detail of the conjectured flow in the vicinity of the rolled up vortex. The detail is of the instantaneous flow in a plane normal to the mean flow; i.e. in the lateral and transverse directions. The significant feature of the detail is the saddle point produced by the counterrotating vortices from the horseshoe vortex and the vortex sheet on the wall. Topological considerations of continuous fluids require a third vortex near the wall, as depicted in the figure. The third vortex contains fluid with low longitudinal momentum.

The above features are conjectured to produce the antisymmetric pockets of correlated fluid shown in Figures 7-9. The figure corresponds to measured data given previously in Figure 6-30. Figure 7-9 contains a description of the flow accelerations and decelerations, and the corresponding displacement of the third (low momentum) vortex producing the various "pockets" of flow structure.

### 7.3 Conclusions

Consideration of the evidence obtained in this investigation of the large scale temporal flow in the wing-body junction supports the following conclusions:

- (1) The onset boundary layer temporal flow structure passes intact, although greatly deformed, through the wing-body junction flow to the trailing edge region of the wing, where it encounters adverse pressure gradients and is modified or replaced to form new flow structures downstream from the wing.
- (2) For the particular configuration studied the wing-body junction flow is characterized by three disturbance structures distinguished by frequency bandwidth. Bandwidth I is initiated in the onset boundary layer and not in the wing-body junction wake flow. Bandwidth II may also be present in the onset boundary layer at positions close to the wall but, in any event, appears away

from the wall in the boundary layer interaction flow around and downstream from the wing. Bandwidth III appears downstream in the wing-body junction wake flow and is clearly the result of the presence of the wing. The three bandwidths contain frequencies at least an order of magnitude smaller than the ordinary Strouhal-type shedding from the wing trailing edge outside the boundary layer.

(3) The large-scale structure downstream from the wing (Bandwidth III) is dependent for its frequency on the nose shape of the wing, probably because of its effect on root vortex intensity.

(4) The horseshoe vortex apex (origin at the wall separation upstream from the wing leading edge) does not exhibit a characteristic or resonant frequency at least for the set of parameters studied in this investigation.

These conclusions on the temporal flow structure should be further tested to ascertain their range of validity.

In the course of this investigation limited studies were made to verify the general features of the mean flow. From those studies, the following additional conclusions were made:

(5) The mean flow in the wing-body junction is characterized by a root vortex originating with the wall separation immediately upstream from the wing leading edge, along with various other forms of three-dimensional separations originating in the trailing edge region.

(6) The pressure effects of the wing leading edge extend upstream a distance on the order of 10 wing thicknesses.

# LIST OF LITERATURE CITED

- Baker, C.J. (1978)  
"Vortex Flow Around the Bases of Obstacles," Ph.D Thesis,  
University of Cambridge.
- Barber, T.J. (1978)  
"An Investigation of Strut-Wall Intersection Losses," Journal  
of Aircraft, Vol. 15, No. 10, p. 676-681.
- Bendat, J.S. and Piersol, A.G. (1980)  
Engineering Applications of Correlation and Spectral  
Analysis, John Wiley & Sons.
- Champagne, F.H.; Harris, V.G.; and Corrsin, S. (1970)  
"Experiments on Nearly Homogeneous Turbulent Shear Flow,"  
Journal of Fluid Mechanics, Vol. 41, Pt. 1, pp. 81-139.
- Chu, J.K. and Young, A.D. (1975)  
"Further Investigation of Viscous Effects in a Wing-Plate  
Junction," Queen Mary College Report QMC ER-1003.
- Comte-Bellot, G. and Corrsin, S. (1971)  
"Simple Eulerian Time Correlation of Full- and Narrow-Band  
Velocity Signals in Grid Generated 'Isotropic' Turbulence,"  
Journal of Fluid Mechanics, Vol. 48, Pt. 2, pp. 273-337.
- Dechow, R. and Felsch, K.O. (1977)  
"Measurements of the Mean Velocity and of the Reynolds Stress  
Tensor in a Three-Dimensional Turbulent Boundary Layer  
Induced by a Cylinder Standing on a Flat Wall," Symposium  
on Turbulent Shear Flows, University Park, Pa.
- East, L.F. and Hoxey, R.P. (1969)  
"Low Speed Three-Dimensional Turbulent Boundary Layer Data,  
Parts 1 and 2," A.R.C. R&M No. 3653.
- Favre, A.J.; Gaviglio, J.J.; and Dumas, R.J. (1958)  
"Further Space-Time Correlations of Velocity in a Turbulent  
Boundary Layer," Journal of Fluid Mechanics, Vol. 3, Pt. 4,  
pp. 344-356.
- Hinze, J.O. (1975)  
Turbulence, Second Edition, McGraw-Hill Book Company.
- Jenkins, G.M. and Watts, D.G. (1968)  
Spectral Analysis and Its Applications, Holden-Day.

Love, R.H. (1963)

"An Investigation of the Effect of the Wall Boundary Layer on the Wake of An Obstacle Protruding from the Wall," University of Maryland Technical Note BN-370.

Oguz, E.A. (1981)

"An Experimental Investigation of the Turbulent Flow in the Junction of a Flat Plate and a Body of Constant Thickness," Ph.D Thesis, Georgia Institute of Technology.

Pal, S. (1981)

"Wake Boundary Layer Interaction in Turbomachinery," Ph.D Thesis, the City College of the C.U.N.Y.

Peake, D.J. and Tobak, M. (1980)

"Three-Dimensional Interactions and Vortical Flows with Emphasis on High Speeds," AGARDograph No. 252.

Peake, D.J.; Galway, R.D.; and Rainbird, W.J. (1965)

"The Three-Dimensional Separation of a Plane Incompressible Laminar Boundary Layer Produced by a Rankine Oval Mounted Normal to a Flat Plate," National Research Council of Canada Report LR-446.

Pierce, F.J. and McAllister, J.E. (1980)

"Near-Wall Similarity in a Pressure-Driven Three-Dimensional Turbulent Boundary Layer," Virginia Polytechnic Institute and State University Report VPI-E-80.32.

Rao, K.N., Narasimha, R., and Narayanan, M.A.B. (1971)

"The 'Bursting' Phenomenon in a Turbulent Boundary Layer," Journal of Fluid Mechanics, Vol. 48, Pt.2.

Schlichting, H. (1979)

Boundary-Layer Theory, McGraw-Hill Book Company.

Scottron, V.E. and Shaffer, D.A. (1965)

"The Low Turbulence Wind Tunnel," David Taylor Model Basin Report 2116.

Schwind, R.G. (1962)

"The Three-Dimensional Boundary Layer Near a Strut," MIT Gas Turbine Laboratory Report No. 67.

Sepri, P. (1973)

"An Investigation of the Flow in the Region of the Junction of a Wing and a Flat Surface Normal to the Wing Span," Queen Mary College Report QMC ER-1002.

Shabaka, I.M.M.A. (1979)

"Turbulent Flow in an Idealized Wing-Body Junction," Ph.D Thesis, Imperial College of Science and Technology.

Simpson, R.L.; Chew, Y.-T.; and Shivaprasad, R.G. (1981)

"The Structure of a Separating Turbulent Boundary Layer: Part 1: Mean Flow and Reynolds Stresses and Part 2: Higher-Order Turbulence Results" Journal of Fluid Mechanics, Vol. 113.

Simpson, R.L.; Shivaprasad, B.G.; and Chew, Y.-T (1983)

as above, "Part 4: Effects of Periodic Freestream Unsteadiness," Journal of Fluid Mechanics, Vol. 127.

Strickland, J.H. and Simpson, R.L. (1975)

"'Bursting' Frequencies Obtained from Wall Shear Stress Fluctuations in a Turbulent Boundary Layer," The Physics of Fluids, Vol. 18, No. 3.

Sung, C.-H. (1983)

"Numerical Wake Prediction Methods for Submerged Appended Bodies, A Literature Survey," David Taylor Naval Ship R&D Center Report DTNSRDC/SPD-1057-01.

Tobak, M. and Peake, D.J. (1979)

"Topology of Two-Dimensional and Three-Dimensional Separated Flows," AIAA 12th Fluid and Plasma Dynamics Conference, Williamsburg, Va.

Tobak, M. and Peake, D.J. (1981)

"Topology of Three-Dimensional Separated Flows," NASA-TM-81294.

White, F.M. (1974)

Viscous Fluid Flow, McGraw-Hill Book Company.

# BIBLIOGRAPHY

- Ainley D.G., and Matheieson, G.C.R., "An Examination of the Flow and Pressure Losses in Blade Rows of Axial Flow Turbines," ARC Reports & Memoranda No. 2891 (1951).
- Andreopoulos, J., "Symmetric and Asymmetric Near Wake of a Flat Plate," Ph.D. Thesis, University of London (1951).
- Armstrong, W.D., "The Secondary Flow in a Cascade of Turbine Blades," ARC Reports & Memoranda No. 2979 (1955).
- Armstrong, W.D., "An Experimental Investigation of the Secondary Flow Occurring in a Compressor Cascade," Aeronautical Quarterly, Vol. 8, p. 240 (1957).
- Arnal, D., and Consteix J., "Subsonic Flow in a Corner," La Recherche Aerospatiale 1981-1982, pp.45-62 (1981).
- Baker, C.J., "Vortex Flow Around the Bases of Obstacles," PhD Thesis, University of Cambridge (1978).
- Baker, C.J., "The Laminar Horseshoe Vortex," Journal of Fluid Mechanics, Vol. 95, pp. 347-367 (1979).
- Baker, C.J., "The Turbulent Horseshoe Vortex," Journal of Wind Engineering and Industrial Aerodynamics, Vol. 6, pp. 9-23 (1980).
- Barber, T.J., "An Investigation of Strut-Wall Intersection Losses," Journal of Aircraft, Vol. 15, pp. 676-681 (1978).
- Belik, L., "The Secondary Flow about Circular Cylinders Mounted Normal to a Flat Plate," Aeronautical Quarterly, Vol. 24 (Feb 1973).
- Bendat, J.S., and Piersol, A.G., (1980) Engineering Applications of Correlation and Spectral Analysis, John Wiley & Sons.
- Booth, T.C., "An Analysis of the Turbine Endwall Boundary Layer and Aerodynamic Losses," ASME Paper No. 75-GT-23 (Mar 1975).
- Bradshaw, P., Shabaka, I.M.M.A., and Mehta, R.D., "Turbulent Vortex Flows," Imperial College of Science and Technology Report I.C. Aero TN 82-103 (1982).
- Came, P.M., "Secondary Loss Measurements in a Cascade of Turbine Blades," Instn. Mechanical Engineers, Conference, Publ. 3, p. 75 (1973).
- Carrick, H.B., "Calculation of End-Wall Flow in Turbine Cascades," ARC 35.916, Turbo. 353, Cambridge Univ., SRC Turbomachinery Lab (1974).

- Carrick, H.B., "Preliminary Experimental Results on the Effect of Skew in the Boundary Layer on the Secondary Flow in an Impulse Turbine Cascade," ARC 35.915, Turbo. 352 (1975).
- Carter, A.D.S., and Cohen, E.M., "Preliminary Investigation Into the Three-Dimensional Flow Through a Cascade of Aerofoils," ARC Report and Memo. No. 2339 (1946).
- Cebeci, T., and Brandshaw, P., Momentum Transfer in Boundary Layers, Hemisphere Publishing Corporation, McGraw Hill Book Co. (1977).
- Cenedese, A., Cerri, G., and Ianeta, S., "Experimental Analysis of the Wake behind an Isolated Cambered Airfoil," Unsteady Turbulent Shear Flows, IUTAM Symposium (May 1981).
- Champagne, F.H., Harris, V.G., and Corrsin, S., "Experiments on Nearly Homogeneous Turbulent Shear Flow," Journal of Fluid Mechanics, Vol. 41, Pt. 1 (1970).
- Chu, J.K., and Young, A.D., "A Further Investigation of Viscous Effects in a Wing-Plate Junction," Queen Mary College Departmental Rept., ER 1003 (1975).
- Comte-Bellot, G., and Corrsin, S., "Simple Eulerian Time Correlation of Full- and Narrow-Band Velocity Signals in Grid Generated 'Isotropic' Turbulence," Journal of Fluid Mechanics, Vol. 48, Pt. 2 (1971).
- Cooke, J.C., and Breoner G.G., "The Nature of Separation and Its Prevention by Geometric Design in a Wholly Subsonic Flow," Boundary Layer and Flow Control, G.V. Lachmann ed., Vol. 1, pp. 144-185 (1961).
- Cumpsty, N.A., and Head, M.R., "The Calculation of Three-Dimensional Turbulent Boundary Layers; Part IV, Comparison with Measurements on the Rear of a Swept Wing," The Aeronautical Quarterly (May 1970).
- Daiguji, H., and Shirahata, H., "The Secondary Flow about a Circular Cylinder," Bulletin of the JSME, Vol. 22, pp. 925-932 (1979).
- Dechow, R., and Felsch, K.O., "Measurement of the Mean Velocity and of the Reynolds Stress Tensor in a Three Dimensional Turbulent Boundary Layer Induced by a Cylinder Standing on a Flat Wall," Symposium on Turbulent Shear Flow, Pennsylvania State University, pp. 9.11-9.20 (1977).
- Dunham, J., "A Review of Cascade Data on Secondary Losses in Turbines," Journal of Mechanical Engineering Science, Vol. 12, No. 1, p. 48 (1970).

- East, L.F., and Hoxey, R.P., "Boundary Layer Effects in an Idealized Wing-Body Junction at Low Speed," Royal Aircraft Establishment, Tech. Report TR68161 (1968).
- East, L.F., and Hoxey, R.P., "Low-Speed Three-Dimensional Turbulent Boundary Layer Data Part 2," Royal Aircraft Establishment Tech. Report TR69137 (1969).
- East, L.F., and Hoxey, R.P., "Low-Speed Three-Dimensional Turbulent Boundary Layer Data, Parts 1 and 2," Aeronautical Research Council, Reports and Memoranda, No. 3653 (1969).
- Favre, A.J., Gaviglio, J.J., and Dumas, R.J., "Further Space-Time Correlations of Velocity in a Turbulent Boundary Layer," Journal of Fluid Mechanics, Vol. 3, Pt. 4 (1958).
- Flax, A.H., and Lawrence, H.R., "The Aerodynamics of Low-Aspect-Ratio Wings and Wing-Body Combinations," Proc. Third Anglo-American Aeronaut. Conf., Brighton, p. 363 (1951).
- Francis, G.P., and Pierce, F.J., "An Experimental Study of Skewed Turbulent Boundary Layers in Low Speed Flows," Journal of Basic Engineering, ASME, Vol. 89 (Sep 1967).
- Gaugler, R.E. and Russell, L.M., "Flow Visualization Study of the Horseshoe Vortex in a Turbine Stator Cascade," NASA Tech Paper 1884 (1982)
- Gersten, K., "Corner Interference Effects," AGARD Report 299 (1959).
- Gessner, F.B., and Ono, S., "Investigations of Adverse Pressure Gradient Corner Flows," Project SQUID Semi-Annual Progress Report (Apr 1978).
- Hawthorne, W.R., "Secondary Circulation in Fluid Flow," Proc. Roy. Soc., Series A., No. 206, p. 374 (1951).
- Hawthorn, W.R., "The Secondary Flow about Struts and Airfoils," Journal of the Aeronautical Sciences (Sep 1954).
- Herzig, H.Z., Hansen, A.G. and Costello, G.R., "A Visualization Study of Secondary Flows in Cascades," NACA Report 1163 (1953).
- Hinze, J.O., Turbulence, Second Edition, McGraw-Hill Book Company (1975).
- Horlock, J.H., and Lakshminarayana, B., "Secondary Flows: Theory, Experiment and Application in Turbomachinery Aerodynamics," Annual Review of Fluid Mechanics, Vol. 5, pp. 247-280 (1973).



- Horlock, J.H., "Cross Flows in Bounded Three-Dimensional Turbulent Boundary Layers," Journal of Mechanical Engineering Science, Vol. 15, pp. 274-284 (1973).
- Hornung, H.G., and Joubert, P.N., "The Mean Velocity Profile in Three-Dimensional Turbulent Boundary Layers," Journal of Fluid Mechanics, Vol. 15, pt. 3 (1963).
- Hubbartt, J., McMahon, H., and Oguz, E., "Exploratory Tests of Flow in Wing-Root Junctions," Georgia Institute of Technology, School of Aerospace Engineering, Final Report, Contract No. P.O. CK27034P, Lockheed-Georgia Company, Marietta, Georgia (Mar 1976).
- Hunt, J.C.R., Abell, C.J., Peterka, J.A., and Woo, H. "Kinematical Studies of the Flows Around Free or Surface-Mounted Obstacles: Applying Topology to Flow Visualization," Journal of Fluid Mechanics, Vol. 86, pp. 179-200 (1978).
- Jenkins, G.M. and Watts, D.G., Spectral Analysis and Its Applications, Holden-Day (1968).
- Johnston, J.P., "On the Three-Dimensional Turbulent Boundary Layer Generated by Secondary Flows," Journal of Basic Engineering, Trans. ASME, Vol. 82, No. 1, p. 233 (1960).
- Johnston, J.P., "Measurements in a Three-Dimensional Turbulent Boundary Layer Induced by a Swept, Forward-Facing Step," Journal of Fluid Mechanics, Vol. 42, pp. 823-844 (1970).
- Johnston, P. James, "The Turbulent Boundary Layer at a Plane of Symmetry in a Three-Dimensional Flow," Journal of Basic Engineering, Trans. ASME, Vol. 82 (Sep 1960).
- Kitchens, C.W., Gerber, N., Sedney, R., and Bartos, J.M. "Streamwise Vorticity Decay Downstream of a Three-Dimensional Protuberance," ARBRL-TR-02375 (1981).
- Klinksiek, W.F., and Pierce, F.J., "Simultaneous Lateral Skewing in a Three-Dimensional Turbulent Boundary-Layer Flow," Journal of Basic Engineering, Trans. ASME, Vol. 92 (Mar 1970).
- Kuchemann, D., "Some Remarks on the Inteferece Between a Swept Wing and Fuselage," Aerodynamic Interference, AGARD Conference Proceedings, No. 71 (Jan 1971).
- Kuchemann, D., The Aerodynamic Design of Aircraft, Pergamon Press (1978).
- Langston, L.S., Nice, M.L., and Hooper, R.M., "Three-Dimensional Flow Within a Turbine Cascade Passage," Journal of Engineering for Power, p. 21 (Jan 1977).

- Langston, L.S., "Crossflows in a Turbine Cascade Passage," Journal of Engineering for Power, Vol. 102, pp. 866-874 (1980).
- Liggett, J.A., Chiu, C.L., and Miao, L.S., "Secondary Currents in a Corner," Journal of Hydraulics Division, Proc. ASCE, Vol. 91, p.99 (1965).
- Loitsianskii, L.G., "Interference of Boundary Layers," Central Aero-Hydrodynamical Institute, Moscow, Report 249 (English Translation - ARC 3186-FM342) (1936).
- Loitsianskii, L.G., and Dolshakov, V.P., "On Motion of Fluid in a Boundary Layer Near Line of Intersection of Two Planes," NACA TM1308 (1951).
- Louis, J.F., "Secondary Flow and Losses in a Compressor Cascade," ARC Report & Memo 3136 (1958).
- Love, R.H., "An Investigation of the Effect of the Wall Boundary Layer on the Wake of an Obstacle Protruding From the Wall," University of Maryland Technical Note BN-370 (1963).
- Marchal, P.H., and Sieverding, C.H., "Secondary Flows Within Turbomachinery Bladings," AGARD C P-214 on Secondary Flows in Turbomachinery, No. 11 (1977).
- McMahon, H., Hubbarth, J., and Kubendran, L., "Mean Velocities and Reynolds Stresses in a Juncture Flow," Status Report, Georgia Institute of Technology (Feb 1981).
- Mojola, O.O., "Turbulent Boundary Layer Along a Streamwise Corner," Ph.D. Thesis, University of London (1972).
- Majola, O.O., and Young, A.D., "An Experimental Investigation of the Turbulent Boundary Layer Along a Streamwise Corner," Turbulent Shear Flows, AGARD Conference Proceedings, No. 93 (Jan 1972).
- Naranjit, S., "An Investigation of the Flow Over a Wing-Body Combination," Ph.D. Thesis, University of London (1976).
- Nomura, Y., "Theoretical and Experimental Investigations on the Incompressible Viscous Flow Around the Corner," Memo. of the Defence Academy of Japan, Vol. 2, No. 3 (1962).
- Oguz, E.A., "An Experimental Investigation of the Turbulent Flow in the Junction of a Flat Plate and a Body of Constant Thickness," Ph.D Thesis, Georgia Institute of Technology (1981).
- Pal, A., and Rubin, S.G., "Asymptotic Features of the Viscous Flow Along a Corner," Quarterly of Applied Mathematics, Vol. 29, p.91 (1971).

- Pal, S., "Wake Boundary Layer Interaction on Turbomachinery," Ph.D Thesis, The City College of the CUNY (1981).
- Peake, D.J., and Galway, R.D., "The Three-Dimensional Separation of a Plane Incompressible Laminar Boundary Layer Produced by a Circular Cylinder Mounted Normal to a Flat Plate," National Research Council of Canada Report LR-428 (May 1965).
- Peake, D.J., Galway, R.D., and Rainbird, W.J., "The Three-Dimensional Separation of Plane Incompressible Laminar Boundary Layer Produced by a Rankine Oval Mounted Normal to a Flat Plate," National Research Council of Canada Report LR-446 (Nov 1965).
- Peake, D.J., Rainbird, W.J., and Atraghji, E.G., "Three-Dimensional Flow Separations on Aircraft and Missiles," AIAA Journal, Vol. 10, No. 5 (May 1972).
- Peake, D.J., "Controlled and Uncontrolled Flow Separation in Three Dimensions," Aeronautical Report LR-591, National Research Council of Canada (Jul 1976).
- Peake, D.J., and Tobak, M., "Three-Dimensional Interactions and Vortical Flows with Emphasis on High Speeds," AGARD-AG-252 (1980).
- Penken, J.H., "Corner Layer and Secondary Flow Within a Straight Compressor Cascade," Paper 21, AGARD-CP-214, on Secondary Flows in Turbomachines (1977).
- Perkins, H.J., "The Turbulent Corner Boundary Layer," Ph.D Thesis University of Cambridge (1970).
- Perkins, H.J., "The Formation of Streamwise Vorticity in Turbulent Flow," Journal of Fluid Mechanics, Vol. 44, Part 4, p. 721 (1970).
- Pierce, F.J., and McAllister, J.E., "Near-Wall Similarity in a Pressure-Driven Three Dimensional Turbulent Boundary Layer," Report VPI-E-80.32, Virginia Polytechnic Institute and State University (Sep 1980).
- Pierce, F.J., and McAllister, J.E., "Measurements in a Pressure-Driven and a Shear-Driven Three-Dimensional Turbulent Boundary Layer," Three-Dimensional Turbulent Boundary Layers, Fernholz, H.H. and Krause, E. (ed.), IUTAM Symposium (1982).
- Prahlad, T.S., "Mean Velocity Profiles in Three-Dimensional Incompressible Turbulent Boundary Layers," AIAA Journal, Vol. 11, No. 3 (Mar 1973).

- Rainbird, W.J., Crabbe, R.S., Peake, D.J., and Meyer, R.F.,  
 "Some Examples of Separation in Three-Dimensional Flows,"  
Canadian Aeronautics and Space Journal, Vol. 12 (Dec 1966).
- Rao, K.N., Narasimha, R., and Narayanan, M.A.B. (1971) "The  
 'Bursting' Phenomenon in a Turbulent Boundary Layer," Journal  
 of Fluid Mechanics, Vol. 48, Pt. 2.
- Rubin, S.G., "Incompressible Flow Along a Corner," Journal of Fluid  
 Mechanics, Vol. 26, Pt. 1, p. 97 (1966).
- Salvage, J.W., "Investigation of Secondary Flow Behaviour and the  
 Endwall Boundary Layer Development Through Compressors'  
 Cascades," VKI, TN107 (1974).
- Sarohia, S., and Young, A.D., "Wind Tunnel Investigations of Some  
 Three-Dimensional Separated Turbulent Boundary Layers," Three-  
 Dimensional Turbulent Boundary Layers, Fernholz, H.H. and  
 Krause, E. (ed.), IUTAM Symposium (1982).
- Schlichting, H., Boundary-Layer Theory, McGraw-Hill Book  
 Company (1979).
- Schwind, R.G., "The Three-Dimensional Boundary Layer Near a Strut,"  
 MIT Gas Turbine Laboratory Report No. 67 (1962).
- Sedney, R., and Kitchens, C.W., "The Structure of Three Dimensional  
 Separated Flows in Obstacle, Boundary Layer Interactions,"  
 AGARD-CP-168: Flow Separation, pp. 37.1-37.15 (1975).
- Sepri, P., "An Investigation of the Flow in the Region of the  
 Junction of a Wing and a Flat Surface Normal to the Wing  
 Span," Queen Mary College Departmental Report, QMC ER-1002  
 (1973).
- Senoo, Y., "The Boundary Layer on the End Wall of a Turbine Nozzle  
 Cascade," Trans. Am. Soc. Mech. Engrs., Vol. 80, p. 1711  
 (1958).
- Sevik, M., "A Discussion on a Paper by J.B. Hadler and Henry M.  
 Cheng, 'Analysis of Experimental Wake Data in Way of Propeller  
 Plane of Single and Twin-Screw Ship Models,'" Transactions of  
 SNAME, Vol. 73, pp. 386-389 (1965).
- Shabaka, I.M.M.A., "A Preliminary Experimental Investigation of  
 Turbulent Flow in a Simplified Wing-Body Junction," Imperial  
 College Aero Report 75-05 (1975).
- Shabaka, I.M.M.A., "Turbulent Flow in an Idealized Wing-Body  
 Junction," Ph.D Thesis, University of London (Apr 1979).
- Shiloh, K., Shivaprasad, B.G., and Simpson, R.L., "The Structure  
 of a Separating Turbulent Boundary Layer. Part III:

- Transverse Velocity Measurements," Journal of Fluid Mechanics Vol. 113 (1981).
- Simpson, R.L., "A Review of Some Phenomena in Turbulent Flow Separation," Journal of Fluid Engineering, Vol. 103, pp. 520-533 (1981).
- Simpson, R.L., Strickland, J.H., and Barr, P.W., "Features of a Separating Turbulent Boundary Layer in the Vicinity of Separation," Journal of Fluid Mechanics, Vol. 79, pp. 553-594 (1977).
- Simpson, R.L., Chew, Y.-T., and Shinaprasad, B.G., "The Structure of a Separating Turbulent Boundary Layer. Part I: Mean Flow and Reynolds Stresses," Journal of Fluid Mechanics, Vol. 113 (1981).
- Simpson, R.L., Chew, Y.-T., and Shivaprasad, B.G., "The Structure of a Separating Turbulent Boundary Layer. Part II: Higher Order Turbulence Results," Journal of Fluid Mechanics, Vol. 113 (1981).
- Simpson, R.L., Shivaprasad, B.G., and Chew, Y.-T., "The Structure of a Separating Turbulent Boundary Layer. Part IV: Effects of Periodic Freestream Unsteadiness," Journal of Fluid Mechanics, Vol. 127 (1983).
- Simpson, R.L., and Shivaprasad, B.G., "The Structure of a Separating Turbulent Boundary Layer, Part V: Frequency Effects on Periodic Unsteady Freestream Flows," Journal of Fluid Mechanics, Vol. 131 (1983).
- Sjolander, S.A., "The End-Wall Boundary Layer in an Annular Cascade of Turbine Guide Vanes," Carleton University, Dept. Mech. & Aerosp. Engng., Ottawa, Canada, TR ME/A 75-4 (1975).
- Smith, J.H.B., "A Review of Separation in Steady Three-Dimensional Flow," Flow Separation, AGARD-CP-168, pp. 31.1-31.17 (1975).
- Smith, L.H., "Secondary Flow in Axial-Flow Turbomachinery," Trans. ASME, Vol. 77, p. 1065 (1955).
- Squire, H.B. and Winter, K.G., "The Secondary Flow in a Cascade of Aerofoils in a Non-Uniform Stream," Journal of Aeronautical Science, Vol. 18, p. 271 (1951).
- Stanbrook, A., "Experimental Observations of Vortices in Wing-Body Junctions," Aeronautical Research Council, Reports and Memoranda, No. 3114 (Mar 1957).
- Steinheuer, J., "Three-Dimensional Boundary Layers on Rotating Bodies and in Corners," in: Recent Developments in Boundary-Layer Research, AGARDograph 97, Part II (May 1965).
- Strickland, J.H., and Simpson, R.L. "'Bursting' Frequencies Obtained

- From Wall Shear Stress Fluctuations in a Turbulent Boundary Layer," The Physics of Fluids, Vol. 18, No. 3 (1975).
- Sung, C.-H., "Numerical Wake Prediction Methods for Submerged Appended Bodies, A Literature Survey," David Taylor Naval Ship R&D Center Report DTNSRDC/SPD-1057-01 (1983).
- Swamy, N.V.C., and Narayana, P.A.A., "Turbulent Boundary Layers Over Yawed Flat Plates at Incidence," Zeitschrift fur Flugwissenschaften, 23, Heft 11 (1975).
- Stewart, W.L., Whitney, W.J., and Wong, R.Y., "A Study of Boundary Layer Characteristics of Turbomachine Blade Rows and Their Relation to Overall Blade Loss," Journal of Basic Engineering Trans. ASME. Vol. 82, Series D, p. 588 (1960).
- Taylor, E.S., "Secondary-Flow," in: Illustrated Experiments in Fluid Mechanics, the N.C.F.M.F. Book on Film Notes, The M.I.T. Press (1972).
- Thwaites, B., Editor, Incompressible Aerodynamics, (Chapter XII), Oxford University Press (1960).
- Tobak, M., and Peake, D.J., "Topology of Two-Dimensional and Three-Dimensional Separated Flow," AIAA 12th Fluid and Plasma Dynamics Conference, Williamsburg, VA (23-25 Jul 1979).
- Tobak, M., and Peake, D.J., "Topology of Three-Dimensional Separated Flows," NASA-TM-81294 (1981).
- Veenhuizen, S.D., and Meroney, R.N., "Secondary Flow in a Boundary Layer," Project THEMIS, Technical Report No. 3, Fluid Dynamics and Diffusion Laboratory, College of Engineering, Colorado State University (Jun 1969).
- Wang, K.C., "New Developments in Open Separation," Three-Dimensional Turbulent Boundary Layers, Fernholz, H.H. and Krause, E. (ed.), IUTAM Symposium (1982).
- Weber, J., "Interference Problems in Wing-Fuselage Combinations - Part 1: Lifting Unswept Wing Attached to a Cylindrical Fuselage at Zero Incidence in Midwing Position," ARC Current Papers, C.P. No. 1331 (1975).
- Werle, H., "Ecoulements Decolles: Etude Phenomenologique at Partie de Visualisations Hydrodynamiques," AGARD CP-168, Paper 39 (1975).
- White, F.M., Viscous Fluid Flow, McGraw-Hill Book Company (1974).
- Winkelmann, A.E., and Melnik, W.L., "An Experimental Investigation of a Two and a Three-Dimensional Low Speed Turbulent Boundary

Layer," University of Maryland, College Park, Department of Aerospace Engineering, Technical Report No. AE-76-2 (Dec 1976).

Young, A.D., "Some Special Boundary Layer Problems," Z. Flugwiss. Weltraumforsch. 1, Heft 6, p. 401 (1977).

Young, A.D., "Some Special Boundary Layer Problems," 20th Ludwig Prandtl Memorial Lecture, Zeitschrift fur Flugwissenschaften und Weltraumforschung, (Nov./Dec. 1977).

Zamir, M., "Boundary Layer Flow in Streamwise Corners," Ph.D Thesis, University of London (1968).

Zamir, M., "Boundary Layer Theory and the Flow in a Streamwise Corner," Aeronautical Journal of the Royal Aeronautical Society, Vol. 74, p. 330 (1970).

Zamir, M., and Young, A.D., "Experimental Investigation of the Boundary Layer in a Streamwise Corner," Aeronautical Quarterly, Vol., 21, p. 313 (1970).

Zamir, M., "On the Corner Boundary Layer with Favourable Pressure Gradient," Aeronautical Quarterly, Vol. 23, p. 161 (1972).

Zamir, M., "Further Solution of the Corner Boundary Layer Equations," Aeronautical Quarterly, Vol. 24, p. 219 (1973).

Zimmerman, D.R., and Abbott, D.E., "An Experimental Investigation of a Three-Dimensional Turbulent Boundary Layer," ASME Paper 77-WA/FE-22 (1977).

REPORT DOCUMENTATION PAGE		READ INSTRUCTIONS BEFORE COMPLETING FORM
1. REPORT NUMBER HA84-1	2. GOVT ACCESSION NO. DDA 139 836	3. RECIPIENT'S CATALOG NUMBER
4. TITLE (and Subtitle) Experimental Investigation of the Turbulent Large Scale Temporal Flow in the Wing-Body Junction		5. TYPE OF REPORT & PERIOD COVERED Doctoral Dissertation
7. AUTHOR(s) Edwin P. Rood, Jr.		6. PERFORMING ORG. REPORT NUMBER
9. PERFORMING ORGANIZATION NAME AND ADDRESS David W. Taylor Naval Ship Research and Development Center, Bethesda, Md.		8. CONTRACT OR GRANT NUMBER(s) RR023-01-01
11. CONTROLLING OFFICE NAME AND ADDRESS		10. PROGRAM ELEMENT, PROJECT, TASK AREA & WORK UNIT NUMBERS
14. MONITORING AGENCY NAME & ADDRESS (if different from Controlling Office) Office of Naval Research 800 N. Quincy Street Arlington, VA 22217		12. REPORT DATE March, 1984
		13. NUMBER OF PAGES
		15. SECURITY CLASS. (of this report) Unclassified
		15a. DECLASSIFICATION/DOWNGRADING SCHEDULE
16. DISTRIBUTION STATEMENT (of this Report) Approved for public release; distribution unlimited.		
17. DISTRIBUTION STATEMENT (of the abstract entered in Block 20, if different from Report)		
18. SUPPLEMENTARY NOTES		
19. KEY WORDS (Continue on reverse side if necessary and identify by block number) Wing-Body Junction Flows Large Scale Temporal Flow Turbulent Flow		
20. ABSTRACT (Continue on reverse side if necessary and identify by block number) An experimental investigation of the fluid dynamic flow in the wing-body junction was made to reveal the existence of large scale, time-dependent structures. These temporal features are discussed relative to the three major parts of the mean flow: the onset boundary layer, the wing-body junction flow characterized by the horseshoe root vortex, and the wing-body junction wake flow. Distinct flow structures, distinguished by bandwidths, were observed in all parts of the flow. One type of structure was due to the distortion of the existing (OVER)		



20. ABSTRACT

structure of the onset boundary layer by the wing. A second and a third structure were newly created in the flow by the presence of the wing. These unique structures along the body were boundary layer phenomena, clearly distinguishable from ordinary Strouhal-type shedding at the wing trailing edge.

The measurements distinguishing the structures were made using applications of two-point spectral correlation analyses of the flow velocities. The application of this established procedure was made possible by modern high speed data techniques. An orderly framework of definitions and discussion is presented around which additional research can be performed to discover the details of the flow structure.

END

FILMED

5-84

DTIC